Iodine plasmas : experimental and numerical studies. Application to electric propulsion

Florian Marmuse



THÈSE DE DOCTORAT
de Sorbonne Université

Spécialité : Physique

École doctorale n°564: Physique en Île-de-France

réalisée

au Laboratoire de Physique des Plasmas

sous la direction de Cyril Drag et Ane Aanesland

présentée par

Florian Marmuse

Sujet de la thèse :

Iodine plasmas: experimental and numerical studies Application to electric propulsion

soutenue le 9 juillet 2020

devant le jury composé de :

Prof.	Riconda Caterina,	Sorbonne Université,	Présidente du jury
Prof.	Gans Timo,	University of York,	Rapporteur
Dr.	Garrigues Laurent,	CNRS,	Rapporteur
Dr.	Packan Denis,	ONERA,	Examinateur
Dr.	Sisourat Nicolas,	Sorbonne Université,	Examinateur
Dr.	Aanesland Ane,	ThrustMe,	Directrice de Thèse
Dr.	Drag Cyril,	CNRS,	Directeur de Thèse

“The point is, you see," said Ford, "that there is no point in driving yourself mad trying to stop yourself going mad. You might just as well give in and save your sanity for later.”

Douglas Adams
Life, the Universe and Everything

Résumé de la thèse

L'iode est un carburant alternatif pour la propulsion électrique des satellites, avec des performances comparables à celles du xénon. En 2020, de tels systèmes de propulsion à l'iode sont déjà sur le marché. Ces bonnes performances sont liées à la très basse énergie de dissociation de I_2, produisant un plasma similaire à un plasma de xénon. À quel point peut-on négliger la nature moléculaire et électronégative des plasmas d'iode ? Un modèle global de plasma d'iode est amélioré et recodé en python, permettant des analyses paramétriques rapides, la quantification des incertitudes, et intégrant des effets électronégatifs. Des outils et procédures sont mis en place pour la pérennité des installations durant les expériences à l'iode. Quatre diagnostics optiques sont développés et installés sur la chambre d'ionisation du propulseur PÉGASES. Ils mènent, pour la première fois, à la température de I, ainsi qu'à la densité de I et I_2: spectroscopie d'émission, spectroscopie d'absorption laser et absorption saturée à $10\,969\,\mathrm{cm}^{-1}$ et $11\,036\,\mathrm{cm}^{-1}$, absorption laser à $7603\,\mathrm{cm}^{-1}$, et absorption large-bande de 480 nm à 500 nm. Confronter ces données et celles issues d'une sonde de Langmuir au modèle global montre que le modèle surestime la dissociation de I_2 et la densité électronique. Ces écarts peuvent être partiellement expliqués par des pertes de puissance sous-estimées dans le plasma, possiblement liées à sa nature moléculaire et électronégative. Ce travail donne des pistes pour de nouvelles études théoriques et de nouveaux diagnostics sur les plasmas d'iode. Il propose un modèle mis à jour et un panel de nouveaux diagnostics, utiles pour le développement de nouveaux systèmes de propulsion à l'iode.

Executive summary

Iodine is an alternative propellant for the electric propulsion of satellites, offering performances comparable to xenon. As of 2020, propulsion systems running on iodine are already on the market. These good performances are linked to the very low dissociation energy of I_2, leading to a plasma similar to an atomic xenon plasma. To which extent can the molecular and electronegative nature of iodine plasmas be neglected? An existing global model for I_2 plasmas is further developed and fully recoded in python, to enable fast parametric studies, uncertainty quantification, and integrate electronegative effects. Tools and processes are developed to ensure the safety of operators and experimental setups during iodine experiments. Four optical diagnostics are developed and installed on the ionization chamber of the PEGASES thruster. They lead for the first time to the density and temperature of I, and the density of I_2: emission spectroscopy, laser absorption coupled to Doppler-free saturated absorption spectroscopy at $10\,969\,\mathrm{cm}^{-1}$ and $11\,036\,\mathrm{cm}^{-1}$, laser absorption spectroscopy at $7603\,\mathrm{cm}^{-1}$, and broadband absorption spectroscopy from 480 nm to 500 nm. Langmuir probe measurements yield the electron density and temperature. Confronting this data to the model shows that the model overestimates the molecular dissociation and the electron density. These discrepancies can be partly explained by underestimated power losses phenomena in the plasma, possibly linked to its molecular and electronegative nature. This work gives leads for future theoretical work and diagnostics on I_2 plasmas. It proposes an updated model and a set of new diagnostics for use to further develop iodine-based propulsion systems.

Acknowledgments

My first acknowledgment goes to Gérard Auvray, who left us in 2018. He was from 2011 the project manager for X-CubeSat, the first student nanosatellite of École polytechnique. X-CubeSat, and Gérard, were my first contacts within the space sector in 2013. His passion, his dedication and his trust in me led me to pursue my studies in the aerospace sector, and I would not be where I am now if I had not met him.

I would like to thank Dr Ane Aanesland, who welcomed me in her team as a master's student in 2014, and as a PhD student under her supervision in 2017. Her ThrustMe endeavor left us little time to work together, but she is the one that truly made me want to complete this PhD. I would like to thank Dr Dmytro Rafalskyi and Dr Trevor Lafleur who introduced me to plasma simulations and experiments back in 2014. I'd like to thank Antoine Poyet, Thomas Baret, Gautier Brunet, Javier Martinez-Martinez, my first colleagues in the lab, during my year as a member of the ThrustMe team.

My work at LPP took a strong turn after one year, and I can only thank so much Dr Anne Bourdon and Dr Pascal Chabert for their support and empathy, their scientific and personal guidance that pushed me to carry this adventure to its end. My next acknowledgment can only be for Dr Cyril Drag, who accepted to take the responsibility of supervising the final two years of my PhD on a topic he did not fully chose. He helped a lot with his lasers but mainly with his fantastic experimental, pedagogic and human skills, as an always-enthusiastic scientist, a rigorous experimentalist and inspiring supervisor with whom *rien n'est jamais laissé au hasard*.

May Dr Olivier Guaitella and Dr Jean-Paul Booth be thanked for their patient guidance and the - different - models of scientists they were for me. My first iodine plasma was turned on thanks to two pieces of copper tape

and the skills and ingenuity of Dr Guaitella, and I'll remember it! I thank him a lot for this, for his time and for showing me that one can be a great scientist and human being altogether. I also thank Dr Christophe Blondel for his precious theoretical insights.

I succeeded in this PhD work partly because I was surrounded by an amazing team of interns and PhD students. People of the PhDarium, Irn Bro's and other colleagues made it possible. I thank Abhyuday, Ana, Antoine, Théo, Benjamin, Thomas, Romain, Federico, Edmond, Audrey, Marlous for sharing this crowded office and so many good times in different places around the world. A special thanks to Thomas Ben Charoy for his presence within the group these three years, bringing a lot to the team, socially in the lab and with the LPPhDs, the football team, the PhD association, and of course scientifically. I thank also Edmond for taking over my role at the *comité convialité* of LPP. I would like to add another special thanks to Théo Courtois and Dr Victor Desangles for teaching me, each in his own way, than one can be both careful and impressively daring in an experimental room. A huge thanks to Marlous Hofmans for being a skilled 3D printer, an amazing scientist and the perfect *binôme* I did not know I needed for this thesis.

Le soutien que j'ai reçu au LPP ne s'arrête pas là, et je remercie l'équipe mécanique pour leur aide, et leur café: Bruno Dufour, et bien sûr Pascal Pariset, qui n'économise pas une heure tant que la moindre petite fuite sur une chambre à vide n'a pas été trouvée. Je veux aussi remercier l'équipe de gestion, Catherine d'abord pour sa disponibilité et son aide toutes ces années, mais aussi Maryline, Chérifa et Édouard qui ont toujours répondu présent, et avec le sourire, quand j'ai eu besoin d'eux. I would like to thank Dr Garrett Curley, who was a precious help for me as research engineer in the team, despite the fact he arrived late during my stay at LPP. Thanks to Alexis Jeandet for introducing me into the linux world early in my thesis, and forgiving me for my early mistakes, I swear I've never *sudo pip* again. I'd like to thank Ali, Michael and Gautier from the technical support, who taught me before they left the laboratory that work relations can also lead to very deep human interactions.

Outside of LPP, I would like to thank the scientists I was lucky to work with, in particular Dr Olivier Le Maitre who taught me all I know about Uncertainty Quantification, and Dr Pietro Congedo that gave me the opportunity to present my work to the Uncertainty Quantification community.

As demanding as it was, my activities at LPP were only a part of my world in the past three and a half years. I was lucky enough to serve as part-time nanosatellite project manager within the student space center of École polytechnique. I would like to thank first those who made it possible, in particular Alain Gaboriaud, Christine Nicolas and Dr Patrick Le Quéré. Working at the student space center, I interacted with more than a hundred students over three years, and they all brought me a lot, making me better as a teacher and as a human being. I would like to thank in particular the students of the IonSat project: Clément Pellouin, Timothée Darcet, Victor François, Hadrien Paugnat and Marie Gruet first, and also Jaafar Chakrani, Thomas Hurot, Nicolas Lequette, Geoffrey Magda, Augustin Tommasini, Arthur Toussaint, Clément Yang, Julie Delgado, Maixent Esmieu-Fournel, Nathan Magnan, Etienne Gourcerol, Dmitry Gaynullin, Benoît Oriel, Paul Ponchon, Bastien Schnitzler, Jonas Schweizer, Baptiste Decord, Thomas Bellier, Lucas Langlois, Samuel Thirion, Hilaire Bizalion, Robin Courson, Vianey Darsel, Brice Douet, Hector Ferrer, Yohan Fis, Florian Girauld, Louis Hart-Davis, Stéphane Latil, Siyuan Lin, William Mpondo, Auguste Poiroux, Xiao Zhang. I'd like to thank as well my colleagues at the space center: Nicolas Hanappier, Ruben di Battista, Dr Pascal Chabert, Sophie Hucher, Alexis Jeandet and our interns Louis-Alban de Marne, Titus Senez, Adrien Garinet and Chris de Claverie. A special thanks to Antoine Tavant, who joined the CSEP at the right time when I couldn't deal with everything. I thank as well Dr Lilia Solovyeva, with whom I learned a lot about team management.

Because life can never be fully about work and the workplace, let me now thank, without any particular order: COVID-19 for providing me the opportunity to focus on my writing, FIP radio for being a faithful companion for writing days, all the plants at work and home, my bike, anyone that took care of the bike paths on my commute for 3 years, RATP and SNCF for carrying me tirelessly any other days, Terry Pratchett, Douglas Adams, Boulet, Marion Montaigne, the people from TheLastJeudi, Alexandra Elbakyan, the judo team of the Paris University Club for all the opportunities to unleash extra energy it offered me, the administrative teams of École polytechnique, Sorbonne Université and EDPIF, *Paris en Selle* and *IPParis à Vélo* for the noble causes they serve, 3D printers, the Space Generation Advisory Council and Audrey Berquand that worked there with me for two long years, X-Space and its board for being a precious inspiration.

Enfin, je remercie mes parents pour leur soutien sans faille depuis le début de ma scolarité, et Marine pour la vie, l'univers, et tout le reste.

Related publications

The work detailed in this thesis has been presented at several conferences. The related proceedings papers are listed here.

Marmuse F., Drag C., Booth J.-P., Aanesland A., *Temperature and density measurements in an iodine RF-CCP plasma with emission and absorption spectroscopy*, ESCAMPIG XXIV, 2018-07, Glasgow, Scotland, United Kingdom (2018) ***Best poster award***

Marmuse F., Courtois T., Booth J.-P., Drag C., Aanesland A., Chabert P., *Spectroscopic study of an iodine plasma in a low pressure RF-ICP ion source*, 71st Annual Gaseous Electronics Conference, 5-9 November 2018, Portland, OR, USA (2018) ***Best poster award***

Marmuse F., Lucken R., Drag C., Booth J.-P., Bourdon A., Sisourat N., Aanesland A., Chabert P., *Iodine as propellant for electric propulsion: updated global model and comparisons to experiments*, International Symposium on Plasma Chemistry, 2019-06-09 / 2019-06-14, Naples, Italy (2019)

Marmuse F., Lucken R., Le Maitre O., Congedo P., Sisourat N., Bourdon A., *Opening chemical reaction paths in a plasma global model: an uncertainty quantification approach*, UQOP: Uncertainty Quantification and OPtimization, 2019-03-18 / 2019-03-20, Paris, France (2019)

Contents

Scope and outline

Iodine molecules are promising candidates for use as propellant for spacecraft electric propulsion, because of their large dissociation cross-sections, and the large mass and ionization cross-sections of the resulting I atoms. While the chemistry of iodine plasmas is eminently more complex that in plasmas of more common noble gases, the very large dissociation cross-sections of iodine molecules yield certain similarities between iodine and xenon plasmas. The available data about iodine and especially iodine plasmas is scarce and needs validation, such as reaction cross-sections, threshold energies, oscillator strengths of atomic transitions, vapor pressure, etc. Likewise, few reliable diagnostics are available to characterize such plasmas, that can present non-negligible molecular and electronegative features. The very usage of iodine in plasma laboratories is rare and the experiments and setups are to be adapted. Used without proper precautions, iodine is toxic for health and the environment, and damaging to experimental setups through deposition and corrosion.

How to adapt an experimental plasma setup for use with iodine? What can the available data tell about the chemistry of an inductively coupled iodine plasma in a thruster? What dedicated optical diagnostics can be developed to characterize a real iodine plasma? How can already available electric diagnostics be used in such a plasma? How do the measured plasma parameters compare with model predictions based on available theoretical data? To what extent can the molecular and electronegative features of iodine plasmas be neglected? To what model improvements can the observed discrepancies between theory and experiments lead?

Chapter 1 of this work introduces space propulsion, electric propulsion, the NewSpace movement from the 2010s, and shows how the present thesis finds its place within these dynamics. It also presents the experimental se-

tups used in this work, heritage of the PEGASES and NEPTUNE concepts developed at LPP during the last fifteen years. The specific tweaks implemented on the setups and in the processes to mitigate iodine deterioration are presented.

On the simulation side, the Chapter 2 improves, corrects when necessary, and further develops the iodine global model available at LPP. On the coding side, this includes a long effort to rewrite the code in python, following more strict coding rules including version control and sharing of code on platforms like GitHub. It also aims at making the code more user-friendly, with the long-term objective of open-sourcing a working version for broad use outside of the laboratory, for any atomic or molecular gas. The code is also oriented to ease parametric analyses, for use as a design tool for thrusters, by being configured to work on parallelized clusters to generate quick performance maps varying multiple parameters at once. On the physics side, the reaction set is completed with richer chemistry and electronegative models of the plasma-wall interactions, to anticipate effects linked to the electronegative nature of iodine.

Making the best use of the material and skills available at LPP during the thesis, five diagnostics are developed to characterize iodine ICP plasmas. Optical diagnostics are presented Chapter 3. Following an in-depth study of the emission spectrum of the plasma, two regions are probed by laser-absorption spectroscopy. In the near infrared, around 900 nm, very large absorption peaks lead by Doppler broadening to a measure of temperature of I atoms with a very good signal-to-noise ratio. This analysis is done after the hyperfine structure of the transitions is understood correctly by means of Doppler-free saturation spectroscopy. Further in the infrared, at 1.3 µm, the very weak forbidden transition in the fine structure of the fundamental state of I is probed by installing a multi-pass setup on PEGASES, to increase the absorption path length to get a signal out of the noise. This absorption experiment yields the density of I atoms, and another measurement of I temperature, which is a first in the literature. Inspired by recent experiments on chlorine plasmas, the method of broadband absorption spectroscopy is successfully implemented, also for the first time, on a I_2 plasma to measure the I_2 density. Work by previous PhD students about the use of Langmuir probes in electronegative gases is carried on and presented Chapter 4, to measure the electron density and temperature, and estimate the electronegativity of the plasma.

Using the diagnostics presented above, the predictions of the global model are compared to experimental data of density and temperatures of the species in Chapter 5. These comparisons partially assess the validity of the model, as the trends as well found. It is shown that the model overestimates the I_2 dissociation and the electron density. In a second time, this work proposes directions to improve the physics contained in the equation set, or the datasets used in the model, for example by integrating new or higher loss phenomena in the plasma, effectively reintegrating effects linked to the molecular nature of iodine that could have been underestimated.

Appendix A presents some insights about the code written and used in this work to solve the global model equations. Appendix B presents the methodology followed in this work to derive the discharge power actually absorbed by the plasma from the RF power that is output by the generator. Appendix C underlines the importance of extrapolating the available cross-section datasets to a wide range of electron energies to compute the reaction rates, and presents the extrapolations that were used in this work. Last, Appendix D lists several key ideas for the design of matching circuitry for inductively coupled plasmas, using the matchbox of the PEGASES thruster as an example.

Chapter 1

Context and generalities

The space sector has been experiencing its largest evolutions since the Apollo era in the last ten years. This chapter introduces space propulsion, electric propulsion, the NewSpace movement from the 2010s, and shows how the present thesis finds its place within these dynamics. It also presents the experimental setups used in this work, heritage of the PEGASES and NEPTUNE concepts developed at LPP during the last fifteen years. Using iodine in a plasma setup can become an experimentalist's nightmare: the specific tweaks implemented on the setups and in the processes to mitigate deterioration by iodine are presented.

1.1 Context of the thesis

1.1.1 Space propulsion

The sky is not a limit for humankind anymore, but it is still for many physical parameters or engineering concepts. In particular, the aerodynamical lift that makes planes stay up in the air up to a few tens of kilometers is not useful anymore above the sky limit. Moving a satellite, a rocket or a space-station in space relies solely on momentum conservation: because the total momentum of the system is conserved, any material ejected from the spacecraft in a particular direction provides a momentum increment to the spacecraft, in the opposite direction.

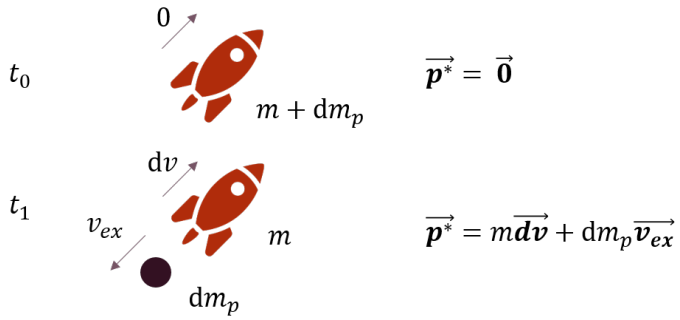

Figure 1.1: Momentum conservation on a closed system composed of a spacecraft and its propellant leads to the rocket equation.

All history of space propulsion is rooted in the work of Constantin Tsiolkovsky (1857-1935), famous author in 1903 of what is now called the *rocket equation* [1]:

$$\Delta v = v_{ex} \ln\left(1 + \frac{m_{\text{propellant}}}{m_{\text{dry}}}\right) = v_{ex} \ln\left(\frac{m_{\text{total}}}{m_{\text{dry}}}\right) \tag{1.1}$$

Equation (1.1) links the increment of speed Δv that can be achieved by a spacecraft of mass without propellant $m_{\text{dry}} = m_{\text{total}} - m_{\text{propellant}}$, using a propellant mass $m_{\text{propellant}}$ with a propulsion system that accelerates it outwards at the exhaust velocity v_{ex}. It can be derived using the conservation of momentum on a closed system such as the one shown Figure 1.1: a rocket and a given mass of propellant at a time t_0, and the same rocket having exhausted its propellant at a speed v_{ex}, at $t_0 + \Delta t$.

The words *rocket equation* are often used in the expression *tyranny of the rocket equation*, as it states that, at constant exhaust velocity, the propellant ratio needed in a spaceship increases exponentially with the increment of speed required for the maneuver. This physical fact has led to several well known engineering strategies, such as rocket staging, and is still today the reason why more than 90 % of rocket mass consists of fuel and tanks, or why humankind hasn't visited the nearest stars. On the other hand, it also shows the linear dependency between exhaust velocity v_{ex} and achievable increment of speed Δv for a given propellant mass. Exhaust velocity of the propellant is then a crucial metrics for designing a propulsion system. It is actually a measure of the efficiency with which the propellant is used. Per definition, thrust is the product of the mass flow rate and the exhaust velocity, therefore, the exhaust velocity in $\mathrm{m\,s^{-1}}$ can also be understood as the thrust produced per unit mass flow, in $\mathrm{N/(kg\,s^{-1})}$:

$$T = v_{ex}\frac{\mathrm{d}m}{\mathrm{d}t} \implies v_{ex} = \frac{T}{\mathrm{d}m\,/\,\mathrm{d}t} \tag{1.2}$$

Another unit has been introduced to enhance this notion, the specific impulse I_{sp}, expressed in seconds so that

$$\frac{T}{g_0} = I_{sp}\frac{\mathrm{d}m}{\mathrm{d}t}$$

In this equation, g_0 is the standard acceleration due to gravity, defined by definition as $g_0 = 9.806\,65\,\mathrm{m\,s^{-2}}$, T/g_0 is the thrust expressed in kg, and $I_{sp} = v_{ex}/g_0$ is the time during which a kilogram of propellant will produce a kilogram of thrust, at any place where the local acceleration g is equal to g_0. The rocket equation shows the interest of large exhaust velocities, but those also come at a cost. Let us define for the present case the power efficiency η of a given propulsion system as the kinetic energy produced per second, divided by the total input power P_{tot}. P_{tot} typically includes the power used to create the plasma, to accelerate the plasma, and unwanted power losses.

With this definition, and with $\dot{m}$ the propellant mass flow rate:

$$\eta = \frac{1/2\dot{m}v_{ex}^2}{P_{tot}} \tag{1.3}$$

Then, including the definition of the thrust in equation (1.3), it leads to the fact that the thrust-to-power ratio, also crucial for aerospace engineers, is inversely proportional to exhaust velocity at a given system efficiency:

$$\frac{T}{P_{tot}} = \frac{2\eta}{v_{ex}} \tag{1.4}$$

As a conclusion, a high exhaust velocity leads to a higher thrust per unit mass flow (1.2), but a lower thrust per unit power (1.4). High exhaust velocities are characteristic of *electric propulsion* devices, as explained in the next subsection. The other main family of propulsion devices is the *chemical propulsion*, where the kinetic energy is produced by converting the chemical energy stored in the propellant. Chemical propulsion exists in multiple forms in the toolbox of an aerospace engineer: solid propulsion in Ariane 5 *Étages d'Accélération à Poudre* (EAP, burning mainly ammonium perchlorate in the ambiant oxygen), bipropellant liquid propulsion in Ariane 5 main Vulcain engine (burning a mix of liquid hydrogen and liquid oxygen) or Falcon 9 Merlin engines (burning a mix of kerosene and liquid oxygen), or monopropellant liquid propulsion featured in hydrazine rocket engines produced by many suppliers around the world. In those cases, the kinetic energy provided to the rocket or satellite was initially stored as chemical energy in the propellant, and converted through combustion chambers and carefully-designed nozzles to accelerate the exhaust flux. The energy per unit mass of the propellants used, or enthalpy, is intrinsically limited and this fundamentally limits the exhaust velocities that can be achieved with chemical propulsion.

1.1.2 Electric propulsion: why and what for?

History and basic principles Electric propulsion is the fact of using electrical energy, not chemical energy, to accelerate particles outside of a spacecraft. In electric propulsion systems, the energy is stored as electricity in batteries, or produced directly on-board through solar generators or nuclear systems such as radio-isotopic generators (RTG). This electrical energy is converted into kinetic energy by either heating a gas with electric arcs or sparks (electrothermal thrusters) and expanding it with nozzles, or more interestingly for this work by ionizing a propellant gas and accelerating the resulting charged particles with electric or magnetic fields. In such systems, although carrying a propellant is still needed, the energy generation is decoupled from the propellant itself, avoiding many chemical limitations. This is illustrated Figure 1.2. In a system where, for example, charged particles are accelerated in an electric potential V, the final exhaust velocity depends on the potential applied and the characteristics of the system, hence on the quantity of power available on board. Such exhaust velocity is not bounded by any chemical limitation. At the cost of a much lower thrust in today's systems, from a few µN to a few N, electric propulsion devices can achieve, and are characterized by, large exhaust velocities compared to their chemical counterparts. Orders of magnitude of I_{sp} are shown Table 1.1.

Example	Technology	Typical ISP
	Cold gas	50 s - 75 s
Ariane 5 EAP	Chemical, solid, monopropellant	274.5 s
Ariane 5 Vinci	Chemical, liquid, bipropellant	466 s
	Resistojet	Up to 500 s
	Arcjet	Up to 700 s
	Pulsed Plasma Thruster	850 s - 1200 s
	Gridded Ion Thruster	2500 s - 3600 s
	Hall Effect Thruster	1500 s - 2000 s
IFM Nano	FEEP	2000 s to 6000 s

Table 1.1: ISP data for different kind of thrusters, real if an example is mentioned, estimated otherwise. Data about Ariane 5 is from Kyle [2]. Data from the IFM Nano FEEP is from Krejci et al. [3]. All other data is estimated from flight-proven devices by Goebel and Katz [4].

Without going into too many details, the propulsion technologies mentioned in Table 1.1 can be grouped in different categories [5].

Electrothermal thrusters use electricity to heat a propellant, and the related gas expansion can be guided through a nozzle to generate thrust. Their behavior is close to chemical thruster, as the electricity or plasma is used only to heat the gas, and they provide the lowest exhaust velocities from electric thrusters. Arcjets and resistojets are classical examples.

Electrostatic thrusters do ionize the propellant to accelerate it with electric fields, and not only by thermal expansion. A classical example is the gridded ion thruster, where charged particles are created in an ionization chamber, and accelerated in a separated acceleration stage by a strong voltage drop created by biased grids, in the direction of thrust. Positive ions are then accelerated along the potential gradient, outwards of the spacecraft. A simple explanation can be the following: the voltage gradient is made between two large biased plates, separated by a distance small compared to their area. In this situation close to the textbook infinite parallel plates scenario, a Lorentz force accelerates the charged particles from one grid to another. Holes are drilled into the first plane so that particles can enter, and into the second plane so that the particles can leave, hence the planes are effectively grids. If the voltage gradient is effectively a voltage drop, positively charged particles are accelerate outwards while negatively charged particles are trapped in the ionization chamber. A third stage is present to neutralize the beam created, to avoid charging effects on the spacecraft. Removing this third stage by ejecting, on average, equal positive and negative currents from the thruster is an active research field. It is the main driver behind the PEGASES and NEPTUNE concepts developed at LPP and presented section 1.1.6.

Electromagnetic thrusters form the last family of electric thrusters, where electric and magnetic fields are combined to generate the thrust. The most famous example of this family is the Hall effect thruster (HET), where a magnetic field is used to reduce the electron mobility, enhancing ionization in a cylindrical canal.

Gridded ion thrusters and Hall effect thrusters compose the vast majority of electric thrusters currently flying in space, the gridded ion thrusters having generally a larger I_{sp} and lower thrust, hence a lower propellant consumption, and the Hall effects thrusters being more popular for applications requiring more thrust.

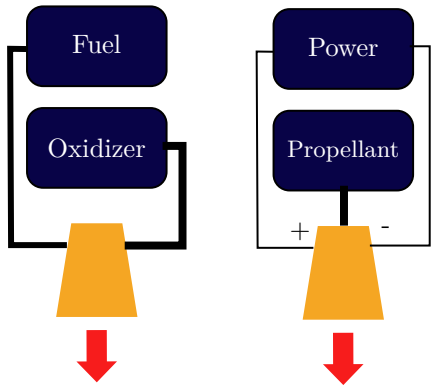

Figure 1.2: Electric propulsion systems (right) decouple the power generation from the propellant. Chemical propulsion systems (left) unleash power by having a fuel and an oxidizer chemically react together.

High thrust-to-mass-flow-rate ratios and low thrust-to-power ratios linked to a high exhaust velocity mean that using electric propulsion makes a lot of sense in two different scenarios: producing large thrust with small amounts of propellant and huge amounts of power, or producing low thrust with really small amounts of propellant with more reasonable power requirements. The former was at the core of the dream of the visionaries of electric propulsion, envisioning human exploration of the far solar system with electric propulsion on-board nuclear-powered spaceships [6]. The latter is the current business model for electric propulsion, where satellite operators trade the speed of the orbital maneuvers for savings on propellant, hence on launch mass. This can translate into cost savings at a time when 1 kg on orbit typically costs between 10 k€ to 40 k€ depending on the launcher.

The concept of electric propulsion is anything but new. Choueiri [6] provides a comprehensive review of the first 50 years of the field, and some of it is recalled in the present work. The aforementioned visionaries, besides Tsiolkovski from Russia, are the famous Robert H. Goddard from the USA that formulated ideas related to electric propulsion in 1906, and submitted a patent for what is now recognized as the first electrostatic ion thruster in 1917 [6]; Hermann Julius Oberth (1894-1989) that first formalized the basis of electric propulsion in a publication from 1929 [7], or Valentin Petrovich Glushko (1908–1989) from Russia that built the first electrothermal thruster

with his team in the period 1929-1923. After what Choueiri [6] considers an era of visionaries came the first true pioneer, Ernst Stuhlinger (1913-2008), that wrote his first paper on the subject in 1954, and the first reference book on electric propulsion in 1964 when he was director of the Space Science Laboratory of the NASA Marshall Space Flight Center [8]. Around this time, his team was producing concepts such a the one illustrated Figure 1.3 : an electric spaceship for Mars, where huge solar panels could supply the thrusters placed away from the spaceship to avoid interaction with the thrusters' plumes.

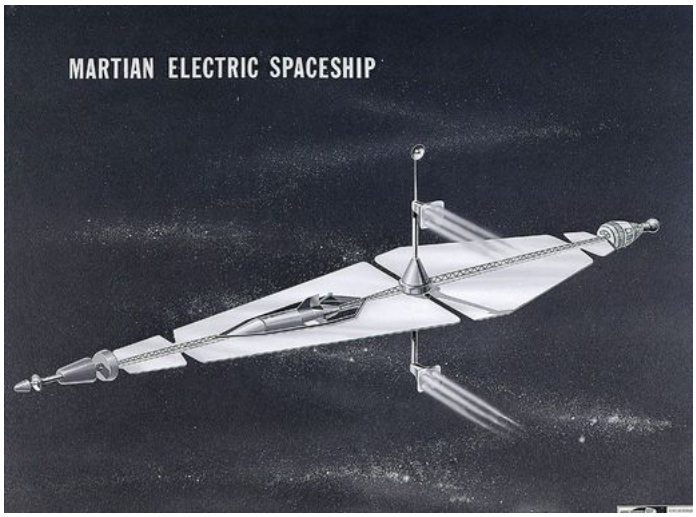

Figure 1.3: An artist view of a Martian electric spaceship based on works from Stuhlinger [8]. Credit: NASA Marshall Space Flight Center. 1962.

The dreams of human spaceflight with electric propulsion never came true in the following sixty years, but the first electric thrusters did fly in the 1960s [4] and imposed themselves as good secondary thrusters for spacecrafts in Earth orbit, performing small maneuvers. As in the entire space sector, a new dynamism appeared in the early 2010s: Boeing flew the first full electric spacecraft in 2015 [9], followed by Airbus with the launch of Eutelsat 172B in 2017, the first all-electric high-power communication satellite. The next paragraph summarizes the current and expected uses of electric propulsion.

Example applications The following applications are compared using as examples a chemical thruster with 300 s of I_{sp}, and an electric thruster with 2000 s of I_{sp}, that can be a Hall effect thruster of a gridded ion thruster.

- **Orbit raising**: it consists in a maneuver to bring a telecommunication satellite from the Geostationnary Transfer Orbit where the launcher delivered it, to Geostationnary Earth Orbit where it can operate. It requires a Δv around $1.5\,\mathrm{km\,s^{-1}}$ for a Hohmann transfer - the type of orbital transfer from an altitude to another that requires the less maneuvers - and slightly more for a transfer with countinuous thrust. Assuming a useful mass of 2.5 t for the spacecraft, this would require 1600 kg of propellant to be performed with the chosen chemical thruster, and the orbit raising would be achieved within few days. With the electric thruster, it would require 200 kg of propellant and would typically take a few months.

- **Drag compensation in Low Earth Orbit**: for a spacecraft in Low Earth Orbit (300 km to 1500 km), the force due to the atmospheric drag is against the spacecraft velocity and will make it reenter in the Earth atmosphere on the long run. It is expressed as [10]:

$$F_D = \frac{1}{2}\rho C_D A V^2$$

  For an example spacecraft of cross-section $A = 1\,\mathrm{m^2}$, at an altitude of 300 km, the atmospheric density is around $\rho = 6 \times 10^{-12}\,\mathrm{kg\,m^{-3}}$, the orbital speed is roughly $V = 7600\,\mathrm{m\,s^{-1}}$ and the drag coefficient is around $C_D = 2.2$. The force amounts then to 500 µN. If the spacecraft mass is 500 kg, this is reducing the orbital speed by $4 \times 10^{-3}\,\mathrm{m\,s^{-1}}$ each orbit. Compensating the speed increment over a 5 years mission results to a budget of $\Delta v = 130\,\mathrm{m\,s^{-1}}$. For such a spacecraft, the rocket equation 1.1 states that the mission planner should plan 22 kg of propellant if using a chemical system with an I_{sp} of 300 s, or 3 kg if using an electric propulsion system with an I_{sp} of 2000 s.

- **Station keeping in Geostationnary orbit**: because of multiple perturbation sources, a GEO spacecraft needs to correct its orbit to maintain its required position. This typically represents a required ΔV of $50\,\mathrm{m\,s^{-1}}$ and can be achieved with very low thrust devices, which makes it a good workplace for electric propulsion devices.

- **Constellation management**: constellations of tens or even hundreds of satellites are envisioned in the early 2020s. Multiple satellites will be located on orbits with parameters next to each other, for example six could follow each other on the same orbit, passing over the same point at 15 min intervals. To avoid using a new launch for each spacecraft, constellation plans involve a single launch for multiple spacecrafts belonging to the same orbital plane: the phasing is later done by the satellites themselves, with on-board electric propulsion.

- **Deep space exploration**: with their low propellant consumption and the ability to perform continuous thrusts during long times to greatly accelerate or decelerate a spacecraft, electric propulsion is often used on board deep-space exploration missions. Uncrewed mission like NASA's Dawn to the asteroid CERES, ESA's SMART-1 to the Moon, NASA's New Horizons to Pluto, ESA's BepiColombo mission to Mercury use electric propulsion as their main propulsion device. Electric propulsion was never seriously mentioned as an option for crewed spaceflight, that requires as fast manoeuvres as possible to limit the time spent in space by the crew. With the development of high power devices, this becomes possible and NASA included the developement of a 200 kW propulsion device in its Mars Plans. The current state of the art of high-power devices is at 100 kW, used only in laboratories [11].

1.1.3 The NewSpace (r)evolution

NewSpace is sometimes considered as a revolution, or maybe only as a noticeable evolution that happened before in other industrial sectors. In the following paragraphs, the NewSpace movement is introduced, and its implication for the world of electrical propulsion and this work is discussed.

What is NewSpace the name of?

The NewSpace is the incursion, in the 2010s, of the entrepreneurship above the sky limit. The first main character of this ongoing period is Elon Musk, founder and CEO of Space Exploration Technologies, also called SpaceX. SpaceX was founded as a private company in 2002 with the hope to dramatically decrease the cost of an orbital launch through a complete overhaul of the industrial methods in place in the sector [12]. At this time, the global space industry was funded mostly by governmental agencies, with public money, on financial systems that would leave only few incentives towards cost reduction to the traditional industries of the sector [13]. Musk developed the Falcon 1 launcher, with a cost-effective approach, on an initial investment of $100 million of his own money. This rocket successfully reached orbit on its 4th attempt, in 2009, and convinced the large American space agencies, NASA and the Department of Defense, to buy several of the larger version of this rocket, the Falcon 9. Only a few years later, SpaceX succeeded the first landing of an orbital rocket in December 2015, an achievement that was widely recognized as both useless and impossible shortly before, and that many companies around the world have been trying to replicate ever since. An illustration of such a landing is shown Figure 1.4. Five years later, SpaceX is a recognized actor in the launch industry, with more than 50 launches in the 2017-2019 period. It shook the entire sector with cost-effective and reusable launchers: from more than $20k per kilogram on orbit in the 2000s, the price for space has been lowered today around $3k per kilogram, and is foreseen to lower even more as SpaceX is increasing the reuse of its rockets and developing larger systems.

Elon Musk has brought two main things to the space sector: first, he made space look like a place where entrepreneurs could strive, where private individuals could make money, where private companies could alter a market defined and controlled by large governmental space agencies until then. Such a transition had happened in many other industrial sectors before. Second, Elon Musk and SpaceX seriously reduced the cost of access to space,

Figure 1.4: Two Falcon Heavy boosters from SpaceX landing after deploying its second stage. Credits: SpaceX.

enabling business models based on equity-funded space segments to emerge. Many private companies follow this trend, in the space launch business (Blue Origin, Vector Space in the USA, RFA, Aurora, PLD Space in Europe, OneSpace, ExPace, i-Space, LandSpace in China, just to name a few.) but also in space imagery (Planet, EarthCube). The boom of investments and of the number of startups in illustrated Figure 1.5. The historical actors are adapting their strategies and risk approaches, developing new programs to support those new actors such as the Commercial Orbital Transportation Services (COTS) program in the USA [14], or the Business Incubation Centers from the European Space Agencies. Such programs have lead for example to the birth of NanoRacks, the first private actor to operate onboard the International Space Station in October 2013. New governmental actors also appear and grow, combining their inherent financial strength with the new cost effective and risk-taking approach. As an example, the Indian space agency ISRO launched in September 2014 its low-cost martian orbiter, called MOM for Mars Orbiter Mission, for a total cost of $74M, ten times less than the cost the NASA MAVEN Mars orbiter. Another example of adaptation of large historic actors is the development by Airbus of the PLEIADES NEO constellation, outside of any governmental contract, to position itself in the commercial market of space imagery.

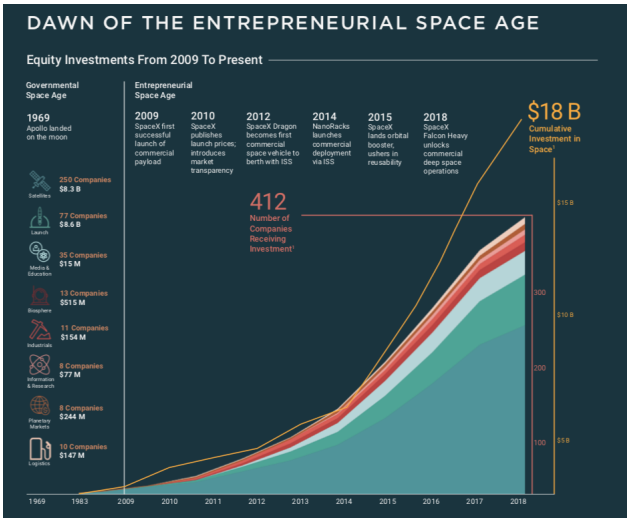

Figure 1.5: Evolution of equity investments in the space sector from 2009 to 2018. Credits: Space Angels.

The CubeSat revolution

In the same timeframe, electronic miniaturization and standardization led to what some called the CubeSat revolution: in the early 2000s, several engineers proposed to standardize the manufacturing and launch of small satellites for "education and industry low-cost space experimentation" [15]. Among them, Dr. Jordi Puig-Suari from the California Polytechnic State University in San Luis Obispo (USA) and Dr. Robert Twiggs from Stanford University (USA) are mainly given as founders of the CubeSat revolution. The CubeSat revolution is before all a deployer revolution: by developing a standard deployer for satellites produced in specific mass, volume or power boundaries, that is brought in space a secondary passenger of larger satellites, it greatly reduced the cost and administrative complexity of access to space for new or small satellite manufacturers such as universities or startups. The CubeSats are build as one or several units, that are cubes with a 10 cm edge, weighing around 1 kg each. CubeSats are therefore described as 1U, 2U, 3U, 6U and sometimes 12U depending on their form factors. Several commercial actors have tried or are trying to develop business models with CubeSats: Planet developed an Earth imagery constellation, NanoRacks developed dedicated

launch services from the International Space Station. If it is somehow acknowledged today that no *serious* business or science can be achieved in form factors smaller than 12U, the CubeSat mentality is at the core of what the satellite industry is becoming today. The extremely low costs of these spacecrafts, associated with the low launch costs due to the standard deployers, led to the introduction of barely mature technologies in satellites, and fast fly-fail-improve-refly cycles, greatly accelerating development cycles. The old adage that space technology is "solving tomorrow's problems with yesterday's technologies" is proven wrong with the latest development. Another heritage of CubeSats is the concept of constellation, whose primary interest was to spread risks over a large number of satellites: flying ten smallsats at the cost of a big one improves the overall reliability of the system even if each satellite is not as much tested or filled with redundancies in itself. Constellations are also fulfulling (and maybe creating) new needs: unable to offer as good image resolution as larger spacecrafts, shoebox-sized spacecrafts in constellation can offer a low revisit time between two pictures of the same place on Earth. OneWeb, Starlink, KINEIS are some of the current or future contellation operators that are, by many aspects, descendants of the CubeSat pioneers, even if they are all operating spacecrafts between 50 kg to 500 kg, larger than a CubeSat but much smaller than the traditional multi-ton GEO telecom satellite. For more information on the impact of NewSpace in the space sector, the reader can refer for example to Yacoubi [16]. It is there emphasized that the NewSpace movement features five main aspects: new actors, improved technology, new risk approaches, private commercial opportunities, and new investors.

NewSpace in the electric propulsion world

The NewSpace revolution is going down to the spacecraft supplier's level. They benefit from the same new funding opportunities that business-to-consumers companies, are driven by the same new risk approaches, and benefit from the flourishing panel of new customers as well as the established ones. The electric propulsion world has been since the 1960s held by few large suppliers linked to their main customers (Fakel, Safran Aircraft Engines, Busek, to name a few) and many laboratories implied in this very *deep-tech* world. The developement of new technologies in laboratories as well as the evolution of the technical requirements of new customers looking for cheaper, smaller, simpler, more seriable or more scalable thrusters led to the creation of many companies in the 2010s, most of them spin-offs from the academic world. Here is a list of most of them, with their year of incorporation, country and where they spin-off from, if applicable: Phase4 (2016, USA), Exotrail (2017, France, spin-off from CNRS), ThrustMe (2017, France, spin-off from CNRS), ApolloFusion (2016, USA), Comat (1977, France), Enpulsion (2016, Austria, spinoff from FOTEC), T4i (2014, Italy, spin-off of the University of Padua), MorpheusSpace (2018, Germany, spin-off from TU Dresden), Hyperion Technologies (2013, the Netherlands), NanoAvionics (2014, Lithuania), AccionSystems (2012, USA), AAC Clyde Space (2005, Scotland), Bradford Space (1984, Netherlands), Aurora Propulsion Technologies (2018, Finland), Tethers Unlimited Inc. (1994, USA), Bellatrix Aerospace (2015, India), ExoTerra Resources LLC (2011, USA). The names of the companies have been found with the help of Curtis [17] from SatSearch. All these companies, whose logos are shown Figure 1.6, feature electric thrusters for smallsats in their catalog, as their main product or as part of a larger catalog.

Nearly all their products have in common to be simple, miniaturized thrusters aiming at the smallsat and constellation market. Startups developing a ground segment can now launch a couple spacecrafts in space as part of a business demonstration, enabling a fast space heritage for these new suppliers. Most of them are not today able to prove the tens of thousands of hours of qualification needed to serve the GEO or institutional market, but several should reach this point in the next years.

In parallel, the first small satellites equipped with electric propulsion reach space. Among the smallest projects, one can mention UWE-4, a 1U university smallsat that became the first to modify its orbit with an electric thruster from Morpheus Space. Several more ambitious project are ongoing, led by

Figure 1.6: Logos of a selection of aerospace companies proposing propulsion solutions for smallsats as of 2020. Most of them propose electric propulsion systems, with a wide variety of technologies, maturity, scientific heritage and performances.

agencies (the projects GOMX-4 and GOMX-5 by ESA, the Lunar Flashlight or Lunar IceCube missions in the USA, to only name of few), but also in universities. In France, the project IonSat developed by the Space Centre of École polytechnique aims at demonstrating the feasibility for a 6U CubeSat to maintain its own altitude in Very Low Earth Orbit, under 300 km, where orbits usually decay in matter of days due to the atmospheric drag. IonSat should use a thruster propelled with iodine, developed by the startup ThrustMe, spin-off of the laboratory where the present work has been done. Another project of 6U CubeSat propelled with an iodine thruster from Busek, i-SAT, in ongoing at NASA [18].

NewSpace and this work

Greatly simplifying, one could say that research about electric propulsion had been, in the 2000s, mostly focused on performance. Companies focused on how to increase thrust, efficiency, exhaust velocity. For a NewSpace entrepreneur aiming at a large constellation or at rapidly evolving prototypes, most systems were too big, too complex, and too expensive. The NewSpace brought new requirements that were addressed first by scientists, and later by the companies they created from their work: spacecraft manufacturers need simpler, smaller, cheaper propulsion devices, and many were easily ready to trade some performance for a lower cost or an increased manufacturing speed. These requirements turned into actual science and engineering questions: how to make small devices when losses are greatly depending on the volume-to-surface ratio of the plasma chambers? How to limit to number of pieces in the thrusters, when all systems feature an external neutralizer for the plasma plume? How to adapt qualification procedures to mass production? How to rationalize testing procedures and models to limit the need for 5-meter long, expensive vacuum chambers along an agile development cycle? These questions were at the core of the research project presented in this work but another became central, building on the heritage of the PEGASES project at the Laboratoire de Physique des Plasmas (see section 1.1.6): what propellant to use to replace xenon?

1.1.4 New propellants: what to look for?

Virtually anything *could* serve as propellant for an electric propulsion device. Given enough energy, all atoms or molecules can be ionized, and any charged particle can be accelerated through electromagnetic fields. Choueiri [6] links the first recommendation for the use of atoms with high atomic mass for propellant to an article from 1949 by Shepherd and Cleaver [19]. The first works by "the visionaries" often considered electron beams to produce thrust. This was not only because the concept of ion was not clear at the time: easier to accelerate due to their low mass, they would require smaller voltages to reach a high exhaust velocity, and this was crucial at a time when high voltage drops were hard to create. But an electron beam would produce a tremendous current to achieve an interesting thrust, and quickly saturate the space charge limitation that is well known today, ruling electrons out of our list of possible carriers of thrust. As reiterated by Stuhlinger [20], the charge-to-mass ratio of the particles used in the propulsion device should be as low as possible to minimize the beam current (number of charges per second, proportional to the charge) for a given thrust (mass per second times exhaust velocity, proportional to the square root of the charge). Among the first propellants studied and tested were cesium and mercury [21], of high mass and low ionization thresholds, that can be used directly as solid and liquid from which electrons are extracted, but their toxicity or very high boiling point temperature discarded their use. The ongoing criteria for propellant are:

- The propellant should have a low ionization potential, and a high energy step between first and second ionization. The power efficiency of any device being determined as the amount of power used for acceleration over the total power used, using a propellant easy to ionize reduces the amount of power needed to turn the neutral propellant into charged particles. A high step between first and second ionization ensures that the amount of doubly-ionized ions, who have twice the charge-to-mass ratio of singly-ionized ions, remains low.
- The propellant should have a high mass. This again ensures a low charge-to-mass ratio, hence a low beam current for a given thrust.
- The propellant should be easy to store, manipulate, integrate, feed in injection lines, for obvious manufacturing reasons. To that extent, very high boiling points discard propellants such as the otherwise promising bismuth. A high storage density is also an important criteria for the use onboard satellites.

Such criteria have led to the hegemony of xenon as propellant in electric propulsion devices. Xenon is a noble gas, hence it barely reacts and can be stored in high-pressure bottles for long time with no specific care. Of atomic number 54, it has an atomic mass of 131.293 u or $2.180\,17 \times 10^{-25}$ kg, being the heaviest noble gas (excluding radon, that has no stable isotope). The first ionization threshold is at 12.129 84 eV, the second at 20.975 03 eV [22, 23]. The main drawback of xenon is its scarcity. It is present is the atmosphere at 87 ppb, and is produced industrially as a by-product of the production of liquid oxygen or nitrogen, at a rate of around 30 t to 40 t per year [24]. This leads to a high price and also a price versatility that is very much hostile to robust constellation business models like those sold by NewSpace entrepreneurs to potential investors.

Recent successes of using krypton as propellant for the Starlink constellation were observed, and the wide use of argon in laboratories must be mentioned. Argon is used a lot in laboratories because of its similarities to xenon and its very low cost, and krypton has been used as a substitute for xenon as propellant for electric propulsion devices, leading to a loss of performance around 20 % with a much cheaper propellant, and very few adaptation of the thruster compared to the xenon version. Nonetheless, those gases do not have the high mass and low ionization potential of xenon that are among its core advantage (see Table 1.2). As no atomic species fill all the criteria for a perfect propellant, some studies focus on molecular propellant. Dietz et al. [25] present a classification between diatomic and multiatomic molecules, and a toolkit they developed to evaluate the suitability of complex molecules for use as propellant. They enhance the interest of iodine, and draw some requirements for future, better propellants. Any diatomic molecule used should have a dissociation energy much lower that the ionization energies to limit losses, aiming at forming a plasma behaving as an atomic plasma. For complex molecules, such as the adamantane studied, of formula $C_{10}H_{16}$, the fragmentation is to be avoided or at least significantly suppressed. They mention the aim for a molecule with an energy gap between fragmentation and ionization energy of at least 10 eV. Anything else leads to lots of collision losses and very complex plasmas.

Iodine is among the most promising candidate in the diatomic molecules family and is the alternative to xenon studied in this work. A specific focus on iodine is given in the next section.

1.1.5 Iodine, the challenger

Neighbor of xenon in the periodic table, the iodine atom I is an halogen, of atomic number 53 and mass 126.9 u. It exists in nature only as molecular iodine I_2, of mass 253.8 u. I_2 exists as dark crystals at room temperature, of density 4.9 g cm^{-1}. It was first discovered by the french chemist Bernard Courtois in 1811 [26], after he worked as a lab assistant at the young École polytechnique, between 1801 and 1804. Since then, studies about iodine remained scarce, and most available data are old and not well validated by the community. At room pressure, I_2 sublimates when heated, turning directly from solid to gas. The boiling point at 1 bar is around 457 K. At low pressure, the vapor pressure of iodine was measured more than 100 years ago by Baxter et al. [27], and 40 years later by Stull [28]. Fitting their data, the relation between iodine vapor pressure p (in Pa) and temperature T (in kelvin) used in this work is:

$$\log_{10}(p) = 9.6 - \frac{1675}{T - 88} \tag{1.5}$$

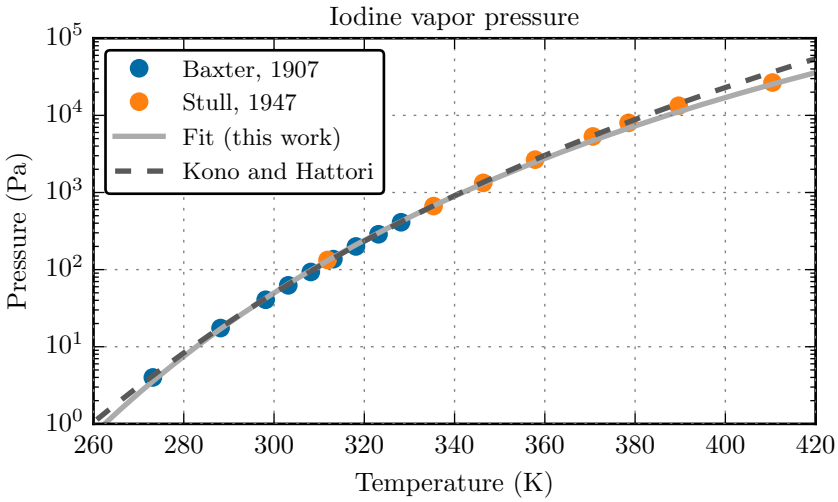

Figure 1.7: Vapor pressure of iodine as a function of Temperature. Data from Baxter et al. [27], Stull [28] are fitted with the law (1.5). The formula from Kono and Hattori [29] is added for information.

Equation (1.5) is expected valid between 260 K and 420 K, which is the amplitude of the data used [27, 28]. In this range, this is in excellent agreement with the formula given by Kono and Hattori [29] and used for example by Steinberger and Scime [30]. Both formula and the historical data are shown Figure 1.7.

Iodine is to be manipulated with basic precautions - gloves, under an aspiring fume hood - as it is harmful when breathed or if it touches bare skin. Trash contaminated with iodine is to be discarded with chemical trash, as it is harmful for the environment [31]. Although the least reactive of the stable halogens, iodine is corrosive with most materials, including for example stainless steel or aluminum, with which it forms iodide volatile compounds. This leads to important precautions or protocols during experimental sessions, detailed section 1.2.3. Once ionized, iodine produces a plasma that is in most cases yellow, but can also appear white or green, as detailed Chapter 3. An example of iodine plasma produced at LPP is shown Figure 1.8.

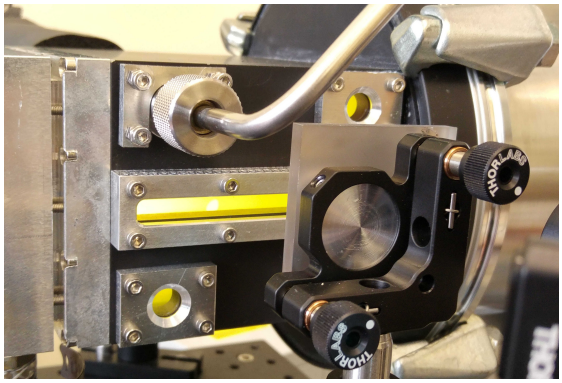

Figure 1.8: A yellow iodine plasma produced at LPP within the PEGASES ion source.

The interest of I_2 arises when compared to other gases, in the context of electric propulsion. The I atom is a neighbor of Xe in the periodic table of the elements. Even though iodine chemistry is incredibly complex compared to anything that has been used as propellant in recent history, the resulting I_2 has therefore certain similarities with a xenon plasma. I is slightly lighter and easier to ionize than Xe, and can be stored as a much higher density.

Properties of mass, ionization potentials and density is given for I, I_2 and the other classic noble gases are given Table 1.2.

Species	Mass	Ionization potential		Density
		1st	2nd	($g\,cm^{-3}$)
Ar	39.95 u	15.76 eV	27.63 eV	1.4
Kr	83.8 u	14.00 eV	24.36 eV	2.4
Xe	131.3 u	12.13 eV [22]	20.97 eV [32]	2.9
I_2	253.8 u	9.31 eV [33]		4.9
I	126.9 u	10.45 eV [34]	19.13 eV [35]	

Table 1.2: Mass, ionization potentials and storage density of different materials considered for use as propellant. I_2 density is given for the solid state at room temperature. Xe, Ar and Kr densities are given for the liquid state at boiling point. These densities are representative of the densities within tanks onboard satellites.

To understand the interest of a propellant used in a plasma, one can used the concept of *energy lost per electron-ion pair created* introduced by Lieberman and Lichtenberg [36]. It encompasses the fact that *while* an ion-electron pair is created in a plasma, several other processes result in energy losses. More details can be found in section 2.4.2. Using this metric, which is a function of the electron temperature T_e, one can compare different species, with the curves plotted Figure 1.9. To analyze these curves, one can see that for any T_e, the energy lost for Xe is lower than for Ar, which is one reason why xenon is a better propellant, easier to ionize. It can be seen that above 2 eV, I atoms lead to less energy lost per electron-ion pair created than xenon atoms, suggesting an even easier ionization. I_2 molecules on this figure are easy to ionize, easier than Cl_2 shown on the same graph. One reason might be that no losses through vibrational or rotational excitation is taken into account here. These low $\mathcal{E}_c$ let us hope that if I_2 molecule dissociate easily, the resulting I plasma will be very efficient. If they don't dissociate that easily, the resulting I_2 plasma will be very efficient too.

Iodine is currently studied as a possible replacement for xenon as a propellant for electric propulsion devices. Besides the chemical advantages detailed above, iodine is much less expensive than xenon, and can be bought from 50 € to 500 € per kilogram depending on the purity, when Xe costs several thousands euros for the same mass. Stored as a solid, it is also much denser

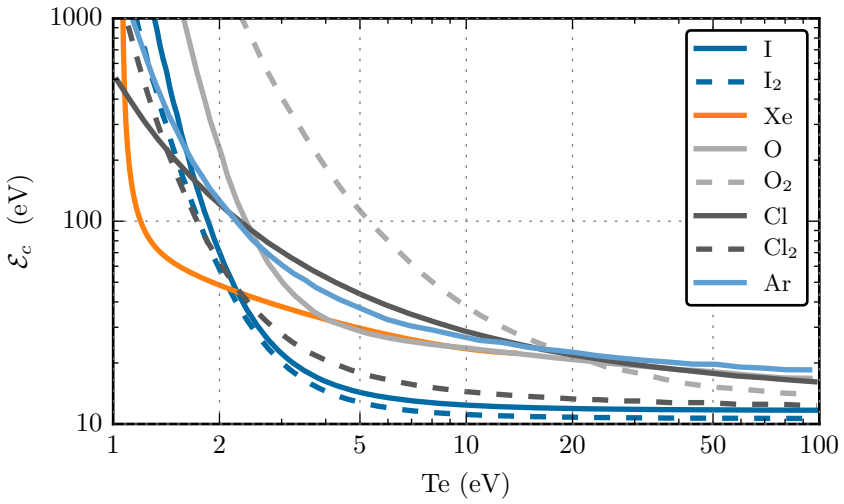

Figure 1.9: Energy loss per ion-electron pair created as a function of the electron temperature T_e, for different atomic and molecular species. Data sources: I and I_2 from this work; O, O_2 and Ar from Lieberman and Lichtenberg [36]; Cl_2 and Cl from Thorsteinsson and Gudmundsson [37]; Xe from Chabert et al. [38].

which facilitates the integration within a spacecraft, and needs less pressurized circuitry to be injected in the ionization chamber. Several teams, in academia or in companies, in the United States [39, 40] and in Europe [41–45] are currently trying iodine as propellant in laboratory electric propulsion devices, at different levels or for different kind of thrusters. They all stated that iodine was competitive with xenon as propellant, and the main results and studies are presented in the next paragraphs.

Grondein [46] was originally interested in iodine because of its electronegative properties, aiming at using it to form an ion-ion plasma for the PEGASES thruster that would accelerate each population successively. Grondein et al. [42] first developed a volume-averaged model of an iodine plasma within a classical RF-thruster, and focused the model development on comparisons with xenon; they calculated that the iodine behavior as propellant is predicted to be very similar to xenon, and the related performances are

also expected similar. The predicted thrust for a large gridded ion thruster thruster is for example presented Figure 1.10. In some cases, especially at low mass flow rate, the efficiency of the thruster running with iodine is calculated to be higher than when running on xenon. Some diagnostics were developed to compare the model to experiments within the PEGASES thruster, and the model predictions were proven coherent with emission spectroscopy and Langmuir probe experiments in a simple I_2 plasma. Iodine in the ion-ion thruster PEGASES was chosen for its electronegativity, and tested with a magnetic barrier designed to enhance electronegativity. At low discharge power, dissociation is not too strong and an ion-ion plasma was effectively detected downstream the grids, with electronegativities (negative ions to electron densities ratio) reaching 2000.

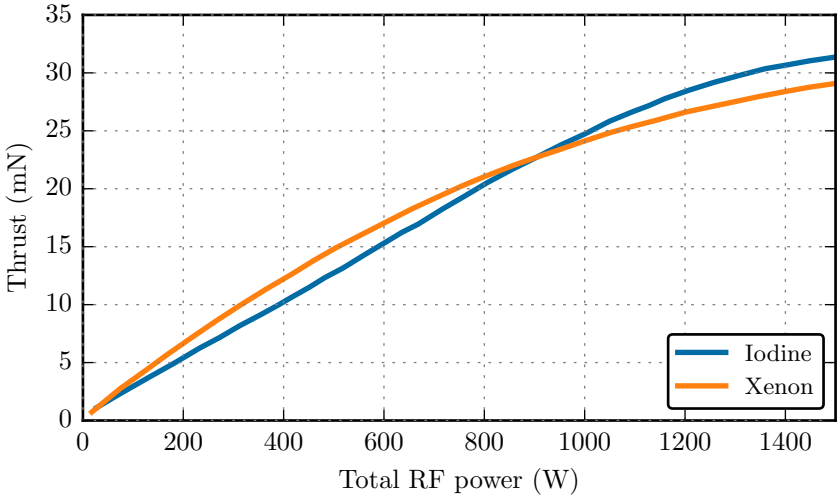

Figure 1.10: Thrust estimated from an example thruster, runing on xenon or iodine, for different total RF power. Reproduced from Grondein [46].

All other works found in the literature, and the one presented here, focus on the use of iodine *despite* its electronegative properties. Holste et al. [41] built a dedicated setup to run the heritage gridded ion thruster RIT-10 on both xenon on iodine on identical setups, in identical operating conditions. They showed that iodine as propellant was compatible as propellant for the RIT technology, and has features making it a viable alternative to xenon.

Their measurements are based on performance maps established by measuring the RF power needed to ensure a specific exhaust current, at a given mass flow rate. Two equal exhaust currents correspond to the same thrust only if the beam divergence is equal, which is a limitation of the comparison. They show that there is an optimum for both gases, where the mean free path between collisions is neither too long and too small, maximizing ionization. Comparing both performance maps shows that iodine is up to 12 % better at very low mass flow rate (1.5 sccm of iodine, in a setup of similar size than PEGASES, with a 22% grid transparency for neutrals), but xenon is better at any larger flow rates. It is assumed that at higher mass flow rates, the molecular nature of I_2 leads to many power loss phenomena. The ratio of the power needed to maintain a specific current on xenon versus on iodine is shown Figure 1.11.

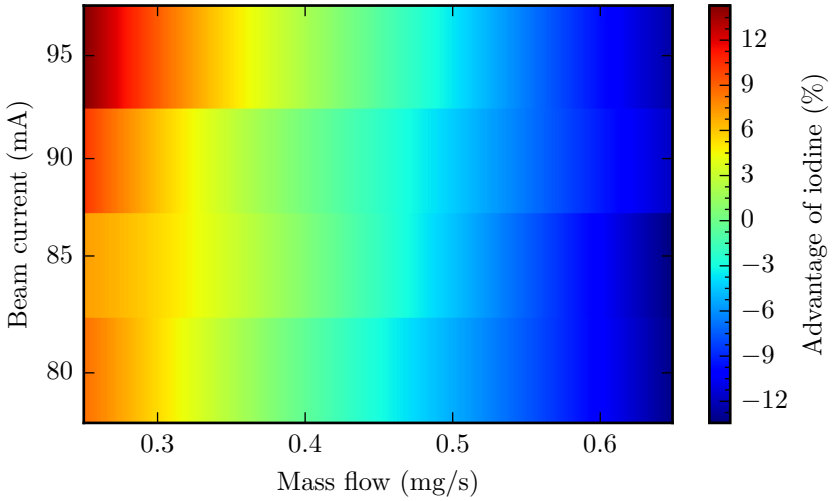

Figure 1.11: Advantage of iodine over xenon depending on beam current and mass flow rate. An advantage of 5 % for iodine means that achieving a given beam current for a given mass flow rate requires 5 % less power when using iodine that when using xenon. Data extrapolated from measurements presented by Holste et al. [41], Fig 5.

Iodine is also tested as propellant for Hall Effect Thrusters. Szabo [47] and Szabo et al. [39] used iodine as propellant for the BHT family, in the medium

power BHT-200 at 200 W, and in the high-power Hall Effect Thrusters, BHT-1000 and BHT-8000. With the BHT-8000, thrusts from 50 mN at 1 kW to around 500 mN at 9 kW were measured with different voltage potentials and an I_{sp} up to 2500 s. They did not perform dedicated comparisons with the same thrusters running on xenon but declare that, in general, measured values for I_{sp}, anode efficiency and thrust-to-power ratio were similar to values measured previously with xenon. They performed measurements on the beam divergence, that is found much lower on I_2, which is an advantage. They conclude that performance data taken with the BHT-8000 and other thrusters indicate that I_2 is competitive with xenon as propellant for the Hall effect thrusters.

Two European NewSpace companies consider iodine for miniaturized electric thrusters and provide direct or indirect comparisons of the use of xenon and iodine on their systems. Martinez-Martinez et al. [44] from ThrustMe developed a miniaturized gridded ion thruster working on iodine, fitting in 1 or 1.5 CubeSat units, delivering from 0.4 mN up to 1.1 mN of thrust, for a power consumpation between 30 W and 60 W. Comparing the commercial datasheets of their fully-integrated systems running on iodine or xenon, they declare better thrust performances on xenon (up to 0.95 mN at 60 W in I_2, up to 1.1 mN at 60 W in xenon) but a much higher total impulse in the I_2 model (1500 s per U in the 2U xenon version, 5000 s to 6000 s per U in the 1U or 1.5U iodine version) maybe due to an increase of I_{sp} but also to the higher density of I_2, and the related simplification of the injection systems. Manente et al. [45] from T4i have tested their Magnetically Enhanced Plasma Thruster (MEPT) in both iodine and xenon, and present after a dedicated analysis very similar performances in both I_{sp} and thrust, although xenon remains slightly better. During the tests, their iodine version produced up to 0.8 mN of thrust, and up to 600 s of I_{sp}, for a consumption from 2 W to 52 W.

1.1.6 PEGASES, NEPTUNE and family

The experimental propulsion setup used in this work has been inherited from the PEGASES (patent filed in 2005 by Chabert [48], and following related patents from the same authors [49, 50]) and NEPTUNE thruster (patent filed in 2014 by Rafalskyi and Aanesland [51]) families developed at LPP since 2005, in the frame of the development of gridded ions thrusters without external neutralizers. The PEGASES family was developed to accelerate successively positive and negative ions, hence required electronegative pro-

pellants. It was successfully tested with SF_6 and I_2. As shown Figure 1.12, it features an electromagnetic barrier to enhance creation of negative ions and a set of grids whose bias was inverted at a frequency in the kHz range to accelerate successively positive and negative ions. The main results of the experimental of numerical investigations of the PEGASES thruster in its successive versions can be found in the PhD work of Leray [52], Popelier [53], Bredin [54], Renaud [55] where it was designed and tested with SF_6 as a propellant, in Grondein [46], Lucken [56] where it was mostly developed with iodine propellant, or in papers from Aanesland et al. [57], Lafleur et al. [58, 59], Rafalskyi et al. [60]. More details about PEGASES as used in the thesis are given section 1.2.2. The PEGASES project inspired and was followed by the NEPTUNE concept. Featuring no magnetic barrier, it worked with noble gases and iodine, used despite its electronegativity, accelerating successively positive ions and electrons with a set of grids biased by the self-bias induced by the plasma. The main principles and results from the beginning of the project can be found in articles by Rafalskyi and Aanesland [61, 62]. This concept led to the creation of the company ThrustMe and thrusters derived from this initial concept are developed and commercialized there under the brand name NPT.

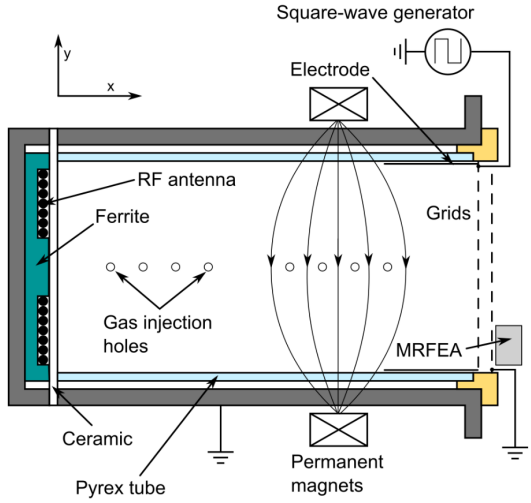

Figure 1.12: Diagram of the PEGASES version of 2014, from Lafleur et al. [58]. A magnetic barrier enhances the plasma electronegativity, and a square-wave generator periodically invert the gris voltage drop, accelerating successively positive and negative ions.

1.2 The experimental room

This section lists some characteristics of the setup used throughout this work, and the tools and processes implemented to ensure the safety of the operators and the sustainability of the setups with respect to the use of iodine.

1.2.1 Vacuum setup

The main vacuum chamber used in this work is a stainless steel spherical chamber from the Kurt J. Lesker company, named BUBBLE, with an internal volume around 50 L, shown Figure 1.13. It is pumped with a TPH 521 PC turbopump from Pfeiffer Vacuum designed to pump 440 $\mathrm{L\,s^{-1}}$ of N_2, and a XDS 35i scroll pump from Edwards. The backpressure is around 10^{-4} Pa and the operating pressure around 10^{-1} Pa for an effective pumping speed around 50 $\mathrm{L\,s^{-1}}$ in Ar.

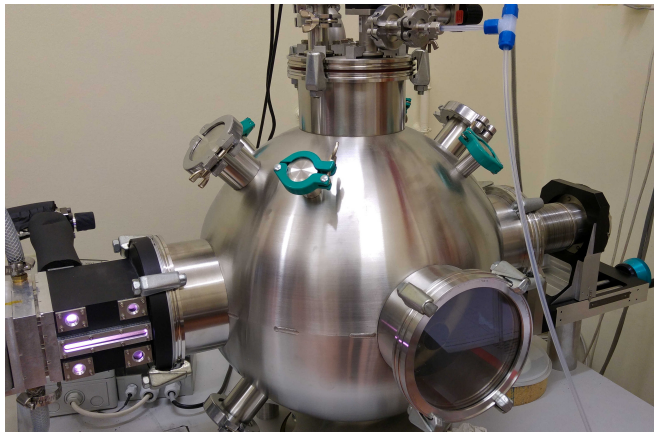

Figure 1.13: Photography of the BUBBLE vacuum setup with PEGASES running on argon, and setup adapted for Langmuir probe measurements.

For most of the results presented, the pressure is monitored by three independent probes: a PIRANI IKR050 from Pfeiffer Vacuum placed on top of the main chamber, indicating pressures from atmospheric pressure down to 1 Pa; a MKS hot cathod transducer on top the main chamber for pressures from 0.5 Pa down to the backpressure; and a capacitance manometer 627D

Baratron from MKS measuring pressure within the ionization chamber PEGASES through a pipe around 15 cm long and with a few millimeter internal width. The inner volume of this pipe is assumed isobar.

A general schematics of the vacuum setup is shown Figure 1.14. The PEGASES ion source presented is connected to the main chamber via a DN160 flange. Two gases can be injected at the same time, with two independent mass flow controllers: iodine on one side, and Xe and Ar on the other. More information about PEGASES as used in this work is given section 1.2.2. A liquid N_2 trap from the Kurt J. Lesker company is placed between the turbopump and the scroll pump to catch the injected I_2 before it reaches the scroll pump where it would solidify and damage the pump, and be released in the environment, two things that need to be avoided.

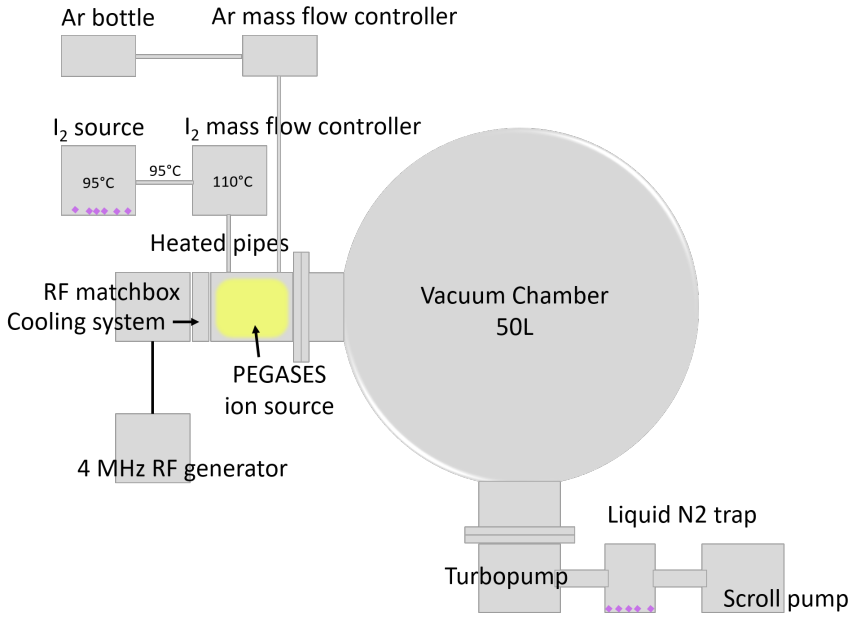

Figure 1.14: General sketch of the BUBBLE vacuum setup: PEGASES is connected to a 4 MHz RF generator through a dedicated matchbox. The cooling systems functions with running water. Two gas injectors can function at the same time. A liquid N_2 trap collects I_2 after the turbopump.

1.2.2 PEGASES as an ion source

Most plasmas studied in this work are done in the ionization chamber of the PEGASES thruster, with no acceleration stage and no magnetic barrier. This subsystem of PEGASES is abusively named PEGASES in this work. A sketch of this system is shown Figure 1.15. The ionization chamber has an inner volume of 8 cm × 12 cm × 12 cm. The RF antenna is a flat coil at the back of the ionization chamber behind a 3 mm thick alumina plate assuring vacuum sealing. Behind the antenna is a water cooling stage in which running water is flown. In the middle of this stage is a hole to let two wires connect the matching circuitry to the flat coil RF antenna. More information about the matching circuitry is given Appendix D. The matching circuit is matching impedance between the loaded coil and a 4 MHz RF generator. On the other side of the ionization chamber, a single grid at floating potential is installed. The grid transparency was varied depending on the experiments, to reach any target pressure while maintaining a I_2 mass flow rate above a few sccm. To mitigate what Godyak et al. [63] call *poorly defined discharge conditions*, the method used to calculate the real discharge power P_d during experiments from the RF power and the coil current is presented Appendix B.

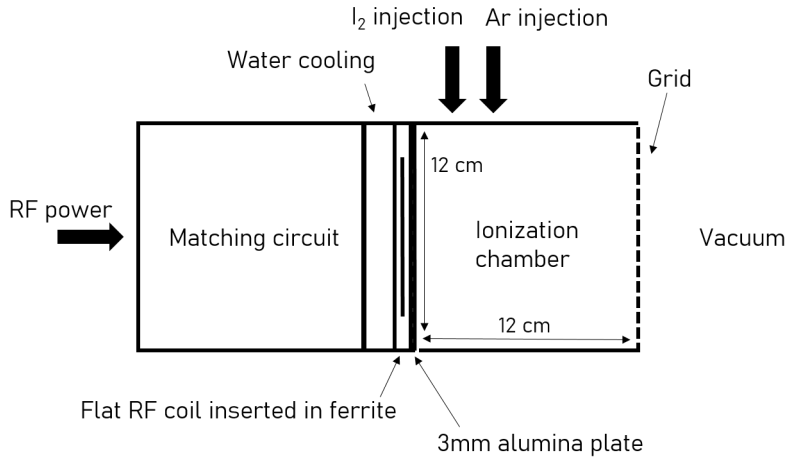

Figure 1.15: View from above. The inner height of the ionization chamber is 8 cm. The grid is at kept at floating potential, the other walls are grounded.

1.2.3 Experimenting with iodine

Using iodine in a plasma source is not as straightforward as plugging an argon or xenon bottle to a mass flow controller. Iodine gas from pellets of category 99.8 to 100.5% purity is injected in PEGASES through a dedicated mass flow controller, the MKS 1150C-4805M calibrated for 50 sccm of I_2. Iodine needs to be gaseous before entering the mass flow controller, so it is heated to around 370 K, hot enough to ensure a relatively high pressure but cold enough to stay colder than the mass flow controller heated at 383 K. This temperature difference avoids deposition in the controller. Two different reservoirs and three different heating systems were tried for the source:

- A large I_2 reservoir with an inner volume around 1 L, with a large flat surface at the bottom. The heating was done with a heating plate. More information is given in the PhD work of Grondein [46]. This solution was abandoned for a smaller volume to better monitor the use of I_2, but also because heating relied more than necessary on the thermal conductivity of the glass used for the reservoir, as I_2 would always solidify on top of the reservoir after each use, not at the bottom.

- A small glass tube, 7 cm long, of 25 mm internal width manufactured at École polytechnique and directly connected to the metal pipes via a KF40 glass-metal connection, wrapped into aluminum tape and plunged into a heat bath filled with Lab Armor Beads, that could move vertically to get the source in and out the bath. The system was heavy and not easy to manipulate, for a not so good thermal conductivity and very long installation procedures, so it was abandoned.

- A small glass tube, 7 cm long, of 25 mm internal width manufactured at École polytechnique and directly connected to the metal pipes via a KF40 glass-metal connection, wrapped with aluminum tape and heating wires connected to a 60 V voltage source. This allows fast mounting and unmounting, which in turn allows to use the setup with only limited amount of I_2 at the same time. The heating and cooling times of the reservoir are around 15 min, with no strong temperature gradient or overshoot, preserving the glass reservoir.

Heating the I_2 source is necessary to turn the iodine crystals in gas that can be injected in the mass flow controller. But iodine will solidify in the injection pipes at any point colder that is surroundings, so it is also necessary to heat all the pipes along the injection lines to avoid solidification and

clogging. Clogging is a problem because it can interrupt flow, and lead to corrosion if not cleaned correctly, but it will often disappear it the pipes are re-heated correctly [40]. In the present work, pipes are heated at 360 K with heating cables wrapped around the stainless steel pipes previously wrapped in aluminum tape. They are then placed in an insulating material used to isolate classic pipes. The heating cables are used with a 220 V voltage source, leading to very short heating times, and large temperature overshoots. The temperature is monitored with PT100 probes connected to a commercial circuit that automatically turns the input voltage ON and OFF. Temperature overshoots are considered smoothed by the stainless steel pipes so that the inner temperature must be rather constant. Pipes temperature was checked and verified with a thermal camera.

Any pipe left uncleaned and in open air after being used in the injection line will be rapidly corroded, such as the one shown Figure 1.16, that participated in a two-month long unscheduled corrosion test. To avoid this, heating on the injection line is kept ON even between experiments, and the entire line is kept under primary vacuum, as well as the main chamber.

After use, a cleaning protocol is set up to limit any chance of corrosion: the iodine accumulates in a liquid N_2 trap that is filled with N_2 before each experiment. This trap is cleaned under a fume hood every day after each experiment from the resulting I_2 layer shown Figure 1.17. It is cleaned with ethanol, and the trash is sent to the lab chemical trash. Another cleaning method was tried using a thiosulfate solution, reacting with I_2 according to the following reaction:

$$2\,S_2\,{O_3}^{2-} + I_2 \rightleftharpoons {S_4O_6}^{2-} + 2\,I^-$$

This method necessitates a subsequent easier cleaning with ethanol to remove the resulting I^- aqueous ions. Between two experimental sessions, if the setup is to be let unused for some time, a purge of the injection line is done by connecting the Ar injection line where the iodine source is usually installed. An argon plasma is run in PEGASES, hence "cleaning" the reactor. The argon flows in the iodine injection line, purging it for remaining iodine. It is not rare that the Ar plasma takes some minutes before yellow color completely disappears.

Figure 1.16: Result of a fortuitous corrosion test: a pipe where the iodine reservoir was attached, not cleaned after the reservoir was removed and left in open air for several weeks.

Figure 1.17: A layer of I_2 remaining on the liquid N_2 trap during a cleaning process. It is removed with ethanol. Using the wash bottle as some kind of pressure washing machine does really help.

1.3 Conclusions

After introducing space propulsion and electric propulsion, this chapter presented first how the present work finds its rationale in the NewSpace dynamics, where new actors in the propulsion sector serve new clients envisioning large satellite constellations. In particular, the quest for less expensive propellants is at the core of a new interest in iodine, but the underlying complex theory of iodine plasmas is lacking behind empirical observations of the good performances of iodine in laboratory thrusters. The second section presented the experimental room. It particularly presented a vacuum setup dedicated to iodine and how it was modified to be able to cope with several successive measurement campaigns.

Chapter 2

Global model of an iodine ICP plasma source

Global models are powerful tools to understand the evolution of a plasma in response to a change in parameters such as the pressure, the discharge power or the wall materials. Well understood for simple electropositive atomic plasmas, global models are also used for molecular, electronegative plasmas. Such a model has been published for I_2 in 2016 and is further improved in this work. A fully rewritten code is presented in this chapter and in Appendix A. It is run to precisely analyze the chemical dynamics within an iodine plasma. Dedicated studies on uncertain or sensible parameters are run to anticipate experimental comparisons, and better understand effects of potential design drivers for plasma thrusters used with iodine.

2.1 Introduction and basic principles

2.1.1 Introduction to global models

A global model of a plasma discharge is a volume-averaged or *zero-D* model. When assuming a uniform plasma bulk in the discharge, it boils down to solving a set of ordinary differential equations: one per species for particle balance and one for power balance. The particle balance expresses that the variation of density of a given species is due to gains through different reactions and losses through other reactions or at the boundaries. When [A] is the number of particles A per cubic meter, G is a gain and L is a loss, it is in its general form for a generic species A:

$$\frac{\mathrm{d[A]}}{\mathrm{d}t} = G_A - L_A \tag{2.1}$$

Let us consider a simple electropositive plasma with three species: for example argon atoms Ar of density [Ar], the corresponding positive ions Ar^+ of density $[\mathrm{Ar}^+]$ and electrons e^- of density n_e. In the simplest case, the only source of Ar^+ and e^- is the ionization $\mathrm{Ar} + \mathrm{e}^- \longrightarrow \mathrm{Ar}^+ + 2\,\mathrm{e}^-$. If K_{iz} is the ionization rate, then the number of particles created per second in the volume $\mathcal{V}$ is $G_A = K_{iz}[\mathrm{Ar}]n_e\mathcal{V}$. Electrons and positive ions are lost at the walls: assuming quasi-neutrality, $[\mathrm{Ar}^+] = n_e$ in the bulk and the positive and negative fluxes to the walls are equal and expressed as hn_eu_B. In this last equation, h is the edge-to-center density ratio and u_B is the speed at which the positively charged particles enter the sheath, called the Bohm speed. If $\mathcal{A}$ is the boundary surface, we have then $L_A = \mathcal{A}h[\mathrm{Ar}^+]u_B$. Equation (2.1) at steady state is then:

$$K_{iz}[\mathrm{Ar}]\mathcal{V} = \mathcal{A}hu_B \tag{2.2}$$

In a simple case, u_B and K_{iz} only depend on the electron temperature T_e and h is considered constant or only depending on [Ar]. Solving (2.2) for stationary state leads by itself to the electron temperature T_e.

The second equation is a power balance on the electron population. It expresses the fact that the absorbed power, also called discharge power P_d, in W, is spent in the plasma either increasing the electron energy or lost by collisions in the volume or at the boundaries. It writes in its general form:

$$P_d = \frac{\mathrm{d}}{\mathrm{d}t}\left(\frac{3}{2}n_eeT_e\right)\mathcal{V} + P_{\mathrm{loss,coll}} + P_{\mathrm{loss,bound}} \tag{2.3}$$

The discharge power P_d can come as an input of the model, or be derived from external parameters such as coil current or RF power using a model for power transfer, including for example matchbox losses [64]. The power lost by collisions corresponds to energy transfers from electrons to other particles through elastic or inelastic collisions. The power lost at the boundaries can be expressed by multiplying the electron flux to the walls by the mean energy carried to the walls by those particles. A detailed example of both powers is given in the following paragraphs in the case of iodine. In simple cases, the equation (2.3) can be solved for steady state and, using T_e from the particle balance, leads to the electron density n_e.

The remaining part of the section will be mainly dedicated to writing such particle and power balance for an iodine electronegative molecular plasma in a realistic reactor with gas injection, five walls and an open surface, solving the generated coupled equations and studying the impact of varying several key parameters. A large part of this global model has been developed with Romain Lucken and is partially presented in his PhD thesis [56], after the work of Chabert et al. [38] and especially Grondein et al. [42].

2.1.2 Discharge geometry and parameters

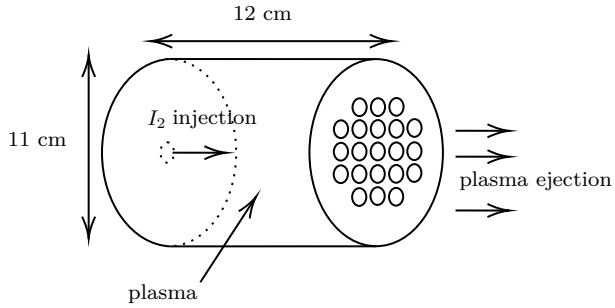

Figure 2.1: Illustration of the ideal ionization chamber used in the global model to be representative of PEGASES. The cylinder has a length $\mathcal{L}$, a radius $\mathcal{R}$, a volume $\mathcal{V}$ and several areas are defined to describe the walls and grids.

The reactor considered in this section is a cylinder of length $\mathcal{L} = 12\,\text{cm}$ and radius $\mathcal{R} = 5.5\,\text{cm}$ closed on one side by a set of biased grids, such as

the one showed Figure 2.1. All walls are grounded. This cylinder has the same volume and the same total grid area as the PEGASES thruster. It is considered that adding such a dual-grid acceleration stage does not affect the plasma parameters, but the presence of an ion focusing phenomenon is assumed: any positively charged particle going through a hole of the first grid will be led out of the thruster, whereas neutrals can also be repelled inside the chamber by the second grid. This is taken into account by defining an open area for positively charged ions $\mathcal{A}_{\text{open},i} = \beta_i \pi \mathcal{R}^2$, and an open area for neutrals $\mathcal{A}_{\text{open},0} = \beta_0 \pi \mathcal{R}^2$, with β_i and β_0 the grid transparency for positive ions and neutrals respectively, and $\beta_i \geq \beta_0$. It is also assumed that this set of grids, usually biased up to several kV, prevents any negatively charged species from leaving the plasma. In this work, all curves are plotted assuming $\beta_i = \beta_0$, to simulate the presence of a single unbiased grid as used in the next chapters. It is also shown later that changing the grid transparency does not affect the plasma parameters for a given plasma pressure. The chamber volume is $\mathcal{V} = \pi \mathcal{R}^2 \mathcal{L}$. Three more areas are defined to characterize the chamber, the total area $\mathcal{A}_{\text{total}}$ and the non-open areas $\mathcal{A}_i$ and $\mathcal{A}_0$:

$$\begin{aligned} \mathcal{A}_{\text{total}} &= 2\pi \mathcal{R}^2 + 2\pi \mathcal{R}\mathcal{L} \\ \mathcal{A}_i &= \mathcal{A}_{\text{total}} - \beta_i \pi \mathcal{R}^2 = \mathcal{A}_{\text{total}} - \mathcal{A}_{\text{open},i} \\ \mathcal{A}_0 &= \mathcal{A}_{\text{total}} - \beta_0 \pi \mathcal{R}^2 = \mathcal{A}_{\text{total}} - \mathcal{A}_{\text{open},0} \end{aligned}$$

A constant injection of I_2 in the chamber is modeled as a constant term in the I_2 particle balance equation.

2.2 Iodine chemistry

2.2.1 Distributions, cross-sections and reaction rates

The electron temperature is through this manuscript expressed in eV. It is defined so that a temperature of 1 eV corresponds to an energy of 1 eV $= \|e\|$J, with the elementary charge $e = 1.602\,176\,634 \times 10^{-19}$ C and $\|e\|$ the dimensionless value of e. It can be converted to J and K units using

$$\|e\| \; T_e[\text{eV}] = k \; \text{T}_e[\text{K}] \tag{2.4}$$

The dimensional homogeneity of this convention is ensured only using $\|e\|$ in (2.4), but for sake of clarity the norm symbol will be omitted and any product eT_e in this manuscript is to be read as an energy in J. The other notations used are: ε to describe the energy in J, and $\mathcal{E}$ to describe it in eV, so that $\varepsilon = e\mathcal{E}$.

The distribution functions are defined so that $f_v(v)$ is the number of particles with speed between v and $v + \mathrm{d}v$ [36, 64]. It follows:

$$n = \int_0^\infty f_v(v)dv = \int_0^\infty f_\varepsilon(\varepsilon)d\varepsilon = \int_0^\infty f_\mathcal{E}(\mathcal{E})d\mathcal{E}$$

With the following relations between the variables:

$$\varepsilon = e\mathcal{E} = \frac{mv^2}{2} \qquad \mathrm{d}\varepsilon = e \; \mathrm{d}\mathcal{E} \qquad \mathrm{d}v = \frac{1}{\sqrt{2m}} \frac{\mathrm{d}\varepsilon}{\sqrt{\varepsilon}}$$

These relations allow to write the Maxwellian distribution functions in different units, with n the density here:

$$f_v(v) = n\left(\frac{m}{2\pi e T_e}\right)^{3/2} 4\pi v^2 \exp\left(-\frac{mv^2}{2eT_e}\right)$$
$$f_\varepsilon(\varepsilon) = \frac{2n}{\sqrt{\pi}}\left(\frac{1}{eT_e}\right)^{3/2} \sqrt{\varepsilon} \exp\left(-\frac{\varepsilon}{eT_e}\right)$$
$$f_\mathcal{E}(\mathcal{E}) = \frac{2n}{\sqrt{\pi}}\left(\frac{1}{T_e}\right)^{3/2} \sqrt{\mathcal{E}} \exp\left(-\frac{\mathcal{E}}{T_e}\right)$$

Given a set of cross sections σ for a given reaction, the reaction rate for an electron-neutral or electron-ion collision is computed by integrating the product of cross section and speed over the particle distribution function:

$$K = \frac{1}{n}\langle\sigma_v(v)v\rangle_v = \frac{1}{n}\langle\sigma_\varepsilon(\varepsilon)v\rangle_\varepsilon = \frac{1}{n}\langle\sigma_\mathcal{E}(\mathcal{E})v\rangle_\mathcal{E}$$

The reduced mass of a system with an electron and an heavy particle is approximately the electron mass, and we can consider the heavy particle at rest before the collision. For a Maxwellian distribution of the electrons, the reaction rate is then, in different units:

$$\begin{aligned} K(T_e) &= \left(\frac{m_e}{2\pi e T_e}\right)^{3/2} \int_0^\infty \sigma_v(v) v \exp\left(-\frac{m_e v^2}{2eT_e}\right) 4\pi v^2 \mathrm{d}v \\ &= \sqrt{\frac{1}{m_e \pi}} \left(\frac{2}{eT_e}\right)^{3/2} \int_0^\infty \sigma_\varepsilon(\varepsilon)\varepsilon \exp\left(-\frac{\varepsilon}{eT_e}\right) \mathrm{d}\varepsilon \\ &= \sqrt{\frac{e}{m_e \pi}} \left(\frac{2}{T_e}\right)^{3/2} \int_0^\infty \sigma_\mathcal{E}(\mathcal{E})\mathcal{E} \exp\left(-\frac{\mathcal{E}}{T_e}\right) \mathrm{d}\mathcal{E} \end{aligned}$$

Several reactions present a reaction rate, either constant or with an analytical formula, that is not necessarily derived directly from a particular set of cross sections. For heavy-heavy collisions such as ion-neutral collisions, the complete formula is, with $v_R = \|v_1 - v_2\|$:

$$K(T_1, T_2) = \int \mathrm{d}^3 v_1 \mathrm{d}^3 v_2 f_{v_1}(v_1) f_{v_2}(v_2) \sigma(v_R) v_R$$

Practically speaking, only one reaction between heavy species is used in this work, and both species are assumed at the same temperature. Therefore, the formula used to compute the reaction rate is the same than the one for electron-neutral collisions, replacing the electron mass m_e by the reduced mass of the heavy-heavy system, and adapting the temperature with the gas temperature T_g.

2.2.2 Plasma species

As in models from Grondein et al. [42], Lucken [56], six different species are considered in the model: molecular iodine I_2, iodine atoms I, iodine ions I^+, I^- and ${I_2}^+$ and electrons e^-. Doubly ionized I^{2+} ions are neglected because of the large gap between first and second ionization potentials. Atomic excitation is taken into account in the power balance of the system but there is no particle balance for excited species in the current work.

2.2.3 Reaction set

The set of reactions and the justification of the associated cross sections or rates is presented in more details in the PhD thesis of Romain Lucken [56], some details are recalled here. This reaction set used here is presented in Tab. 2.1. The iodine plasma is made by ionizing an iodine propellant that comes as a I_2 molecule. The I_2 molecule can dissociate by direct dissociation through electron impact, dissociative attachement or dissociative ionization. The dissociative attachment in an electronegative plasma is always the main, and here the only, reaction to create negative ions. I_2 molecules are subject to elastic collisions with electrons, and can be directly ionized, forming an I_2^+ ion. No excitation levels are considered for I_2, even vibrational or rotational. No electron excitations to higher electronic states are considered as the first excited level (at 2.5 eV) is well above the dissociation energy (at 1.6 eV) [42]. The I atoms resulting from I_2 dissociation can be excited, with a single equivalent level considered, ionized or undergo elastic collisions with electrons. All those reactions are described by cross sections calculated by Hamilton [33].

Two more reactions are added after recent work from Hamilton [65]: the dissociation by electron impact of I_2^+ and the detachment of I^- by electron collision, contributing to reduce the density of these two minor populations. Three more gas-phase reactions are considered but poorly characterized, mainly by *guesstimates* from work on chlorine plasmas: mutual neutralization between I^- and I_2^+ [66], mutual neutralization of I^- and I^+ [67], and the non-resonant charge exchange between I_2 and I^+. The relative importances of these reactions are detailed in the following paragraphs. Last, it is considered that I atoms can stick to the walls and recombine there to give an I_2 molecule. The recombination coefficient of iodine, linked to the sticking coefficient, has never been studied in the literature. Different estimates have been tried in the mentioned models, based on chlorine plasmas, and will be discussed in section 2.9.

Table 2.1: Global model reaction set used in this work. The left column presents the corresponding notations used in this work.

Notation	Process	Reaction formula
	Electron impact on I_2	
el,I_2	I_2 elastic collision	$I_2 + e^- \longrightarrow I_2 + e^-$
iz,I_2	I_2 ionization	$I_2 + e^- \longrightarrow {I_2}^+ + 2\,e^-$
diss.att.	I_2 dissociative attachment	$I_2 + e^- \longrightarrow I^- + I$
diss	I_2 dissociation	$I_2 + e^- \longrightarrow 2\,I + e^-$
diss.iz.	I_2 dissociative ionization	$I_2 + e^- \longrightarrow I^+ + I + 2\,e^-$
	Electron impact on I	
el,I	I elastic collision	$I + e^- \longrightarrow I + e^-$
exc	I excitation	$I + e^- \longrightarrow I^* + e^-$
iz,I	I ionization	$I + e^- \longrightarrow I^+ + 2\,e^-$
	Electron impact on I_2^+	
diss,I_2^+	${I_2}^+$ dissociation	${I_2}^+ + e^- \longrightarrow I^+ + I + e^-$
	Electron detachment of I^-	
detach	I^- detachment	$I^- + e^- \longrightarrow I + 2\,e^-$
	Gas phase recombination	
neut,I^-,I_2^+	I^- and ${I_2}^+$ neutralization	$I^- + {I_2}^+ \longrightarrow I + I_2$
ion.rec	I^- and I^+ neutralization	$I^- + I^+ \longrightarrow 2\,I$
	Charge exchange	
c.ex,I^+,I_2	I_2 and I^+ charge exchange	$I_2 + I^+ \longrightarrow {I_2}^+ + I$
	Surface recombination	
rec	I_2 recombination	$I \longrightarrow \frac{1}{2}\,I_2$

Cross sections

The cross-sections presented in the following figures are used solely to compute the reaction rates through integration over electron energy distribution functions. Some datasets are limited to a few tens or hundreds of eV. When needed, the elastic collision cross sections have been extrapolated at high energy with a law proportional to $1/T_e$ and the excitation cross-sections with a law proportional to $\ln(T_e)/T_e$ [68, 69], so as to have data from 0.01 eV to 1000 eV. A comparison of different extrapolations and their effect on the final reaction rates is presented in Appendix C.

All the threshold energies are regrouped Tab. 2.2. When a cross-section dataset from Hamilton [33, 65] is used, the threshold energy used in this work is the energy corresponding to the first non-zero value, for coherence. The admitted value in other works in given too, when applicable.

Figure 2.2a shows the cross sections for the reactions involving I as a reactant, all computed by Hamilton [33]. The threshold energy for excitation is $\mathcal{E}_{exc,I} = 0.95\,\text{eV}$, coherent with the admitted value of energy of the first state above the ground state. It is here the upper state from the fundamental state fine structure. A secondary threshold is seen for the first excited state, at 6.8 eV [70], where electric dipolar collisions come to play. The threshold energy (corresponding to the first non-zero cross-section) for ionization is $\mathcal{E}_{iz,I} = 11.6\,\text{eV}$, when the NIST database mentions 10.45 eV [23, 34].

In Figure 2.2b are shown the cross sections for I_2, all computed by Hamilton [33]. Like for the I atom, the elastic cross sections are extrapolated at high energy with a law so that they are proportional to $1/T_e$, and the dissociation cross sections with a law proportional to $\ln(T_e)/T_e$ [68, 69]. The threshold energy for dissociative ionization is $\mathcal{E}_{diss.iz} = 10.9\,\text{eV}$, the threshold energy for ionization is $\mathcal{E}_{iz,I_2} = 9.31\,\text{eV}$, and the threshold energy for dissociation is $\mathcal{E}_{diss,I_2} = 1.57\,\text{eV}$.

In Figure 2.3 are presented the cross-sections for I^- and ${I_2}^+$, computed by Hamilton [65]. The threshold energy for I^- detachment is $\mathcal{E}_{detach} = 4\,\text{eV}$. This value is the first energy corresponding to a non-zero cross-section of detachment. It is biased because the dataset from Hamilton [65] has a resolution of 1 eV. The admitted value is 3.059 eV [71]. The threshold energy for ${I_2}^+$ dissociation is $\mathcal{E}_{diss,{I_2}^+} = 2.18\,\text{eV}$.

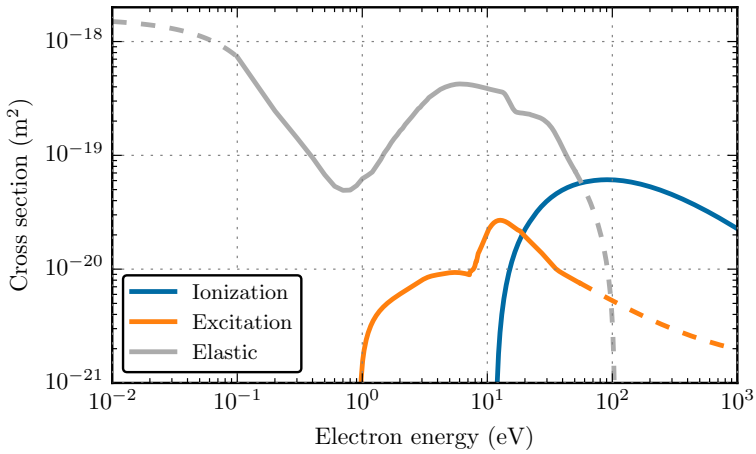

(a) Cross sections for the reactions of ionization, excitation and electron-atom collisions with the iodine I atom.

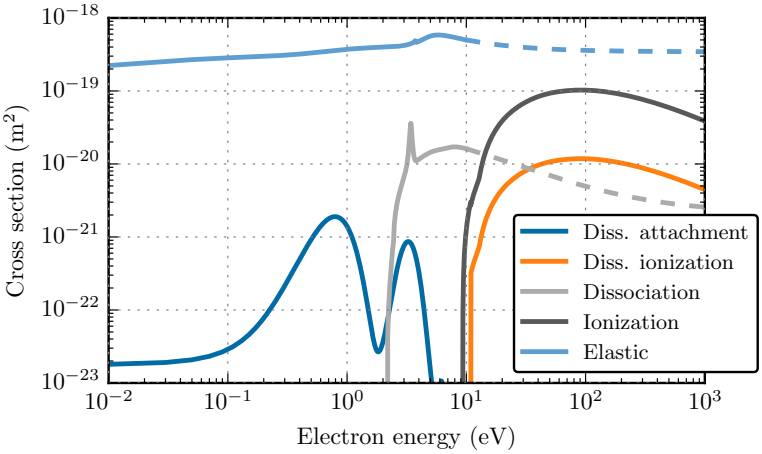

(b) Cross sections for the reactions of dissociative attachement, dissociative ionization, dissociation, ionization and electron-molecule collision for the iodine I_2 molecule.

Figure 2.2: Cross sections for I and I_2. The solid lines present the available datasets. The dashed lines are extrapolations from this work detailed in the current section and Appendix C.

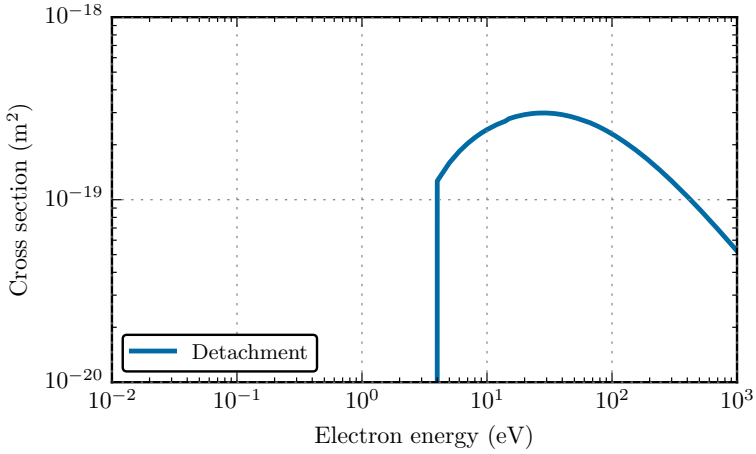

(a) Cross sections for the reaction of detachment of the iodine I^- ion.

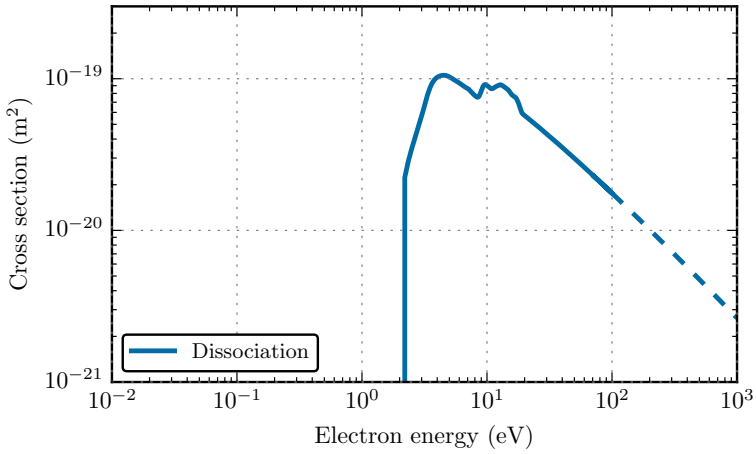

(b) Cross sections for the reaction of dissociation of the iodine $I_2{}^+$ ion.

Figure 2.3: Cross sections for I^- and $I_2{}^+$. The solid lines present the available datasets. The dashed lines are extrapolations from this work detailed in the current section and Appendix C.

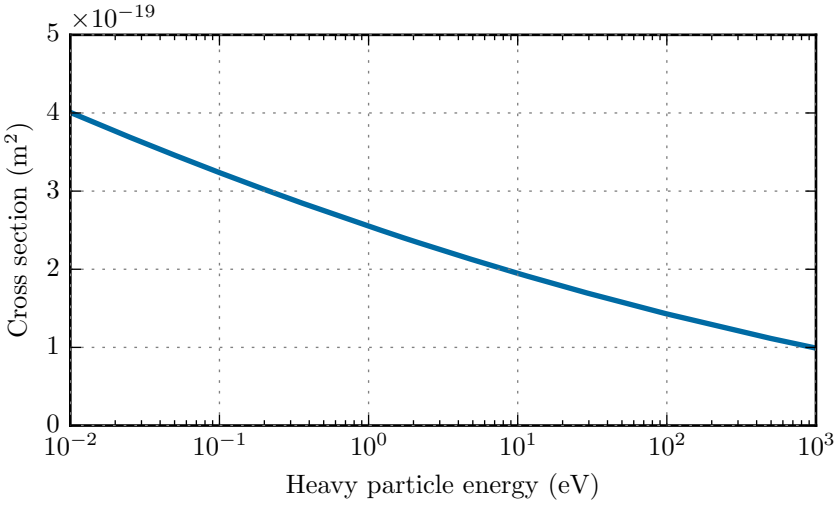

Figure 2.4: Cross sections for the I_2 - I^+ non-resonant charge exchange reaction, as a function of the energy of the particles. Model from Lucken [56].

Table 2.2: Threshold energies of the reaction used in the model, found as the energy corresponding to the first non-zero cross-section (left), and the other admitted value from the literature (right), if applicable.

Energy	Used in this work	Other admitted value
$\mathcal{E}_{diss.iz}$	10.9 eV [33]	
$\mathcal{E}_{iz,I_2}$	9.31 eV [33]	
$\mathcal{E}_{diss,I_2}$	1.567 eV [33]	1.529 eV [72]
$\mathcal{E}_{exc,I}$	0.95 eV [33]	0.94 eV [70]
$\mathcal{E}_{iz,I}$	11.6 eV [33]	10.45 eV [34]
$\mathcal{E}_{detach}$	4 eV [65]	3.059 eV [71]
$\mathcal{E}_{diss,I_2^+}$	2.1768 eV [65]	

Reaction rates

To obtain the reaction rates, the cross-sections presented above are integrated over a Maxwellian distribution for the electrons. Two exceptions are $K_{\text{neut,I}^-,\text{I}_2^+} = 1.22 \times 10^{-13}\,\text{m}^3\,\text{s}^{-1}$ (from Greaves [66]) and $K_{\text{ion.rec}} = 9.311 \times 10^{-15}\,\text{m}^3\,\text{s}^{-1}$ (from Yeung [67]) that were already used by Grondein et al. [42]. On Figure 2.6a are displayed the reaction rates for the iodine I atom, and on Figure 2.6b for the iodine I_2 molecule. Reaction rates for I^- are shown Figure 2.7a and those for $I_2{}^+$ on Figure 2.7b.

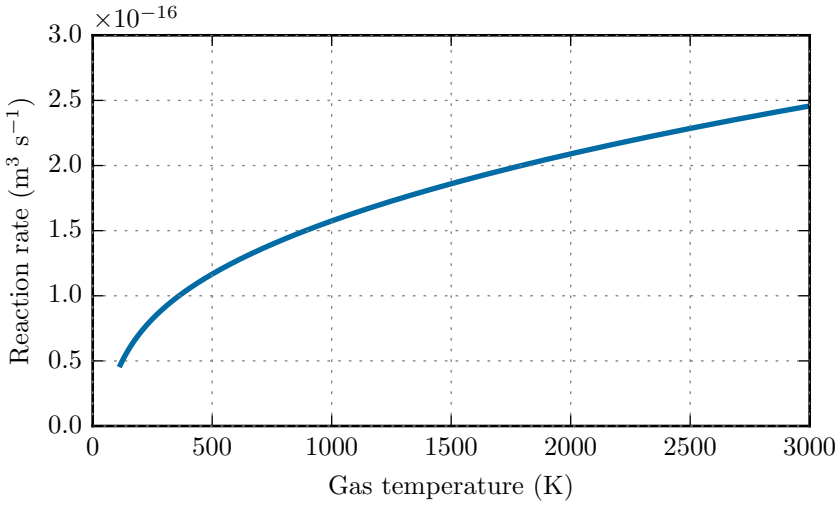

Figure 2.5: Reaction rate for the I_2 - I^+ non-resonant charge exchange, obtained by convolution of the cross-sections from Figure 2.4 with a Maxwellian energy distribution function for the gas, and a reduced mass of $2/3m_I$.

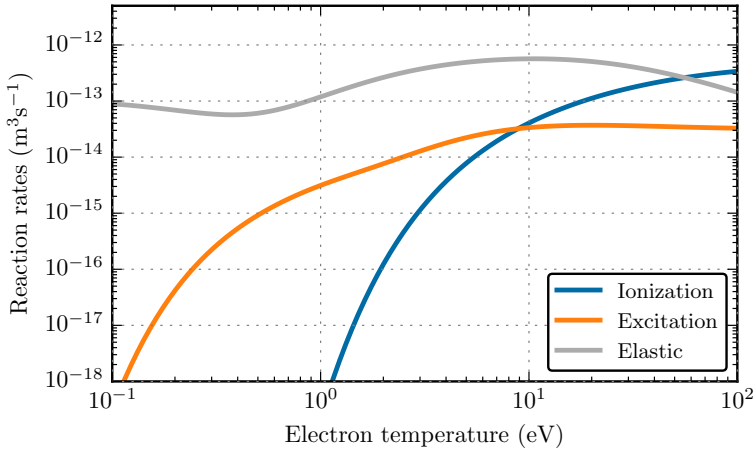

(a) Reaction rates for the iodine I atom as a function of electron temperature.

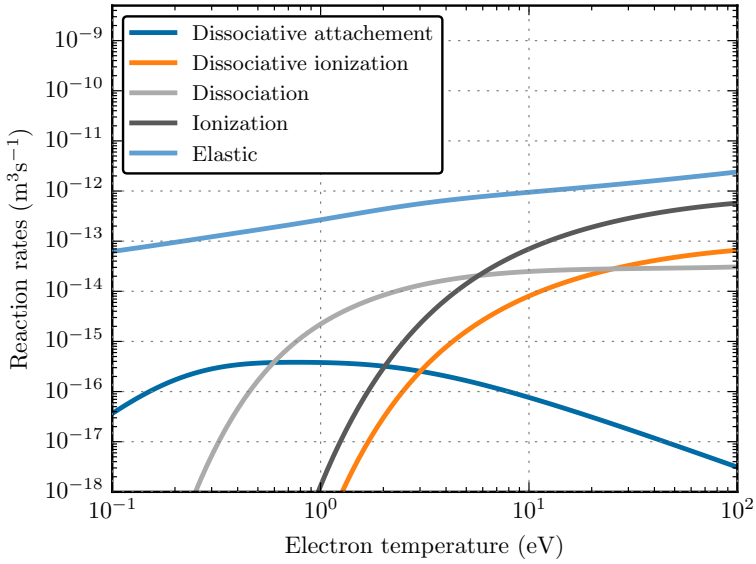

(b) Reaction rates for the iodine I_2 molecule as a function of electron temperature.

Figure 2.6: Reaction rates for the iodine I atom and I_2 molecule, obtained by integration of the cross-sections from Figure 2.2 over a Maxwellian EEDF.

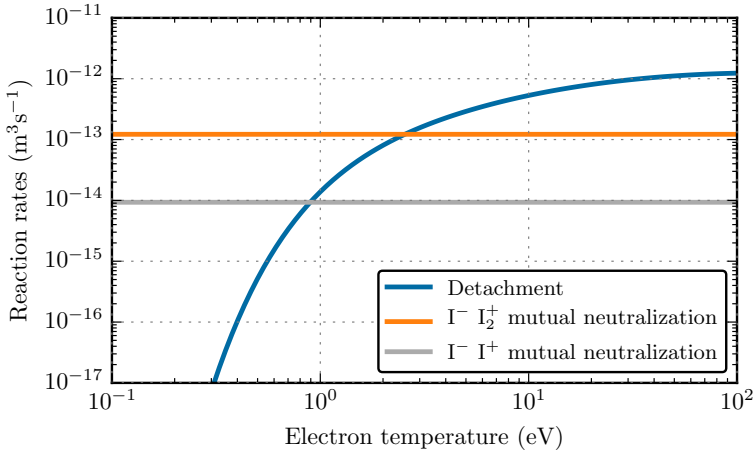

(a) Reaction rate for the iodine I^- ion

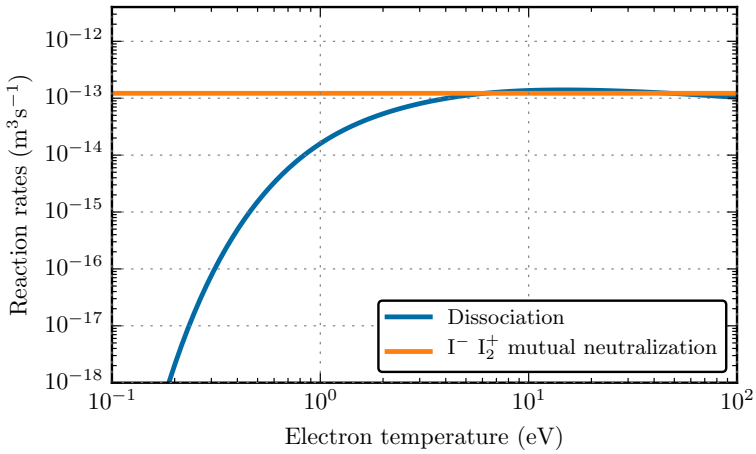

(b) Reaction rate for the iodine $I_2{}^+$ ion

Figure 2.7: Reaction rates for detachment and dissociation of iodine I^- and $I_2{}^+$ ions, obtained by convolution of the cross-sections from Figure 2.2a with a Maxwellian electron energy distribution function for the detachment. Mutual neutralization rates independent from electron energy are added for comparison.

2.3 Particle balance

The equations for the global model are given section 2.5, here is exposed the general structure of a particle balance equation. For each species, a particle balance in time is written in the general form, with G characterizing a gain and L characterizing a loss:

$$\frac{\mathrm{d}n}{\mathrm{d}t} = (G_{\mathrm{gas}} - L_{\mathrm{gas}}) + G_{\mathrm{inflow}} + (G_{\mathrm{walls}} - L_{\mathrm{walls}})$$

The writing of these different contributions to the particle balance, as well as the power balance presented later, has been automatized given a set of reactions and the geometry of the plasma boundaries, in a *chemistry parser* developed in python. More information about the code is given Appendix A.

2.3.1 Gas phase

Gains and losses in gas phase are linked to reactions such as

$$\mathrm{A} + \mathrm{B} \xrightarrow{\mathrm{K}} \mathrm{C} + \mathrm{D}$$

And the corresponding terms are here (with G_C characterizing a gain for species C and L_A characterizing a loss a loss for species A) $L_A = L_B = G_C = G_D = K[\mathrm{A}][\mathrm{B}]$, with the densities in m^{-3} and K the reaction rate in $\mathrm{m}^3\mathrm{s}^{-1}$. If there are more than two reactants, then this formula is generalized by having the product of densities of each reactant instead of only [A][B] and changing the unit of K accordingly.

2.3.2 Inflow

G_{inflow} describes the gas injection in the plasma. It is 0 if a species is not injected, and is equal to the number of particles entering the reactor per second and per cubic meter otherwise. The inflow unit is Standard Cubic Centimeter per Minut (sccm). We use $1\,\mathrm{sccm} = 4.477\,96 \times 10^{17}\,\mathrm{s}^{-1}$ for all gases [4]. In particular, neglecting variations from an ideal gas, this corresponds to $1\,\mathrm{sccm} = 0.19\,\mathrm{mg\,s}^{-1}$ for I_2 injection.

2.3.3 Boundaries

Boundaries are of three types in the chamber - walls, holes and grids - but are in the model divided into two categories: walls and holes. Indeed a grid of area $\mathcal{A}$ is treated as a hole of surface $\beta\mathcal{A}$ and a wall of surface $(1-\beta)\mathcal{A}$, with β the grid transparency. The particle flux to a boundary for a particle A is written Γ_A, in $\mathrm{m^{-2}\,s^{-1}}$. The particle behaviors at the wall boundaries or at open boundaries defined in section 2.1.2 are the following:

- When a positively charged particle reaches a wall, it is neutralized. In term of population, this particle is lost and the corresponding neutral particle is reinjected in the plasma at the same temperature. For example, to consider the neutralization of $\mathrm{I^+}$ at the walls, we add
$$L_{\mathrm{I^+}} = G_{\mathrm{I}} = \Gamma_{\mathrm{I^+}}\mathcal{A}_i\mathcal{V}^{-1}$$
- When any particle reaches an open boundary, it is lost. We write for example
$$L_{\mathrm{I}} = \Gamma_{\mathrm{I}}\mathcal{A}_{\mathrm{open},0}\mathcal{V}^{-1} \qquad L_{\mathrm{I^+}} = \Gamma_{\mathrm{I^+}}\mathcal{A}_{\mathrm{open},i}\mathcal{V}^{-1}$$
- When a particle involved as reactant in a recombination process reaches a wall, it can stick to the walls and be recombined. The only recombination reaction considered here is $\mathrm{I} \longrightarrow \frac{1}{2}\,\mathrm{I_2}$, a recombination that cannot happen in gas phases for momentum conservation. A molecule of $\mathrm{I_2}$ is formed at half the rate at which a I atom sticks to a wall. If γ_{stick} is the wall sticking coefficient of a single particle, Chantry [73] and Lucken [56] have shown in two different ways that in very low pressure cases, an incident flux Γ_{I} leads to a sticking flux of $\Gamma_{\mathrm{I}}[2\gamma_{\mathrm{stick}}/(2-\gamma_{\mathrm{stick}})]$, which is equal to $\gamma_{\mathrm{stick}}\Gamma_{\mathrm{I}}$ at low γ_{stick}. Due to the limitations of this sticking model at intermediate and high-pressure and the inexistence of any data on the sticking coefficient of iodine, a simple γ_{rec} factor is used in (2.5) as the ratio between the recombined flux and the impinging flux. It has to be kept in mind for potential future dedicated analysis that this factor is not directly the sticking coefficient of a single particle unless this sticking coefficient is small. The default value in this work, unless stated otherwise, is $\gamma_{\mathrm{rec}} = 0.1$, and effects of this choice are studied section 2.9.

  The corresponding terms are then:
$$L_{\mathrm{I}} = 2G_{\mathrm{I_2}} = \gamma_{\mathrm{rec}}\Gamma_{\mathrm{I}}\mathcal{A}_n\mathcal{V}^{-1} \tag{2.5}$$

2.3.4 Particle fluxes to the walls

All the previous formula imply to know the particle fluxes Γ to the boundaries. Neutral particles can be considered in a random thermal motion. A sheath is present at the walls to ensure that no net current is drawn from the plasma, as shown Figure 2.8. Positively charged particles are then attracted to the walls if they can enter the sheath, whereas electrons and negative ions are slowed down to reduce the net negative flux to the boundaries. The precise formula used for each flux is explained in this section, and a summary is given at the end of the section.

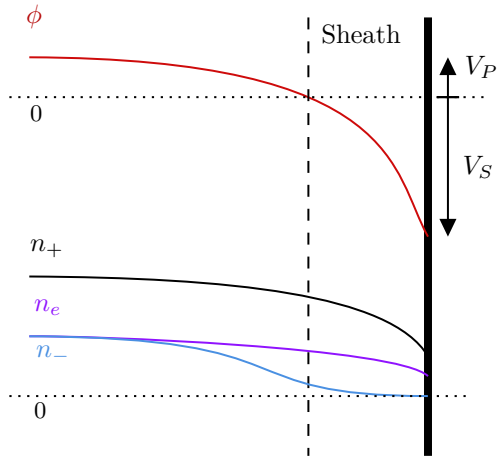

Figure 2.8: Reminder about sheath physics, in a schematic case where the bulk electronegativity is 1. The potential ϕ drops slightly in the presheath, repelling most of the negative ions. In the sheath, positive ions are accelerated towards the walls, hence n_+ decreases, per flux conservation. The negative ion flux to the walls is neglected, but not the negative ion density at the sheath edge. The positive ion flux to the walls is equal to the electron flux to the walls.

Neutral species

The random thermal flux of particles not subject to a boundary or a specific electric field can be computed as the flux crossing any particular plane in the plasma, hence integrating the distribution over all components of velocity in two directions but only on the positive part of the last direction [64]. Namely:

$$\Gamma_{\text{th}} = n\Big(\frac{m}{2\pi eT}\Big)^{3/2} \int_{-\infty}^{\infty} \mathrm{d}v_x \int_{-\infty}^{\infty} \mathrm{d}v_y \int_{0}^{\infty} v_z \exp\Big(-\frac{mv^2}{2eT}\Big)\mathrm{d}v_z$$

This leads for example for the thermal flux of I atomic species to the wall to:

$$\Gamma_{\text{th,I}} = \frac{1}{4}[\text{I}]v_{\text{th,I}}$$

Where $v_{\text{th,I}}$ is the mean thermal speed, defined as:

$$v_{\text{th,I}} = \sqrt{\frac{8eT_I}{\pi m_I}}$$

Negatively charged species

Negatively charged species are confined in the plasma by the sheaths formed at the walls to balance positive and negative current to the plasma boundaries [36, 64]. A reminder about sheath physics is given Figure 2.8. Therefore in steady state a negatively charged particle can reach a wall if it overcomes the total potential difference between the plasma bulk and the walls, noted here $\Delta\phi$ and explicited in section 2.4.1. Assuming populations in the Boltzmann equilibrium, this means for example that the electron flux to the walls is:

$$\Gamma_e = \frac{n_e v_{\text{th,e}}}{4} \exp\Big(-\frac{\Delta\phi}{T_e}\Big)$$

And the negative ions I^- flux is, with T_- the corresponding temperature,

$$\Gamma_{\text{I}^-} = \frac{[\text{I}-]v_{\text{th,I}^-}}{4} \exp\Big(-\frac{\Delta\phi}{T_-}\Big)$$

Practically speaking, although electronegativity at the sheath edge will be taken into account, the negative ion flux to the walls can and will be neglected, as an effect of a very low thermal speed due to a lower temperature ($\gamma_- = T_e/T_- > 10$) and larger mass compared to electrons ($m_I/m_e > 10^6$).

Therefore and to ensure that no net current is drawn from the plasma, the electron flux to the walls is taken as the sum of the fluxes of positive species to the walls. Equating those fluxes is the main way to compute the voltage drop in the sheath and presheath $\Delta\phi$, as detailed section 2.4.1.

Positively charged species: the h factors

In electropositive plasmas, positively charged species can enter the sheath if they reach a characteristic speed called the Bohm speed [64, 74]. The electropositive Bohm speed is, with m the mass of the considered heavy species:

$$u_B = \sqrt{\frac{eT_e}{m}}$$

The location where ions reach the Bohm velocity is used as the definition of the sheath edge, where the density is by definition written with an s subscript. When the positively charged particles reach the sheath, they are accelerated towards the wall. If no ionization occurs in the sheath, then the flux reaching the wall is equal to the flux entering the sheath. With I^+ as an example, it leads to:

$$\Gamma_{I^+} = [I^+]_s \; u_{B,I}$$

The density at the sheath edge is defined as a fraction h of the bulk density, so that

$$\Gamma_{I^+} = h[I^+]u_{B,I}$$

The factor h is often precised as h_l, if calculated with a planar surface, or h_r, for use with a cylindrical geometry. Qualitatively, both factors behave similarly with pressure or electronegativity, hence the study is focused here on h_l and extrapolated to h_r later. Both the traditional Bohm speed u_B and h factor are usually computed for electropositive plasmas, and sometimes used without modifications for electronegative gases [42]. This is valid only in the case of low electronegativity $\alpha = n_-/n_e$. As shown later, iodine plasmas can lead to electronegativities above 1 at pressures above a few Pa, or much higher values if a system is used to enhance electronegativity, as in the work from Bredin [54] or Grondein [46] who measure values up to 2000 in cases where electronegativity is increased by magnetic fields.

To address plasmas presenting a wide range of electronegativity, several authors propose corrective terms for the Bohm velocity [75] or the h factors [37, 76], in order to compute the flux reaching the walls. Thorsteinsson and Gudmundsson [37] use electronegative factors for both u_B and h in their study of Cl_2 plasmas. They will be noted with a tilde, so that

$$\widetilde{\Gamma}_{I^+} = \widetilde{h}[I^+]\widetilde{u}_{B,I}$$

Chabert [76] proposes another approach modifying only the h factor, that will be noted $\widehat{h}$. With this, it would lead to:

$$\widetilde{\Gamma}_{I^+} = \widehat{h}[I^+]u_{B,I}$$

The approach from Thorsteinsson and Gudmundsson [37] is based on analytical resolutions of the fluxes equality including a strong assumption on the multivalued sheath electronegativity, when Chabert [76] uses numerical resolutions of the fluid equations, expected to yield better results. Let us explain and compare both approaches, starting with Thorsteinsson and Gudmundsson [37]. To compute the negative Bohm criterion for plasma sheaths in the case of an electronegative plasma, Braithwaite and Allen [75] propose an expression valid when positive ions are significantly colder than negative ions of temperature T_-. This assumption is considered valid because negative ions do not reach the walls that usually cool the gas and the positive ions. They show that writing the Bohm criterion in an electronegative plasma leads to a Bohm criterion written for an heavy particle A:

$$\widetilde{u}_B = \sqrt{\frac{eT_e}{m_A}}\left(\frac{1+\alpha_s}{1+\gamma_-\alpha_s}\right)^{1/2} = u_B\left(\frac{1+\alpha_s}{1+\gamma_-\alpha_s}\right)^{1/2} \tag{2.6}$$

Where $\alpha_s = n_{-s}/n_{es}$ is the electronegativity at the sheath edge, lower than the bulk electronegativity and detailed in section 2.4.1, $\gamma_- = T_e/T_-$ is the electron-to-negative ion temperature ratio, and we reintroduce the electropositive Bohm speed u_B. The related edge-to-center density ratio $\widetilde{h}$ used in their work is based on a study by Kim et al. [77] and not reproduced here.

On the other hand, Chabert [76] proposes an expression for the planar edge-to-center density ratio $\widehat{h}_l$, in case of a planar surface, defined with the electropositive Bohm velocity u_B. This result uses the approximation of a Boltzmann equilibrium for the negative ion population, which is unlikely to stay true at high pressure. The coefficient proposed is $\widehat{h}_l$:

$$\widehat{h}_l = 0.86\left(3 + \frac{L}{2\lambda_i} + (1+\alpha)^{1/2}\frac{\gamma_+}{5}\left(\frac{L}{\lambda_i}\right)^2\right)^{-1/2}\left(\frac{\gamma_- - 1}{\gamma_-(1+\alpha)^2} + \frac{1}{\gamma_-}\right)^{1/2}$$

In this result, L is the distance between both planar planes, λ_i is the mean free path for ion-neutral scattering and charge-exchange collisions, and we use $\lambda_i = ((n_\mathrm{I} + n_{\mathrm{I}_2})\sigma_i)^{-1}$, with $\sigma_i = 1 \times 10^{-18}\,\mathrm{m}^{-2}$ an equivalent cross section [42]. $\gamma_+ = T_+/T_e$ is the temperature of the positive ion species to electron temperature ratio, and in this work we use $T_+ = T_{\mathrm{I}^+}$ the temperature of the main ion population. The similar reasoning leads to an expression for the radial h coefficient:

$$\widehat{h}_r = 0.8\left(4 + \frac{R}{\lambda_i} + (1+\alpha)^{1/2}\gamma_+\left(\frac{R}{\lambda_i}\right)^2\right)^{-1/2}\left(\frac{\gamma_- - 1}{\gamma_-(1+\alpha)^2} + \frac{1}{\gamma_-}\right)^{1/2}$$

Figure 2.9 shows a comparisons of two models for iodine plasmas at low pressure (Figure 2.9a, 0.2 Pa) and higher pressure (Figure 2.9b, 2.4 Pa). The deviation from the electropositive case appears from electronegativities as low as 0.1 with a decrease of the flux around 10 %. At $\alpha = 1$, the flux is divided by two according to Chabert [76], where Thorsteinsson and Gudmundsson [37] anticipate a strong decrease of the flux to 10 to 20 % of its initial value from $\alpha \approx 2$.

The comparisons of the h factors themselves make less sense than comparing the fluxes as different authors don't use the same Bohm speed. Nonetheless, Figure 2.10 shows the equivalent value of the planar h factor h_l used by each authors. For Thorsteinsson and Gudmundsson [37], the value is calculated by normalizing the flux to the electropositive Bohm velocity. For $\alpha = 0$, the h factors are, for Chabert [76], Thorsteinsson and Gudmundsson [37] and Grondein et al. [42] respectively:

$$\widehat{h}_l(\alpha = 0) = 0.86\left(3 + \frac{L}{2\lambda_i} + \frac{\gamma_+}{5}\left(\frac{L}{\lambda_i}\right)^2\right)^{-1/2}$$

$$\widetilde{h}_l(\alpha = 0) = 0.86\left(3 + \frac{2\gamma_-}{\gamma_+ + \gamma_-}\frac{L}{2\lambda_i}\right)^{-1/2}$$

$$h_l(\alpha = 0) = 0.86\left(3 + \frac{L}{2\lambda_i}\right)^{-1/2}$$

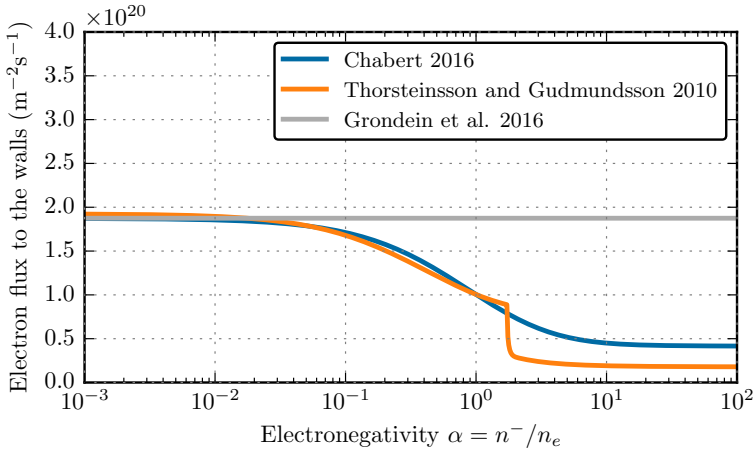

(a) Electron flux to the walls as a function of bulk electronegativity at 0.2 Pa.

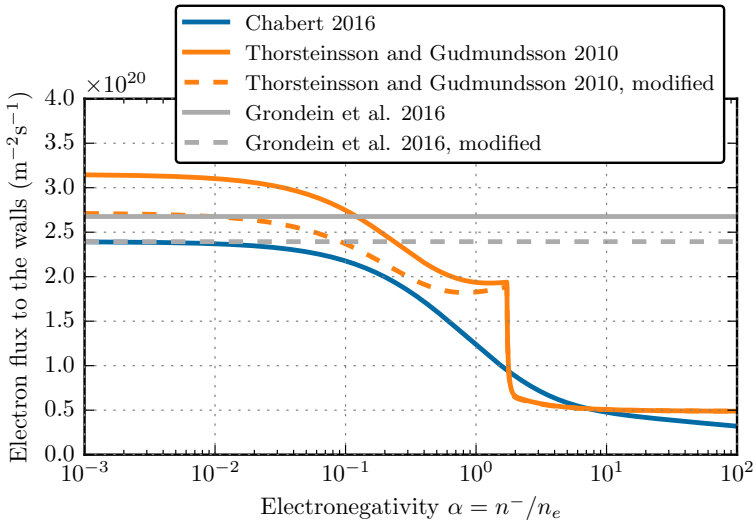

(b) Electron flux to the walls as a function of bulk electronegativity at 2.4 Pa.

Figure 2.9: Comparisons of different models of fluxes by Grondein et al. [42], Chabert [76] and Gudmundsson [78]. The dashed lines correspond to the models modified for higher pressures to extend the author's theories.

At low pressure, the term in λ_i^2 is negligible and all terms would be equal if $T_+ = T_-$. The slight difference for $\alpha = 0$ shown Figure 2.10a then comes from the fact that Thorsteinsson and Gudmundsson [37] takes into account a different temperature for both ions. The three factors cannot be directly compared at higher pressure as [37] and [42] did not incorporate a term for higher pressure. The comparison shown Figure 2.10b and Figure 2.9b is then done as well with modified versions of the h_l factors, copying the term in λ_i^2 from [64]. With these modifications, the difference for $\alpha = 0$ is once again due to the discrepancy between positive and negative ions temperatures taken into account by Thorsteinsson and Gudmundsson [37].

$$\widetilde{h}_l(\text{modified}, \alpha = 0) = 0.86\left(3 + \frac{2\gamma_-}{\gamma_+ + \gamma_-} + \frac{L}{2\lambda_i}\frac{\gamma_+}{5}\left(\frac{L}{\lambda_i}\right)^2\right)^{-1/2}$$

$$h_l(\text{modified}, \alpha = 0) = 0.86\left(3 + \frac{L}{2\lambda_i} + \frac{\gamma_+}{5}\left(\frac{L}{\lambda_i}\right)^2\right)^{-1/2}$$

To get a general coefficient $\widehat{h}$, the number of positively charged particles leaving the plasma per seconds to any boundaries is:

$$\mathcal{A}_{\text{total}}\widetilde{\Gamma}_{\text{I}^+} = 2\pi R^2 \widehat{h}_l [\text{I}^+] u_{B,\text{I}^+} + 2\pi R L \widehat{h}_r [\text{I}^+] u_{B,\text{I}^+}$$

The h factor used in this work in then:

$$\widehat{h} = 2\pi R \frac{R\widehat{h}_l + L\widehat{h}_r}{\mathcal{A}_{\text{total}}}$$

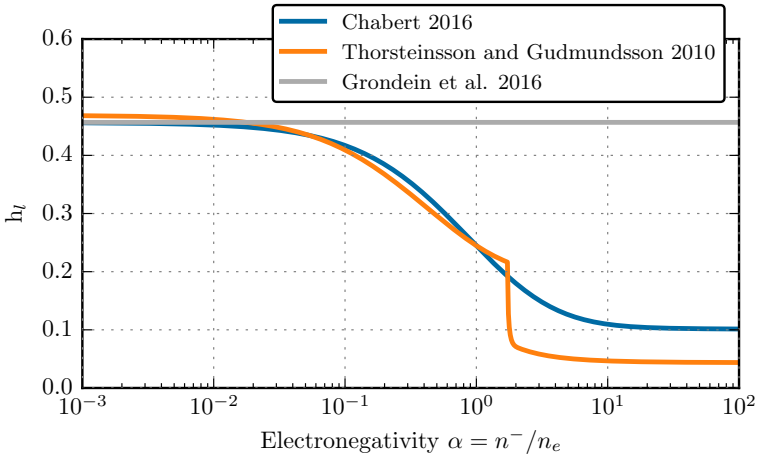

(a) Equivalent h_l factor as a function of bulk electronegativity at 0.2 Pa.

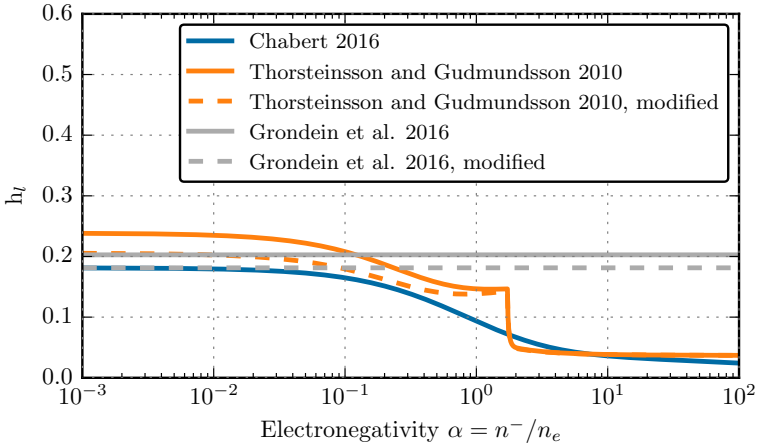

(b) Equivalent h_l factor as a function of bulk electronegativity at 2.4 Pa.

Figure 2.10: Equivalent h_l factors from different models at different pressures, from [42], [76] and [37]. The dashed lines correspond to the models modified for higher pressures to extend the author's theories at higher pressures. For [37], this is an equivalent h_l after normalization of the flux by the positive Bohm speed.

Summary of fluxes to the walls

As a conclusion, the fluxes of different particles to the walls are written:

$$\widetilde{\Gamma}_{\mathrm{I}^+} = \widehat{h}_l[\mathrm{I}^+]u_{B,\mathrm{I}}$$
$$\widetilde{\Gamma}_{\mathrm{I_2}^+} = \widehat{h}_l[\mathrm{I_2}^+]u_{B,\mathrm{I_2}}$$
$$\Gamma_{\mathrm{I}} = \frac{1}{4}[\mathrm{I}]v_{\mathrm{th,I}}$$
$$\Gamma_{\mathrm{I_2}} = \frac{1}{4}[\mathrm{I_2}]v_{\mathrm{th,I_2}}$$
$$\Gamma_e = \widetilde{\Gamma}_{\mathrm{I}^+} + \widetilde{\Gamma}_{\mathrm{I_2}^+}$$
$$\Gamma_{\mathrm{I}^-} = 0$$

2.4 Power balance

There are in the literature two main ways of explaining the plasma power balance, one by Lieberman and co-authors [36, 79, 80] and a second one by Chabert and co-authors [38, 42, 64]. The former aims at a total power balance over the discharge, when the latter considers only a power balance on the bulk electron population. While both models are mostly equivalent due to the predominance of electrons as energy-carriers in the plasma, small discrepancies remain. Both models express that the power injected in the plasma - the discharge power P_d - is either used to heat up electrons, or lost during collision processes in the plasma, or lost at the plasma boundaries:

$$P_d = \frac{\mathrm{d}}{\mathrm{d}t}\left(\frac{3}{2} n_e e T_e\right)\mathcal{V} + P_{\text{loss, coll}} + P_{\text{loss,bound}}$$

2.4.1 Power lost at the boundaries

Considering a balance on the whole plasma, Lieberman and Lichtenberg [36] calculate the power lost at the boundaries by the electrons and the positive ions. Because they are much slower than the electrons, negative ions are confined by the sheaths and, in the model, never reach the walls. The equation is then:

$$P_{\text{loss,bound}} = P_{\text{loss,bound,e}} + P_{\text{loss,bound,i}}$$

The (positive) ion kinetic energy lost at the surface correspond to the energy acquired by the ion to enter the sheath, and the energy acquired during the acceleration in the sheath, with V_s the absolute value of the sheath voltage and V_p the plasma potential:

$$\varepsilon_i = eV_p + eV_s$$

The electron kinetic energy lost at the surface is the energy that can be found by computing the average energy flux along one axis for a Maxwellian distribution :

$$\varepsilon_e = 2eT_e$$

so that

$$P_{\text{loss, bound}} = \Gamma_e(2eT_e + eV_s + eV_p)\mathcal{A} \tag{2.7}$$

In the model from Chabert and Braithwaite [64] however, the balance is made only on the bulk electrons. In this model, the power lost by the electrons is not only the power lost at the wall ($2eT_e$) but also the power deposited - transfered to the leaving ions - between the plasma bulk and the wall, with $\Delta\phi$ the associated potential drop:

$$\tilde{P}_{\text{loss,bound,e}} = \Gamma_e(2eT_e + e\Delta\phi)\mathcal{A}$$

This equation is equivalent to (2.7) if $\Delta\phi$ is substituted by $V_s + V_p$. This formula for power lost at the walls is applied by Chabert et al. [38] (with $\Delta\phi = 5T_e$) and Lucken [56], Despiau-Pujo and Chabert [81] (with $\Delta\phi = V_s$). Lucken [56] mentions using V_s and not $V_s + V_p$ because the isothermal sheath models usually slightly overestimate sheath voltage drops and that the plasma potential is usually small in front of the sheath potential.

In this work, I use $\Delta\phi = V_s + V_p$ and values of sheath and plasma potential adapted to electronegative plasmas presented in Thorsteinsson and Gudmundsson [37]. From the generalized Bohm velocity (2.6), and with α_s the electronegativity at the sheath edge, the plasma potential is found to be

$$V_p = \frac{T_e}{2}\frac{1+\alpha_s}{1+\gamma_-\alpha_s} \tag{2.8}$$

And it is also shown that equating all fluxes *including from negative particles* to the walls and adapting the analytic solution to the model leads to a sheath potential written here:

$$V_s = T_e \ln\left(4\frac{\langle\widetilde{u}_B\rangle}{v_{\text{th,e}}}\frac{1+\alpha_s}{1+\alpha_s(v_{\text{th,I}^-}/v_{\text{th,e}})^2}\right)$$

Where $\langle\widetilde{u}_B\rangle$ is the weighted average of the Bohm speeds:

$$\langle\widetilde{u}_B\rangle = \frac{[\text{I}^+]\widetilde{u}_{B,\text{I}^+} + [\text{I}_2{}^+]\widetilde{u}_{B,\text{I}_2{}^+}}{[\text{I}^+] + [\text{I}_2{}^+]}$$

If the sheath electronegativy is zero, V_s is proportionnal to T_e:

$$V_s = T_e \ln\left(\frac{[\text{I}^+]}{[\text{I}^+]+[\text{I}_2{}^+]}\sqrt{\frac{2\pi m_e}{m_I}} + \frac{[\text{I}_2{}^+]}{[\text{I}^+]+[\text{I}_2{}^+]}\sqrt{\frac{2\pi m_e}{m_{\text{I}_2}}}\right)$$

With no sheath electronegativity and if a single positive ion species is present, one finds again the classical formula:

$$V_s = \frac{T_e}{2} \ln\left(\frac{2\pi m_e}{m_I}\right)$$

To include those formula in the model, one only needs now an estimation of the electronegativity at the sheath edge as a function of electronegativity in the plasma bulk. It is defined as:

$$\alpha_s = \alpha \exp\left(\frac{V_p}{T_e}(1-\gamma_-)\right)$$

Where V_p is the plasma potential, itself depending on α_s, as defined in equation (2.8). The solution to this system of coupled equations is showed and explained elsewhere [37, 64, 77], detailing 3 regions of interest depending on the electronegativity in the center. For $\alpha \leq 2$, the plasma is stratified: negative ions are repelled by the presheath, leaving a sheath that is essentially electropositive, with $\alpha_s \approx 0$ and $u_{B,A} \approx \sqrt{eT_e/m_A}$. At very high electronegativity, the plasma is nearly uniform, the Bohm speed decreases $u_{B,\mathrm{A}} \approx \sqrt{eT_-/m_A}$ and there is nearly no potential drop in the presheath. The zone in-between is multivalued. Thorsteinsson and Gudmundsson [37] propose a numerical scheme to join both solutions for $\gamma_- > 10$ in Cl_2 plasmas:

$$\alpha_s = \alpha \max(a_1 \frac{\mathrm{erf}(a_2\varrho + a_3)\exp\left(-\frac{a_4}{\varrho^{1.35}}\right)}{\exp\left(\frac{\gamma_- - 1}{2\gamma_-} - 0.49\right)}, 0)$$

With $a_1 = 0.607$, $a_2 = 5.555$, $a_3 = -11.16$, $a_4 = 1.634$, $a_5 = 12 \times 10^{-3}$, $a_6 = -107 \times 10^{-3}$, and

$$\varrho = |\alpha + a_5(\exp(a_6(\gamma_- - 50)) - 1)|$$

This solution is plotted Figure 2.11. We verify that the limit is, for $\alpha \to \infty$, $\alpha_s = \alpha \exp((1-\gamma_-)/2\gamma_-)$, which is 0.6 α if $\gamma_- \to \infty$. Using this value for sheath electronegativity, value of sheath and plasma potential are given Figure 2.12, for an example a plasma where $[\mathrm{I}] = 2[\mathrm{I}_2]$. It can be seen than the total potential drop is constant at low electronegativity, raises slightly when α approaches 2 and then continuously decreases as the electronegativity increases.

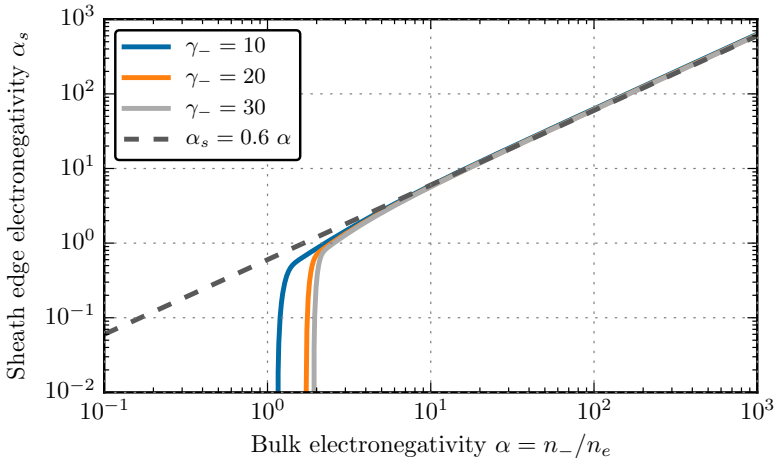

Figure 2.11: Sheath edge electronegativity as a function of the bulk electronegativity. Model developed for Cl_2 plasmas by Thorsteinsson and Gudmundsson [37] and used in this work without modification.

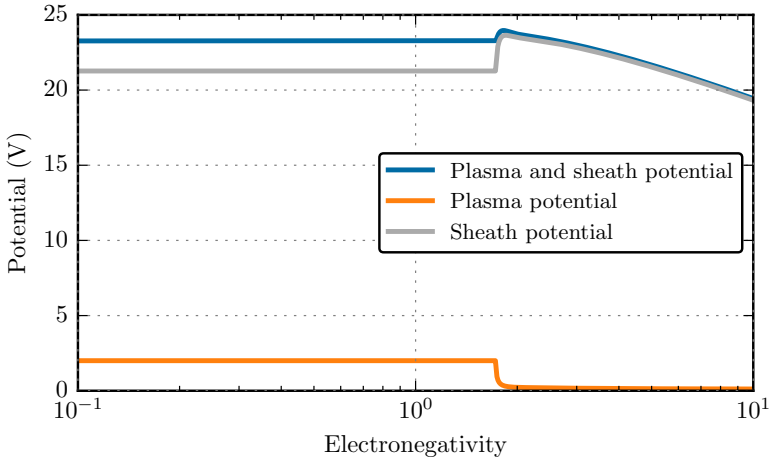

Figure 2.12: Plasma, sheath, and total potential as a function of the bulk electronegativity. Model developed in this work using the sheath electronegativity model from Thorsteinsson and Gudmundsson [37].

2.4.2 Power lost in the volume

Although built with different logics, both models create equivalent equations for the power lost in the volume. Lieberman and Lichtenberg [36] introduce the notion of *energy lost per electron-ion pair created*. It encompasses the fact that *while* an ion-electron pair is created, several other processes result in energy losses. For a simple electropositive plasma with a single ion species, adding all these energies leads to computing the energy lost per ionizing collision ε_c:

$$K_{\mathrm{iz}}\varepsilon_c = K_{\mathrm{iz}}\varepsilon_{iz} + K_{\mathrm{ex}}\varepsilon_{ex} + K_{\mathrm{el}}\varepsilon_{\mathrm{el}}$$

For a molecular propellant, dissociation losses or losses by negative ions formation are added. This effective ionization energy is then considered lost at each ionization reaction, so that

$$P_{\mathrm{loss,\ coll}} = n_e n_g \mathcal{V} K_{\mathrm{iz}}\varepsilon_c$$

Chabert and Braithwaite [64] reach the same conclusion by writing that when an electron is involved in a collision, it loses the corresponding threshold energy. The power lost is then this energy times the number of reaction per volume and per second, which is the product of the reaction rate times the density of all the reactants. Written mathematically it is, with i being among the reactions involving an electronic impact on another reactant written A:

$$P_{\mathrm{loss,\ coll}} = \sum_{\mathrm{i}} \varepsilon_i [\mathrm{A}] n_e K_i$$

For an elastic collision, the same formalism than the other reactions can be used after writing an equivalent of the elastic energy, written $\varepsilon_{\mathrm{el}}$. This is done integrating the fraction of energy lost by the projectile in elastic collisions over the differential scattering cross section, and multiplying by the mean electron energy. The energy for the elastic collision terms is then, for a heavy particle A:

$$\varepsilon_{el,A} = \frac{2m_A m_e}{(m_A + m_e)^2} \cdot \frac{3}{2} eT_e \approx 3\frac{m_e}{m_A} eT_e \tag{2.9}$$

2.5 Global model equations

In this section are listed the equations as they are used in the model, built upon the principles detailed in the paragraphs above.

2.5.1 Electrons

$$\begin{aligned}
\frac{\mathrm{d}n_e}{\mathrm{d}t} = &- [\mathrm{I_2}]n_e K_{\mathrm{diss.att}} && \textit{I2 dissociative attachment}\\
&+ [\mathrm{I_2}]n_e K_{\mathrm{diss.iz}} && \textit{I2 dissociative ionization}\\
&+ [\mathrm{I_2}]n_e K_{\mathrm{iz,I_2}} && \textit{I2 ionization}\\
&+ [\mathrm{I}]n_e K_{\mathrm{iz,I}} && \textit{I ionization}\\
&+ [\mathrm{I}-]n_e K_{\mathrm{detach}} && \textit{I}^- \textit{ detachment}\\
&- \Gamma_e \frac{\mathcal{A}_{\mathrm{total}}}{\mathcal{V}} && e^- \textit{ flux to the walls}
\end{aligned}$$

In this equation, the flux of electrons to the wall is noted Γ_e. To maintain quasi-neutrality, and considering that the negative ions are confined in the plasma and positive ions are lost at the entire thruster walls and holes area, we use $\mathcal{A}_{\mathrm{total}}$ and

$$\Gamma_e = \Gamma_{\mathrm{I}^+} + \Gamma_{\mathrm{I_2}^+} = h u_{B,\mathrm{I}}[\mathrm{I}^+] + h u_{B,\mathrm{I_2}}[\mathrm{I_2}^+]$$

2.5.2 I^- ions

$$\begin{aligned}
\frac{\mathrm{d}[\mathrm{I}^-]}{\mathrm{d}t} = &+ n_e[\mathrm{I_2}]K_{\mathrm{diss.\ att}} && \textit{I2 dissociative attachment}\\
&- [\mathrm{I}-][\mathrm{I_2}^+]K_{\mathrm{neut,I^-,I_2}^+} && \textit{I}^- \textit{ I2}^+ \textit{ charge exchange}\\
&- [\mathrm{I}-][\mathrm{I}^+]K_{\mathrm{ion.\ rec}} && \textit{I}^- \textit{ I}^+ \textit{ mutual neutralization}\\
&- n_e[\mathrm{I}-]K_{\mathrm{detach}} && \textit{I}^- \textit{ detachment}
\end{aligned}$$

2.5.3 I_2 molecules

$$
\begin{aligned}
\frac{\mathrm{d}[\mathrm{I_2}]}{\mathrm{d}t} = &+ \frac{Q_0}{\mathcal{V}} && \textit{I_2 injection}\\
&- n_e[\mathrm{I_2}]K_{\mathrm{diss.att}} && \textit{I_2 dissociative attachment}\\
&- n_e[\mathrm{I_2}]K_{\mathrm{diss.iz}} && \textit{I_2 dissociative ionization}\\
&- n_e[\mathrm{I_2}]K_{\mathrm{iz,I_2}} && \textit{I_2 ionization}\\
&- n_e[\mathrm{I_2}]K_{\mathrm{diss}} && \textit{I_2 dissociation}\\
&- [\mathrm{I^+}][\mathrm{I_2}]K_{\mathrm{c.ex,I^+,I_2}} && \textit{I^+ I_2 charge exchange}\\
&+ [\mathrm{I-}][\mathrm{I_2}^+]K_{\mathrm{neut,I^-,I_2^+}} && \textit{I^- ${I_2}^+$ charge exchange}\\
&- \Gamma_{\mathrm{I_2}}\frac{\mathcal{A}_{\mathrm{open,\ n}}}{\mathcal{V}} && \textit{I_2 flux to grid holes}\\
&+ \Gamma_{\mathrm{I_2^+}}\frac{\mathcal{A}_{\mathrm{i}}}{\mathcal{V}} && \textit{${I_2}^+$ flux to the walls}\\
&+ \frac{1}{2}\gamma_{rec}\Gamma_{\mathrm{I}}\frac{\mathcal{A}_{\mathrm{n}}}{\mathcal{V}} && \textit{I surface recombination}
\end{aligned}
$$

2.5.4 ${I_2}^+$ ions

$$
\begin{aligned}
\frac{\mathrm{d}[\mathrm{I_2}^+]}{\mathrm{d}t} = &+ [\mathrm{I^+}][\mathrm{I_2}]K_{\mathrm{c.ex,I^+,I_2}} && \textit{I^+ I_2 charge exchange}\\
&- [\mathrm{I-}][\mathrm{I_2}^+]K_{\mathrm{neut,I^-,I_2^+}} && \textit{I^- ${I_2}^+$ charge exchange}\\
&+ n_e[\mathrm{I_2}]K_{\mathrm{iz,I_2}} && \textit{I_2 ionization}\\
&- n_e[\mathrm{I_2}^+]K_{\mathrm{diss,I_2^+}} && \textit{${I_2}^+$ dissociation}\\
&- \Gamma_{\mathrm{I_2^+}}\frac{\mathcal{A}_{\mathrm{total}}}{\mathcal{V}} && \textit{${I_2}^+$ flux to walls and grid holes}
\end{aligned}
$$

2.5.5 I atoms

$$
\begin{aligned}
\frac{\mathrm{d}[\mathrm{I}]}{\mathrm{d}t} = &+ n_e[\mathrm{I_2}]K_{\mathrm{diss.att}} && \textit{I}_2\textit{ dissociative attachment}\\
&+ n_e[\mathrm{I_2}]K_{\mathrm{diss.iz}} && \textit{I}_2\textit{ dissociative ionization}\\
&+ 2\ n_e[\mathrm{I_2}]K_{\mathrm{diss}} && \textit{I}_2\textit{ dissociation}\\
&+ n_e[\mathrm{I_2}^+]K_{\mathrm{diss,I_2}^+} && \textit{I}_2^+\textit{ dissociation}\\
&+ [\mathrm{I}^+][\mathrm{I_2}]K_{\mathrm{c.ex,I}^+,\mathrm{I_2}} && \textit{I}^+\textit{ I}_2\textit{ charge exchange}\\
&+ [\mathrm{I}-][\mathrm{I_2}^+]K_{\mathrm{neut,I}^-,\mathrm{I_2}^+} && \textit{I}^-\textit{ I}_2^+\textit{ charge exchange}\\
&+ 2\ [\mathrm{I}-][\mathrm{I}^+]K_{\mathrm{ion.rec}} && \textit{I}^-\textit{ I}^+\textit{ mutual neutralization}\\
&+ n_e[\mathrm{I}-]K_{\mathrm{detach}} && \textit{I}^-\textit{ detachment}\\
&- n_e[\mathrm{I}]K_{\mathrm{iz}} && \textit{I ionization}\\
&- \Gamma_{\mathrm{I}}\frac{\mathcal{A}_{\mathrm{open,\ n}}}{\mathcal{V}} && \textit{I flux to grid holes}\\
&+ \Gamma_{\mathrm{I}^+}\frac{\mathcal{A}_{\mathrm{i}}}{\mathcal{V}} && \textit{I}^+\textit{ flux to the walls}\\
&- \gamma_{rec}\Gamma_{\mathrm{I}}\frac{\mathcal{A}_{\mathrm{n}}}{\mathcal{V}} && \textit{I surface recombination}
\end{aligned}
$$

2.5.6 I^+ ions

$$
\begin{aligned}
\frac{\mathrm{d}[\mathrm{I}^+]}{\mathrm{d}t} = &+ n_e[\mathrm{I_2}]K_{\mathrm{diss.iz}} && \textit{I}_2\textit{ dissociative ionization}\\
&+ n_e[\mathrm{I_2}^+]K_{\mathrm{diss,I_2}^+} && \textit{I}_2^+\textit{ dissociation}\\
&- [\mathrm{I}^+][\mathrm{I_2}]K_{\mathrm{c.ex,I}^+,\mathrm{I_2}} && \textit{I}^+\textit{ I}_2\textit{ charge exchange}\\
&- [\mathrm{I}-][\mathrm{I}^+]K_{\mathrm{ion.rec}} && \textit{I}^-\textit{ I}^+\textit{ mutual neutralization}\\
&+ n_e[\mathrm{I}]K_{\mathrm{iz}} && \textit{I ionization}\\
&- \Gamma_{\mathrm{I}^+}\frac{\mathcal{A}_{\mathrm{total}}}{\mathcal{V}} && \textit{I}^+\textit{ flux to walls and grid holes}
\end{aligned}
$$

2.5.7 Electron power balance

It has been stated before that the power balance is written:

$$P_d = \frac{\mathrm{d}}{\mathrm{d}t}\left(\frac{3}{2} n_e e T_e\right)\mathcal{V} + P_{\mathrm{loss}}$$

Rewriting this equation so as to isolate the temporal derivative of T_e, we get the last equation of the equation set:

$$\frac{\mathrm{d}T_e}{\mathrm{d}t} = \frac{2}{3}\frac{P_d - P_{\mathrm{loss}}}{e n_e \mathcal{V}} - \frac{T_e}{n_e}\frac{\mathrm{d}n_e}{\mathrm{d}t}$$

And we write P_{loss} by considering every electron-neutral collisions. The rates are defined above, and the energies are the thresholds energies (the first electron energy where the cross-section is non zero) for $\varepsilon_{\mathrm{diss.iz}}$, $\varepsilon_{\mathrm{diss}}$, $\varepsilon_{\mathrm{iz,I_2}}$, $\varepsilon_{\mathrm{iz,I}}$, $\varepsilon_{\mathrm{detach}}$, $\varepsilon_{\mathrm{exc}}$, $\varepsilon_{\mathrm{diss,I_2{}^+}}$. The elastic energies are defined Equation (2.9). The energy lost by electrons through dissociative attachment is taken as $\varepsilon_{\mathrm{diss.att}} = 1.5 e T_e$, the mean electron energy.

$$\begin{aligned}
\frac{P_{\mathrm{loss}}}{\mathcal{V}} = &+ \varepsilon_{\mathrm{diss.att}}\ n_e[\mathrm{I_2}]K_{\mathrm{diss.att}} && \textit{I}_2\textit{ dissociative attachment}\\
&+ \varepsilon_{\mathrm{diss.iz}}\ n_e[\mathrm{I_2}]K_{\mathrm{diss.iz}} && \textit{I}_2\textit{ dissociative ionization}\\
&+ \varepsilon_{\mathrm{diss}}\ n_e[\mathrm{I_2}]K_{\mathrm{diss}} && \textit{I}_2\textit{ dissociation}\\
&+ \varepsilon_{\mathrm{iz,I_2}}[\mathrm{I_2}]n_e K_{\mathrm{iz,I_2}} && \textit{I}_2\textit{ ionization}\\
&+ \varepsilon_{\mathrm{iz,I}}[\mathrm{I}]n_e K_{\mathrm{iz,I}} && \textit{I ionization}\\
&+ \varepsilon_{\mathrm{detach}}\ [\mathrm{I}]n_e K_{\mathrm{detach}} && \textit{I}^-\textit{ detachment}\\
&+ \varepsilon_{\mathrm{exc}}\ [\mathrm{I}]n_e K_{\mathrm{exc,I}} && \textit{I excitation}\\
&+ \varepsilon_{\mathrm{el,I}}[\mathrm{I}]n_e K_{\mathrm{el,I}} && \textit{I - electron elastic collision}\\
&+ \varepsilon_{\mathrm{el,I_2}}[\mathrm{I_2}]n_e K_{\mathrm{el,I_2}} && \textit{I}_2\textit{ - electron elastic collision}\\
&+ \varepsilon_{\mathrm{diss,I_2{}^+}}[\mathrm{I_2{}^+}]n_e K_{\mathrm{diss,I_2{}^+}} && \textit{I}_2{}^+\textit{ - dissociation}\\
&+ \Gamma_e(2eT_e + eV_p + eV_s)\frac{\mathcal{A}_{\mathrm{total}}}{\mathcal{V}} && e^-\textit{ flux to the walls}
\end{aligned}$$

2.6 First insights

Before studying the details of the global model, it is useful to understand the main trends in the plasma parameters when pressure and power vary. This section shows the results of parametric studies, varying the plasma discharge power for a fixed mass flow rate of iodine, or varying the pressure at a given discharge power. All curves in this section were plotted with $\beta_i = \beta_0 = 0.22$, $\gamma_{\text{rec}} = 0.1$ and $T_g = 1000\,\text{K}$. The dependency of the results to the grid transparency is explained section 2.8.

Figure 2.13 and Figure 2.14 explain the variations of the plasma by estimating the contributions to the total pressure from each species, each species considered an ideal gas, with $T_I = T_{\text{I}_2} = T_g = 0.086\,\text{eV} = 1000\,\text{K}$, $T_{\text{I}^+} = T_{\text{I}_2^+} = 1000\,\text{K}$ and $T_{\text{I}^-} = 1500\,\text{K}$. Only the contributions from I, I_2 and the electrons are not negligible. It is shown that, while the pressure increases at constant power, the main contributor to the total pressure is first the electron population, then the I atoms, then I_2 molecules. From 0.2 Pa, neutrals account for more than half the pressure, mostly I to begin with. At 2 Pa, I_2 accounts for 10 % of the pressure and this contribution further increases as pressure goes up.

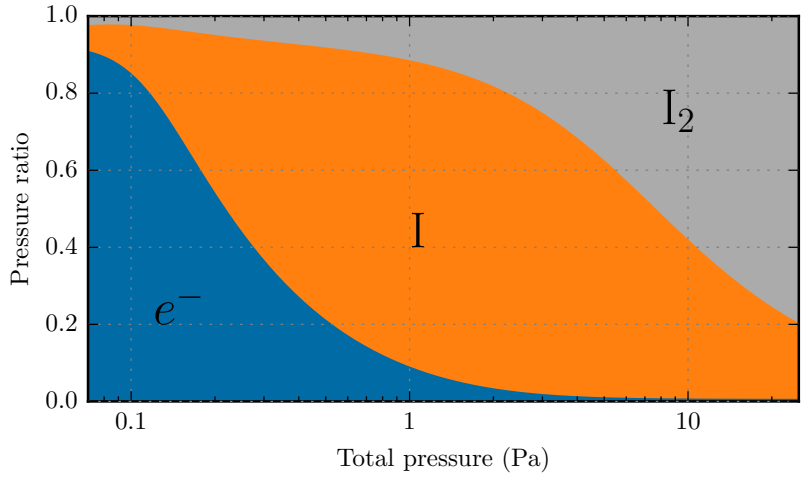

Figure 2.13: Repartition of the contribution to the total pressure as a function of pressure, if $T_I = T_{\text{I}_2} = T_g$. Other contributions are negligible.

Keeping a constant mass flow rate, the partial pressure of electrons increases constantly, as shown Figure 2.14. The ratio of I_2 molecules is high at very low discharge power, showing a poor dissociation there. All following curves will be plotted against neutral partial pressure, which betters corresponds to the usage in the literature, and to the experimental observations, as explained section 5.1.3.

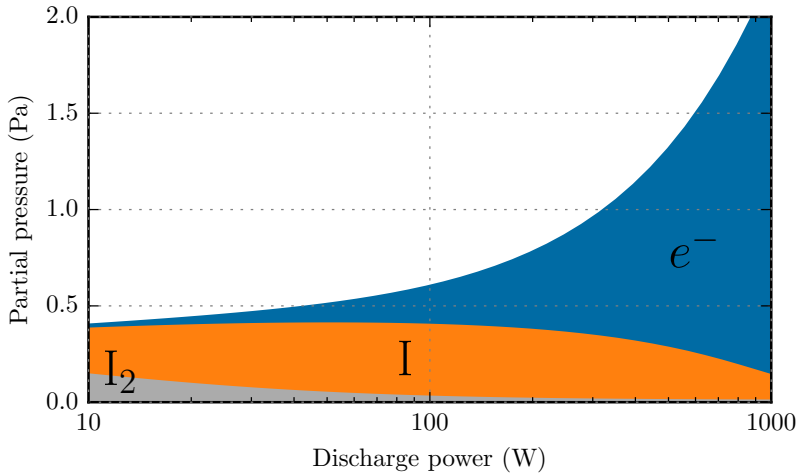

Figure 2.14: Repartition of the contribution to the total pressure as a function of discharge power, at 7.5 sccm. Other contributions are negligible.

Figure 2.15 shows the ionization degree, defined as the density of ionized species over the sum of neutral and ionized densities. The maximum ionization degree increases with discharge power, at 30 % at 350 W and 0.02 Pa for example. It reaches a maximum at low pressure. That corresponds to the evolution of the electron density. It is shown in Figure 2.16 that n_e is increasing linearly with discharge power, before a decrease linked to neutral depletion in the thruster occurs. Figure 2.17 shows that n_e initially increases with pressure and then decreases, like in a classical Ar or Xe plasma. This can be seen in a simple power balance such as the equation (2.3): at low pressure, any pressure increase leads to a decrease of the h factor and a decrease of the electron flux to the walls, hence increasing the electron density. At higher pressure, T_e decreases, hence the energy lost per ion-electron pair created increases, therefore the electron density decreases.

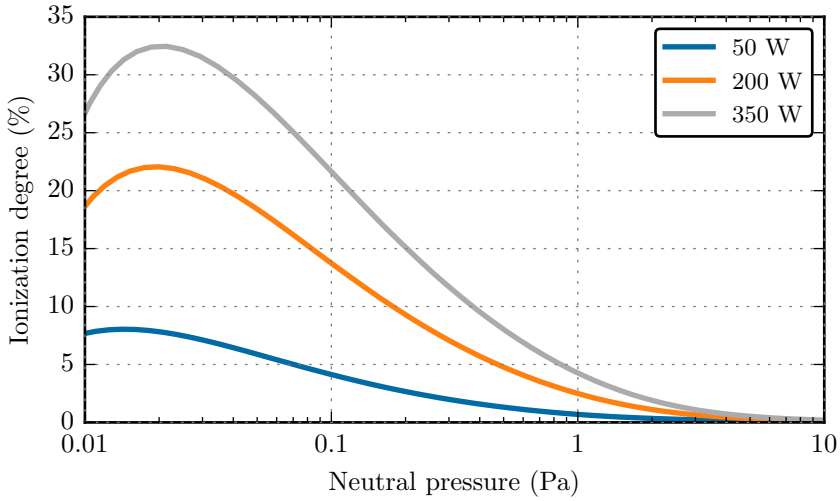

Figure 2.15: Ionization degree as a function of the total plasma pressure, for three different discharge powers.

Figure 2.18 shows that the electron temperature is quasi-constant with discharge power, as shown in simpler plasmas of Ar or Xe. A small local minimum below 2 eV is seen between 1 Pa and 10 Pa depending on the discharge power. At very low pressure, T_e increases strongly when the pressure decreases, from 4 eV at 0.1 Pa to 8 eV at 0.03 Pa.

Two more parameters are important to describe an iodine plasma: the electronegativity, which is the ratio of the negative ions density (here only I^-) over the electron density, and the I_2 dissociation fraction, which is computed as the ratio $[I]/([I]+[I_2])$. The electronegativity decreases nearly linearly with discharge power, and Figure 2.19 shows that it also increases quasi-linearly with pressure. It stays under 1 except at low power and high pressure, for example $\alpha = 2$ at 50 W and 3 Pa, or at 200 W and 7 Pa. This low electronegativity is due to the high dissociation fraction of I_2, as I_2 is the only source of I^-. Figure 2.20 indicates that the dissociation fraction goes higher than 95 % when the plasma discharge power goes above 100 W, and only drops below 90 % at high pressure: above 0.3 Pa at 50 W, or above 6 Pa at 200 W,

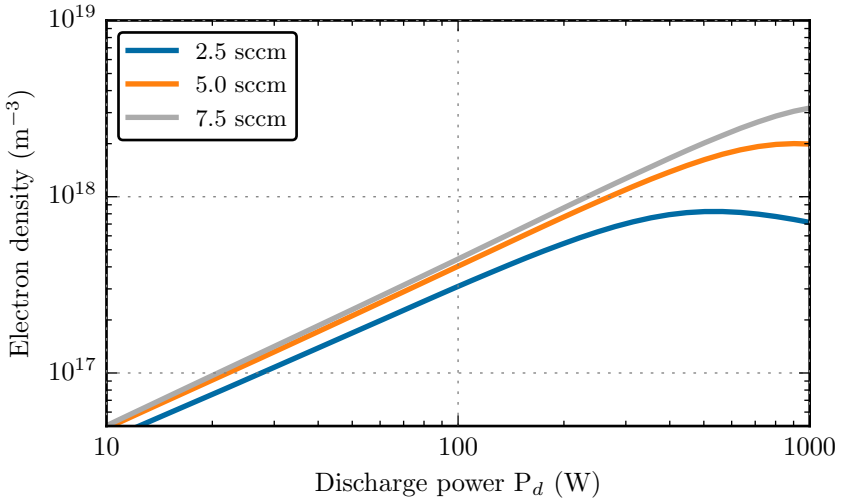

Figure 2.16: Electron density as a function of discharge power, for three different constant mass flow rates.

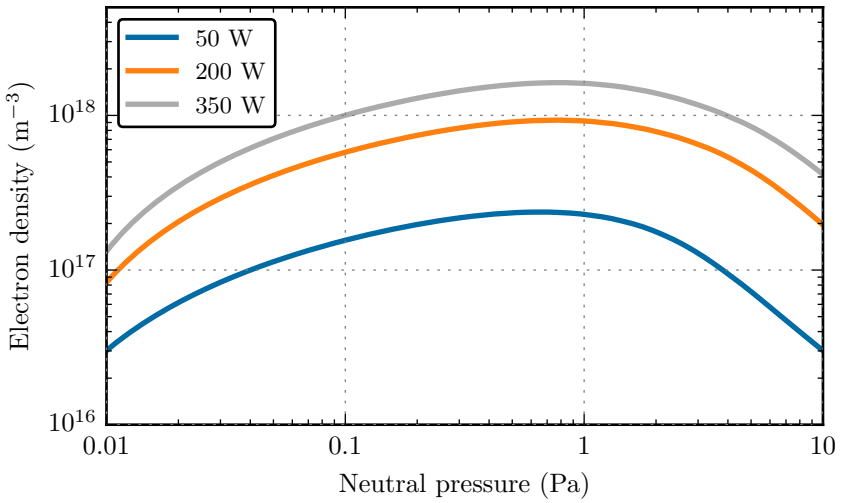

Figure 2.17: Electron density as a function of the total plasma pressure, for different discharge powers.

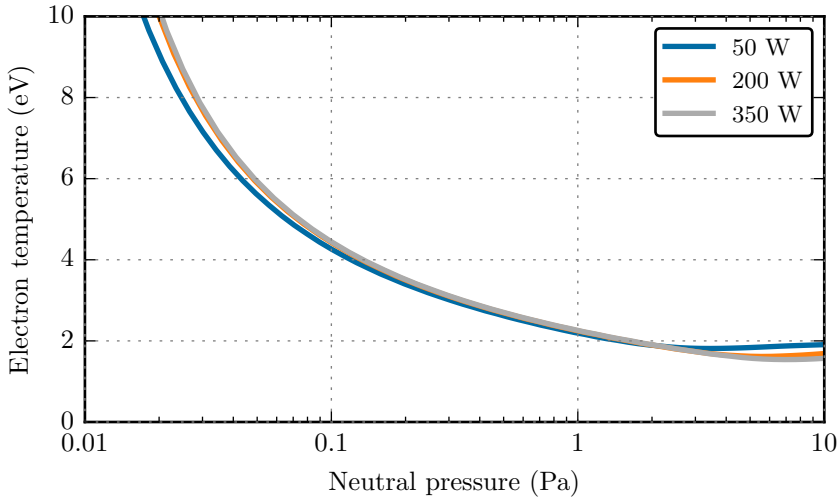

Figure 2.18: Electron temperature as a function of pressure, for three constant discharge power.

for example. On the same curve, the ratio of I^+ ions among positive ions in the exhaust plume is plotted in dashed lines. It follows the dissociation degree: a highly dissociated plasma will produce a plume with mostly singly ionized ions.

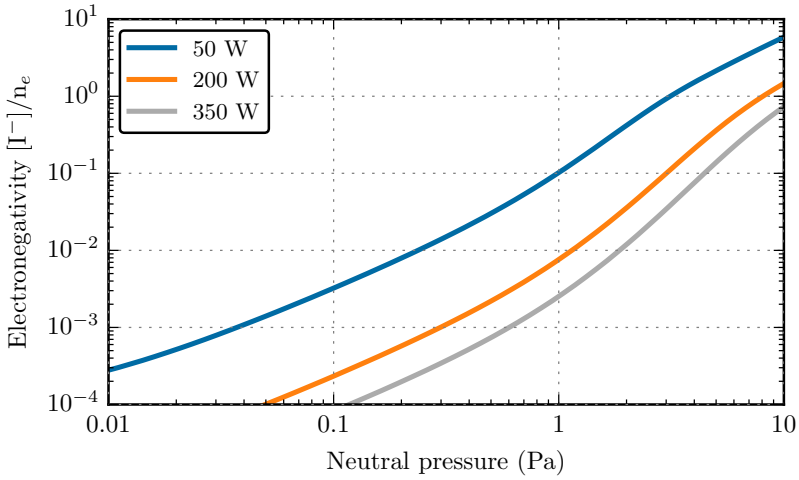

Figure 2.19: Bulk electronegativity [I−]/n_e as a function of pressure, for different discharge power.

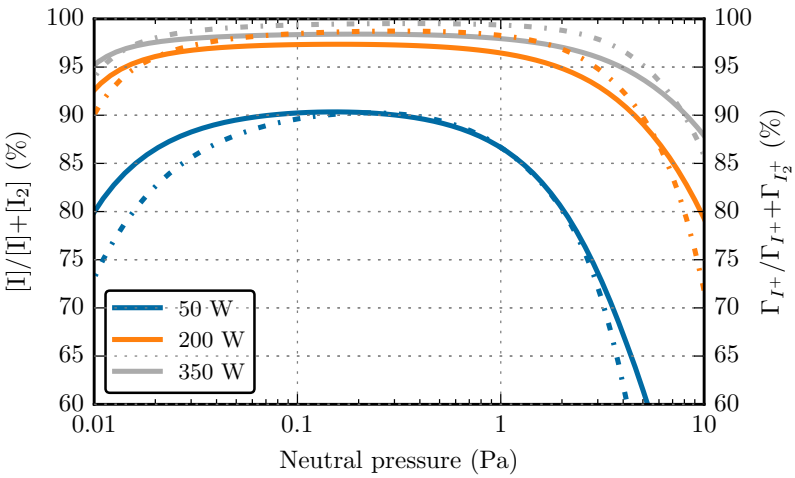

Figure 2.20: Dissociation degree as a function of discharge power (solid lines), and ratio of I^+ ions over positive ions in the exhaust plume (dashed lines), for three constant iodine mass flow rates.

2.7 Chemical dynamics

The current section aims at understanding the dominant reactions and mechanisms in the plasma. We consider a plasma at $P_d = 150\,\mathrm{W}$ and $Q_0 = 10\,\mathrm{sccm}$ with a grid transparency of 0.22 and a fixed gas temperature at 1000 K. The equilibrium state is found to be for $T_e = 2.6\,\mathrm{eV}$ and the densities are shown Figure 2.21. This corresponds to a neutral pressure of 0.5 Pa, an electronegativity of 4.2×10^{-3}, an atomic iodine to neutral gas ratio of 96 %, and an ionization degree of 3.5 %. The errorbars are generated using Monte-Carlo simulations on the global model. The parameters and distributions used are shown Tab 2.3, and explained below. Considering each species an ideal gas, one can compute the partial pressure for each species. Figure 2.22 shows that electrons account for one third of the total pressure, the rest being mostly I atoms.

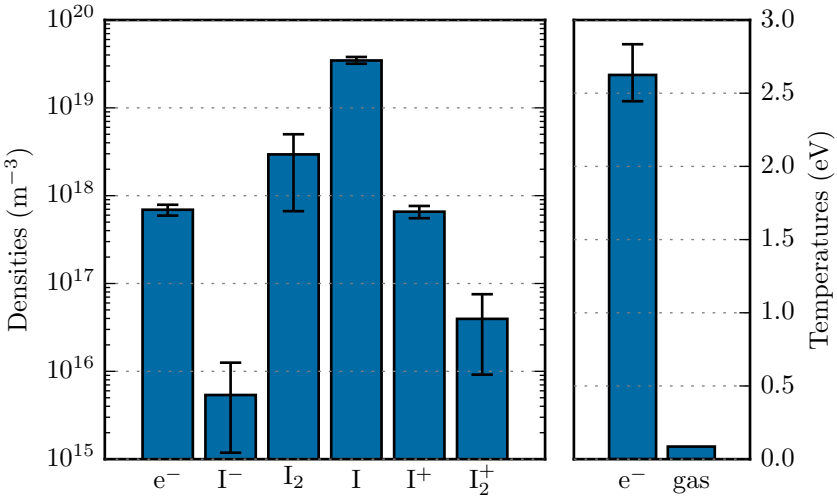

Figure 2.21: Densities of the reference plasma as predicted by the global model. The related gas temperature was fixed at $T_g = 0.086\,\mathrm{eV} = 1000\,\mathrm{K}$. The errorbars materialize the 2.5 and 97.5 percentile, so that 95 % of the simulation runs fall within the errorbars.

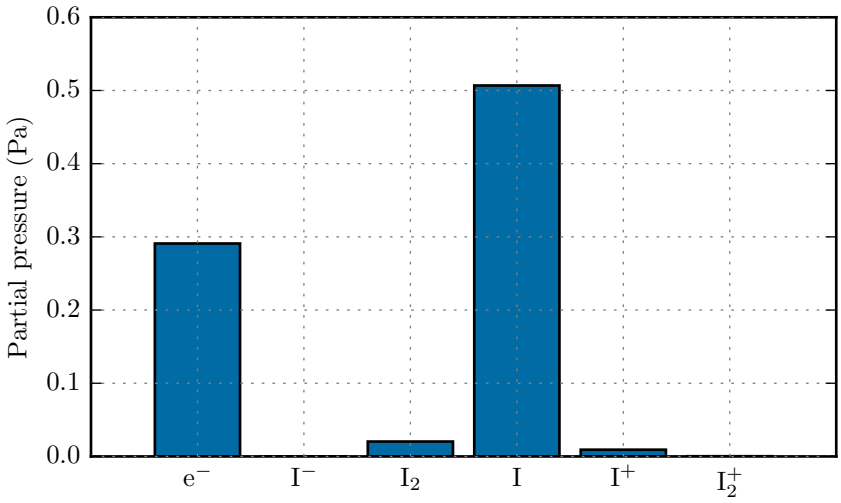

Figure 2.22: Partial pressure of each species, calculated with $T_g = 1000\,\mathrm{K}$, $T_+ = 1000\,\mathrm{K}$, $T_- = 1500\,\mathrm{K}$, and all densities shown Figure 2.21.

2.7.1 Uncertainty quantification

To run a Monte-Carlo simulation, each variable listed on Tab 2.3 is multiplied before the run by a factor drawn at random within the distribution mentioned, always centered on 1 and whose width depends on an estimation of the uncertainty associated to the coefficient. The log-normal distribution is the probability distribution of a random variable whose logarithm is normally distributed. At low standard deviation, it behaves like a normal distribution while avoiding negative values, as shown Figure 2.23. Here a standard deviation $\sigma = 0.2$ is used for reactions whose parameters have been calculated recently, meaning that they are considered solid. $\sigma = 0.5$ is used for lesser known reactions. A standard deviation of even $\sigma = 0.5$ is quite small for reaction rates and in some cases a realistic uncertainty could rather make it span over several orders of magnitude. The present analysis is preliminary and meant as an introduction towards a more general uncertainty quantification approach in the model.

Variable	Distribution	Parameters	
$K_{\mathrm{iz,I}}$	log-normal	$\mu = 0$	$\sigma = 0.2$
$K_{\mathrm{iz,I_2}}$	log-normal	$\mu = 0$	$\sigma = 0.2$
$K_{\mathrm{exc,I}}$	log-normal	$\mu = 0$	$\sigma = 0.2$
$K_{\mathrm{el,I}}$	log-normal	$\mu = 0$	$\sigma = 0.2$
$K_{\mathrm{el,I_2}}$	log-normal	$\mu = 0$	$\sigma = 0.2$
$K_{\mathrm{diss.att}}$	log-normal	$\mu = 0$	$\sigma = 0.2$
$K_{\mathrm{diss.iz}}$	log-normal	$\mu = 0$	$\sigma = 0.2$
$K_{\mathrm{diss.iz}}$	log-normal	$\mu = 0$	$\sigma = 0.2$
$K_{\mathrm{ion.rec}}$	log-normal	$\mu = 0$	$\sigma = 0.2$
$K_{\mathrm{neut,I^-,I_2^+}}$	log-normal	$\mu = 0$	$\sigma = 0.5$
$K_{\mathrm{c.ex,I_2,I^+}}$	log-normal	$\mu = 0$	$\sigma = 0.5$
$K_{\mathrm{detach,I^-}}$	log-normal	$\mu = 0$	$\sigma = 0.2$
h factor	uniform	$a = 0.95$	$b = 1.05$
γ_{rec}	uniform	$a = 0.01$	$b = 0.5$

Table 2.3: Parameters varied to calculate errorbars through Monte-Carlo simulations, and distributions used for the multiplication factor applied to the default value. Except for γ_{rec} where the distribution shown is for the value of γ_{rec} used.

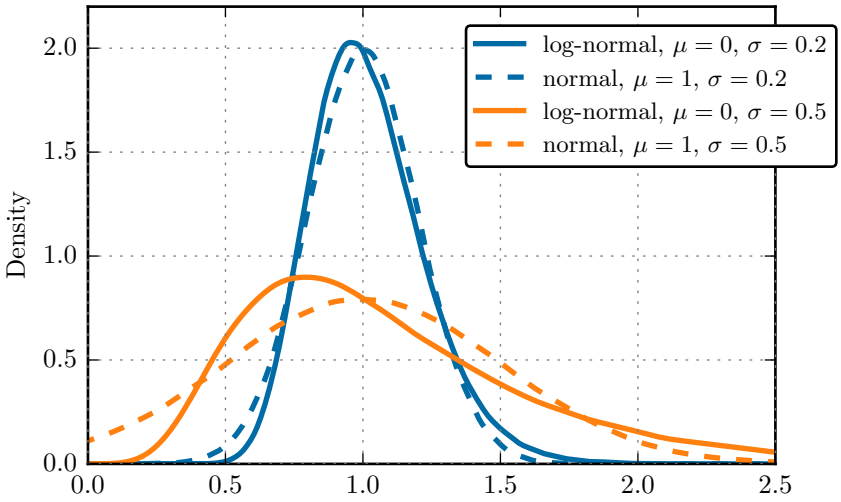

Figure 2.23: The difference between a normal and a log-normal simulation is small for low σ. The log-normal distribution does not reach negative values.

By combining Monte-Carlo simulations or using more complex algorithms, a sensitivity analysis can be achieved. These sensitivity analyses lead to the computation of the Sobol indices, measuring individual contributions to the global uncertainty or each model output, for each input parameters. With the help of Dr. Olivier le Maître, such Sobol indices have been calculated for a simplified iodine plasma using an adapted version of the global model code designed to run on clusters, with computing cores running independently in parallel. Preliminary results are presented elsewhere [82], and are not reproduced here.

2.7.2 Particle balances

This subsection exhibits the main processes for the creation and losses of each species at $P_d = 150\,\mathrm{W}$ and $10\,\mathrm{sccm}$, corresponding to $0.5\,\mathrm{Pa}$, using equations presented section 2.5. Such information can be used to build a reduced reaction set to study the plasma, depending of the parameters of interest: a model dedicated to estimate thrust would focus on I^+ ions, when a pure plasma model would emphasize on n_e and T_e, etc. Different reactions could also be included in the particle and power balances depending on their preeminence in each equation.

Electron gains and losses Electrons are mostly created by ionization of I atoms, and to a lesser extent by direct ionization of I_2 molecules. As shown Figure 2.24a, other channels are nearly negligible. Figure 2.24b shows that losses are quasi exclusively happening at the walls, the other loss source being the dissociation attachment of I_2.

I_2 gains and losses On Figure 2.25a, it it shown that the main creation processes for I_2 are the I recombination at the walls and the gas injection. Other channels are much lower. Loss processes, shown Figure 2.25b, are dominated by dissociation by electron impact and, around four times less important, ionization.

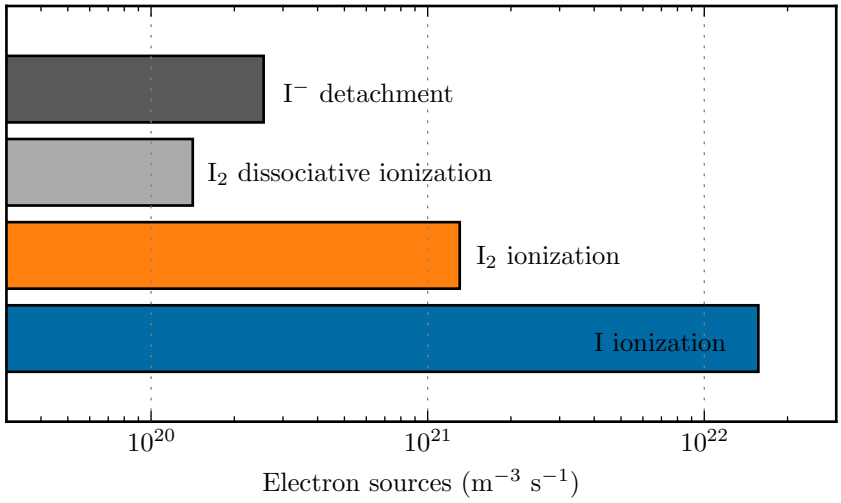

(a) Electron gains

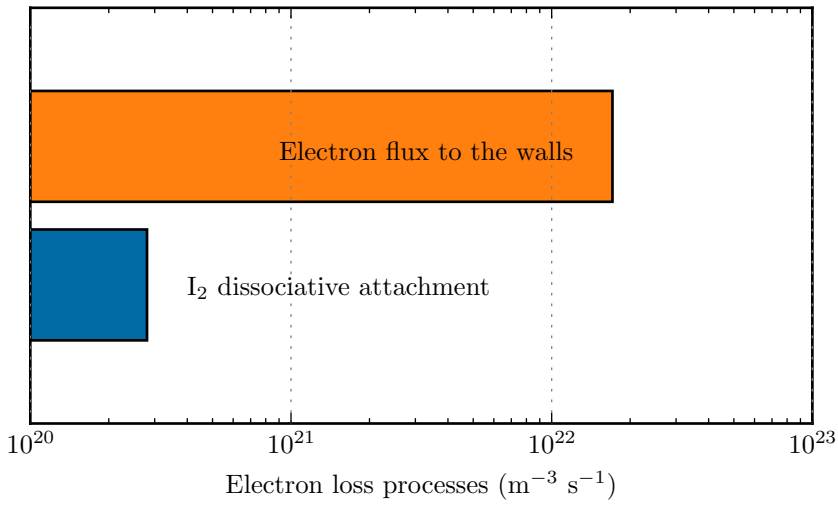

(b) Electron losses

Figure 2.24: Electron gain and loss mechanisms in an iodine plasma at $P_d = 150\,\mathrm{W}$ and $Q_0 = 10\,\mathrm{sccm}$, corresponding to $0.5\,\mathrm{Pa}$.

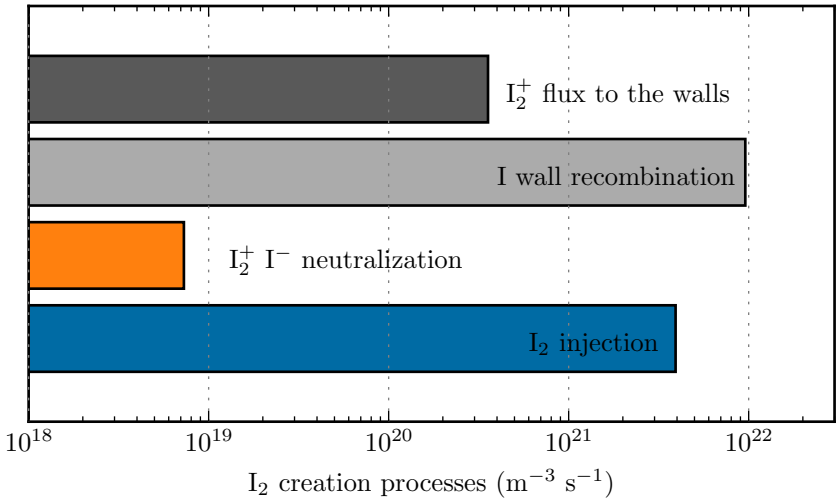

(a) I_2 gains

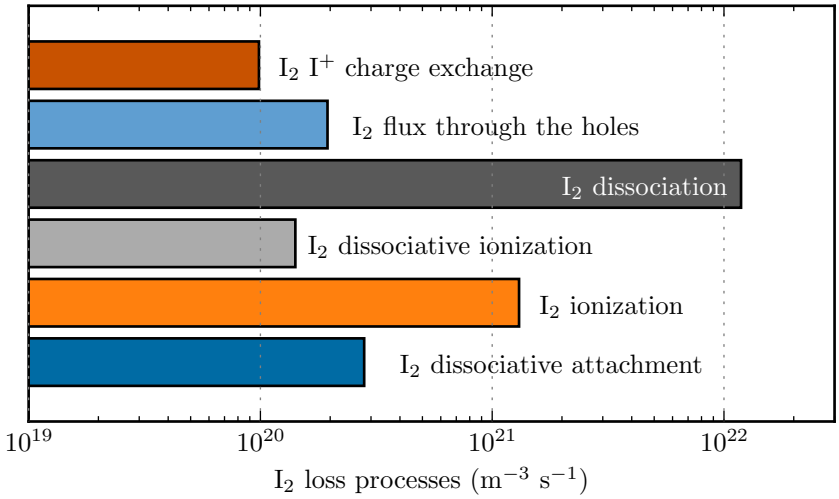

(b) I_2 losses

Figure 2.25: I_2 gain and loss mechanisms in an iodine plasma at $P_d = 150\,\mathrm{W}$ and $Q_0 = 10\,\mathrm{sccm}$, corresponding to $0.5\,\mathrm{Pa}$.

I gains and losses As shown Figure 2.26, I atoms are mostly produced by neutralization of I^+ ions at the walls and dissociation of I_2, with more than $10^{22}\,m^{-3}\,s^{-1}$ particles created. 10^{21} I atoms are created through ${I_2}^+$ dissociation per second per cubic meter. All other reactions produce no more than 4×10^{20} particles per second per cubic meter. The main destruction process, shown Figure 2.27, is wall recombination, twice more important as ionization, and around four times more important that the thermal flux of I through the holes. This value depends strongly on γ_{rec}, here equal to 0.1.

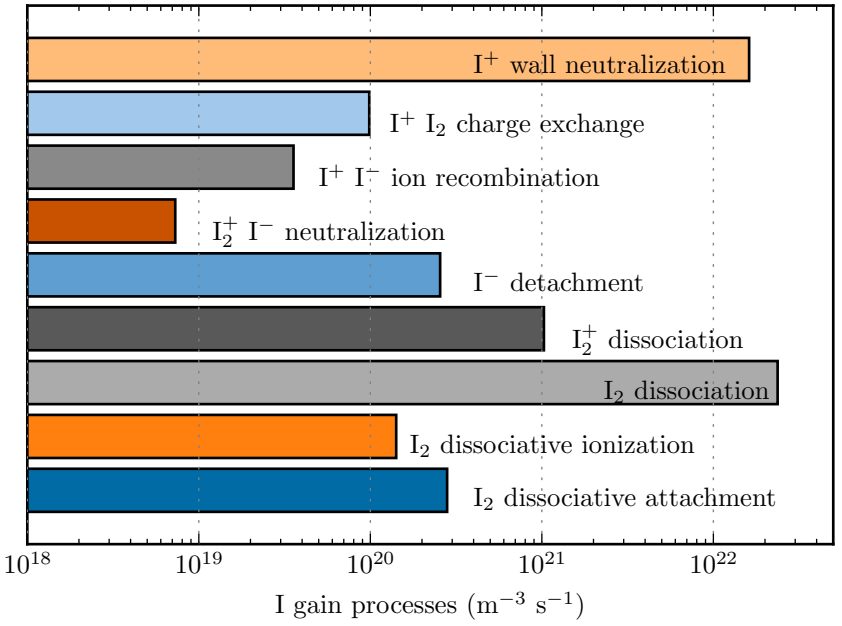

Figure 2.26: I gain mechanisms in an iodine plasma at $P_d = 150\,W$ and $Q_0 = 10\,sccm$, corresponding to $0.5\,Pa$.

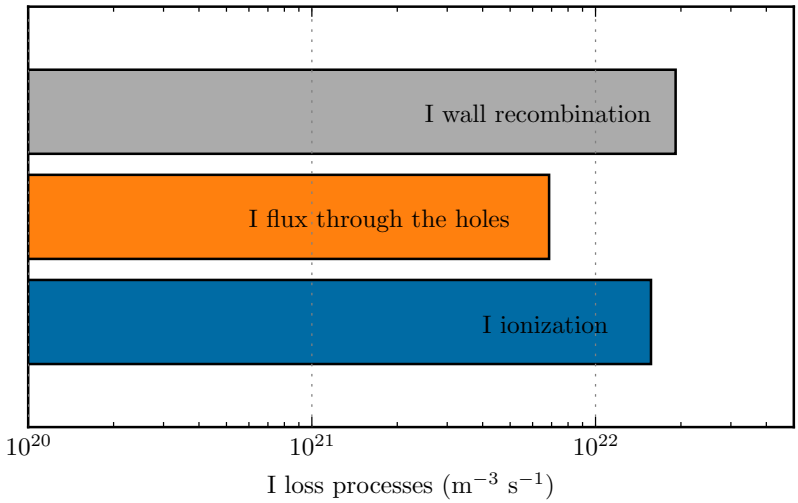

Figure 2.27: I loss mechanisms in an iodine plasma at $P_d = 150\,\mathrm{W}$ and $Q_0 = 10\,\mathrm{sccm}$, corresponding to $0.5\,\mathrm{Pa}$.

I^+ gains and losses I^+ ions are created nearly exclusively through direct ionization of I atoms, and destroyed by being neutralized at the walls. Those processes and the others are shown Figure 2.28.

I^- gains and losses I^- are solely created by dissociative attachment of I_2, and destroyed nearly-exclusively through detachment after electron collisions, as show Figure 2.29.

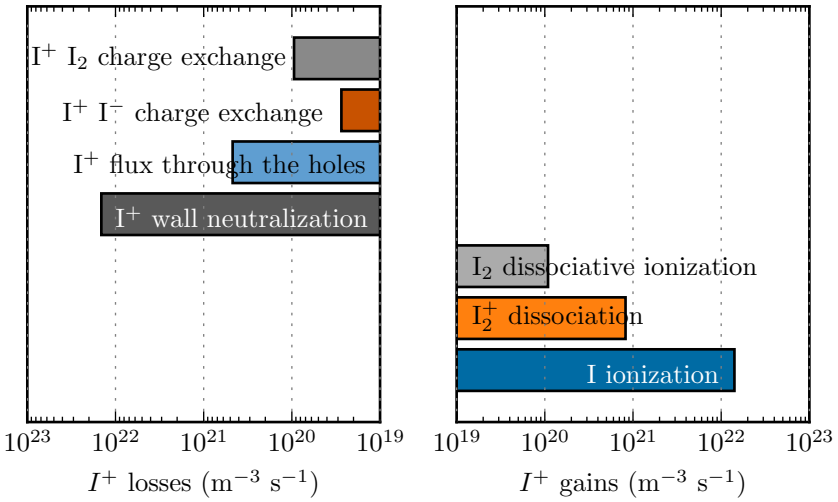

Figure 2.28: I^+ gain (right) and loss (left) mechanisms in an iodine plasma at $P_d = 150\,\mathrm{W}$ and $Q_0 = 10\,\mathrm{sccm}$, corresponding to 0.5 Pa.

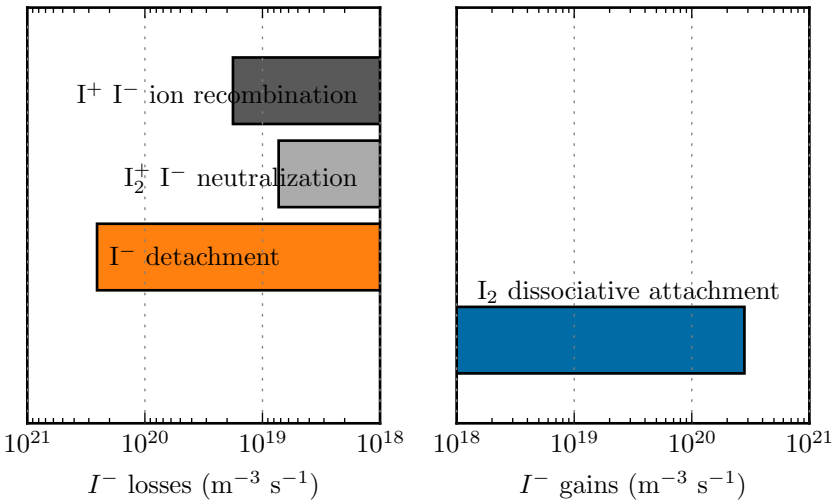

Figure 2.29: I^- gain (right) and loss (left) mechanisms in an iodine plasma at $P_d = 150\,\mathrm{W}$ and $Q_0 = 10\,\mathrm{sccm}$, corresponding to 0.5 Pa.

I_2^+ gains and losses I_2^+ ions are created nearly exclusively through ionization of I_2. The main channel for losses is the dissociation of I_2^+, nearly twice as important as the wall neutralization. As shown Figure 2.30, the part of I_2^+ ions going through the holes and thus being part of the produced thrust is very small, compared to other loss mechanisms but also compared to I^+ leaving through the holes.

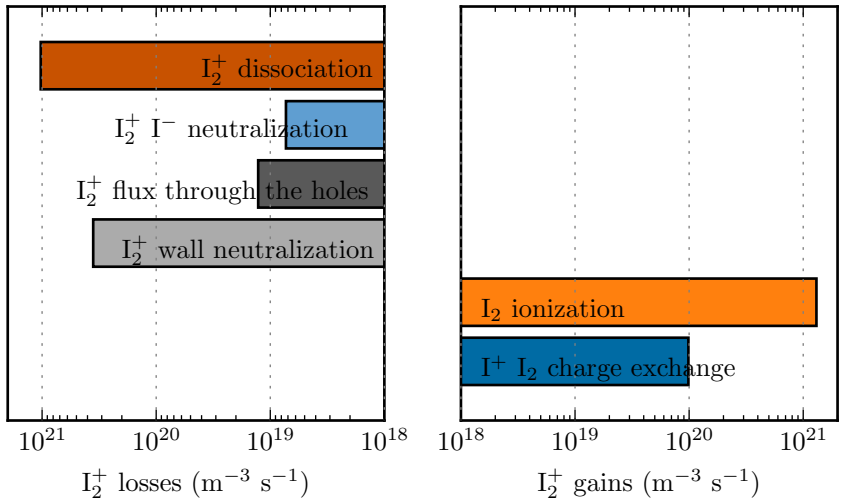

Figure 2.30: I_2^+ gain (right) and loss (left) mechanisms in an iodine plasma at $P_d = 150\,\mathrm{W}$ and $Q_0 = 10\,\mathrm{sccm}$, corresponding to 0.5 Pa.

2.7.3 Power balance

Figure 2.31 shows how much power is lost by the electrons through all the loss processes considered. Multiplying those values by the thruster volume, here is the repartition. The input power is 150 W. Among those, 63 W are spent exciting I atoms. 52 W are lost at the walls. 30 W are spent to ionize I atoms, 4 W are used to dissociate I_2 into two I atoms, 2 W are used to ionize I_2. All other reactions contribute to less than 0.5 W out of the 150 W of the power budget.

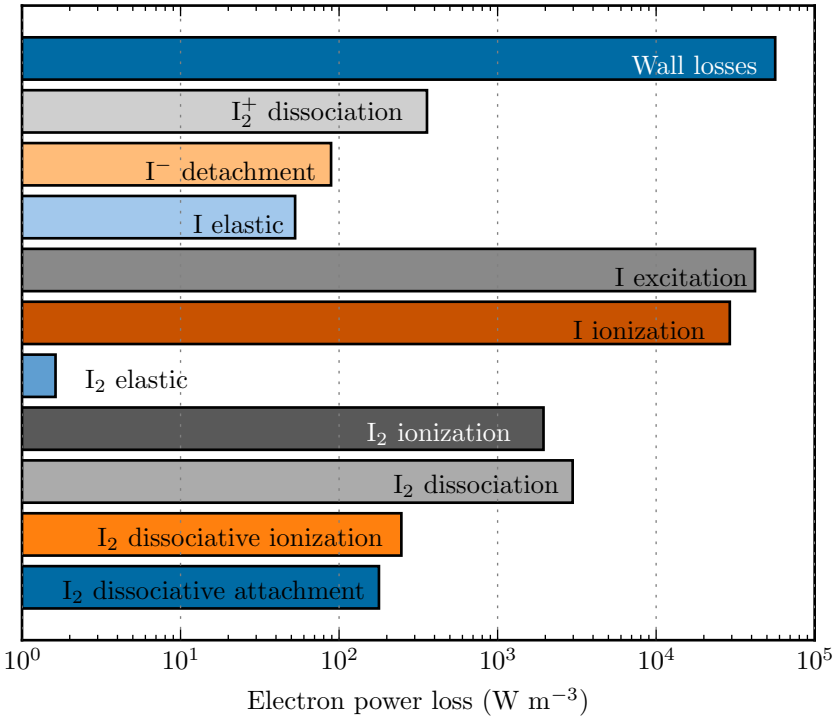

Figure 2.31: Losses of electron energy per second and per cubic meter for each reaction included in the power balance equation.

2.8 Effects of grid transparency

Different simulations or different experiments can be done modifying the grid transparency. For propulsion, varying the transparency of both grids is a way to improve the ion focusing, to reduce grid erosion during use. It is interesting to see whether, and how, the grid transparency is affecting the simulation. The grid transparency only appears in the model in the definition of the thruster areas. A larger grid transparency means a larger loss area for neutral, a smaller neutralization area for ions. The pressure will decrease for a given mass flow rate. The following simulations are done with $\gamma_{\mathrm{rec}} = 0.1$.

Figure 2.32 and Figure 2.33 shows that the effects on the electron population are negligible at a given neutral pressure. It is explained because the loss area for charged species did not change: they are loss at the walls or at the holes in any case.

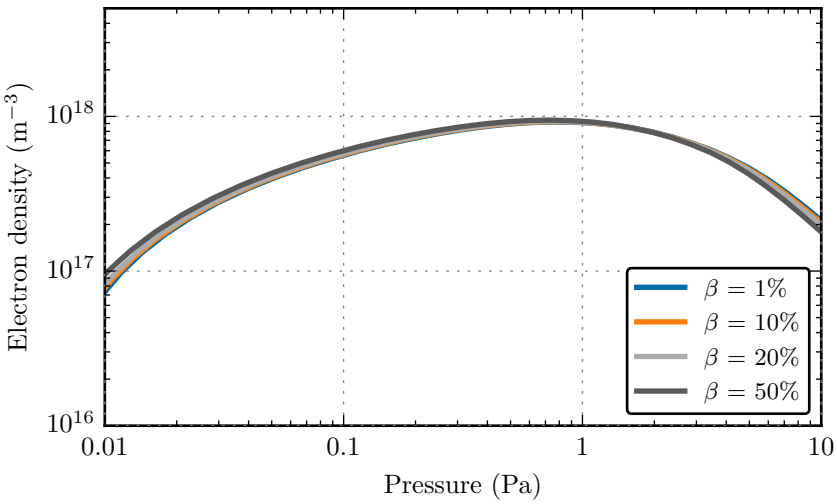

Figure 2.32: Electron density as a function of neutral partial pressure for different grid transparency.

Increasing the transparency means lowering the wall area available for recombination, but this does not lead to a higher dissociation degree, as seen Figure 2.34. The reason is that, because I_2 molecules are twice heavier than

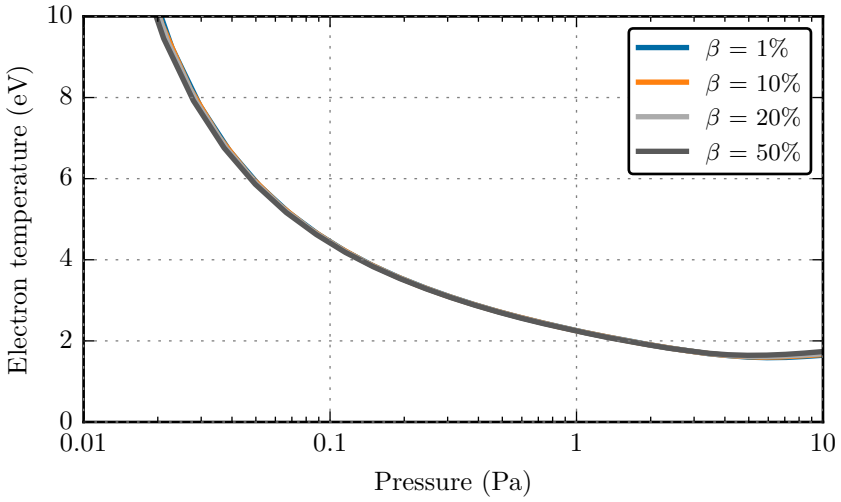

Figure 2.33: Electron temperature as a function of neutral partial pressure for different grid transparency.

I atoms, the flux ratio of I over I_2 is $\sqrt{2}$ greater than the density ratio. The flux of I increases faster than the flux of I_2 and the dissociation decreases with β.

$$\Gamma_{I_2} = \frac{1}{4}[I_2]\sqrt{\frac{8eT_g}{\pi m_{I_2}}}$$

So that, with $m_{I_2} = 2m_I$:

$$\frac{\Gamma_I}{\Gamma_{I2}} = \sqrt{2}\frac{[I]}{[I_2]}$$

This change in dissociation degree does not have a major effect on electronegativity, as shown Figure 2.35.

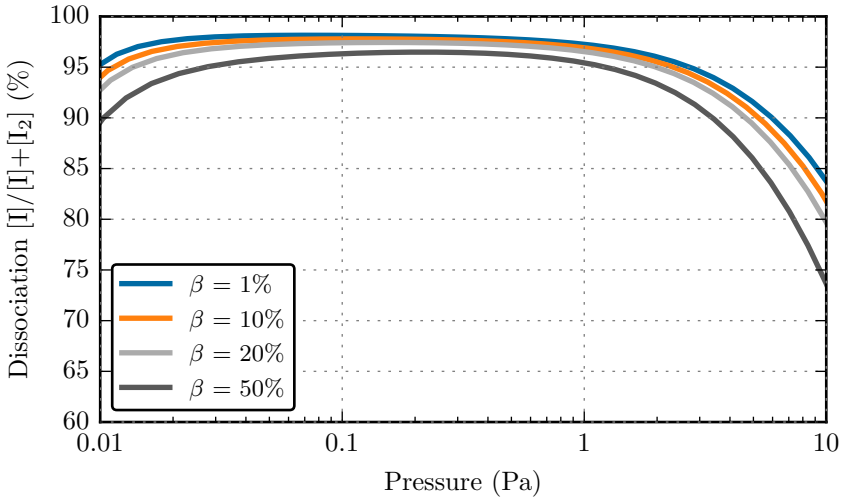

Figure 2.34: Dissociation degree as a function of neutral partial pressure for different grid transparency.

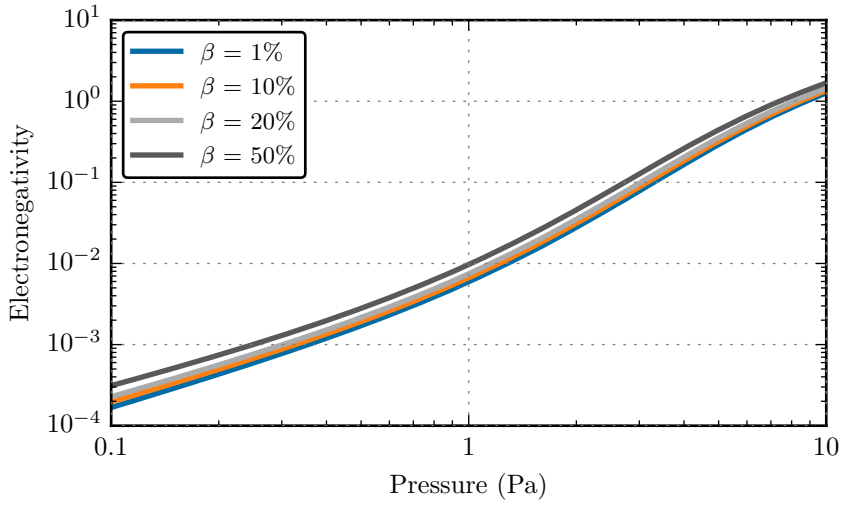

Figure 2.35: Electronegativy [I−]/n_e as a function of neutral partial pressure for different grid transparency.

2.9 Effects of wall recombination

The coefficient of recombination at the wall is unknown for $2\,I \longrightarrow I_2$, whatever the wall properties, and the value used is merely a *guesstimate* based on chlorine values in certain situations [42]. Like the transparency, the effects of changing γ_{rec} is equivalent to changing some areas in the thruster and the equations, here the recombination area. A greater wall recombination coefficient would decrease the I density, increase the I_2 density, hence increase I^- density through dissociative attachment. The effects on T_e and n_e are at first unclear. To assess the role of wall recombination of I into I_2 molecule, let's model a plasma at 10 sccm and vary the factor γ_{rec} from 0 - the I flux to the walls does not change I density - to 1 - the entire I flux is turned into I_2 molecules. Let's recall that the factor γ_{rec} is here defined as the ratio of the I flux that is recombined over the total impinging flux of I atoms. Figure 2.36 confirms that a higher γ_{rec} lowers the dissociation degree. Both the maximum (that is around 87 % in the extreme case of $\gamma_{\text{rec}} = 1$) and the pressure at which the dissociation degree starts falling are lower.

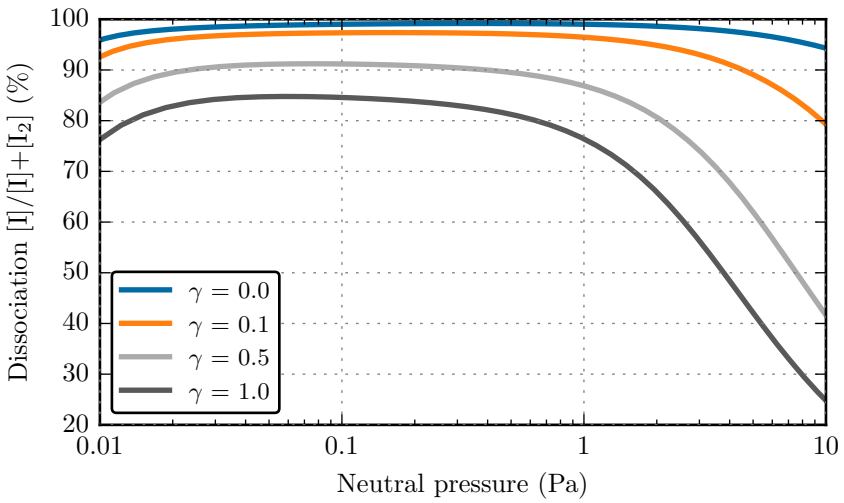

Figure 2.36: Dissociation degree as a function of total plasma pressure for different recombination rates. The recombination rate at the walls has a strong impact on the iodine molecule dissociation fraction.

Figure 2.37 also confirms that this increase in I_2 density leads to an increase in electronegativity: going from $\gamma_{\text{rec}} = 0$ to $\gamma_{\text{rec}} = 1$ increases the electronegativity around 20 times at pressures up to 1 Pa, five to ten times at higher pressures.

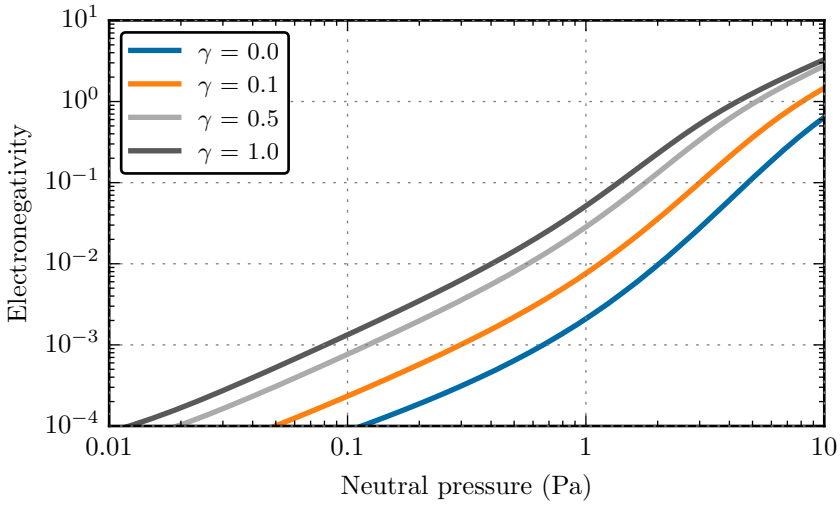

Figure 2.37: Bulk electronegativity $[I-]/n_e$ as a function of total plasma pressure for different recombination rates. The recombination rate at the walls has a strong impact on the electronegativity of the plasma.

Figure 2.38a and Figure 2.38b show that the effects of γ_{rec} on T_e and n_e are nearly negligible, except at pressures above a few Pa.

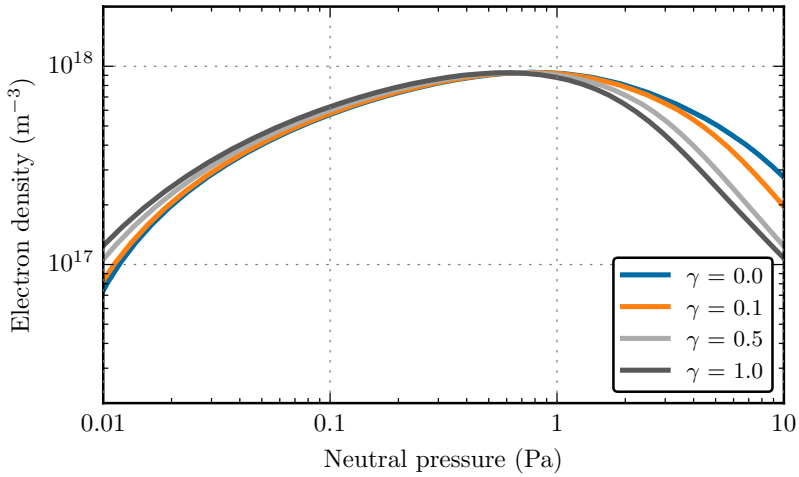

(a) n_e against pressure for different γ_{rec}.

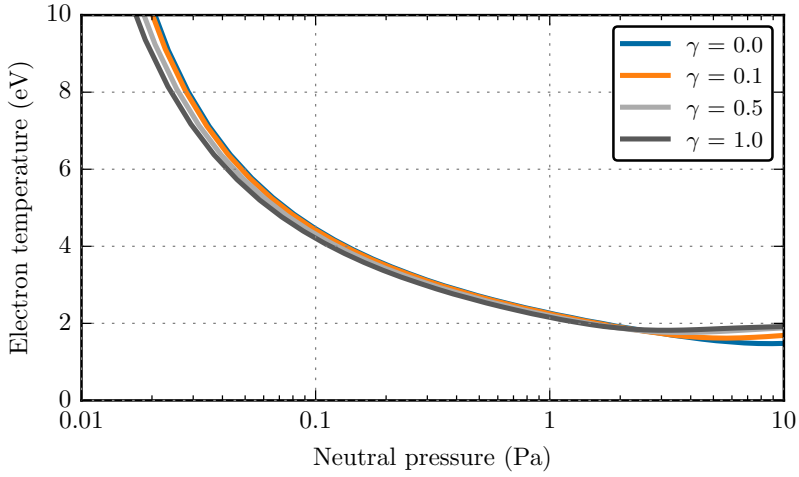

(b) T_e against pressure for different γ_{rec}.

Figure 2.38: Electron density and temperature as a function of discharge power for different recombination rates. The recombination rate at the walls has little to no impact on the electron temperature and density.

Interestingly, the effects on n_e and [I−] compensate at high pressure, so that the overall ionization degree does not change. At very low pressure on the contrary, both n_e and the electronegativity increase, leading to a slight increase of the ionization degree if γ_{rec} is increased, as shown Figure 2.39.

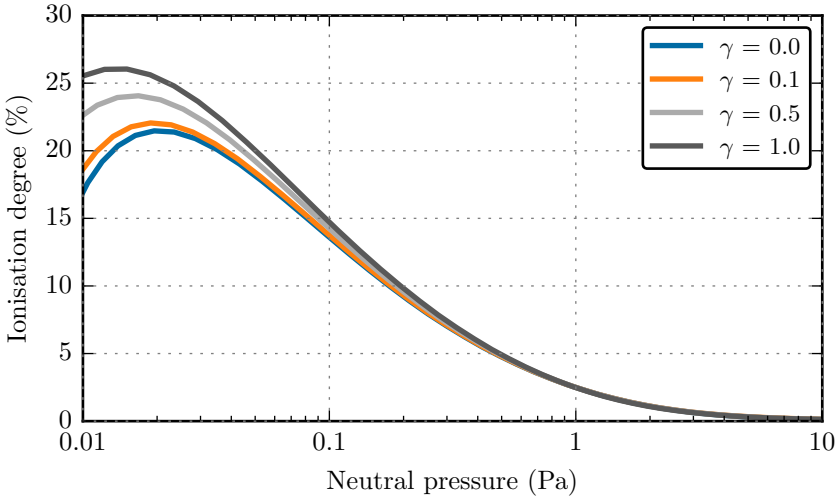

Figure 2.39: Ionization degree as a function of total plasma pressure for different recombination rates. The recombination rate at the walls has little to no impact on the ionization degree, except at very low pressure.

2.10 Effects of the gas temperature

In this chapter, the gas temperature in the global model was fixed at a value of 1000 K, derived from the measurements presented in the next chapters. It is also kept constant while it will be shown Chapter 3 that it increases with pressure. These choices could influence the results, and the present section details how gas temperature acts on the model results. Increasing the gas temperature at constant mass flow rate and discharge power has two effects working in opposite directions.

Increasing T_g increases gas pressure because gas pressure is directly proportional to gas temperature, $p = ([\mathrm{I}] + [\mathrm{I}_2])kT_g$. Figure 2.40 shows that, decreasing temperature by 50 % from 1000 K to 500 K decreases pressure by 30 %.

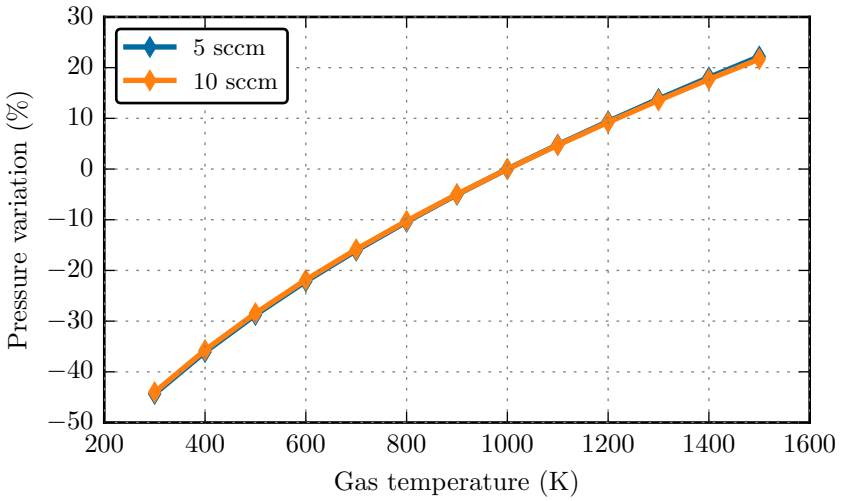

Figure 2.40: Variation of pressure with gas temperature, for two different mass flow rates and $P_d = 150$ W.

Increasing T_g decreases neutral gas density because the thermal fluxes out of the thruster are increased. Figure 2.41 shows that decreasing temperature by 50 % from 1000 K to 500 K increases neutral density by 40 %.

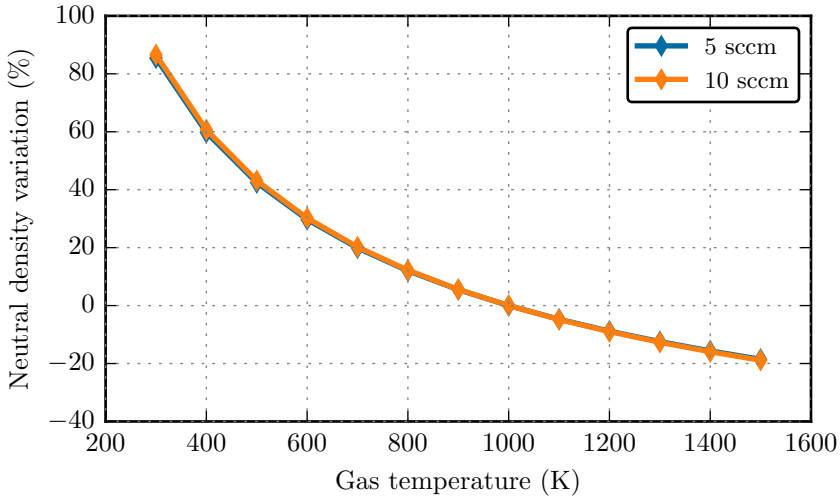

Figure 2.41: Variation of neutral gas density with gas temperature, for two different mass flow rates and $P_d = 150\,\mathrm{W}$.

The fact that, for a given neutral density, the pressure is increased, is to be joined with the fact that most plasma parameters depend only on the neutral density, not directly on pressure. This means that most curves plotted against pressure are shifted along the x-axis when the gas temperature changes. This is shown Figure 2.42: the maximum electron density is achieved for a larger pressure if T_g is increased, but Figure 2.43 shows that the true dependence is with neutral density, and that the peak appears for the same neutral density at each temperature. If the temperature is not fixed but varies with pressure, then the x-axis will not only be shifted, but also stretched accordingly, as will be shown Chapter 5.

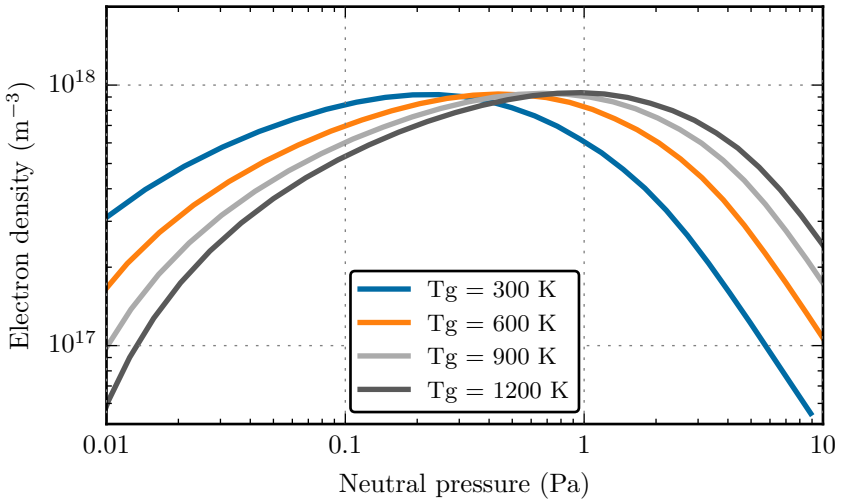

Figure 2.42: Electron density as a function of pressure for different gas temperatures.

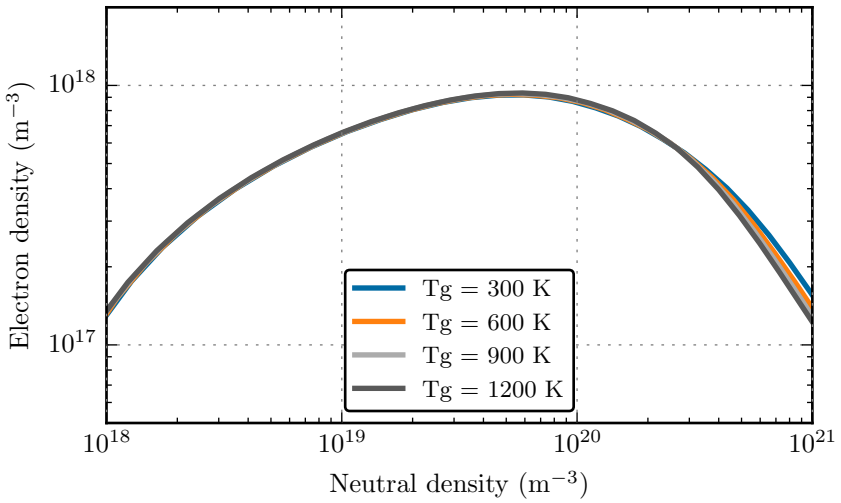

Figure 2.43: Electron density as a function of neutral density [I] + [I_2] for different gas temperatures.

2.11 Effects of the electron energy distribution

2.11.1 Introduction

All previous analyses have been done assuming a Maxwellian distribution of the electron energy. It is often asked how much this assumption affects the model, and this paragraphs aims at answering such questions. Following the schemes deployed by Gudmundsson [78] for an argon discharge, one can try and estimate the effect of varying the electron energy distribution function in the models. To this extent, two classical functions are often used. The first one is the Maxwellian distribution that has been used in this work until now, and is characteristic of an electron population in thermal equilibrium. The second one is the Druyvesteyn distribution, that features more electrons with average energy and fewer at high energy, therefore used to describe a situation with a depletion of high-energy electrons, depletion coming from surface interaction or reactions at high threshold energy for example. This distribution is well suited for a plasma if elastic collisions are dominating over inelastic collisions, if $T_e > T_g$, if the electron-electron collisions are neglected, and if the cross-sections of electron-neutral collisions are independent from T_e [83]. The two distributions are represented Figure 2.44, normalized so that the area is 1 and at a temperature of 3 eV. Gudmundsson [78] presents a continuous variation between Maxwellian and Druyvesteyn distribution, whereas this work considers only those two extrema.

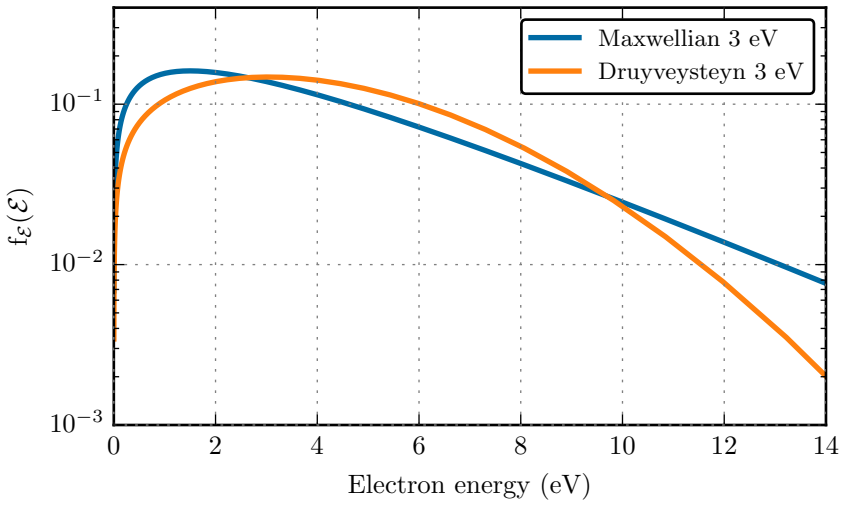

Figure 2.44: Maxwellian and Druyvesteyn distribution functions at 3 eV, normalized so that the areas are 1.

In a parameter space where the energy is expressed in eV, the distribution functions are expressed as [78]:

$$f_{\mathcal{E},maxwellian}(\mathcal{E}) = \frac{2}{\sqrt{\pi}}\left(\frac{1}{T_e}\right)^{3/2}\sqrt{\mathcal{E}}\exp\left(-\frac{\mathcal{E}}{T_e}\right)$$

$$f_{\mathcal{E},druyvesteyn}(\mathcal{E}) = \tilde{c_1}\left(\frac{1}{T_e}\right)^{3/2}\sqrt{\mathcal{E}}\exp\left(-\tilde{c_2}\frac{\mathcal{E}^2}{T_e^2}\right)$$

With

$$\tilde{c_1} = \frac{2}{1.5^{3/2}}\frac{\Gamma(5/4)^{3/2}}{\Gamma(3/4)^{5/2}} \approx 0.57$$

and

$$\tilde{c_2} = \frac{1}{1.5^2}\left(\frac{\Gamma(5/4)}{\Gamma(3/4)}\right)^2 \approx 0.24$$

2.11.2 Reaction rates

The only effect of changing the EEDF at a given temperature in our model before running it is to effectively change the reaction rates, that are built as an integration of the cross-sections over the EEDF. Studying the effect of varying the EEDF is effectively studying the effects of varying some or the reaction rates. Figure 2.45a and Figure 2.45b shows that between 1 eV to 10 eV, the main effect of transitioning to a Druyvesteyn distribution is the decrease of the ionization and dissociative ionization rates of I and I_2, letting us expect a decrease in electron density.

Figure 2.46a and Figure 2.46b show that the EEDF does not affect the rates for reactions related to I^- or ${I_2}^+$ above 1 eV.

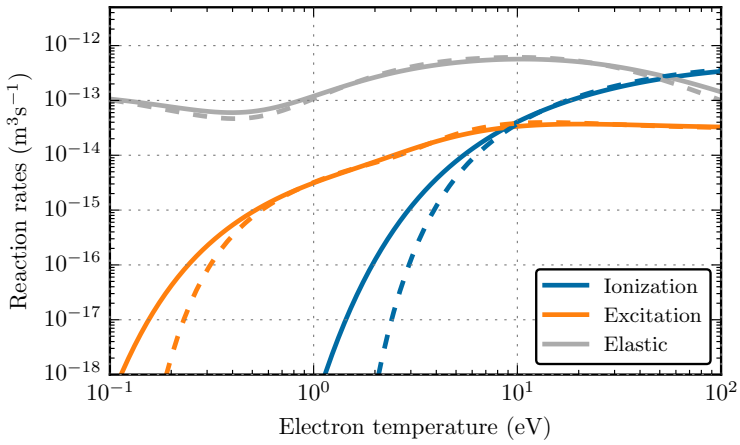

(a) Reaction rates for the iodine I atom.

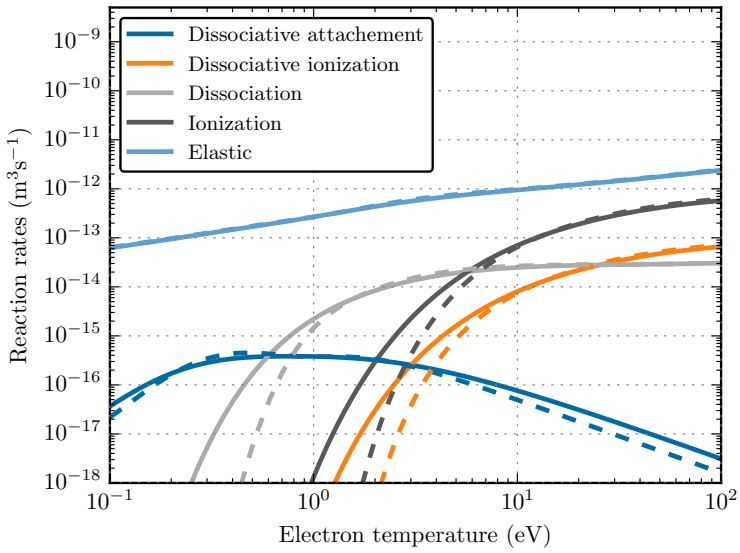

(b) Reaction rates for the iodine I_2 molecule.

Figure 2.45: Comparisons of rates built on Maxwellian and Druyvesteyn distributions for I and I_2. Solid lines: Maxwellian distribution. Dashed lines: Druyvesteyn distribution.

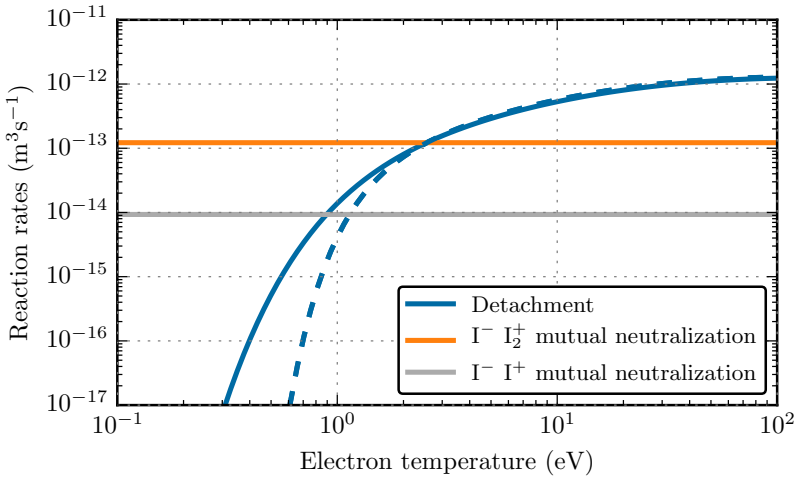

(a) Reaction rates for the iodine I^- ion..

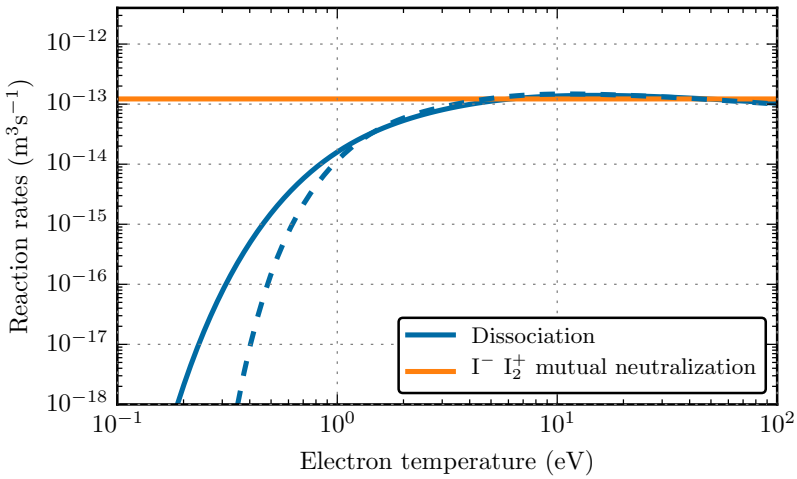

(b) Reaction rates for the iodine $I_2{}^+$ ion.

Figure 2.46: Comparisons of rates built on Maxwellian and Druyvesteyn distributions for I^- and $I_2{}^+$. Solid lines: Maxwellian distribution. Dashed lines: Druyvesteyn distribution.

2.11.3 Results

The following figures reproduce the parametrical analysis presented before, adding in dashed lines the new simulation with a Druyveststeyn distribution. Even if this effect is small, it is shown Figure 2.47a that, like in the study by Gudmundsson [78] and as expected from the preliminary analysis of the rates, the electron density decreases at all pressure. At very low pressures, the rapid increase of T_e moves the plasma at a high electron temperature space where Maxwellian and Druyvesteyn rates look alike, as shown Figure 2.45a for example. The main effect of moving from Maxwellian to Druyvesteyn EEDF between 0.1 Pa and 10 Pa is to increase T_e by 1 eV, as shown Figure 2.47b, all other parameters are only marginally affected (Figure 2.49a, Figure 2.48, Figure 2.49b).

Having a closer look at the modified rates presented above, one can see that an increase of T_e by 1 eV in the current range (2 eV to 4 eV) means that the effective values of all the reaction rates is virtually unchanged, which explains why most parameters are not much affected. Depending on the distribution, the model outputs a different value of T_e so that the balance is unaffected in the plasma: the model is rather independent from the distribution used, except for the electron temperature.

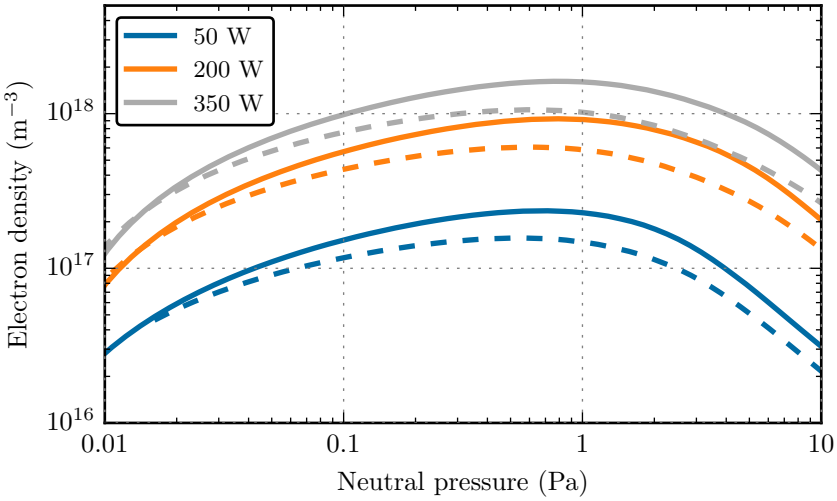

(a) Electron density.

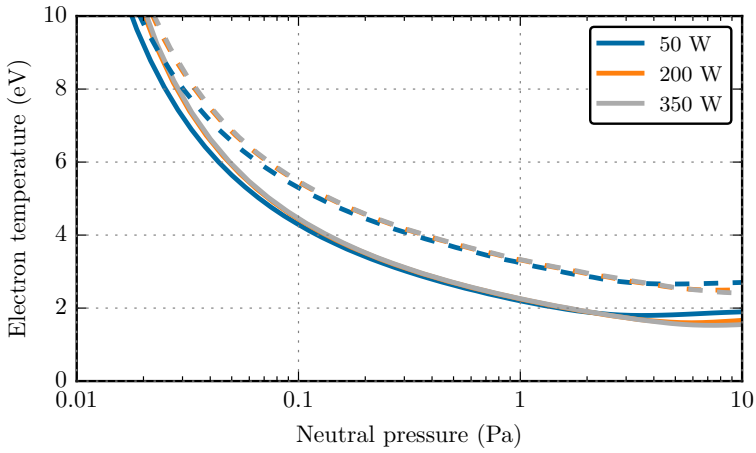

(b) Electron temperature.

Figure 2.47: Electron density and temperature as a function of plasma pressure for different mass flow rates and EEDF. Solid lines: Maxwellian distribution. Dashed lines: Druyvesteyn distribution.

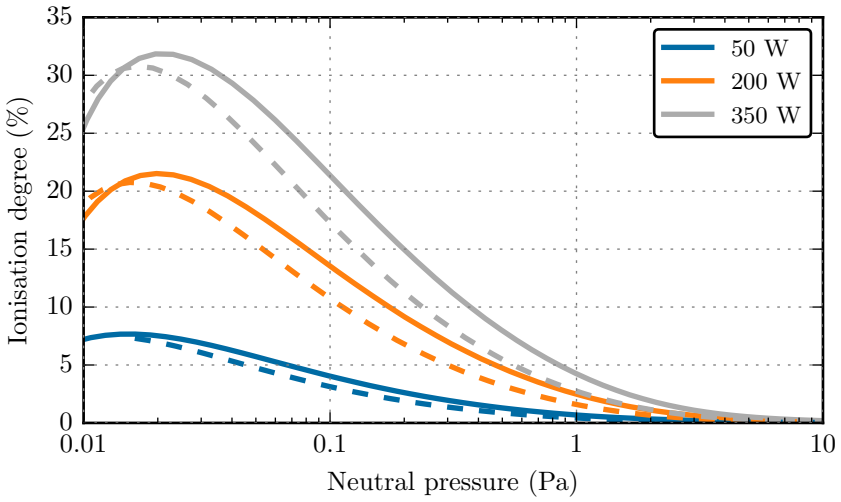

Figure 2.48: Ionization degree as a function of plasma pressure for different mass flow rates and EEDF. Solid lines: Maxwellian distribution. Dashed lines: Druyvesteyn distribution.

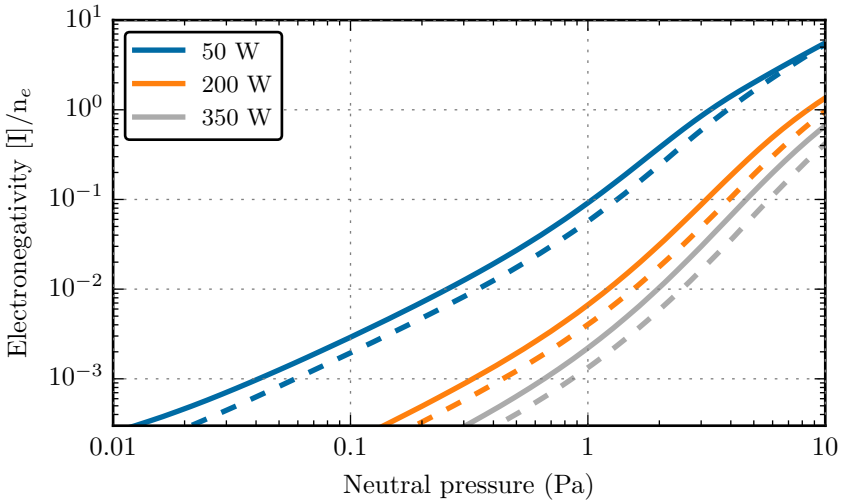

(a) Electronegativity [I−]/n_e.

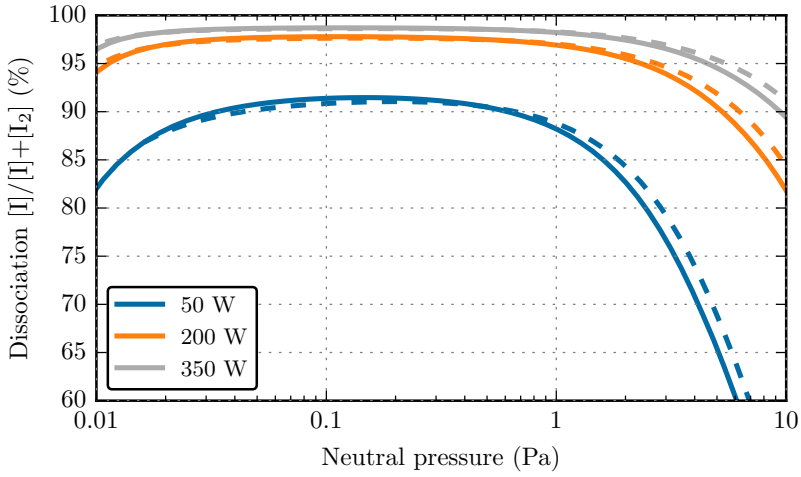

(b) Dissociation degree.

Figure 2.49: Electronegativity and dissociation degree as a function of plasma pressure for different mass flow rates and EEDF. Solid lines: Maxwellian distribution. Dashed lines: Druyvesteyn distribution.

2.12 Conclusions

The code of the global model from LPP has been fully rewritten to ease parametric studies and uncertainty quantification, and enable fast chemistry modifications. Motivated by measurements of high values of electronegativity in some iodine plasmas by Grondein [46], several electronegative features are incorporated and are shown to affect the results mainly above a few Pa, where the electronegativity is calculated to be between 1 and 10. The plasma behaves quite differently at very low pressures and at pressures higher than a few Pa. A method is presented to calculate errorbars for all outputs of the model, based on estimations of the uncertainty of the model inputs such as the wall recombination rate of I atoms, of the reaction rate of each reaction. Preliminary errorbars are presented, as a first step towards a more systematic uncertainty quantification approach in global models, to evaluate our confidence in the model and to guide further efforts to improve the reaction set. The dominant processes for creation and losses of each species are exhibited, as well as the main processes of power losses, to pave the way for a reduced reaction set for use in more complex codes such as the PIC code developed by Lucken [56]. Four parameters used as model inputs are specifically studied: the grid transparency β_0, the wall recombination rate of I atoms γ_{rec}, the gas temperature T_g, and the shape of the electron energy distribution function. It is shown that β_0 and γ_{rec} does not affect n_e or T_e, that γ_{rec} has a strong effect on the dissociation degree mainly at high pressure, that increasing the gas temperature increases pressure but decreases neutral densities, and that the model is rather independent from the distribution used (Maxwellian or Druyvesteyn), except for T_e that changes to adapt the rates and maintain the plasma balance.

The rewritten code of the global model accelerates parametric analysis to isolate and understand the impact of every parameter of the model, and enables some uncertainty quantification. These studies led to new understandings of, on one hand, how hypotheses in the model could affect the predictions and, on the other hand, what design drivers are available for real propulsion systems. Such a work should also motivate the community to better track uncertainties in the models so that no code is run without errorbars, to work towards making their code available online, to open-source them, and to embrace a more collaborative approach for their developments. The improved model will be validated against experimental measures in the next chapters.

Chapter 3

Optical diagnostics for iodine plasmas

In this chapter, four different optical diagnostics using spectroscopy to gather information about the density and temperature of the neutral species I and I_2 are presented. Emission spectroscopy is used to understand the spectral landscape from 200 to 1100 nm. Infrared laser absorption in two different spectral regions yields the density and temperature of I atoms. Broadband absorption spectroscopy in the visible range leads to the molecular density of I_2. The diagnostics are demonstrated in the case of a relatively high-pressure plasma, between 0.9 and 4.5 Pa, in the ionization chamber of the PEGASES thruster, without magnetic barrier or acceleration stage.

3.1 Introduction

3.1.1 Context and objectives

The global model of I_2 inductively coupled plasmas presented Chapter 2 needs to be validated against experimental results, before it can produce actual performance predictions for iodine plasma thrusters. Ideally, density and temperature of each atomic and molecular species must be measured for a wide range of external parameters to compare with the model, for validation. This would in addition constrain the values of several unknown coefficients, such as the wall recombination rate of I_2. No optical diagnostics dedicated to iodine had been installed at LPP prior to this thesis. Preliminary tests of the first method installed, spectroscopy at 1.3 µm, were performed by Théo Courtois and Jean-Paul Booth.

Optical diagnostics are non-perturbative methods used in this work to probe the iodine plasma. Even without complex acquisition tools, eye-averaged emission-spectroscopy can discriminate yellow, white, green or even blue iodine plasmas. These strong variations of emitted light are characteristic of the prominence of different excited species or different levels of the same excited species depending on plasma parameters. Most of the diagnostics used on the PEGASES and NEPTUNE setups by previous authors ([46, 53, 54] to only cite a few) are electrical diagnostics. Five types of optical diagnostics can be mentioned as suitable to gather information about the iodine plasma in PEGASES.

Emission spectroscopy At high resolution, emission spectroscopy can provide data such as the rotational temperature of molecules. When the setup allows absolute calibration of the emission, data such as the electron energy distribution function and gas temperature can be extracted [84]. Without absolute calibration but with addition of other gases, actinometry can lead to atomic densities [85]. Unfortunately, the iodine cell or PEGASES setup did not allow absolute calibration, and the available spectrometers have a resolution too low to resolve the vibrational structure. Interesting qualitative information about the dissociation degree have nonetheless been obtained. Emission spectroscopy also provides a wide spectral landscape, so as to identify strong atomic or ionic transitions that can later be probed by other methods such as absorption or LIF.

Broadband absorption spectroscopy At high resolution, broadband absorption spectroscopy can lead to line-integrated molecular densities in different excited levels, as well as line-integrated densities of negative species [86]. With a low resolution detector such as the one used in this work, line-integrated molecular density is measured by comparing the light emitted by an halogen lamp before and after a pass in the plasma, assuming that the population is the upper states is negligible compared to the population in the lower states probed.

Laser absorption spectroscopy at resonance Using a laser tuned at a transition frequency for any atomic or ionic species leads to measurement of line-integrated density and temperature for this species, for example via Doppler-broadening, as done here after preliminary measurements to ensure the validity of the method. Two different wavelength zones are studied in this work. Only the transition connected to the fundamental state at $7603\,\mathrm{cm}^{-1}$ can give meaningful information about I density.

Laser induced fluorescence LIF uses laser excitation of atomic or molecular transitions but with another observable, monitoring desexcitation of the excited transition through other channels. This allows to measure local values of densities and temperature. The phenomenon is easily observable with a green laser pointer typically used for astronomy: using this laser in the iodine cell leads to a yellow emission along the laser path, typical of the I_2 molecules. A LIF scheme has been studied on I^+ elsewhere [30], but not implemented here as the optical access to PEGASES does not allow to easily collect the LIF emission.

Two-photo Laser Induced Fluorescence On atoms, transitions are more often localized in the visible ultra-violet range, and can be probed using TALIF: the energy needed for the transition is brought by two separated photons. This method has been experienced on iodine atoms in the early 1980s [87, 88].

3.1.2 The iodine cell

Given the complexity of operating an iodine plasma in PEGASES, the few optical accesses available and the very low mobility of the entire PEGASES setup, a small iodine cell in quartz coupled to a RF generator on wheels has been used to try and optimize some diagnostic tools before use on the real thruster. The iodine cell, shown in use Figure 3.1 is a quartz cell in which a vacuum has been made and some iodine crystals put in. The main cylinder is 25 cm long and has a 3 cm internal diameter. A "finger" is attached to this main cylinder to store the solid iodine, 12 cm long and around 1 cm of external diameter. Two electrodes made of copper tape of 25 mm width are placed on the external surface of the cell. The distance between them can be changed, the results presented here were taken with a spacing of 183 mm between the electrodes' inner edges. Without cooling of the finger, a fan is used to cool down the setup. An ice reservoir was later installed around the quartz finger, to decrease the iodine vapor pressure in the cell. Iodine vapor pressure was shown Figure 1.7. A thermometer is used to monitor the temperature within the ice reservoir. The setup is covered during measurements to avoid parasitic light and minimize ozone production from the strong UV emission of the plasma, due to strong atomic lines between 180 nm and 210 nm. The electrodes are connected through a matching circuit to a 13.56 MHz RF generator. The input and reflected power are given by a Vigilant Monitor Probe from Solayl. The discharge power is the difference between incident and reflected power: losses in the circuitry are neglected.

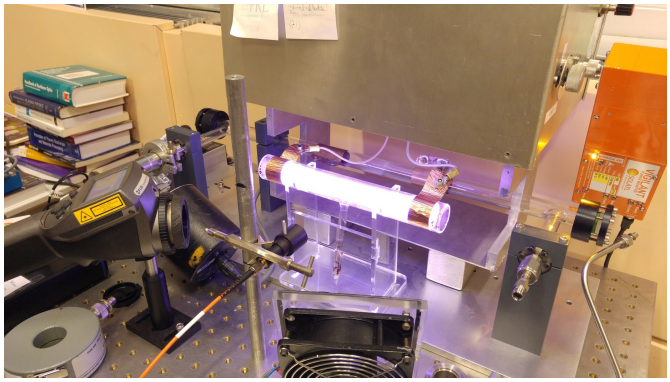

Figure 3.1: Iodine cell, here during an emission spectroscopy measurement. The metal box on top contains the matching circuitry.

3.2 Emission spectroscopy

Emission spectroscopy in visible and infrared ranges was proven to give useful qualitative insights about the plasma. Quantitative measurements would require adding another gas in the mixture (towards actinometry) or being able to precisely measure emission areas, which is not feasible in any of the available setups. The plasma setup used during the measurements is shown Figure 3.1 and described in the previous paragraph. Two detectors are used: a FLAME-S-UV-VIS-ES spectrometer from OceanOptics in a wide visible range, from 200 nm to 810 nm; and the AvaSpec-ULS2048 StarLine from Avantes in IR, from 600 nm to 1100 nm. In both cases, the resolution is between 0.5 nm and 1 nm.

Joining a visible and an infrared spectrum leads to a complete emission landscape from 210 nm to 1100 nm, shown Figure 3.2. No absolute calibration was done to join both spectra: the emission spectrum is not corrected for the effects of the detectors. Several lines for I and I_2 are identified, and a partial landscape for both species is shown below. No lines for any other species were visible. In particular, the main I^+ lines shown by Grondein [46] at 516 nm and 695 nm are not visible.

This spectrum evolves with the plasma parameters and the setups, from the cell CCP to the PEGASES ICP. Figure 3.3 shows three infrared spectra in different conditions: two in the iodine cell with different positions of the detector and different power, and one in PEGASES. Interestingly, a very small peak at 516 nm from I^+ can be detected in PEGASES, not in the cell at any conditions. It should also be noted that the lines ratio is poorly verified compared to literature data [23, 70], which could be due to a different repartition in the atomic levels in the plasma. Hence, using those intensities to characterize the plasma would require a collisional-radiative model.

The emission spectroscopy allows to discriminate plasmas with more or less molecules in the ground state due to excitation or dissocation. For a given setup, it is also possible to observe qualitatively the evolution of the different species: Figure 3.4 shows the I_2 bands disappearing as the discharge power increases, as the I bands increase. Similar effects were also visible in infrared but not presented here.

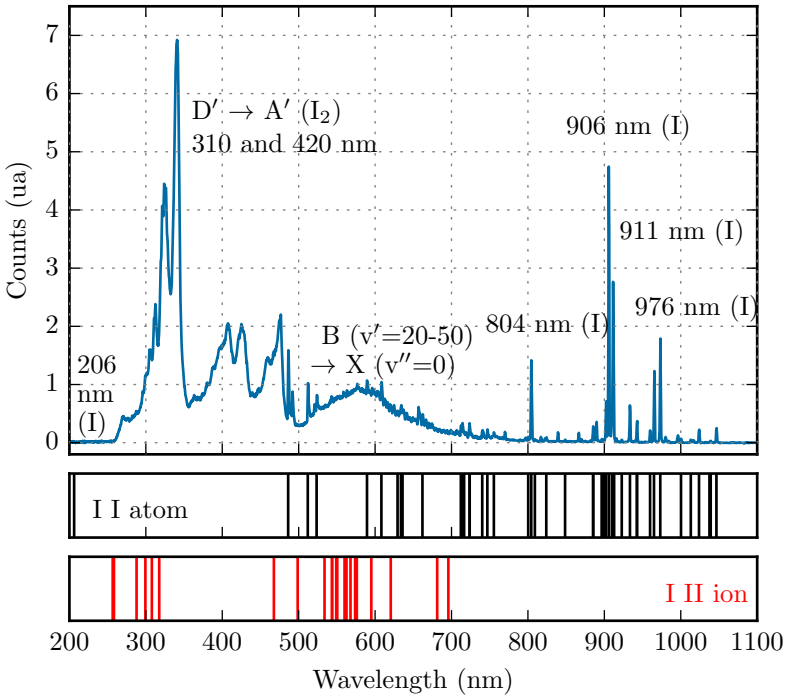

Figure 3.2: Emission spectrum from the iodine cell. Two spectra with an overlapping region have been reconnected. The visible spectrometer ranges from 200 nm to 810 nm, the IR spectrometer from 600 nm to 1100 nm. Wavelength under 250 nm are cut by the optical fiber on this figure. No absolute recalibration to correct detector effects has been done. Some information about the levels involved in the transitions are indicated, and the largest theoretical lines predicted by Luc-Koenig et al. [70] for I I (atomic I), Martin and Corliss [35] for I II (ionic I^+) are plotted as an indication.

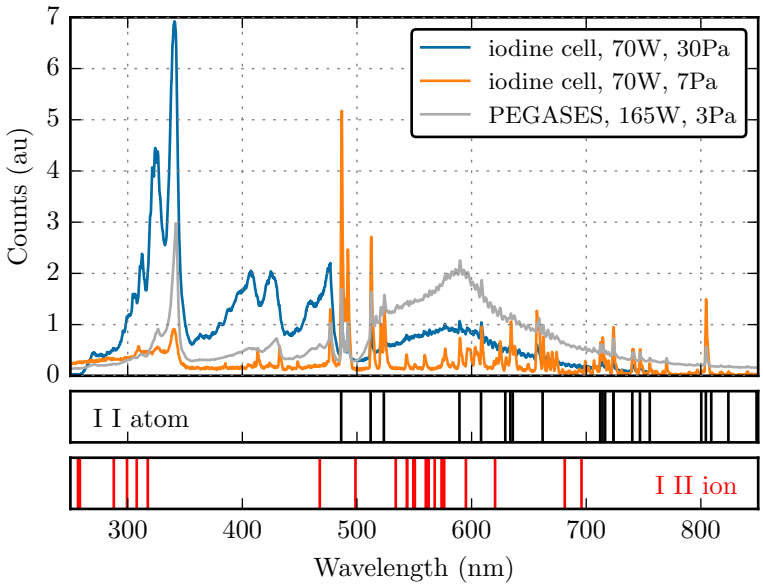

Figure 3.3: Three emission spectra of different iodine plasmas. The orange curve shows little to no emission band of I_2 around 590 nm, hinting for a highly dissociated plasma.

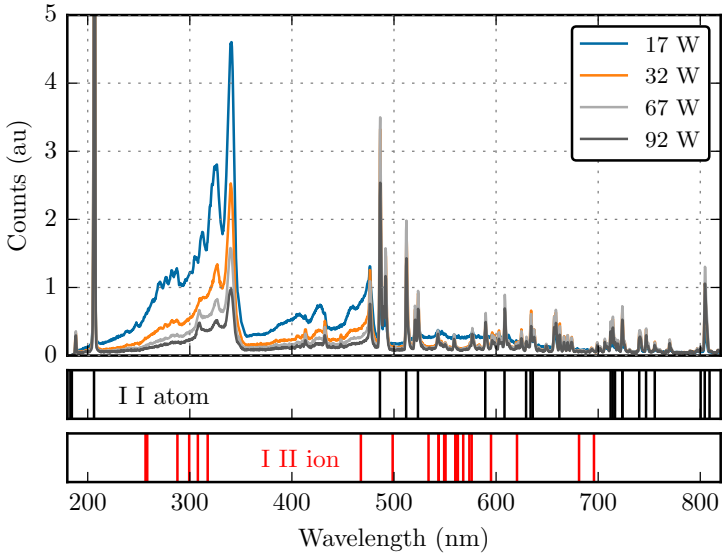

(a) Four spectra at constant pressure and increasing power in the iodine cell. The I_2 emission bands disappear progressively while the power increases. The strong line at 206 nm is visible because the optical fiber was removed.

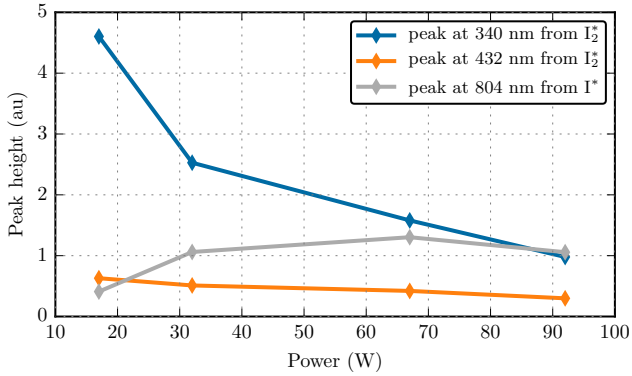

(b) A closer look on three different peaks: while the peaks on I_2 emission bands decrease in intensity, a peak from I emission tends to increase in intensity.

Figure 3.4: Qualitative information about I_2 dissociation can be inferred from emission spectroscopy.

3.3 Infra-red laser absorption spectroscopy at 10 969 cm^{-1} and 11 036 cm^{-1} in the iodine atom excited states

3.3.1 Introduction and spectral data

The emission spectroscopy of iodine plasma shows three strong I lines at 10 969 cm^{-1}, 11 036 cm^{-1} and 12 429 cm^{-1} (respectively 911 nm, 906 nm and 804 nm), clearly visible on Figure 3.2. These emission lines highlight the presence of electronic transitions that can be probed by absorption with a laser in the relevant wavelength range, and where the absorption would be strong. Such transitions show degeneracy due to the hyperfine structure of the atomic levels, with many distances between peaks smaller than the Doppler width. Doppler-free saturated absorption was used to discriminate single, double or even triple absorption lines. A single line, corresponding to a single hyperfine transition, can then be analyzed to extract the atomic temperature from its Doppler broadening. No information about the density of the levels can be extracted due to the lack of related theoretical data, the impossibility to assume that the populations of the upper levels are negligible in front of the lower levels, and the lack of a collisional-radiative model. Table 3.1, Table 3.2 and Figure 3.5 list different information about the atomic levels probed in the present measurements, with data gathered by Luc-Koenig et al. [70] and available on the NIST database [23].

Line name	A	B	C
Wavelength (nm)	804.374	905.8334	911.387
Wavenumber (cm^{-1})	12 428.7	11 036.6	10 969.3
Relative intensity	140 000	33 000	20 000
Lower level	c	c	d
Upper level	f	e	f

Table 3.1: Characteristics of the main emission and absorption lines of the I atom [23, 70]. The levels names are defined Table 3.2.

Level name	Energy (cm^{-1})	Configuration	Term	J
a	0	$5s^2 5p^5$	$^2P^o$	3/2
b	7602.970	$5s^2 5p^5$	$^2P^o$	1/2
c	54633.460	$5s^2 5p^4(^3P_2)6s$	$^2[2]$	5/2
d	59092.881	$5s^2 5p^4(^3P_2)6s$	$^2[2]$	3/2
e	65669.988	$5s^2 5p^4(^3P_2)6p$	$^2[3]^o$	7/2
f	67062.130	$5s^2 5p^4(^3P_2)6p$	$^2[1]^o$	3/2

Table 3.2: Iodine atomic levels involved in the three lines studied in this section. The levels names are arbitrary and only used in this work. The spectroscopic notation $< \{5s^2(5p^4)S_cL_cJ_c, l\}KsJ >$ used for levels c to f is from Minnhagen [34].

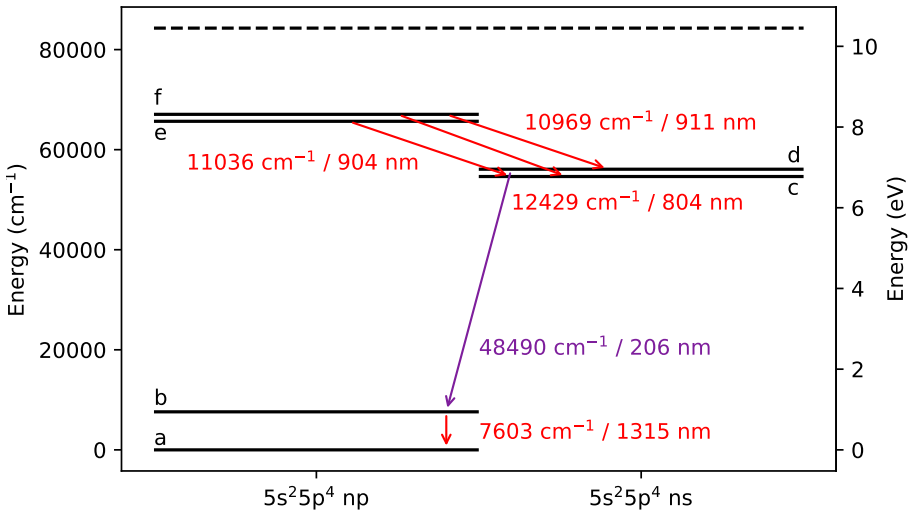

Figure 3.5: Graphical representation of six energy levels of atomic iodine involved in this work. The names are defined in Table 3.2 where their definitions are given. The dashed line is the first ionization threshold from the NIST atomic spectra database [23].

3.3.2 Experimental setup

The absorption and Doppler-free saturated absorption setup used for the IR absorption in the I excited stated is shown Figure 3.6. A Titanium-Sapphire (Ti-Sa) MBR110 continuous laser from Coherent, pumped by a Verdi-10W laser also from Coherent, tunable - via numerical control within the same experiment or with a change or internal optics - from 690 nm to 960 nm is injected in the cell. A glass separation device is used to sample parts of the beam to inject to a lambdameter WSU-10 from HighFiness. The lambdameter indicates in real-time the wavenumber of the laser and a normalization photodiode is installed. The main beam goes through an optical isolator to prevent return beams in the laser. The beam goes through a first $\lambda/2$ polarization plate that is used to bring the beam to an horizontal polarization. In this polarization state, the beam goes undisturbed through the cube beam splitter and then in the plasma. It is then led to a quarter-wave plate transforming the light to circular polarization and then to a a 4% beam splitter. 96% of the beam goes to the absorption photodiode used for normal absorption experiments. 4 % goes back to the quarter-wave plate. The two passes in the quarter wave plate are equivalent to a half-wave plate and the objective is to bring the beam to a vertical polarization. Polarized vertically, the beam passes again in the plasma and is then fully reflected in the beam splitter towards a second photodiode dedicated to saturated absorption.

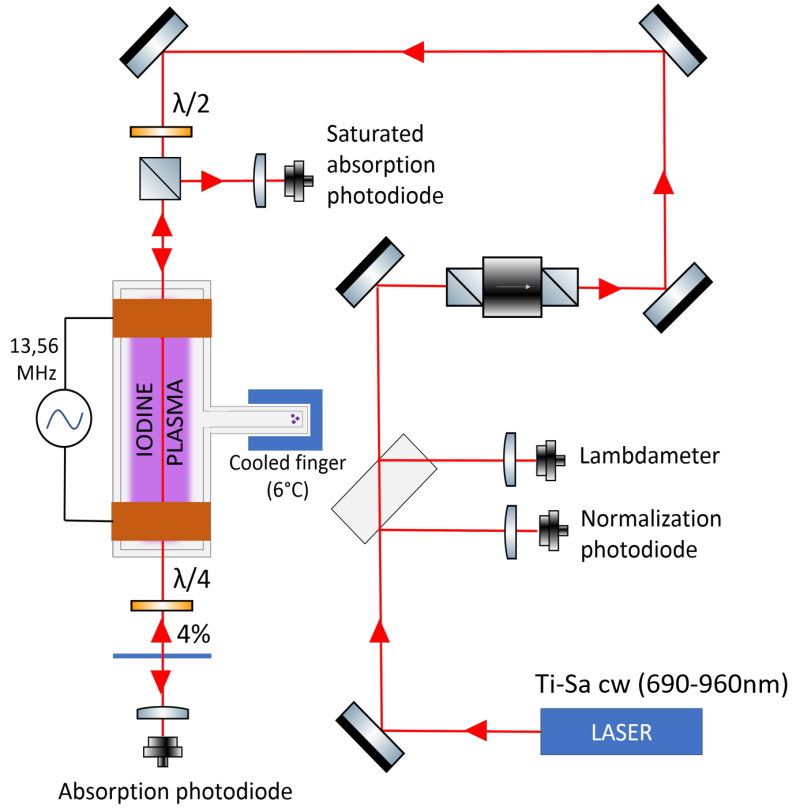

Figure 3.6: Experimental setup used for the normal and Doppler-free absorption measurements in the iodine cell. The cooled finger is used to regulate the pressure in the iodine cell, following the vapor pressure relation given Figure 1.7.

3.3.3 First insights

Figure 3.7 shows the absorption lines obtained by absorption. An hyperfine structure is clearly visible, with 7 peaks at 10 969 cm^{-1} and 7 peaks at 11 036 cm^{-1} (only six are presented on the figure, a seventh peak is seen a 11 036.2 cm^{-1} in other figures not shown). Each of these peaks can hide multiple hyperfine transitions if the distance between two peaks is smaller than the Doppler width. The theoretical number of hyperfine lines depends on the number of hyperfine states in each level. It is calculated as such: iodine has an atomic spin $I = 5/2$. Level e has a spin of $J = 7/2$. This leads to F sublevels from $F = |I - J|$ to $F = I + J$. Therefore, level c has six sublevels (0 to 5), level d and f have four sublevels (1 to 4) and level e has six sublevels (1 to 6). Electrons can desexcite from one level to another following a strict selection rule $\Delta F = 0, -1, +1$. Hence, line B from level f to level d has 10 sublines, line C from level e to c has 15 sublines, and line A from level f to c has 12 sublines. As less peaks can be seen, it means that some peaks are composed of several lines, and using them to determine a temperature would invalidate the results.

3.3.4 Line identification

To ensure that a line is a single line, two methods are possible: do the absorption spectrum at extremely low temperature until the Doppler broadening is smaller than the distance between any pair of lines, or do a Doppler-free saturated absorption spectrum. Doppler-free saturated absorption is achieved by using two lasers to probe the transition. The first laser is the pump, and is used to saturate the transition. The second laser is called the probe. For atoms that are not a zero velocity, their velocity cause a Doppler shift that is not the same for both lasers, preventing any coupling between the pump and probe lasers except at certain cross-over frequencies: the medium is therefore not transparent and the probe laser is absorbed. If the two lasers are placed so that the beam go in opposite directions, the atoms whose velocity is exactly zero are saturated by the pump, hence the medium is transparent for the probe laser. As a result, the absorption line from the pump laser is modified with a transparency zone cause by the atoms of velocity zero, in the middle of the Doppler-broadened absorption line. More information about Doppler-free saturated absorption can be found for example in works by Letokhov [89]. Results from the Doppler-free saturated absorption experiment are shown Figure 3.8, with arrows identifying each sublines.

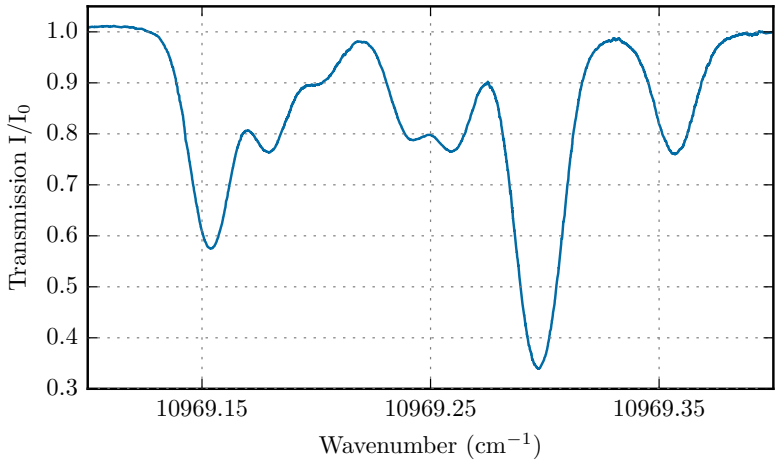

(a) Absorption spectrum, line C.

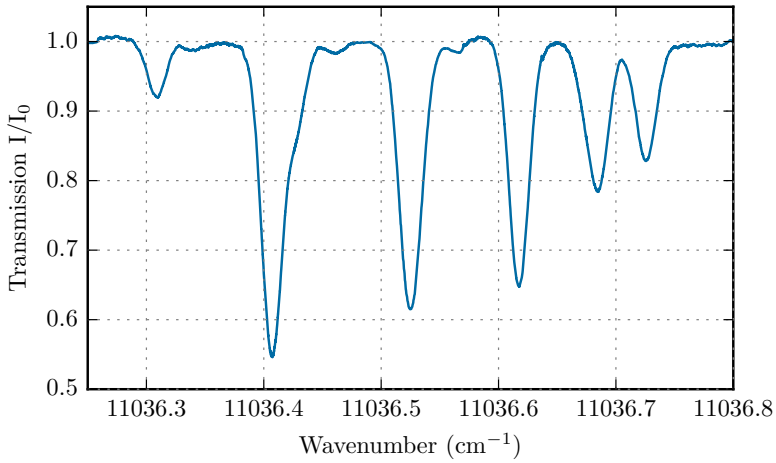

(b) Absorption spectrum, line B. One more line at 11 036.2 cm^{-1} was not captured in this scan but seen in later measurements.

Figure 3.7: Spectra obtained by regular absorption measurements in the cell, at 8 Pa and 25 W, with 2 mW of laser power. The hyperfine structure is clearly visible but some peaks are too close to be distinguished under the Doppler broadening.

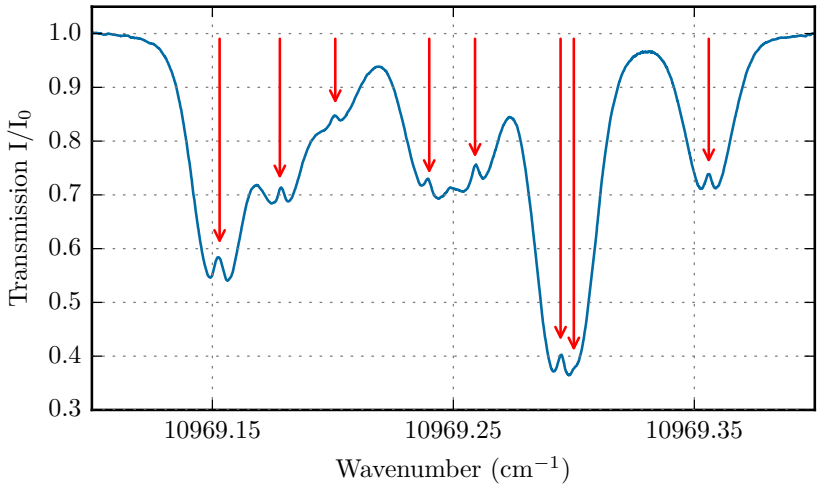

(a) Doppler-free absorption spectrum, line C.

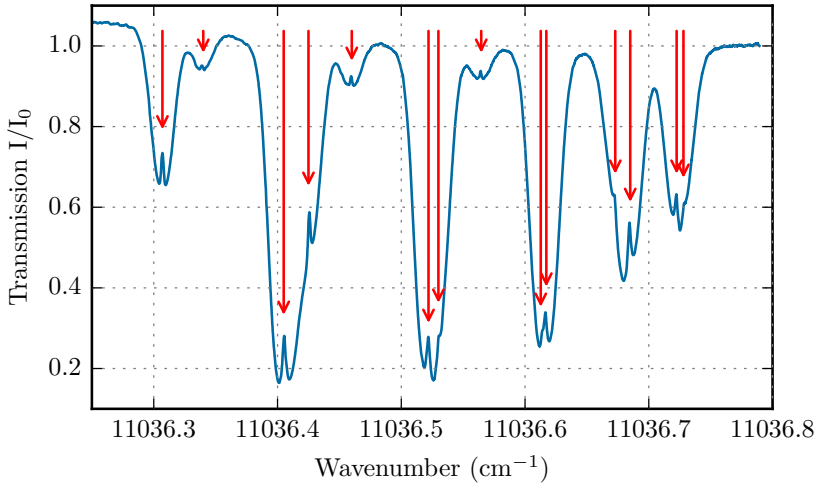

(b) Doppler-free absorption spectrum, line B. One more line was observed at 11 036.2 cm^{-1} but not reported here.

Figure 3.8: Doppler-free saturated absorption spectra obtained by regular absorption measurements in the cell, at 30 Pa and 67 W.

3.3.5 Saturation analysis

Once a single line is identified, one has to check that the transition is not saturated. Figure 3.9a shows the optical depth as a function of the wavenumber for different laser powers. The optical depth decreases with laser power when the power increases too much, showing a saturation effect because of the equalization of the populations.

Reporting the value at maximum as a function of laser power, on Figure 3.9b, we find a good agreement with the saturation formula (3.1) [90], with $d_{\max} = 0.66$ and $P_{\text{sat}} = 3\,\text{mW}$. The saturation power could in the future be coupled to a fine analysis of the laser beam, to extract the spatial intensity of the laser beam in a plane perpendicular to the propagation axis. Knowing the saturation *intensity* of the transition would lead to the transition oscillator strengths, one of the data missing to extract the densities from the present measurements.

$$d(P) = \frac{d_{\max}}{\sqrt{1 + P/P_{\text{sat}}}} \tag{3.1}$$

As the photodiode signal-to-noise ratio greatly decreases when laser power is decreased, and to ensure that the data can be analyzed despite an unstable signal baseline, some saturation is always present in the current data. It is assumed to be negligible if the relative error is below 10 %, which corresponds to a laser power inferior to 0.6 mW here. Practically speaking, the quantitative data about temperatures and densities shown later are taken with a laser power between 95 µW and 125 µW. Some qualitative data such as the broad spectral landscapes or the saturation absorption are taken with larger laser power, as high as 60 mW to increase the photodiode signal-to-noise ratio.

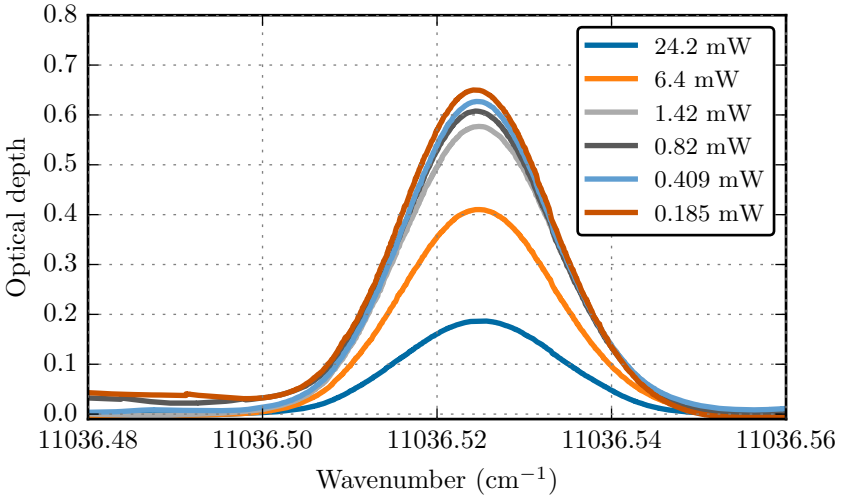

(a) Optical depth profile for different laser powers.

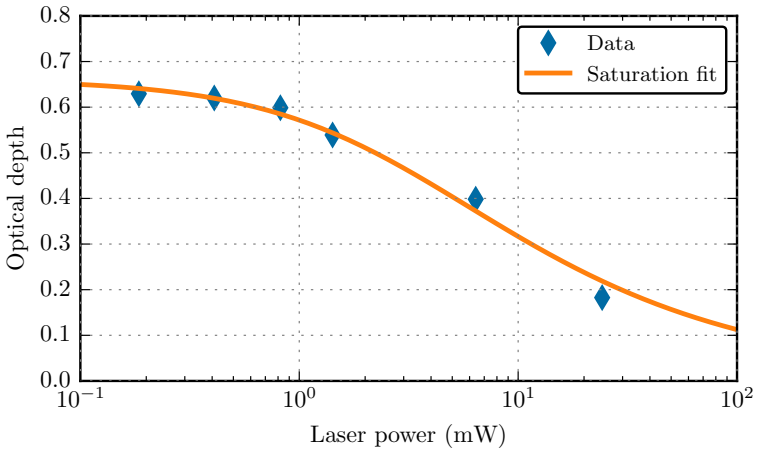

(b) Maximum optical depth for different laser powers.

Figure 3.9: Effect of the laser power on the apparent optical depth: above 0.6 mW, the transition is saturated and the effective optical depth decreases artificially. A lower laser power also leads to a smaller signal-to-noise ratio.

3.3.6 Temperature measurements

If a peak corresponds to a single Doppler-broadened absorption line, then it can be analyzed to give a temperature. The method is explained later, section 3.4.3. Figure 3.10 shows such a fit done on two peaks fitted with the same temperature - 378 K - and showing a excellent agreement.

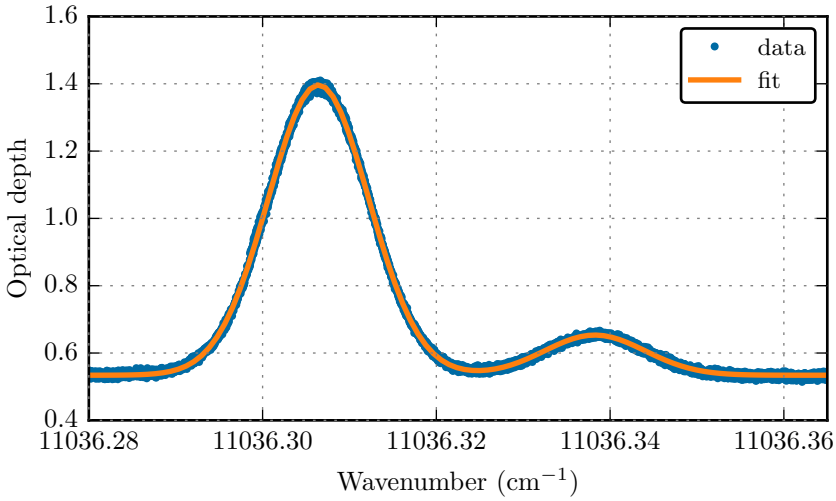

Figure 3.10: Example data treatment on an absorption measurement at 30 W. The individual data are shown with a fit by the sum of a constant baseline and two independent Gaussian curves at 378 K.

Doing such an analysis over a range or discharge power in the cell, one can infer a single temperature for both peaks, or fit each peak with an independent temperature. Figure 3.11 shows the temperature of both peaks on the two lines presented above: the smaller line sometimes give inconsistent results due to a low signal to noise ratio, but overall gives results that are in agreement with the larger line. The largest line shows a temperature slowly increasing from 360 K at 14 W to 380 K at 30 W.

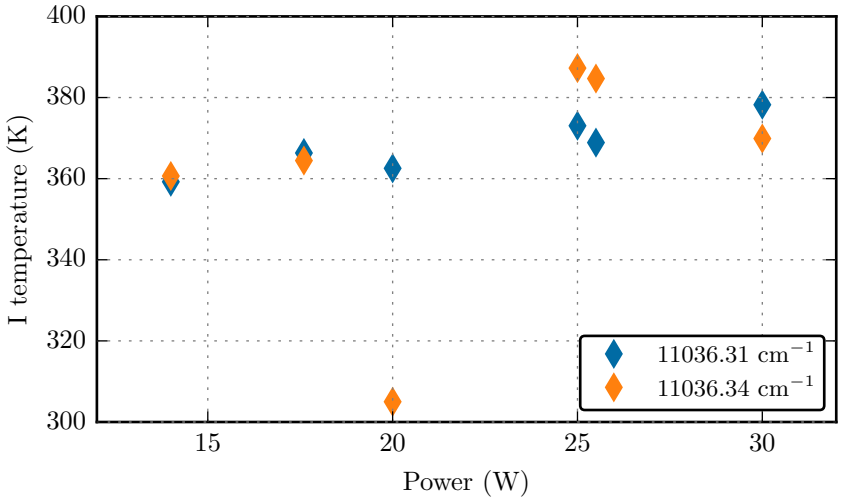

Figure 3.11: Temperature measured on two single lines at 11 036.31 cm^{-1} and 11 036.34 cm^{-1} in an iodine cell with a cold finger maintained at 9 °C. Both lines show a good agreement overall. The signal-to-noise ratio is much better at 11 036.31 cm^{-1} as the absorption is much stronger. The temperature increases slightly with power, but stays close to room temperature in this iodine cell.

3.3.7 Density measurements

An absorption experiment allows to measure the difference in density between the lower state of the transition and the upper state. However, in the current case, the lower states are excited states above 50 000 cm^{-1}, meaning that their population is negligible compared to the ground state. Assuming a Boltzmann distribution, knowing the density in these levels could give an estimate of the ground state population, but the Boltzmann distribution cannot be assumed in such a plasma. But those problems are not the biggest: the absorption oscillator strengths f needed to go from line integral to density are not known for those levels in iodine, hence no density at all can be extracted by studying these three transitions at 10 969 cm^{-1}, 11 036 cm^{-1} and 12 429 cm^{-1}.

3.4 Absorption spectroscopy at $7603\,\mathrm{cm}^{-1}$ in the iodine atom fundamental state

3.4.1 Principle and objectives

The iodine I atom has a transition with the smallest energy from the fundamental state at $7602.970\,\mathrm{cm}^{-1}$, or $1.315\,\mu\mathrm{m}$, as shown Figure 3.5. The splitting between both states that share the same electronic configuration and spectral term is due to a spin-orbit coupling. The transition between this state and the fundamental is in the near infrared and has been studied by Ha et al. [91]. The upper level has a quantum number $J = 1/2$ and the fundamental state has a quantum number $J = 3/2$. Such a inverted fine structure is common when the electronic layer is more than half-full, in any atoms. These levels lead to six possible transitions in the hyperfine structure, shown Figure 3.12a. The resulting lines, reproduced from Ha et al. [91], are shown Figure 3.12b. The notation used is $F_{\text{lower level}} \rightarrow F_{\text{higher level}}$. Analysis of an absorption spectrum in this wavelength will lead to two line-of-sight-integrated values: I temperature from any of the six peaks via Doppler broadening, and I density from the total area of the peaks, or from the area of a single peak, as the line ratios are available in the literature [91, 92]. The transition probed in this section is an electric quadrupolar and dipolar magnetic transition, hence a *forbidden* transition, leading to very low absorption. This is why the data taken in this section, and the next about I_2, are produced at a rather high pressure between 1 Pa and 5 Pa, even though the comparison with the global model is less fruitful at those pressures. Measurement campaigns run at lower pressure using a higher-transparency grid and Cavity-Ring Down Spectroscopy were prepared but prevented by problems in the plasma ignition that were solved later.

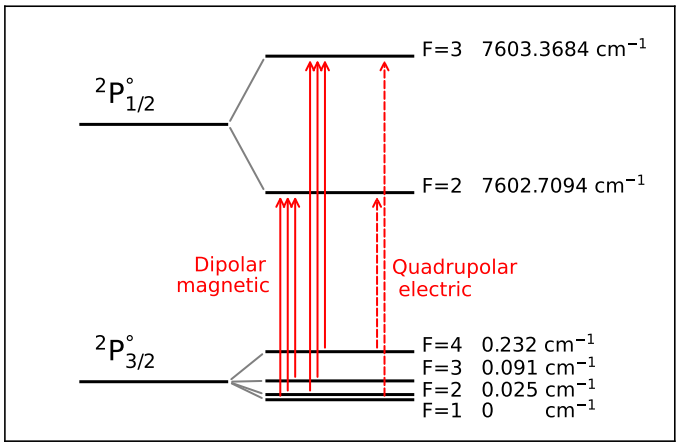

(a) I atom energy levels, focusing on the first transition at 7603 cm^{-1}. The lower state is the fundamental state, the zero energy fixed at $F = 1$.

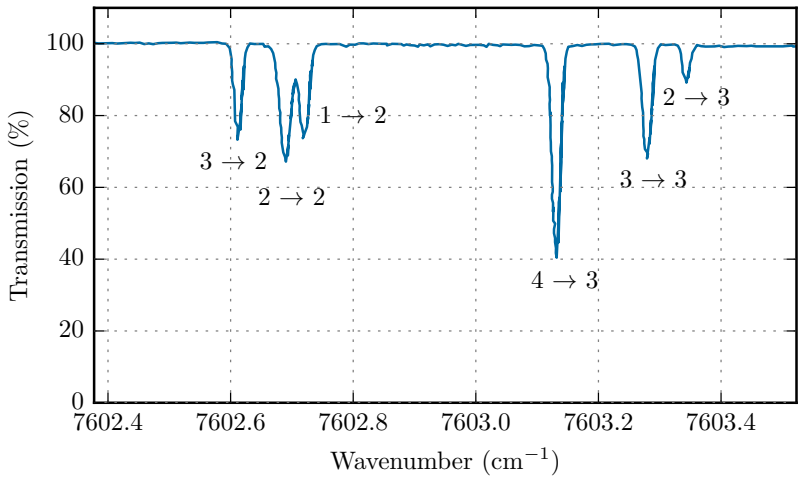

(b) Expected spectral transmission. Six lines from the hyperfine structure compose the dipolar magnetic part of the transition. The quadrupolar electric part is not detected, and was not included in the detailed analysis from Ha et al. [91] either.

Figure 3.12: Data about the studied transition, available in the literature and reproduced from Ha et al. [91], He et al. [92].

3.4.2 Experimental setup

The optical setup is shown Figure 3.14. A dedicated tunable laser diode emitting around 1.3 µm and its control hardware from Toptica is used to produce the light beam, that is directed to pass 7 or 9 times in the plasma and is collected by an InGaAs photodiode placed behing a IR band-pass filter. The diode is modulated in current, leading to a modulation in wavenumber with time. A lambdameter lent by ONERA was used to validate calibration but could not be used during normal operation, hence the range of the spectra is recalibrated using a reference point and a Fabry-Perot interferometer, as described below. Windows inclined at Brewster angle are installed on each side of the PEGASES thruster to cancel reflexion at each pass, as shown Figure 3.13. They are mounted one facing up and one facing down so that the distance between both planes does not depend on the laser height. One optical isolator is used to protect the diode for the counter-propagating light. Acquisition was done on LabView using a NI-DAQ USB system. The method to derive the discharge power from the RF power is described in Appendix B.

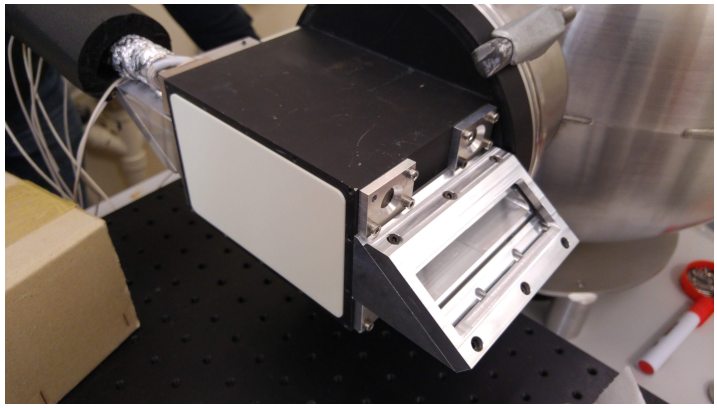

Figure 3.13: Brewster angle windows installed on PEGASES ionization chamber. The water cooling and matchbox have been removed in this picture.

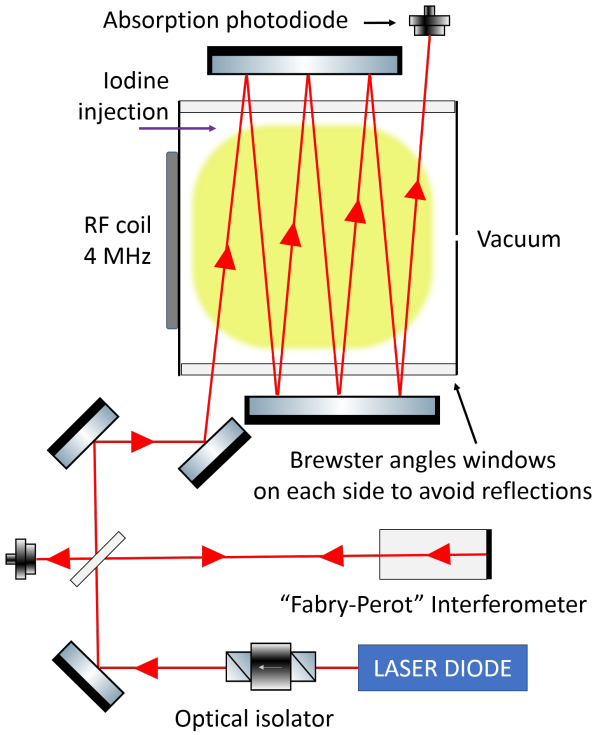

Figure 3.14: Optical setup with the PEGASES ion source. The setup was later modified to make 9 passes through the plasma. Photodiodes are InGaAs diodes placed behind IR filters.

3.4.3 Method

The spectrum is measured as a function of the acquisition time, and is first recalibrated to show absorption against wavenumber. Then, the calibrated spectra of the fine structure of the transition are fitted with six Doppler-broadened Gaussian peaks, leading to line-of-sight values of the I temperature and density of atomic iodine.

Farby-Perot interferometry for wavelength calibration

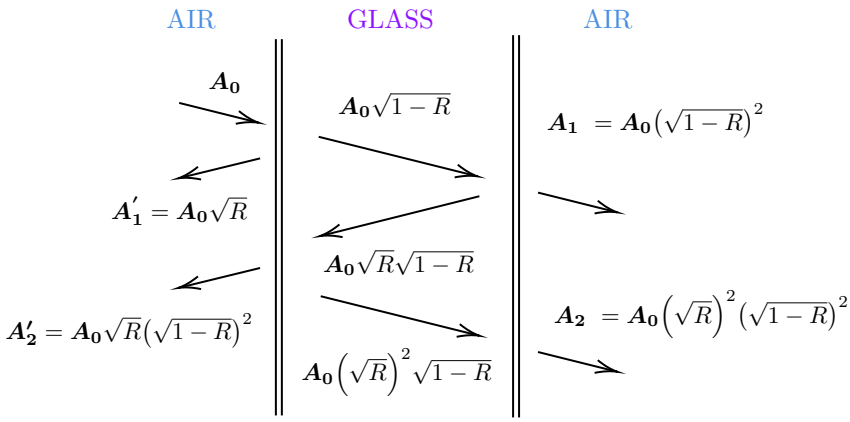

Figure 3.15: Evolution of the modulus $\boldsymbol{A_k}$ of the complex amplitude $A_k = \boldsymbol{A_k}\exp^{-j\phi}$ in the first passes of a Fabry-Perot interferometer

To convert the time-range to a wavenumber-range, a basic Fabry-Perot interferometer is used, consisting of a single piece of glass, of length 10 cm, made of BK7 of refractive index $n = 1.5035$ at 1.3 µm, with perfectly parallel faces. The analysis of the interference pattern generated by the interferometer gives the variation of the wavenumber in the time range. The largest peak on the spectrum is used as a reference point for wavelength, using the value in the literature [70, 91]. The principles to retrieve the wavenumber evolution from the interference pattern of Fabry-Perot interferometer placed in front of a modulated diode are briefly recalled here. We consider a perfect glass cylinder of length L and optical index n, and laser light entering the cylinder parallel to its axis with intensity I_0 and amplitude A_0 such that $I_0 = A_0^2$. We write $A = \boldsymbol{A}\exp^{-j\phi}$. Let's consider first the evolution of the modulus of the light complex amplitude. At each reflection at one of the cylinder's

edges, the intensity is multiplied by R, hence the amplitude is multiplied by $\sqrt{R}$. At each transmission, the intensity is multiplied by $T = 1 - R$, hence the amplitude is multiplied by $\sqrt{1-R}$. Figure 3.15 shows the evolution of this modulus after a few passes in the glass, and the notation that will be used. In reflection and transmission the path length difference for two adjacent rays is $\delta = 2nL\cos\alpha$, where α is the angle of the light from the normal to the surface taken to be 0 in this work. Therefore, the phase difference is $\phi = \frac{2\pi\delta}{\lambda} = 4\pi nL\tilde{\nu}$, with $\tilde{\nu}$ the wavenumber.

In transmission, when the light is collected on the other side compared to the injection, amplitude is written A_k for $k - \frac{1}{2}$ passes both way - i.e. a path length of $(2k-1)L$ in the cylinder - for $k \geq 1$, as shown for example Figure 3.15. We can then write

$$A_{k+1} = RA_k \exp^{-j\phi}$$

As $A_1 = (1-R)A_0$, the amplitude in transmission after $k - \frac{1}{2}$ passes both way in the cylinder, $k \geq 1$, is

$$A_k = \left(R\exp^{-j\phi}\right)^{k-1}(1-R)A_0$$

The total amplitude collected on the spectrometer can be explicitly calculated:

$$A_\infty = \sum_{k=1}^{\infty} A_k = A_0 \frac{1-R}{1-R\exp^{-j\phi}}$$

The intensity received by the spectrometer is then the modulus of the amplitude squared. Recalling that $\phi = 4\pi nL\tilde{\nu}$, we have

$$I = A_\infty A_\infty^* = \frac{I_0}{1 + \frac{4R}{(1-R)^2}\sin^2(4\pi nL\tilde{\nu})}$$

In the data analysis presented here, the inverse of the intensity is used to ease the numerical fits, done on python using the scipy.optimize.curve_fit function and the associated library. I_0 has been shown to be linear with time. The formula used in the data analysis when the glass cylinder is used in transmission is then, with the free parameters for the fit in bold:

$$\frac{1}{I(t)} = \frac{1}{\boldsymbol{\alpha}t + \boldsymbol{\beta}} * \left(1 + \frac{4\boldsymbol{R}}{(1-\boldsymbol{R})^2}\sin^2(4\pi nL\tilde{\boldsymbol{\nu}}(\boldsymbol{t}))\right) \tag{3.2}$$

For practical reasons, the photodiode was sometimes placed on the same side of the glass cylinder than the light input, collecting light for example through a 4% beam splitter. The reflection case is identical to a case in transmission where the initial amplitude would be modified by a coefficient to take into account that the first ray A_1' has experienced one reflection more and two transmission less than A_1. Practically speaking, it means replacing A_0 by $A_0 \frac{\sqrt{R}}{1-R}$. Given that I_0 is here an output of the fit and not an input, the formula (3.2) is still working. Hence, the wavenumber was shown to be well fitted as a quadratic function of time. Hence it is inputed in the fit under the form

$$\tilde{\nu}(t) = \boldsymbol{a}t^2 + \boldsymbol{b}t + \boldsymbol{c}$$

These three free parameters can incorporate any multiplicative prefactor in the sinus. Finally the fit for the Fabry-Perot interference pattern is done with 6 free parameters, with the formula

$$\frac{1}{I(t)} = \frac{1}{\boldsymbol{\alpha}t + \boldsymbol{\beta}} \left(1 + \frac{4\boldsymbol{R}}{(1-\boldsymbol{R})^2} \sin^2\left(\boldsymbol{a}t^2 + \boldsymbol{b}t + \boldsymbol{c}\right) \right)$$

An example analysis is given in the next paragraphs. When three peaks can be seen on the same spectrum, a direct re-calibration using the location of the three peaks from the literature and a quadratic wavenumber was found to give the same results as the Fabry-Perot method. Therefore, if the shape of the evolution of the wavenumber with time can be estimated and enough peaks are measured to constrain the function $\tilde{\nu}(t)$ - here three peaks for a second order polynomial, the experiment can be performed without measuring the Fabry-Perot interference pattern.

Extracting I density and temperature

Once recalibrated, the spectra are fitted with Doppler-broadened Gaussian peaks. As an example, here is described the analysis of one spectrum of the three smaller peaks between 7602.6 cm^{-1} and 7602.75 cm^{-1}. Each data point comes from the acquisition of two spectra, one with plasma and a reference spectrum without plasma, both of them shown Figure 3.16a. The laser diode's wavelength is swept in time by changing the diode current and moving the diode inner reflector with piezo actuators. Therefore, an increase in time along the x-axis corresponds to an increase in intensity and an decrease in wavenumber. The increase in intensity and possible non-linearities are corrected by dividing the data by the reference spectrum, giving transmission, that is plotted against recalibrated wavenumber on Figure 3.16b. The reference spectrum is not taken at the same time as the other spectrum, resulting in a transmission sometimes not being equal to 1. This is not taken into account when first calculating the optical depth, which is calculated using the classical formula (3.3), where n is the average density of absorbing species, σ the cross section and l the path length in the absorbing medium.

$$d(\tilde{\nu}) = -\ln\left(\frac{I}{I_0}\right) = nl\sigma(\tilde{\nu}) \tag{3.3}$$

However, with this transmission not peaking to 1, the optical depth is the sum of the real optical depth corresponding to absorption and an artificial optical depth due to the difference between the spectrum and the reference spectrum in the zones without absorption, shown Figure 3.16a. Indeed, considering that the discrepancy comes from a linear variation of the intensity of the diode between the acquisition of both spectra, we can write for example that the reference spectrum is now αI_0 with α an unknown coefficient characterizing the variation of the intensity of the diode. We have then

$$d = -\ln\left(\frac{I}{\alpha I_0}\right) = -\ln\left(\frac{I}{I_0}\right) + \ln(\alpha) = d_{\text{plasma}} + d_\alpha$$

In fact, more deformation of the signal can happen and the baseline d_α is characterized by a unknown third-order polynomial during the fit process. Let's now characterize the real optical depth d_{plasma}. The optical depth is here described as the sum of three Gaussian peaks. The final fit is then

$$d = d_\alpha(\tilde{\nu}) + \sum_1^3 d_i(\tilde{\nu})$$

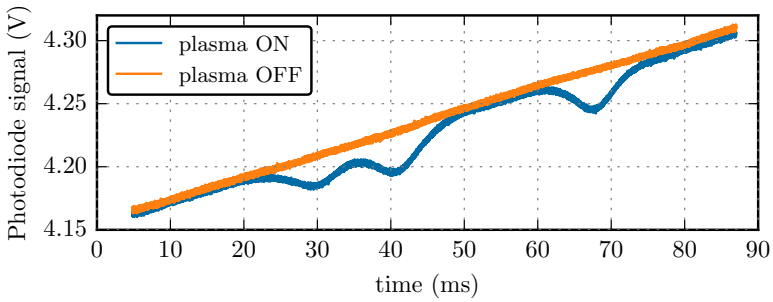

(a) Raw data and reference spectrum

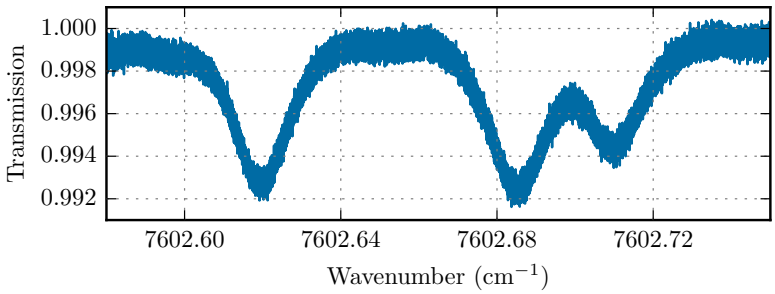

(b) Transmission

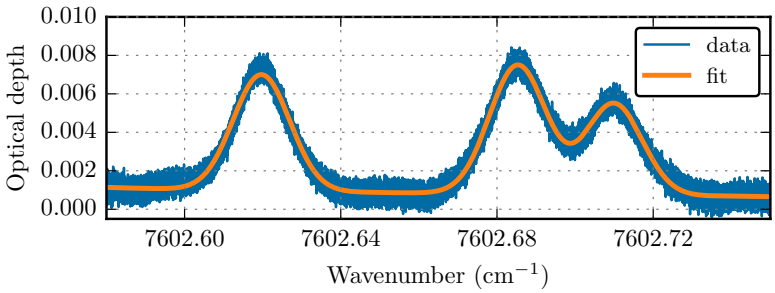

(c) Experimental optical depth and fit with gaussian Doppler broadening. The three peaks are fitted here with the same temperature, 1279 K, much higher in PEGASES than in the iodine cell. Further results include allowing different temperatures for each peak to study possible discrepancies.

Figure 3.16: Data analysis sequence for I absorption at 7603 cm^{-1}

Each peak is written as a Doppler profile:

$$d_i(\tilde{\nu}) = B_i \exp\left(-\frac{(\tilde{\nu} - \tilde{\nu}_{0,i})^2}{\alpha T_i}\right) \tag{3.4}$$

With α kept constant, and defined as

$$\alpha = \frac{2k\omega_0^2[\mathrm{rad\,s^{-1}}]}{mc^2} = \frac{8k\pi^2 10^4 \tilde{\nu}^2[\mathrm{cm^{-1}}]}{m}$$

The resulting fit is shown Figure 3.16c, with the three peaks being forced to the same temperature for illustration purposes. This fit leads to a I temperature for each peak. In units of angular frequency, the total I density can be calculated using any of the peaks, by dividing the peak area $B_i\sqrt{\pi\alpha T}$ by the path length l, the mean angular frequency ω_0, the total cross section G and the relative line strength for the hyperfine transition Q_i [91, 93].

$$n_i = \frac{B_i\sqrt{\pi\alpha T_i}}{GQ_i l\omega_0} = \frac{B_i}{GQ_i l}\sqrt{\frac{2k\pi T_i}{mc^2}} \tag{3.5}$$

The value of G given by Ha et al. [91] is $G = 1050 \pm 250\,\mathrm{fm}^2$. As [I] is inversely proportional to G, it means that the uncertainty directly propagates and that there is a minimum systematic uncertainty on n_i of 48 % due to the cross section only.

3.4.4 Effects of plasma inhomogeneity

The plasma is not homogeneous, but the measurements are integrated along the line of sight. Simple 1D models can be done to estimate the spatial evolutions along the line-of-sight. It is supposed that no I atoms are present in the window regions, so the absorption length taken is the inner length of PEGASES, not accounting for the windows. For I atoms, a simple model considers a cosine repartition of the density of I, with [I] maximum at the center and zero at the walls, valid for example if the wall recombination is very important. The window space of 4 cm each side is supposed empty from I atoms. Such profiles are shown Figure 3.17. As for the temperature, in a simple case, the heat equation leads to a quadratic evolution in space, assumed symmetrical along the x-axis and maximum at the centre. Therefore, with x going from $-l/2$ to $l/2$, T_w the wall temperature and T_0 the central temperature, and $[\mathrm{I}]_0$ the density at the center, the formulas are:

$$[\mathrm{I}](x) = [\mathrm{I}]_0 \cos\left(\frac{\pi x}{l}\right) \tag{3.6}$$
$$T_I(x) = (T_w - T_0)\left(\frac{2x}{l}\right)^2 + T_0$$

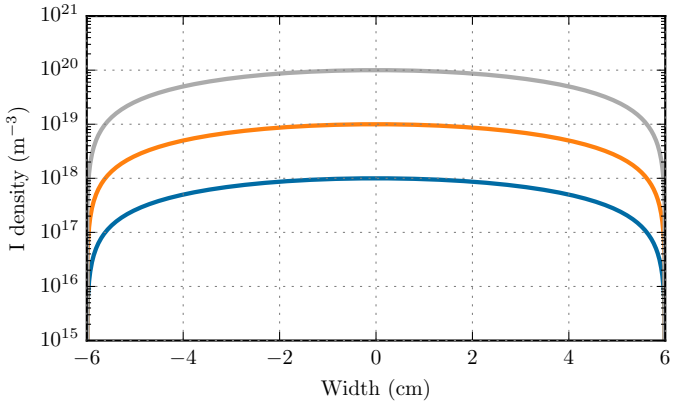

Figure 3.17: Cosine distribution of the I density along the line of sight. Windows are located at −6 cm and 6 cm. The window space of 4 cm each side is supposed empty from I atoms.

Those profiles do not necessarily lead to an isobar situation, except if the I_2 density and temperature profiles are defined so that $[\mathrm{I}]kT_I + [\mathrm{I}_2]kT_{\mathrm{I}_2}$ is constant. These profiles are case study for first analysis. The densities measured are the average density along the light of sight. This value can be used to constrain the previously-mentioned spatial distribution of I density along the axis probe. Having assumed a cosine repartition of the density of I on Equation (3.6), it means that the measured density is $(2/\pi)[\mathrm{I}]_0$, with $[\mathrm{I}]_0$ the density at the center.

The atomic I temperature measured is expected to be close to the central temperature, as more I atomic particles are expected in the center. A simulation of Doppler-broadening along the line of sight in the case of non-homogeneous temperatures and densities is proposed in this work. Using explanations from Kunze [93], we can generalize Equation (3.3) to any kind of temperature and density profile. We define $I(x, \omega)$ the spectral radiance at a position x along the line of sight and angular frequency ω, $I(\omega) = I(x = l/2, \omega)$ the final radiance $I_0(\omega) = I(x = -l/2, \omega)$ the initial radiance, and $\kappa(x, \omega)$ the absorption coefficient. Therefore we can write the law of absorption:

$$\mathrm{d}I(x, \omega) = -\kappa(x, \omega) I(x, \omega)\, \mathrm{d}x$$

κ can be written as its maximum value multiplied by a line shape function that depends on the local temperature. The maximum value is the product of local density and local cross section, g being the line shape of integral 1:

$$\kappa(x, \omega) = [\mathrm{I}](x)\ \sigma_0\ g(\omega, T(x))$$

Then we can extend Equation (3.3) to

$$\int_{-l/2}^{l/2} \frac{-\,\mathrm{d}I(x, \omega)}{I(x, \omega)} = -\ln\left(\frac{I(\omega)}{I_0(\omega)}\right) = \sigma_0 \int_{-l/2}^{l/2} [\mathrm{I}](x) g(\omega, T(x))\, \mathrm{d}x$$

If T is constant, the right hand sight becomes $[\mathrm{I}]_{avg} l \sigma_0$ and gives Equation (3.3) again, with $[\mathrm{I}]_{avg}$ the average density along the x axis and l the plasma length. We assume that the broadening is locally Gaussian, so we can use the following relation [94]:

$$g(\omega, T) = \frac{1}{\omega_0} \sqrt{\frac{mc^2}{2\pi kT}} \exp\left(-\frac{mc^2}{2kT}\left(\frac{\omega - \omega_0}{\omega_0}\right)^2\right)$$

Integrated over the line-of-sight, the final line shape is:

$$-\ln\left(\frac{I(\omega)}{I_0(\omega)}\right) = \sigma_0 \frac{1}{\omega_0}\sqrt{\frac{mc^2}{2\pi k}} \int_{-l/2}^{l/2} \frac{[\mathrm{I}](x)}{\sqrt{T(x)}} \exp\left(-\frac{mc^2}{2kT(x)}\left(\frac{\omega-\omega_0}{\omega_0}\right)^2\right) \mathrm{d}x$$

This formula works for any temperature and density profile. Either this complete formula can be used for the analysis, or it can be seen, Figure 3.18, that in the present case the final line shape is very close to a Gaussian, and then perform a classical fit using Equation (3.4).

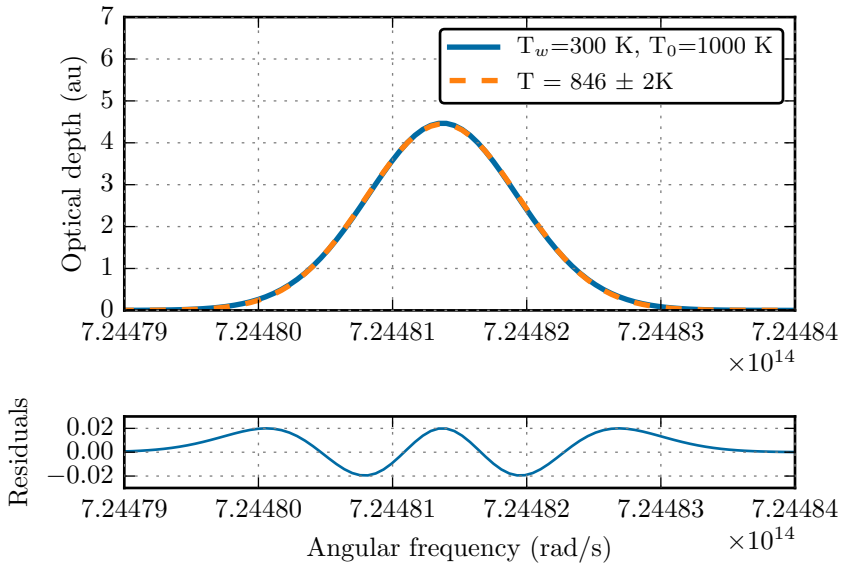

Figure 3.18: Simulated profile (in blue) obtained with a cosine distribution of [I] and a fixed quadratic distribution of T_I between $T_w = 300\,\mathrm{K}$ and $T_0 = 1000\,\mathrm{K}$. The Gaussian fit (in orange) gives a good agreement and leads to a temperature of $846 \pm 2\,\mathrm{K}$.

With the latter method, the measured temperature is, as expected, close to the central temperature but not exactly. Running the simulations for different wall and centre temperatures, a relation can be found - Figure 3.19 - and an analytical formula derived. In the present study, the central temperature at the plasma center can then be fitted with respect to both the measured temperature and the wall temperature by:

$$T_0(K) = 1.3T_{\text{measured}} - 0.23T_{\text{walls}} - 30 \tag{3.7}$$

With walls at 300 K, $T_0 = 1.3T_{\text{measured}} - 99$. The temperatures shown in the following parts of this chapter are either the *measured* temperatures, or the centre temperature estimated with walls at 300 K.

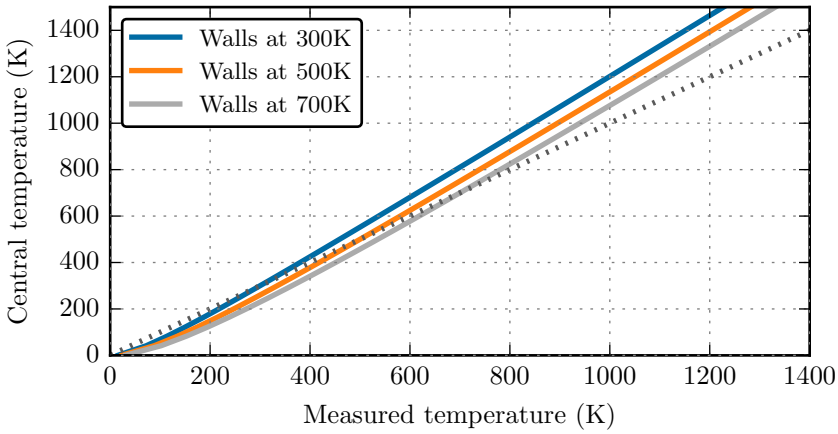

Figure 3.19: Temperature at the core of the plasma depending on the line-of-sight temperature measured and the wall temperature. The dotted line is the reference line where the central temperature would be equal to the measured temperature, which happens only if wall, measured and center temperatures are equal.

3.4.5 Results: complete spectrum

Figure 3.20 shows the six measured peaks from the hyperfine structure, after recalibration of the spectra with the method described above, on a single functioning point of the thruster (fixed discharge power around 180 W and fixed mass flow rate of 7.5 sccm here, giving a pressure around 4.5 Pa). Those six lines are acquired in two sets of three, and each set is fitted with a sum of a baseline and three independent Gaussian peaks, as explained in the previous paragraphs.

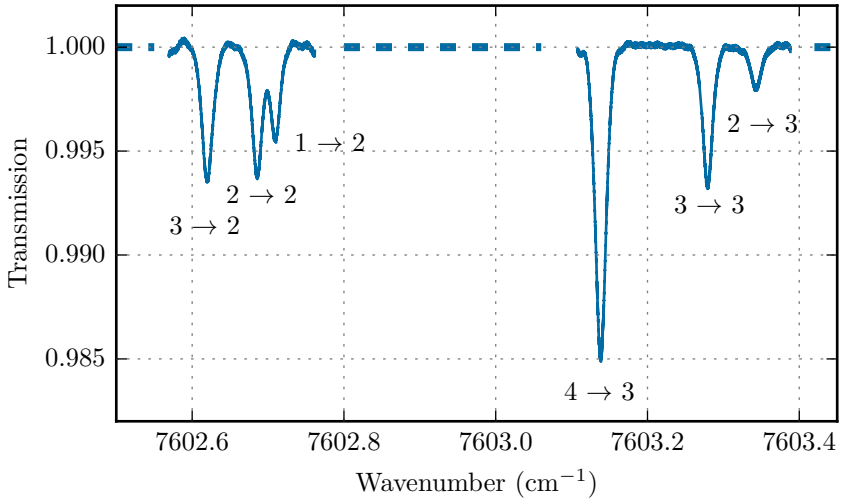

Figure 3.20: Actual transmission landscape measured in this work, showing the complete hyperfine structure of the probed transition, with line ratios not matching the literature.

A temperature and density is extracted for each peak. The temperatures are shown Figure 3.21 and densities Figure 3.22. The line ratios are not in agreement with those from Ha et al. [91], He et al. [92] shown Figure 3.12b. For example, lines $3 \rightarrow 2$ and $2 \rightarrow 2$ present the same depth in this work. Such a discrepancy does not come from a change in state distribution from temperature effects, as the energies between hyperfine levels of the lower state are much lower than the plasma temperature. The discrepancy could come from optical pumping between Zeeman levels, but is not really understood at this point. A solution is still presented to derive I density from this data.

Temperatures Several lessons can be extracted from the temperature analysis shown Figure 3.21. First, the peak $2 \rightarrow 3$ gives temperatures not consistent with the other peaks and not reliable. It is the smallest peak and very sensitive to measurement noise. It will not be considered in the analysis. The other five peaks show a good agreement, within a range of a few hundreds of Kelvin. The average temperature is constant with the discharge power, around 1200 K. This is much higher that was measured in the iodine cell, but temperatures above 1000 K can be explained with a small model such as the one developed by Chabert et al. [38]. The constant temperature was unexpected and would mean that the plasma-related heat is very well evacuated through the water-cooling system. Results varying pressure and discharge power are presented later.

Densities The surface area of the fitting gaussian gives the I density in each peak. It is proportional to the product of the peak height by the square root of the temperature, as detailed Equation (3.5). The average densities along the line-of-sight are plotted Figure 3.22. Once again, the noise on $2 \rightarrow 3$ discards the use of this small peak for the analyses. The density of the five other peaks varying a lot and this variation cannot be attributed to a noise. As the temperatures do match, the discrepancies comes either from the peak weight distribution not matching the literature, and possibly, to a lower extent, from a variation of plasma parameters between the two different experimental sessions measuring the first three and the last three peaks. The distance between the peaks is much smaller than gas or plasma temperature, so that the level distribution is independent from temperature above a few Kelvin, and once again there is no reason to expect a distribution different than the one presented by Ha et al. [91], He et al. [92].

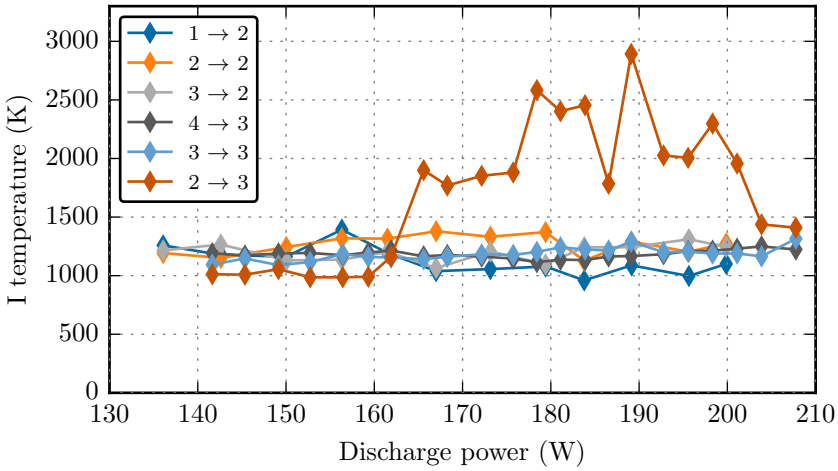

(a) Temperature obtained from independent Doppler-broadened Gaussian fits to the six peaks, at 7.5 sccm

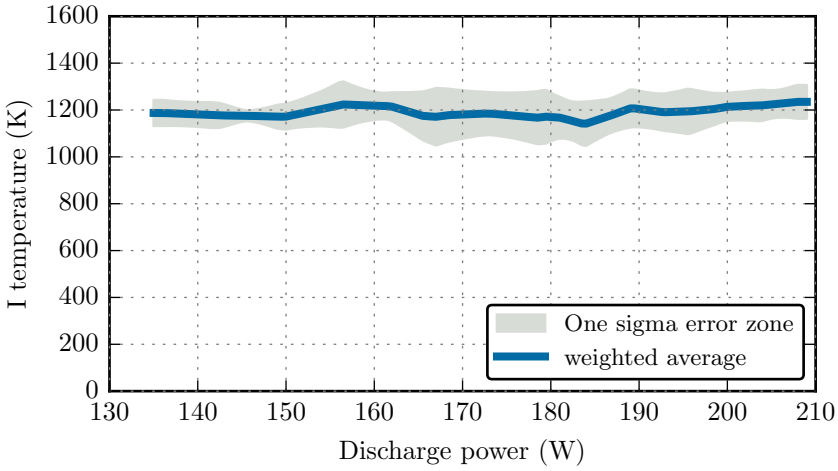

(b) Average temperature on the five first peaks, at 7.5 sccm

Figure 3.21: Measurement of the atomic temperature of I through absorption at 7603 cm^{-1}. One peak does not show coherent results. The I temperature is constant with discharge power.

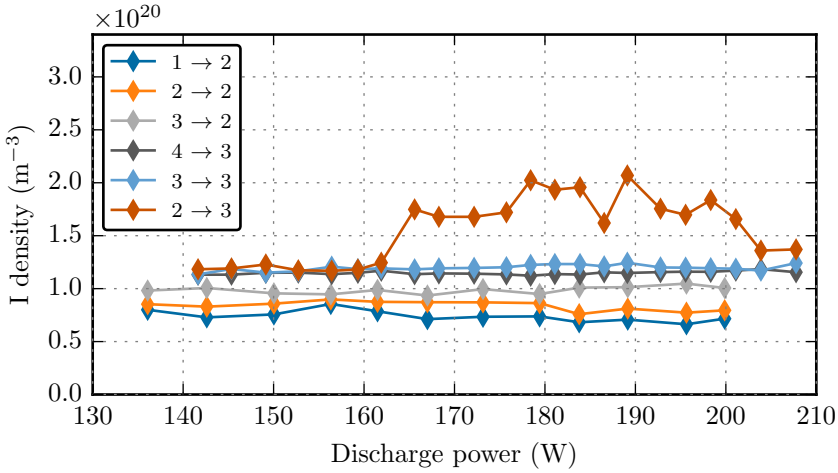

Figure 3.22: Line-of-sight integrated I density obtained from independent Doppler-broadened Gaussian fits to the six peaks, at 7.5 sccm.

3.4.6 Results varying mass flow rate

In the next plots, the temperatures and densities plotted are the average of the densities given by the lines $3 \rightarrow 3$ and $4 \rightarrow 3$. This choice has been made for several reasons: both lines are intense, they give matching results in the preliminary analysis, they can be taken simultaneously in a single measurement. Unless stated otherwise, the values are the measured values, not corrected using a 1D model. The displayed error bars are the discrepancy between those two lines, the systematic error bar due to the uncertainty on the cross section is not shown. The run are done at constant mass flow rate, leading to a nearly constant pressure for each run, shown Figure 3.23.

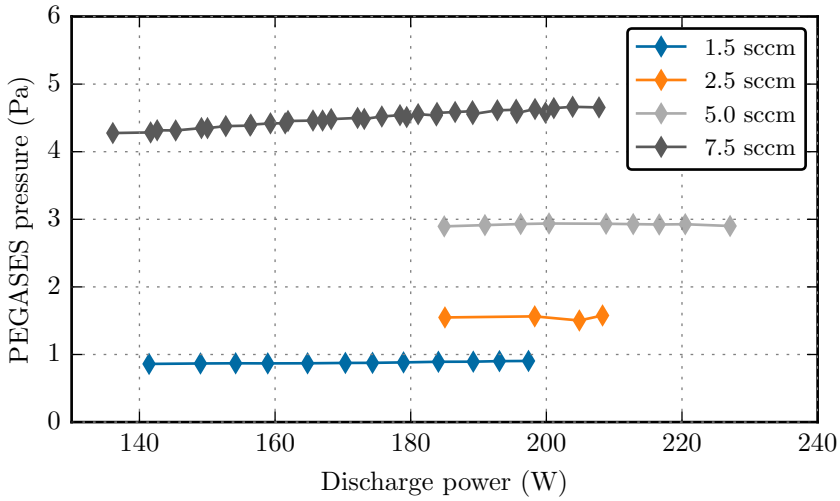

Figure 3.23: Total pressure as a function of mass flow and RF power measured with a capacitance manometer in PEGASES during the absorption measurements. The pressure stays nearly constant for a given mass flow rate, any increase being due to gas heating or increased dissociation.

Temperature Figure 3.24a shows the temperatures for four different values of the mass flow rate of iodine. The temperature is nearly constant with discharge power and increases with mass flow rate. As it is constant with power, we can plot the measured temperature T_{mes} against pressure, shown Figure 3.24b. A linear fit relation is found between temperature and pressure, written equation (3.8). The central temperature calculated with equation (3.7) and $T_{\text{walls}} = 300\,\text{K}$ would be $T_c = 1.3T_{\text{mes}} - 99 = 90\ p(\text{Pa}) + 1045$.

$$T_{\text{mes}}(\text{K}) = 88\ p(\text{Pa}) + 796 \tag{3.8}$$

Density Figure 3.25a shows the densities for the same four functioning points and, as expected, the densities increase with mass flow rate. It also shows that the densities are nearly constant with discharge power, indicating that the plasma has reached a stable value where the dissociation of I_2 is balanced by other recombination phenomena. Like for the temperature, we can plot the mean I density against pressure and the centre density derived from these measurements coupled to the small 1D model, shown Figure 3.25b.

Estimation of dissociation An estimate of the species distribution in PEGASES can be drawn using the pressure measurements made in the chamber during the absorption experiment. Two parameters can be discussed. First, the ratio of the atomic I partial pressure to the total pressure, and second the dissociation degree α, defined as:

$$\alpha = \frac{[\text{I}]}{[\text{I}] + [\text{I}_2]}$$

The dissociation degree is equal to the pressure ratio if all gases are considered ideal and $T_I = T_{I_2}$. This is assumed here as no data is available for I_2. To get the atomic I partial pressure, I is considered to be a perfect gas so that $p_I = [\text{I}]kT_I$, with [I] and T_I measured in the current experiment. Figure 3.26 shows this I partial pressure divided by the total pressure as a function of the pressure. The external (total) pressure is measured by a BARATRON capacitance manometer. Data shows that if the average densities and temperature are considered, the I partial pressures accounts for around 40 % of the total pressure and that the dissociation increases with pressure. Using the values from the center, this ratio is 60 % at 1 Pa and increases to 80 % at 4.5 Pa.

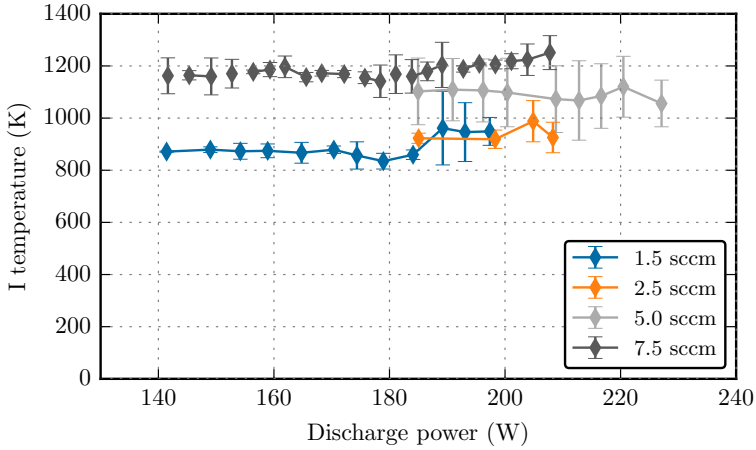

(a) Atomic iodine temperature as measured by absorption for different discharge power and input mass flow rate.

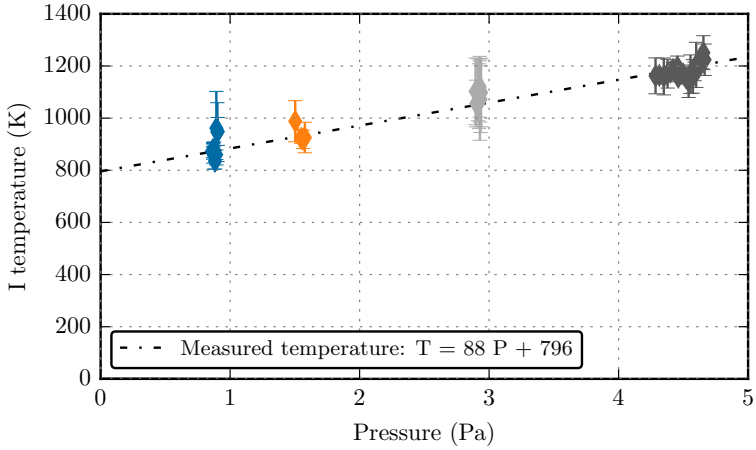

(b) Atomic I temperature measured by absorption as a function of the pressure measured by a capacitance manometer on PEGASES for each data set. The correspond central temperature using a 1D model is $T_c = 1.3\ T_{mes} - 99$.

Figure 3.24: I temperatures from laser absorption at $7603\,cm^{-1}$.

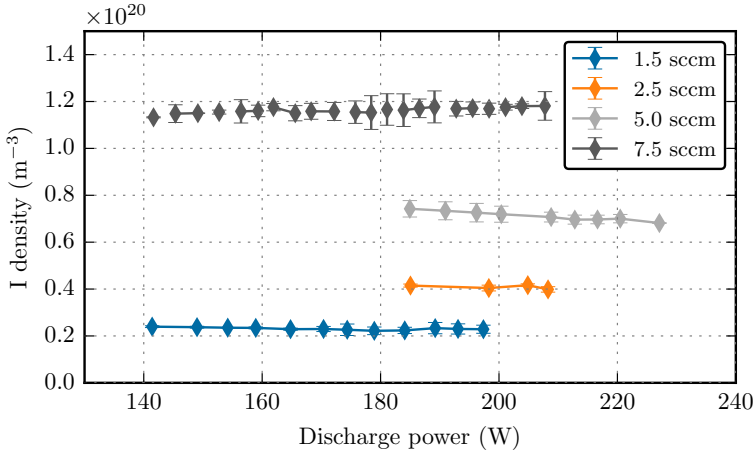

(a) I atomic density as a function of discharge power for four different input mass flow rate. The I atomic density is constant with discharge power.

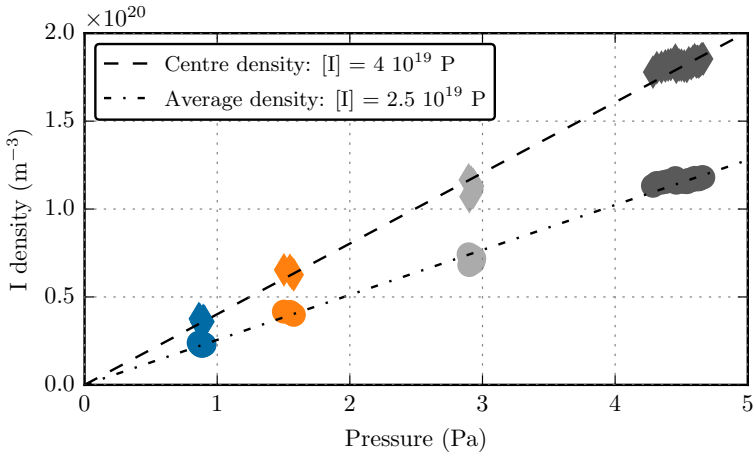

(b) Mean I atomic density measured by absorption as a function of the mean pressure measured by a capacitance manometer on PEGASES for each data set, and central I density calculated from this measured density using a 1D model.

Figure 3.25: I densities from laser absorption at 7603 cm^{-1}.

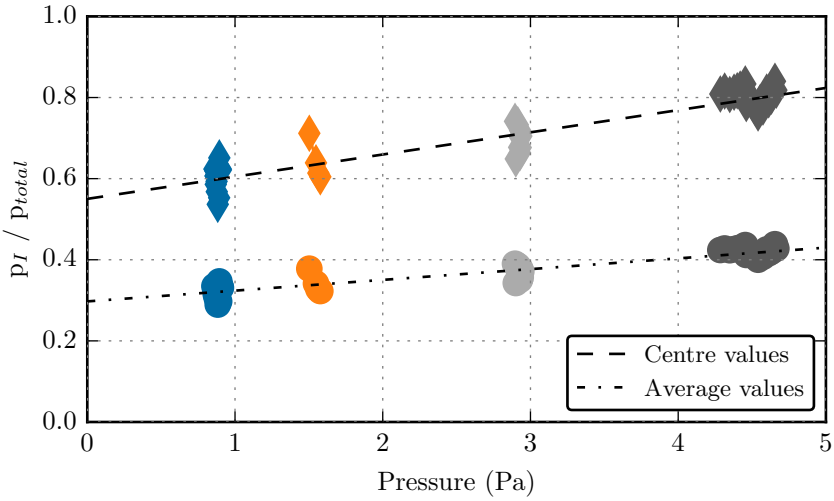

Figure 3.26: Ratio between the atomic iodine partial pressure obtained with I density and temperature and the total pressure measured during the experiment, as a function of the pressure. On average, I accounts for 40 % of pressure. In the center, this ratio goes up to 60 % at 1 Pa to 80 % at 4.5 Pa.

3.5 Broad-band absorption spectroscopy in the 450 nm to 505 nm range in the iodine molecule $X \rightarrow C$ continuum

3.5.1 Principle and objectives

The large molecular emission bands seen on the emission spectra Figure 3.2 correspond to large absorption bands. Location of these bands can be deduced from energy diagrams such as the one presented Figure 3.27 or Figure 3.28. Molecular absorption bands allow to perform broadband spectroscopy, an absorption method that uses a large wavelength range. Marinov et al. [86] use this method on a Cl_2 plasma with a high-resolution spectrometer, measuring plasma parameters as precise as repartition of vibrational levels. The present experiment was realized with a - relatively - low cost low resolution spectrometer and a broadband halogen lamp, and measures the density of I_2. This allows to average the measurements on a spectral range, to minimize parasitic effects brought by specific lines hidden in the continuum used. With an optimized signal-to-noise ratio at lower wavelength, information on [I−] could be obtained below 405 nm, the electronic affinity of I^- [71].

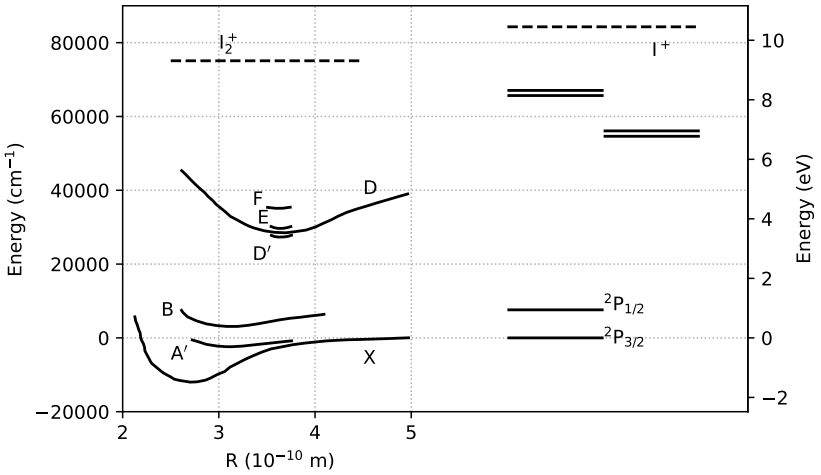

Figure 3.27: Energy diagrams of I and I_2, data from Barnes and Kushner [95]. The zero is fixed at the fundamental state of I.

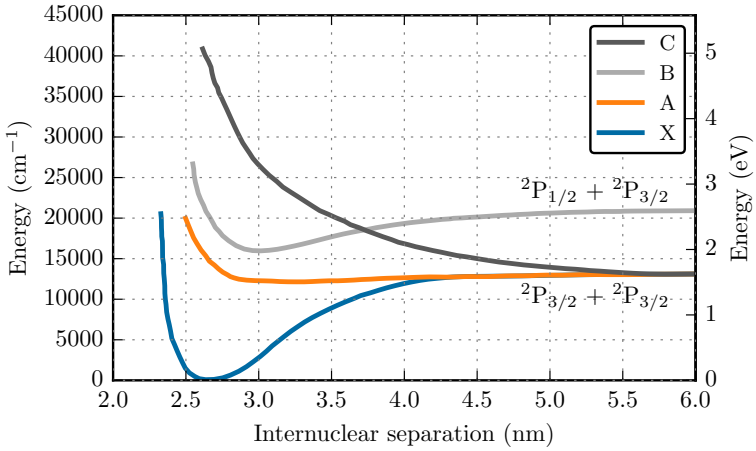

Figure 3.28: Energy diagram of I_2, data from Mathieson and Rees [72]. The zero is fixed at the fundamental state of I_2.

I_2 molecular cross sections

A matter of importance for atmospheric physics, the latest measurements of the absorption cross-sections of the I_2 molecule in the 400 nm to 800 nm have been reviewed by Burkholder et al. [96] as part of JPL-Caltech committee about standards for atmospheric cross sections. The recommended data are those computed by Saiz-Lopez et al. [97] averaged over a 5 nm window. This average brings those data in 15 % agreement with Tellinghuisen [98]. In this work, the raw data from Saiz-Lopez et al. [97] are used, and presented Figure 3.29. Figure 3.29a shows two main absorption bands, under 300 nm (level $D' \rightarrow A'$) and from 450 nm to 700 nm (level $B \rightarrow X$). The structure of the second band is detailed Figure 3.29b: an absorption continuum leading to a dissociative state is present until 500 nm and a second part presents a strong rovibrational structure until 650 nm [98]. This spectrum of the second band does depend on the ambient pressure at which the measurements are made which has been widely studied and debated in the community until recently [99]. The continuum from 400 nm to 500 nm, corresponding to molecules going to the B state with a high enough energy to lead to dissociation, does not present such variety and is valid at any pressure (see for example analysis at 500 nm by Spietz et al. [99]).

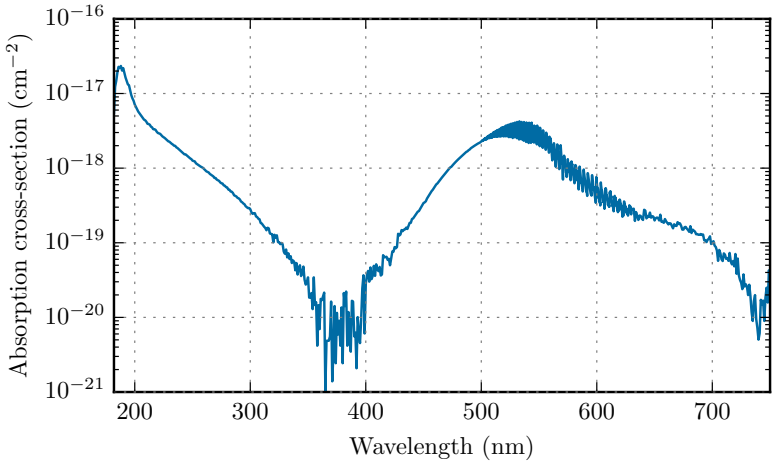

(a) Complete I_2 cross-section set including two strong peaks at 190 nm and 530 nm, from Saiz-Lopez et al. [97]. A rovibrational structure is present between 500 nm and 620 nm.

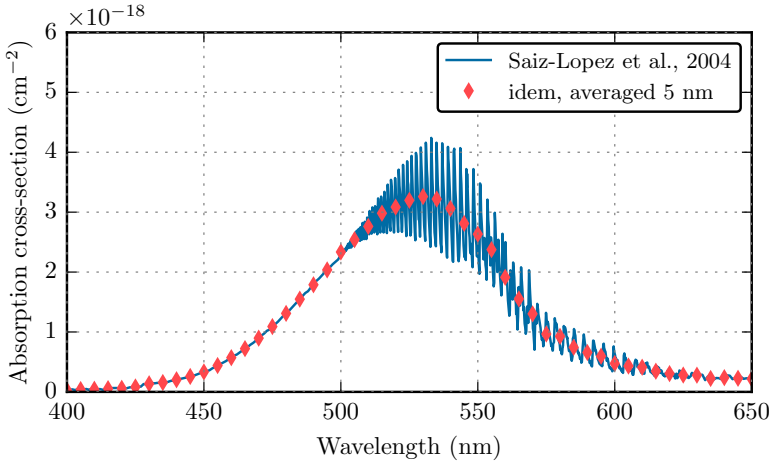

(b) Absorption cross-section around 530 nm and the 5 nm average recommended by NASA [96].

Figure 3.29: Absorption cross-section as a function of wavelength for the iodine I_2 molecule, from Saiz-Lopez et al. [97].

Vibrational distribution function

Absorption cross sections are different for every vibrational levels of I_2. The data from Saiz-Lopez et al. [97] does not discriminate between vibrational levels and are taken at a gas temperature around 300 K. Marinov et al. [86] mention in their broadband absorption experience on Cl_2 that the apparent vibrational temperature, the one controlling the vibrational distribution, remains low even though the core temperature is much higher. Figure 3.30 shows the vibrational distribution in the first six levels of I_2. A higher vibrational temperature flattens the distribution but the general distribution in not much modified by a change in the order of 100 K. Moreover, the continuum part of the absorption spectrum used in this section is way less sensible to the repartition in the lower states that the parts with transitions between discrete levels. Therefore, it is assumed that the vibrational distribution stays close to the one at 300 K and we use the cross sections from Saiz-Lopez et al. [97].

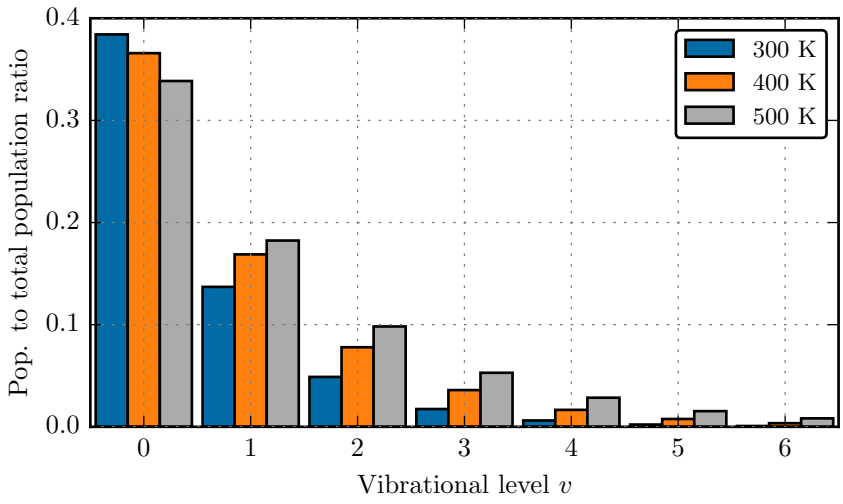

Figure 3.30: Repartition of the I_2 population in the first six vibrational levels depending on the temperature, assuming a Boltzmann distribution.

Dependency with pressure

A debate in the I_2 atmospheric community, mentioned for example by Saiz-Lopez et al. [97], leads to an ongoing uncertainty of the conditions of applications of the cross-sections shown Figure 3.29. In particular, the dependency of those cross-sections with external pressure is mentionned, and the behavior observed in this work (and later shown Figure 3.40) is very well described by Spietz et al. [99]: after the continuum, from 500 nm, the absorption cross-sections are strongly dependent on the external pressure, hence the presence of foreign gases. This is true even for the gas alone, without plasma. Spietz et al. [99] also confirm that the behavior of the continuum does not depend on the ambient pressure, assessing the validity of the method discussed here, at least in a case without plasma. The continuum is the region of the $X \rightarrow B$ transition under 500 nm, where the excess energy leads to dissociation. See Figure 3.28. The behavior of the continuum with pressure in a case with plasma is coherent as well. Above 500 nm, different behaviors are observed with or without plasma and discussed section 3.5.6.

3.5.2 Experimental setup

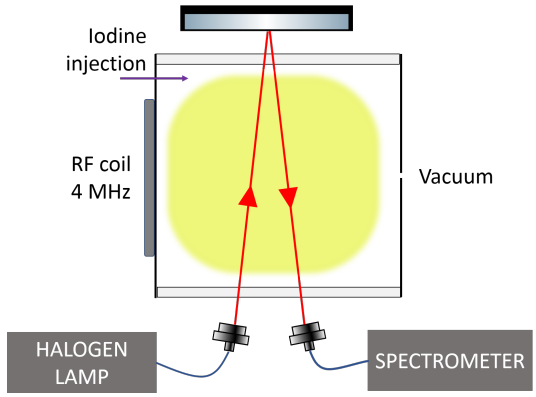

Figure 3.31: Optical setup for the broadband I_2 absorption experiment.

The experiment is installed on PEGASES. The plasma setup is the same that was presented Figure 3.14, with the windows at Brewster angle shown Figure 3.13. The use of Brewster angle windows is not necessary as only two passes are done in each window, but windows in closer contact to the plasma showed a very fast degradation (with an evolution visible across a few minutes) preventing measurements. The optical setup in shown Figure 3.31. Light from the tungsten-halogen bulb in the DH-2000 UV-VIS-NIR lamp from Mikropack-OceanOptics is injected in the plasma through an optical fiber. After reflection on a flat mirror on the other side of PEGASES, the light is collected through a collector and a optical fiber by a FLAME-S-UV-VIS-ES spectrometer from OceanOptics. The spectrometer has a range from 200 nm to 850 nm and a resolution around 1 nm. A typical output of the lamp as given by the spectrometer, integrated over 1 ms and averaged over 500 integrations is shown in blue on Figure 3.32. The dark signal from the diode was removed.

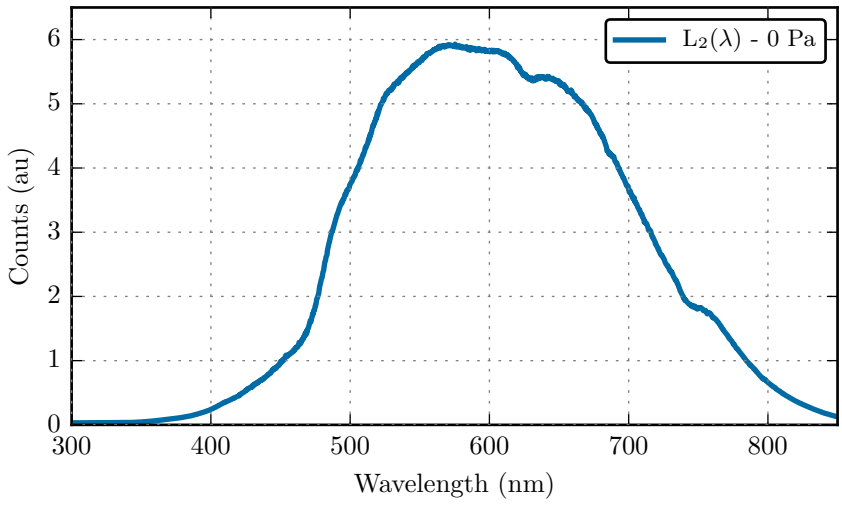

Figure 3.32: Reference lamp spectrum through the setup as seen by the detector, with an empty reactor.

3.5.3 Method

The data is taken in five different configurations of the reactor, the plasma and the lamp, listed here:

- $L_1(\lambda)$: plasma ON, lamp ON
- $L_1'(\lambda)$: plasma OFF, lamp ON, full chamber
- $L_2(\lambda)$, reference spectrum: plasma OFF, lamp ON, empty chamber
- $L_3(\lambda)$, plasma emission: plasma ON, lamp OFF
- $L_4(\lambda)$, detector's dark: plasma OFF, lamp OFF

If the plasma is OFF, the spectra can be used to measure I_2 density by dividing the light intensity after a pass in the chamber L_1' by the reference intensity taken with an empty chamber L_2. Each of these data must be corrected by subtracted the *dark*, or background signal of the photodiode L_4.

$$\frac{I}{I_0}(\lambda) = \frac{L_1'(\lambda) - L_4(\lambda)}{L_2(\lambda) - L_4(\lambda)} \qquad \textit{without plasma} \tag{3.9}$$

When a plasma is ON, the plasma emission L_3 must be subtracted from the main signal L_1. The detector's dark in then removed in the process. This signal is then divided by the corrected reference $L_2 - L_4$.

$$\frac{I}{I_0}(\lambda) = \frac{L_1(\lambda) - L_3(\lambda)}{L_2(\lambda) - L_4(\lambda)} \qquad \textit{with plasma} \tag{3.10}$$

Assuming that most of the probed medium, whether gas or plasma, is in the lower level of the fundamental state, we can use the Beer-Lambert law again, previously discussed Equation (3.3), to get the I_2 density averaged along the line of sight. A 1D model is discussed section 3.5.7.

$$-\ln\left(\frac{I}{I_0}(\lambda)\right) = [\mathrm{I_2}] L_{\mathrm{abs}} \sigma_{\mathrm{I_2}}(\lambda)$$

L_{abs} is the effective absorption length in PEGASES. Adding the length of the chamber and the Brewster angle window leads to a distance of 20 cm. With two passes in the plasma, it means that $L_{\mathrm{abs}} = 40\,\mathrm{cm}$. The final density value is the average over the upper part of the continuum, between 480 nm and 500 nm, where the signal-to-noise ratio is best. It is illustrated on an example section 3.5.4.

3.5.4 Validation without plasma

Without plasma, I_2 absorption is measured for a certain flow of gaseous I_2. Figure 3.33 shows the typical signals L_1' and L_2 at very high pressure, as well as the lamp dark L_4, magnified 10 times. A large absorption is visible between 500 nm and 600 nm.

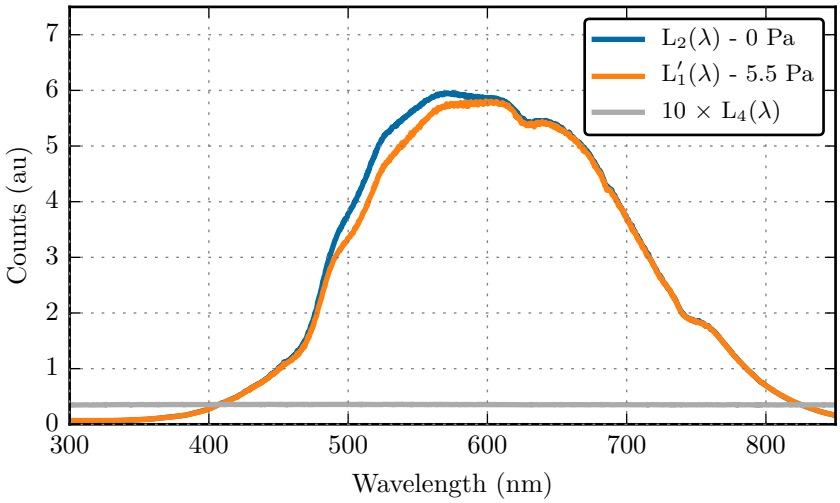

Figure 3.33: Lamp spectrum through the setup as seen by the detector, with an empty reactor and with a filled reactor at 5.5 Pa, without plasma.

Using formula (3.9), the optical depth $d(\lambda) = [I_2]L_{abs}\sigma_{I_2}(\lambda)$ is calculated. Figure 3.34a shows the optical depth in the spectral region of interest for the different pressures in PEGASES, without plasma. A wide absorption band can be seen, more important as the pressure goes up, as expected. Figure 3.34b shows the densities obtained in the reduced spectral range 430 nm to 505 nm - the continuum - when dividing each data point by the corresponding cross section from Saiz-Lopez et al. [97]. The density is not constant over the entire continuum as it should be. The noise and slight decrease under 450 nm are most probably related to the strong decrease both in intensity of the lamp and of the cross section. For future plots, the value that is kept is the average over the 480 nm to 500 nm range, and the error bar is 1 standard deviation each side, calculated over the same range.

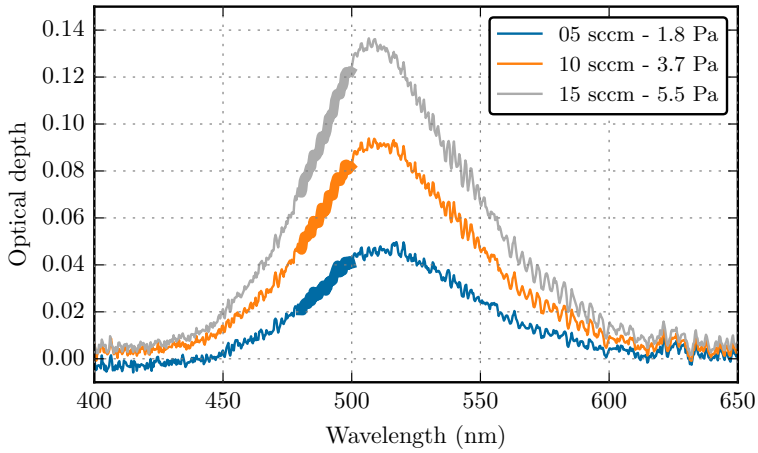

(a) Optical depth measured from 400 nm to 650 nm at three different pressure, without plasma. The range 480 nm to 500 nm, within the continuum, is used to determine densities.

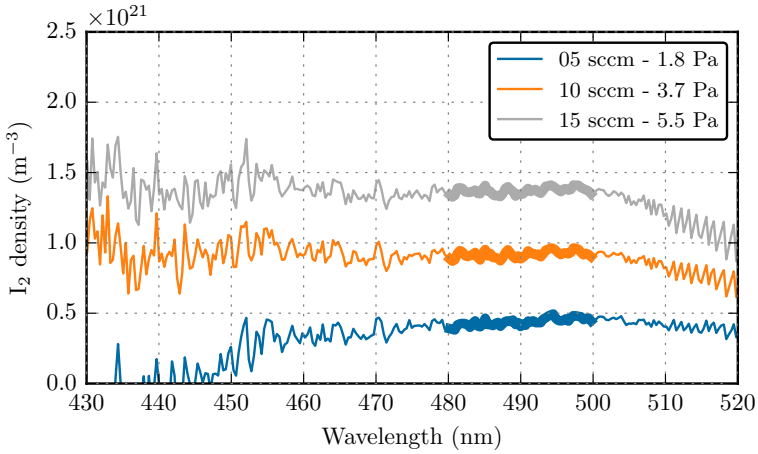

(b) I_2 density obtained by dividing the optical depth by the cross section and the absorption length. The continuum stops after 500 nm. The signal-to-noise ratio is not good enough before 480 nm.

Figure 3.34: Optical depth measured from 400 nm to 650 nm and associated density measured, from 430 nm to 520 nm.

Figure 3.35 shows the density of I_2 measured with this method against the pressure measured by the capacitance manometer on PEGASES. It can be seen that the linearity is respected, and the data can be very well fitted with an ideal gas law, $P = [I_2]kT$, with $T = 311\,\mathrm{K}$. There is not other measurements of the temperature of the gas to compare with, but the I_2 enters a chamber at room temperature after going through an injection pipe heated around 350 K to 360 K, so the value is considered coherent and the method validated in a case without plasma.

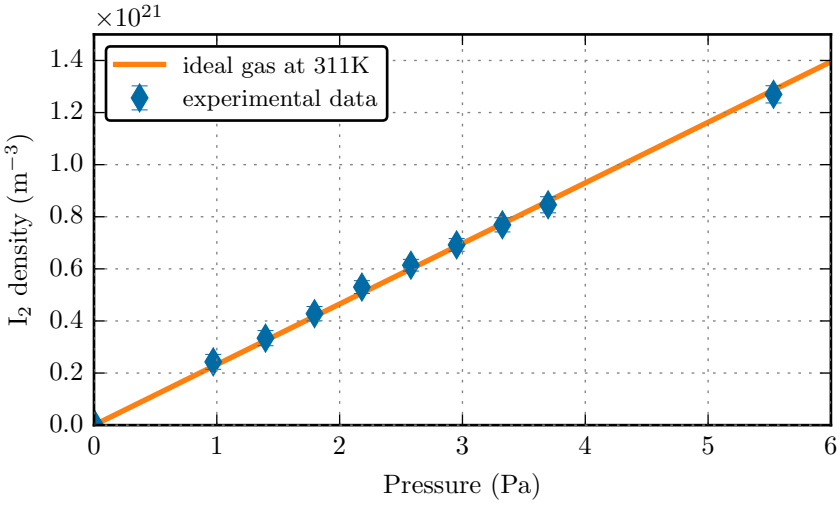

Figure 3.35: Experimental data points of I_2 density as a function of pressure measured independently on PEGASES, well fitted by an ideal gas law at 311 K. Errorbars are smaller than the markers.

3.5.5 Example data treatment with plasma

With plasma, the plasma emission masks the absorption in the raw data shown Figure 3.36. The plasma emission is in the same range of intensity than the absorption, but not in the same wavelength, so this can be corrected. The plasma intensity is recorded after each data point with the lamp OFF. Example of this emission is shown Figure 3.37 in 4 sets of parameters, as an illustration: the intensity increases a lot with pressure, less with power. No further analyses have been done on emission data during this experiment. The four signals are combined according to formula (3.10) so as to get the optical depth shown Figure 3.38. Only data between 480 nm and 500 nm are used, each data point being divided by the corresponding cross-section and absorption length, to get the line-of-sight averaged I_2 density.

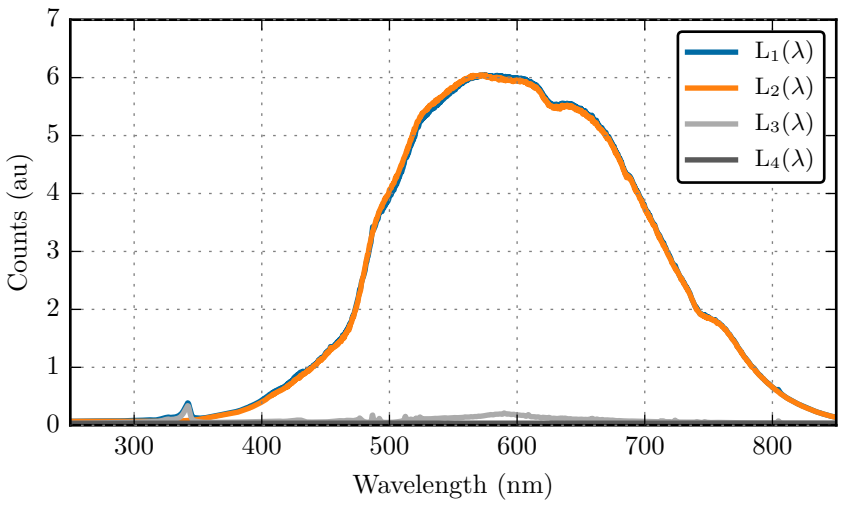

Figure 3.36: Example data at 4 Pa and 165 W. The plasma emission L_3 and the probe signal L_4 are very small in front of the lamp signal. The absorption seen corresponds to an optical depth of 4×10^{-2}, the order of magnitude of all data presented here.

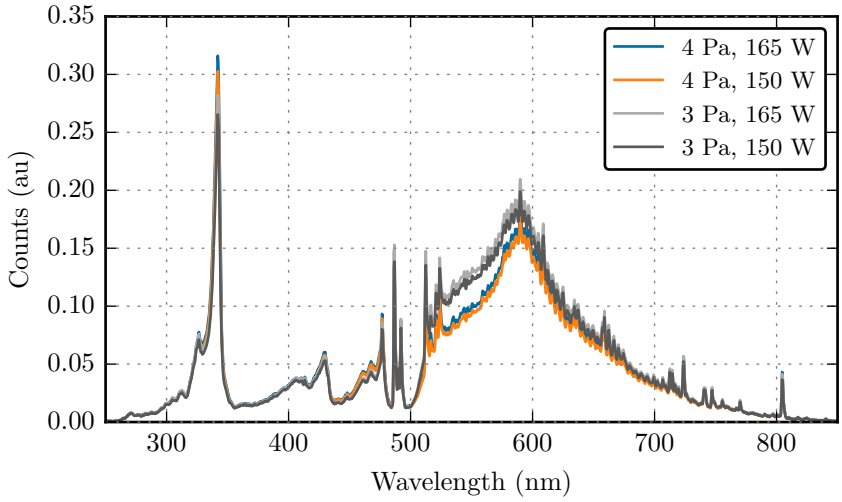

Figure 3.37: Plasma emission for different pressure and discharge power.

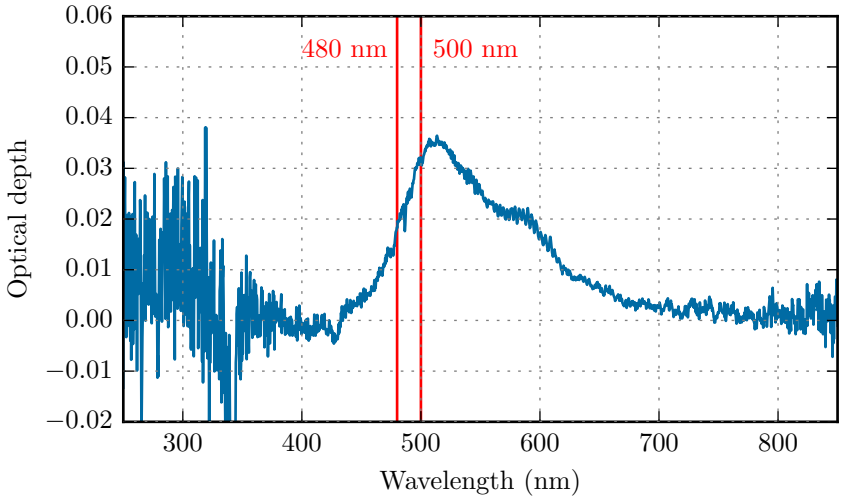

Figure 3.38: Optical depth obtained with formula (3.10) in the entire wavelength range. Only data between the two red lines are used to compute I_2 density.

3.5.6 Absorption band shape

It was explained in section 3.5.1 that only the continuum part of the transition showed suitable cross-sections for our analysis, because the rest of the spectrum depended on the external pressure [99]. The presence of a plasma leads to an even more complex situation as turning the plasma ON leads to the apparition of a new absorption band around 590 nm. This is shown Figure 3.40 where the data are superimposed with the theoretical cross sections. This new absorption band does not behave like the continuum with pressure, as shown Figure 3.39. This could come from a variation of the vibrational population of I_2, or from I_2^+ ions.

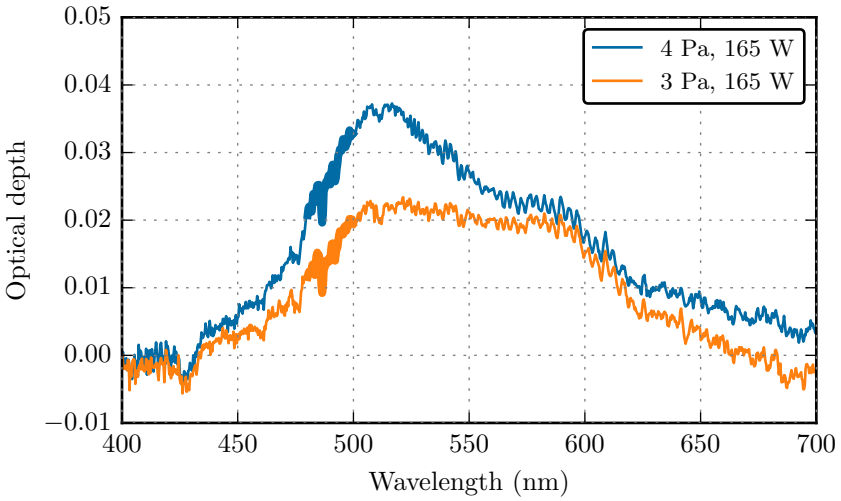

Figure 3.39: Absorption profiles from 400 to 700 nm at two different high pressures, highlighting the non-linear behavior of the absorption band at 590 nm with pressure. The part of the continuum used for density measurement, between 480 nm and 500 nm is shown in thicker lines.

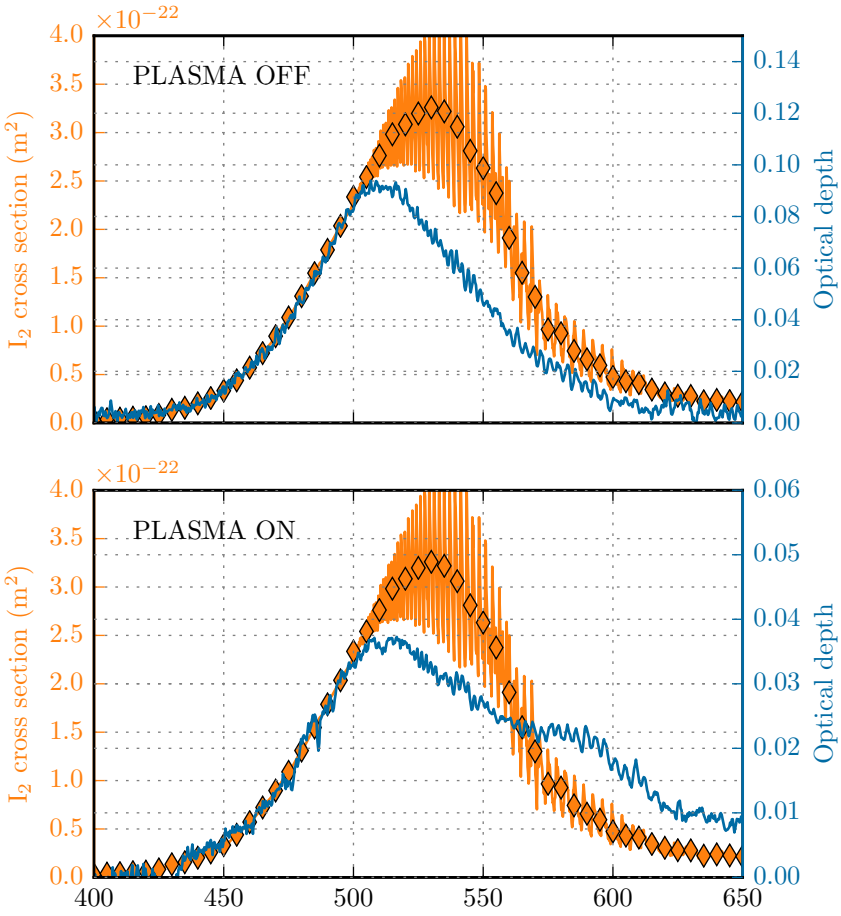

Figure 3.40: Absorption profiles (blue, right) juxtaposed to the theoretical cross-sections (orange, left), highlighting significant differences out of the continuum that goes up to 500 nm, and the apparition of a new absorption band around 590 nm when plasma is ON.

3.5.7 Effects of plasma inhomogeneity

As for I atoms, it is possible to make small models of I_2 distribution along the line-of-sight. I atoms were localized in the center, I_2 molecules are expected to be more present next to the walls. A simple model is to consider a parabolic profile constrained by the measured integral and the value of pressure, assuming that the pressure measured at the wall is the I_2 partial pressure: $p = [I_2]_w kT_w$. The I_2 molecules are supposed to be at the same temperature than the I atoms. This model does not lead to an isobar situation in the plasma.

$$[I_2](x) = \left(\frac{p}{kT_w} - [I_2]_0\right)\left(\frac{2x}{l}\right)^2 + [I_2]_0$$

In this case the average density along the line-of-sight is

$$\langle [I] \rangle_x = \frac{1}{l}\int_{-l/2}^{l/2} [I_2](x)\mathrm{d}x = \frac{1}{3}[I_2]_w + \frac{2}{3}[I_2]_0$$

As an example, Figure 3.41 shows the corresponding distribution in a case at 3 Pa, where the wall temperature is estimated at 300 K and the measured average I_2 density was $3 \times 10^{20}\,\mathrm{m}^{-3}$. It can be seen that the center density is in this case $9 \times 10^{19}\,\mathrm{m}^{-3}$, around one third of the average density.

Another possible model taking into account the specifity of the setup (long windows not containing plasma) is to suppose that the windows are full of I_2, coherent with the fact that we assumed that there was no I atoms in the windows. In this case the I_2 density is constant at $[I_2]_w$ over 4 cm on each side. In this case, it can be seen Figure 3.41 that windows account for most of the absorption, and a constant I_2 density of $2 \times 10^{19}\,\mathrm{m}^{-3}$ in the plasma leads to the overall average of $3 \times 10^{20}\,\mathrm{m}^{-3}$ that was measured. There is no way to constrain one model or the other with only line-of-sight experiments. In this work, an intermediate model is imagined, average of both models presented earlier so that the integral and the value at the walls do not change.

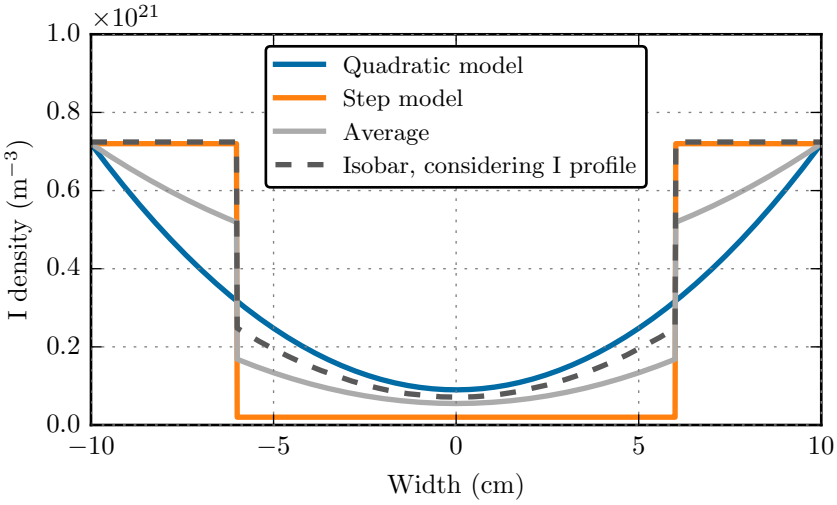

Figure 3.41: Case with a wall temperature at 300K. Quadratic, step and average curves have the same value at the edge and the same integral. The isobar is what the I_2 density would be if deduced from the I density model and an isobar assumption.

With this hybrid value, the centre density of I_2 is linked to the other parameters and measurements with:

$$[I_2](0) = \frac{1}{2}\Big([I_2]_{\text{quadratic}}(0) + [I_2]_{\text{step}}(0)\Big)$$

With

$$[I_2]_{\text{quadratic}}(0) = \frac{1}{2}\left(3\langle[I_2]\rangle_x - \frac{P}{kT_{\text{walls}}}\right)$$

$$[I_2]_{\text{step}}(0) = \frac{1}{l_{\text{plasma}}}\left(l_{\text{total}}\langle[I_2]\rangle_x - l_{\text{windows}}\frac{P}{kT_{\text{walls}}}\right)$$

On the same figure is added an isobar case, computed with the 1D models for I (presented section 3.4.4) extended with constant values in the Brewster windows ($[\mathrm{I}] = 0$, $T_{\mathrm{I}_2} = T_I = T_{\mathrm{walls}}$):

$$[\mathrm{I}_2]_{\mathrm{isobar}}(x) = \frac{p}{kT_I(x)} - [\mathrm{I}](x)$$

This isobar model greatly overestimates the average I_2 density along the line-of-sight and is therefore not compatible with the measurements, but is a good indication for future better model, and also shows that the average option is not too far in the center.

3.5.8 I_2 density in PEGASES

Figure 3.42 shows the results of a measurement campaign performed at 5 different mass flow rates in the PEGASES thruster equipped with its Brewster-angle windows. The density of I_2 is constant with the discharge power in the studied range. The average I_2 density is increasing with mass flow rate, as more iodine is brought in the thruster.

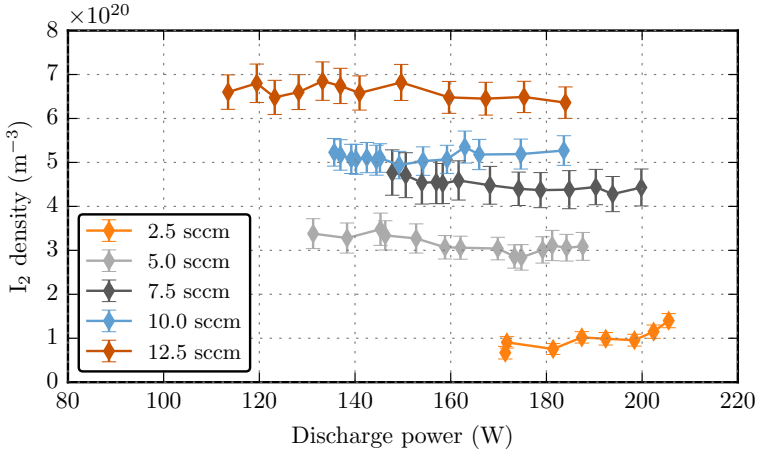

Figure 3.42: Line-of-sight averaged I_2 density as a function of discharge power for different mass flow rates. The density is averaged over the 480 nm - 500 nm range and the errorbar is one standard deviation each side.

When neglecting the variation in pressure during a measurement run at fixed mass flow rate, it is possible to plot the average I_2 density against the average pressure, Figure 3.43. There is also plotted the estimated central density based on this average density and the 1D models detailed in the previous paragraphs. The model, at low pressure, overestimates the I_2 density at the walls, and so leads to negative center densities to maintain the required average density. It means that the plasma is more depleted in I_2 in the center at least at lower pressures, and that the I_2 density drops faster once further from the walls.

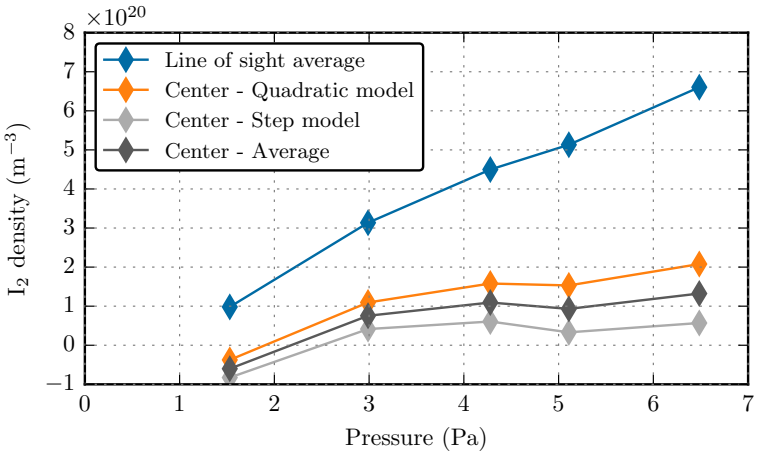

Figure 3.43: Line-of-sight averaged density at different pressures, averaged on the power range studied, and center density derived from these averaged values. The model leads to negative center densities at low pressure.

But the pressure is not perfectly stable during a run at fixed mass flow rate and the 1D model used is extremely sensible to pressure. This allows to look behind the averages, as shown Figure 3.44. It can be seen that for any mass flow rate (discarding 2.5 sccm) the center density decreases with discharge power, and is rather stable with pressure, as shown Figure 3.43.

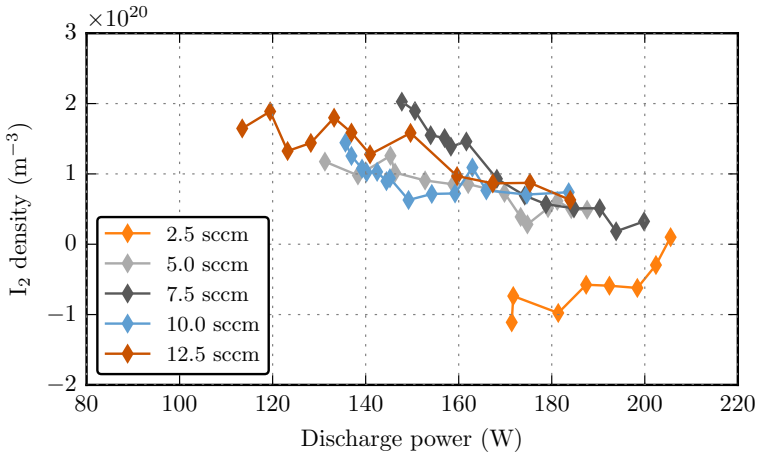

Figure 3.44: Corrected I_2 density at the center as a function of discharge power for different mass flow rates.

3.6 Characterizing ions

Several other possible optical diagnostics have been envisioned but not implemented during this work. They are briefly presented here.

3.6.1 I^+ Laser Induced Fluorescence

Laser Induced Fluorescence (LIF) is an absorption experiment whose observable is the light emitted by the particles de-exciting in the laser path. The excitation is made at one wavelength and the observation at another. This allows to measure the species densities and temperatures with spatial resolution, which is not possible with a normal absorption measurement. Hargus et al. [100] propose a LIF-scheme further studied by Steinberger and Scime

[30]. Using wavenumber data from Martin and Corliss [35], excitation is done at 19 369.97 cm^{-1} (516.26 nm), from the lower level $5s^2 5p^3(^4S^o)6s$ with term $^5S^o$ and $J = 2$ at 81 032.70 cm^{-1} to the upper lever $5s^2 5p^3(^4S^o)6p$ with term ^5P and $J = 3$ at 100 402.68 cm^{-1}. The fluorescence is monitored at 14 366.36 cm^{-1} (696.07 nm), from the same upper level to a lower level $5s^2 5p^3(^4S^o)5d$ with term $^5D^o$ and $J = 4$ at 86 036.32 cm^{-1}. Actual wavelengths found during the measurements are reported in the dedicated work from Steinberger and Scime [30]. Spectroscopic notation is from Minnhagen [34] and the complete data have been retrieved with Kramida et al. [23].

Like for the absorption at 7603 cm^{-1} presented in this work, the fluorescence transition presents an hyperfine structure. Unlike the transition used in this work, the parameters such as cross-section and weight ratios are not known yet. Steinberger and Scime [30] propose a method to extract the *most probable* temperature from their data, and an estimation about magnetic dipole and electric quadrupole coefficients.

3.6.2 I^- photodetachment

Measurement of I^- density can be performed using broad-band absorption spectroscopy, following a method presented on Cl_2 plasmas by Marinov et al. [86]. In their work, an additional absorption was seen under a threshold at 343 nm corresponding to the electron affinity of chlorine. This additional absorption comes from the continuum absorption due to photo-detachement of electron from Cl^- negative ions.

In iodine, as measured by the team of Peláez et al. [71], the electron affinity is 3.059 046 3(38) eV, which corresponds to 24 672.874(29) cm^{-1} or a wavelength around 405.3 nm. It is expected that with a UV lamp emitting around this threshold, unlike the one used in this work, an absorption feature similar to the one seen in Cl_2 plasmas will allow to gather information about I^- density.

3.7 Conclusions

Four different optical diagnostics using spectroscopy to gather information about the density and temperature of the neutral species I and I_2 are presented. The diagnostics are demonstrated in the case of a relatively high-pressure plasma, between 0.9 Pa and 4.5 Pa, in the ionization chamber of the PEGASES thruster, without magnetic barrier or acceleration stage.

Emission spectroscopy is first implemented by collecting the light emitted by the iodine plasma with a spectrometer. Identification of the molecular and atomic emission bands and lines leads to qualitative information about the prominence of species in different setups and at different operating conditions. It also helps identifying strong lines and bands that can be probed by laser or broadband absorption. Infra-red laser absorption is performed using a Titanium-Sapphire laser on two of the strongest lines of the I atom, at $10\,969\,cm^{-1}$ and $11\,036\,cm^{-1}$ (911 nm and 906 nm). It exhibits rich hyperfine structures that are explored and characterized with Doppler-free spectroscopy. A saturation analysis is also performed to fully characterize the transition. This experiment leads to the temperature of atomic iodine with a very large signal-to-noise ratio. A very weak dipolar magnetic and electric quadrupolar transition at $7603\,cm^{-1}$ (1.315 µm), within the fine structure of the fundamental state of the I atom, was probed by laser absorption. Absorption data successfully leads to the line-of-sight integrated temperature and density of the I atoms within the ion source. A measurement campaign is presented using broad-band absorption spectroscopy on I_2 molecules. An absorption continuum of the I_2 molecule allows to effectively retrieve the I_2 density from absorption between 480 nm and 500 nm. I temperature, I density and I_2 density from these experiments are values integrated along the laser or lamp line-of-sight: small 1D models are proposed to estimate the repartition within PEGASES, and to get an estimation of the dissociation degree of I_2 in the plasma. Last, Laser Induced Fluorescence and photodetachment are discussed as next steps of using spectroscopy to characterize the plasma, this time for charged species I^+ and I^-.

Future measurements need to include optical accesses more resistant to iodine to reduce dead volumes, radial measurements, localized measurements (for example with Laser-Induced Fluorescence), measurements at lower pressure (for example with Cavity Ring-Down spectroscopy to increase the signal-to-noise ratio) and more precise 1D or 2D models of neutral distribution.

Chapter 4

Electrical diagnostics for iodine plasmas

To measure the electron density and temperature in an I_2 plasma, a measurement campaign is performed with a cylindrical Langmuir probe, in a wide range of pressure, varying the discharge power and, to a certain extent, the probe position within PEGASES. Data analysis includes an attempt to estimate the plasma electronegativity from the measured I-V curves.

4.1 Introduction to Langmuir probe measurements

Electrostatic and electromagnetic diagnostics are among the easiest to implement to get information about the plasma. They mostly consist in inserting a conductive material in the plasma and measuring a collected current depending on the probe voltage bias. Other diagnostics emit waves or collect particles with electrostatic filters. They are perturbative and provide local measurements, and are often limited by complex data analysis. A good introduction to electrical diagnostics is proposed by Chabert and Braithwaite [64]. Langmuir probe measurements will be further developed in the rest of the section. Other probes include for example Mach probes [101], impedance probes such as the matched dipole probe [102], Retarding Field Analyzers (RFA) [64] and Magnetized RFA [60], hairpin probes [103], planar probes. Electric diagnostics can give information such as electron temperature and density, charged particles energy and fluxes (for example in a plasma beam or a thruster's plume), electron energy distribution, plasma and floating potentials.

The Langmuir probe principles were first used in the 1920s by Langmuir himself: placing a small electrically conducting wire in a plasma leads to current collection on this wire. Biasing the wire to certain potentials with respect to, for example, the plasma walls modifies the collected current and gives access to several plasma parameters such as the electron density n_e or the electron temperature T_e. It can also give access to the Electron Energy Distribution Function [104]. The traditional Langmuir probe is often an asymmetrical double probe where the second electrode is made by the plasma walls [64]. Basics of the analysis of the results of a Langmuir probe analysis in an electropositive plasma are detailed in many sources, for example Chen [105] and Désangles [106]. The case of electronegative plasmas is treated by Bredin et al. [107], a work done after some studies on iodine by Amemiya [108]. Sweeping voltage on the Langmuir probe leads to collection of current and the production of an I-V curve: collected current as a function of the probe voltage.

4.1.1 Simulating an I-V curve

The current collected on the Langmuir probe for a given probe voltage bias is the sum of the electron current, the positive ion current and the negative ion current:

$$I(V) = I_e(V) + I_+(V) + I_-(V)$$

A complete simulated Langmuir curve is shown Figure 4.1b. It is the sum of the three currents simulated numerically Figure 4.1a. The rest of this section is dedicated to explain how these three curves are built, with a double interest: it explains how a Langmuir probe functions, and it presents the mathematical function that is later used to fit the experimental data. The explanations are directly based on the work from Bredin et al. [107], with some parameters adapted with recent results, such as the h factor for positive ions with the value from Chabert [76] already used Chapter 2.

4.1.2 Electron current

Below V_p

All three species considered (electrons, positive ions, negative ions) have a different behavior depending if the probe voltage bias V is above or below the plasma potential V_p: all three functions $I_e(V)$, $I_+(V)$, $I_-(V)$ are built by pieces. For a probe bias below the plasma potential V_p, the electrons are repelled by the probe and a Boltzmann relation is assumed for the electron current:

$$I_e(V) = I_e(V_p) \exp\left(\frac{V - V_p}{T_e}\right)$$

The electron current at the plasma potential V_p is the mean thermal current, with $v_{\mathrm{th,e}}$ the electron mean velocity and $\mathcal{A}_p$ the physical probe area:

$$I_e(V_p) = \frac{1}{4} n_e v_{\mathrm{th,e}} e \mathcal{A}_p = e \mathcal{A}_p n_e \sqrt{\frac{eT_e}{2\pi m_e}}$$

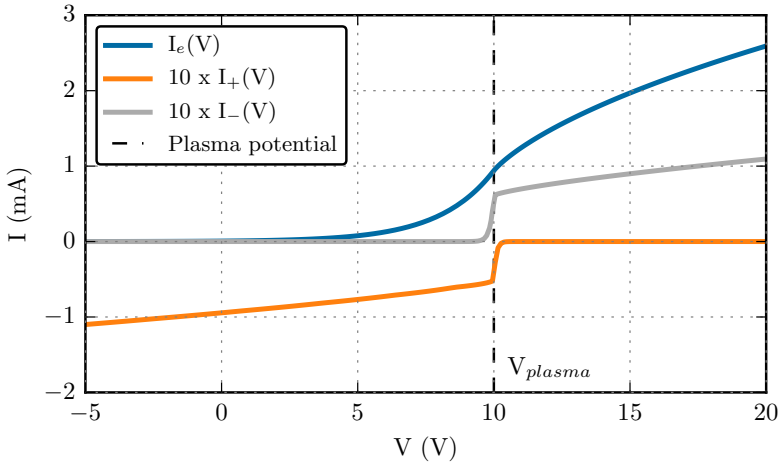

(a) I-V curve decoupled for ion and electron populations. The ions current are magnified 10 times for readability.

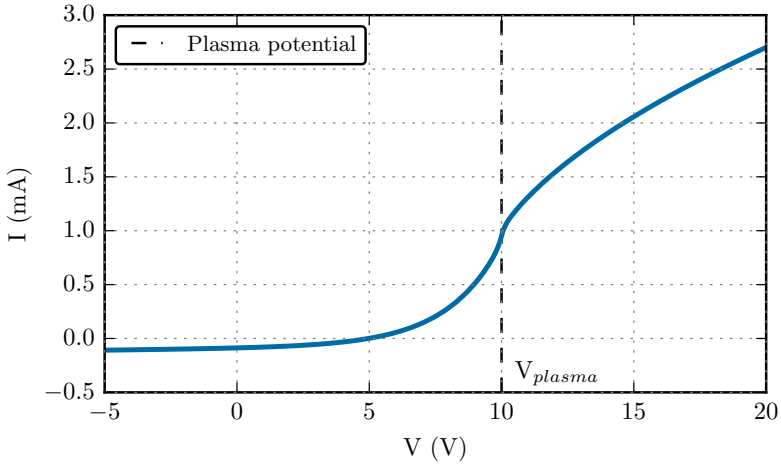

(b) Complete I-V curve obtained by additions of its three contributions.

Figure 4.1: Example I-V curve calculated numerically, in an example iodine plasma at 1 Pa, with $T_+ = 1000\,\mathrm{K}$, $T_- = 1500\,\mathrm{K}$, $T_e = 2\,\mathrm{eV}$, $V_p = 10\,\mathrm{V}$, $n_e = 1 \times 10^{16}\,\mathrm{m}^{-3}$ and $\alpha = [\mathrm{I}-]/n_e = 100$. The electronegativity α is large to enhance the effect of negative ions in this example.

Above V_p

Above the plasma potential, the electron current is at saturation: it continues to increase only because the higher the voltage, the larger the potential dwell around the probe. And the larger the potential dwell, the more electrons are attracted to the probe from the surrounding plasma. Chabert and Braithwaite [64] propose a formula for the orbital-motion-limited saturation electron current in the case of a cylindrical probe, essentially describing the sheath expansion around the probe:

$$I_e(V) = e\mathcal{A}_p \frac{n_e v_{\text{th,e}}}{4} \left(2\sqrt{\frac{V - V_p}{\pi T_e}} + \exp\left(\frac{V - V_p}{T_e}\right) \text{erfc}\left(\sqrt{\frac{V - V_p}{T_e}}\right) \right)$$

4.1.3 Positive ion current

Above V_p

Above the plasma potential, the positive ions are repelled by the probe and a Boltzmann relation is assumed:

$$I_+(V) = I_+(V_p) \exp\left(\frac{V - V_p}{T_+}\right)$$

Below V_p

Below and at the plasma potential, the positive ion flux follows the law detailed section 2.3.4, because the probe area can be seen as another *wall area*. The radial $\widehat{h}_r$ factor is used because the probe is generally a thin long cylindrical wire, hence the probe area general quasi exclusively radial. It leads to, with Γ_+ the positive ion flux:

$$I_+(V) = -\Gamma_+ e\mathcal{A}_{\text{eff}}(V) = -\widehat{h}_r n_+ u_B e\mathcal{A}_{\text{eff}}(V) \tag{4.1}$$

Effective probe area

In formula (4.1), the effective collection area $\mathcal{A}_{\text{eff}}(V)$ of the probe depends on the probe bias, because of the sheath around the cylindrical tip of the probe that acts like a potential dwell, attracting more ions if the dwell is deeper. A model from Bredin et al. [107], not reproduced here, is used for this area. It gives the effective radius shown Figure 4.2. The h factor does not depend on the probe bias, and is taken equal to $\widehat{h}_r$, the radial version of the $\widehat{h}$ factor from Chabert [76] already used in the global model section 2.3.4, in its radial version as the main part of the probe surface is radial.

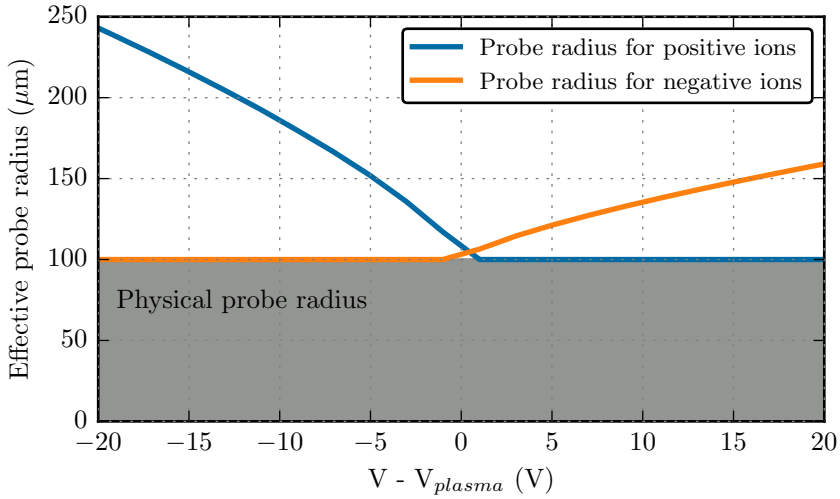

Figure 4.2: Effective probe radius calculated in an example iodine plasma at 1 Pa, with $T_+ = 1000\,\text{K}$, $T_- = 1500\,\text{K}$, $T_e = 3\,\text{eV}$, $n_e = 1 \times 10^{17}\,\text{m}^{-3}$ and $\alpha = [\text{I}-]/n_e = 0.01$. The physical probe radius is 100 µm, corresponding to the probe used in this work. The low electronegativity α is typical of the plasmas probed in this work. The probe length changes are neglected, only the radius changes are considered.

4.1.4 Negative ion current

Below V_p

Like electrons, negative ions are repelled if the probe is biased below the plasma potential, and a Boltzmann equilibrium is assumed. The validity of this approximation is discussed by Chabert [76], and the approximation should not be used in this model except at very low pressure, according to the predictions of the global model, as shown Figure 4.3. The approximation is expected to become quickly inapplicable due to the high mass and high recombination rate of I_2, but will be used here for lack of a better theory.

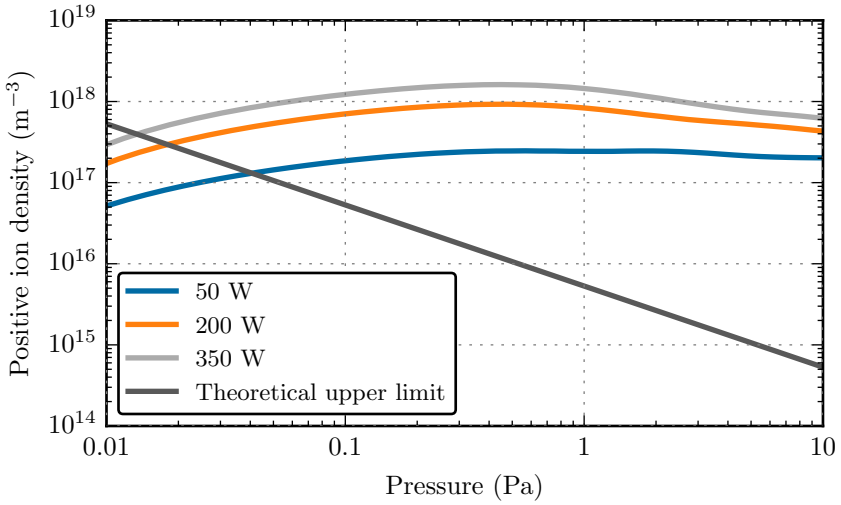

Figure 4.3: Validity region of the hypothesis *the negative ions follow a Boltzmann distribution*, hence Equation (4.2), compared to predictions of the global model. Chabert [76] states that the hypothesis is valid only at low positive ion density, under the black curve.

With a Boltzmann distribution:

$$I_-(V) = I_-(V_p) \exp\left(\frac{V - V_p}{T_-}\right) \tag{4.2}$$

Above V_p

Above and at the plasma potential, a Bohm relation is assumed:

$$I_-(V) = \Gamma_- e\mathcal{A}_{\text{eff}}(V) = h_r n_- e u_{B-} \mathcal{A}_{\text{eff}}(V)$$

With the lack of a better theory for negative ions, the electronegativity is taken into account by considering an electropositive h factor unchanged from Bredin et al. [107] ($h_r = 0.6$) but an adapted Bohm speed: $u_{B-} = \sqrt{eT_+/m_-}$. More information about the h factors and treatment of the wall fluxes in this work is given section 2.3.4.

4.2 Setup and method

The Langmuir probe

The probe used is made of two tungsten wires inserted in a two-hole quartz tube. The probe tip length is 3.9 mm and the diameter is 200 µm, as shown Figure 4.5a. The probe is mounted on an arm able to move along the x-axis of PEGASES, as shown Figure 4.5b.

The length of the arm and the length of the probe allow to probe coordinates from $x = 1.7$ cm to outside of PEGASES. The center of PEGASES is the reference point $(x, y, z) = (0, 0, 0)$. During normal operations, the probe is positioned in the plasma at $x = 1.7$ cm, $y = 0, z = 0$ in PEGASES through the 1 cm-hole in the exhaust grid.

Two grids were used in this experiment: a first grid identical to the one used during the optical experiments, in aluminium with a single 1 cm-diameter hole in the center, leading to a transparency of 3.3 %. The second one is a grid in stainless steel, covered with aroud 4500 holes of 1 mm in diameter in the middle of which a 1 cm-diameter hole was later drilled. The transparency is therefore around 35 %. A set of measurements was also made without any grids to further decrease the pressure for a given mass flow rate. More information about the grids is available section 5.1.2.

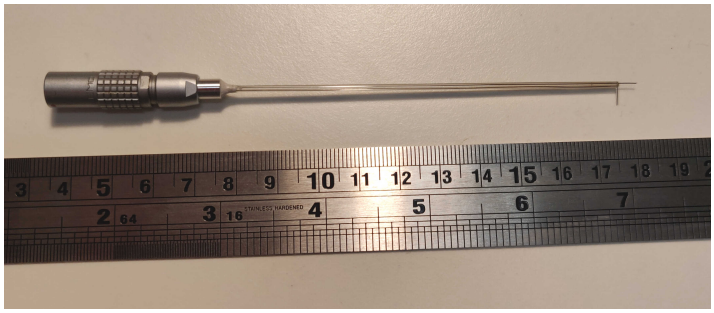

Figure 4.4: Picture of the short Langmuir probe used in this work. Experiments with a longer probe were delayed due to the COVID-19 pandemic.

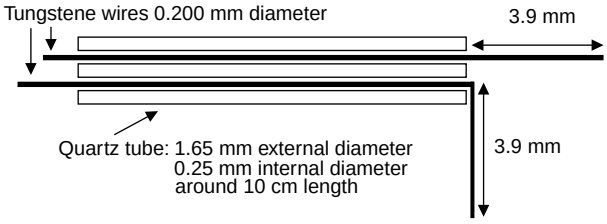

(a) Design and characteristics of the Langmuir probe used in this work, with the second Tungsten wire used as reference probe.

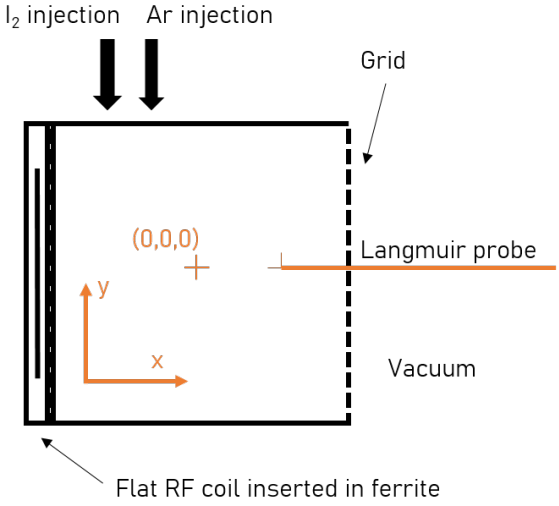

(b) Reminder of PEGASES geometry and definition of the axis. The z axis is upwards, towards the reader here. The reference is at the center of the ionization chamber. PEGASES interior dimensions are 12 cm along the x and y axis, and 8 cm along the z axis. The probe can move along the x axis here, from outside the thruster down to $x = 1.7$ cm, its default location.

Figure 4.5: Geometry of the Langmuir Probe and installation in PEGASES.

The VGPS acquisition system

The acquisition is done using the VGPS system from PlasmaSensors, detailed for example by Godyak and Alexandrovich [109], that uses a reference probe. There is no RF compensation used as it was proven not needed by previous work on the same setup [54]. The VGPS interface is shown Figure 4.6. The system provides datafiles with the I-V curve, its first derivative, its second derivative, and the Electron Energy Probability Function (EEPF) in $\mathrm{eV}^{-3/2}\,\mathrm{cm}^{-3}$.

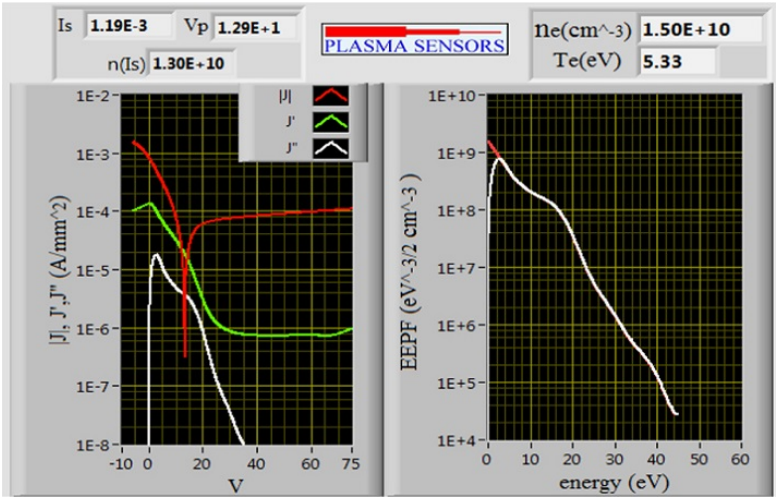

Figure 4.6: Exemple interface of the VGPS system, from the vendor's website. This does not correspond to real measurements from this work. The left panel shows the I-V curve and its first and second derivative, in log scale, with the x-axis inverted compared to the curves in this work. The right panel shows the EEPF.

The EEPF $f_\mathcal{E}$ is linked to the EEDF $F_\mathcal{E}$ by the relation $F_\mathcal{E} = \sqrt{\mathcal{E}} f_\mathcal{E}$, with $\mathcal{E}$ the electron energy in eV. The VGPS system also provides a value for n_e and T_e, calculated by integration of the EEPF. The values based on the EEDF (or EEPF) are considered the most reliable for analysis of Langmuir probe data [104]. They neglect electronegativity, an assumption that will be validated later for the pressures probed. Unless stated otherwise, these are the values used in this chapter. The complete formula are:

$$n_e = \int \sqrt{\mathcal{E}} f_\mathcal{E}(\mathcal{E}) \, \mathrm{d}\mathcal{E}$$

$$T_e = \frac{2}{3}\langle\mathcal{E}\rangle = \frac{2}{3n_e} \int \mathcal{E}^{3/2} f_\mathcal{E}(\mathcal{E}) \, \mathrm{d}\mathcal{E}$$

In these equations, $\mathcal{E}$ is in eV, $f_\mathcal{E}$ is the Electron Energy Probability Function (EEPF), linked to the EEDF $F_\mathcal{E}$ by the relation $F_\mathcal{E} = \sqrt{\mathcal{E}} f_\mathcal{E}$. A Maxwellian EEPF is a straight line.

Example data

For illustration purposes, Figure 4.7 shows the data given by the VGPS system with the probe at nominal position $x = 1.7\,\mathrm{cm}$, at discharge power $P_d = 188\,\mathrm{W}$ and pressure $p = 0.3\,\mathrm{Pa}$. The electron density calculated with the EEDF is $n_e = 1.51 \times 10^{17}\,\mathrm{m}^{-3}$ and electron temperature $T_e = 2.11\,\mathrm{eV}$.

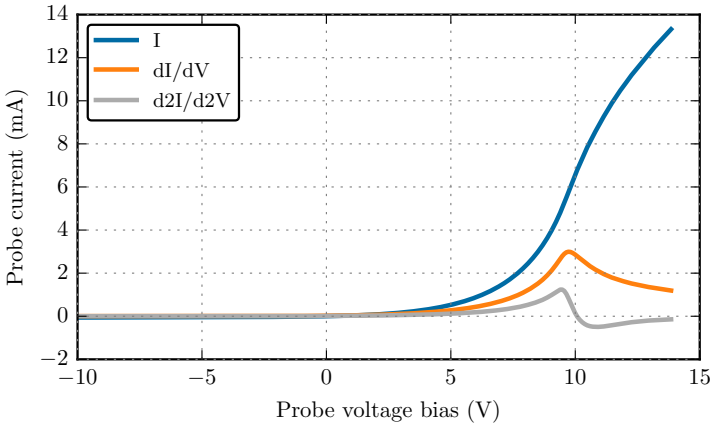

(a) I-V curve and derivatives, as given by the VGPS system.

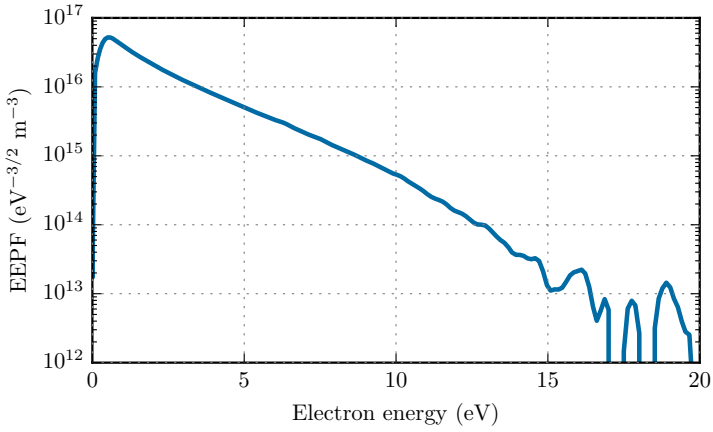

(b) EEPF, as given by the VGPS system.

Figure 4.7: Example data at $x = 1.7\,\mathrm{cm}$, $P_d = 188\,\mathrm{W}$, $p = 0.3\,\mathrm{Pa}$.

4.3 Results

This section presents and comments the experimental results. The comparison with the model is done in the Chapter 5. The results at low pressure have been obtained with the help of Benjamin Esteves.

4.3.1 Varying pressure at 100 W and 190 W.

The electron density and temperature have been measured next to the plasma center ($x = 1.7\,\mathrm{cm}$) in a wide range of plasma pressures. Varying pressure in PEGASES leads to large changes in electron density and temperature. As it is not always feasible to keep a constant discharge power, all data about electron density shown Figure 4.8 have been slightly corrected: if the measurement discharge power was not exactly the target power, the electron density was modified using cross-multiplication assuming the electron density n_e was proportional to the discharge power, as expected from the global model (Figure 2.16) and confirmed in the next section. For example, if n_e was measured at 109 W when the target power was 101 W, the value that was plotted is the measured value multiplied by 101/109. T_e was not modified assuming it was very little dependent on discharge power, as expected from the global model and confirmed in the next section.

The electron density shown on Figure 4.8a features a peak around 0.1 Pa, higher at higher power: at $P_d = 190\,\mathrm{W}$ the electron density is maximum around 0.12 Pa with $2.5 \times 10^{17}\,\mathrm{m}^{-3}$. This maximum at 100 W is 0.9 Pa and $1.4 \times 10^{17}\,\mathrm{m}^{-3}$. The maximal value of n_e is 1.8 times higher while P_d was multiplied by 1.9, coherent with the proportionality expected from the models. The data at high pressure (above 1 Pa) are coherent with the data at lower pressure. Electron temperature shown on Figure 4.8b presents a sharp increase at very low pressure for both discharge powers and then a slower curve down to 1.6 eV at 3 Pa. It shows slight local minima at 0.12 Pa and 0.09 Pa respectively, corresponding to the maximum of electron density. These minima were expected from the model (Figure 2.18). Contrary to these predictions, the electron temperature does not reach a stable value while pressure increases, and keeps decreasing with pressure: this is due to a strong localization of the plasma closer to the antenna and away from the probe, as shown by the data section 4.3.3.

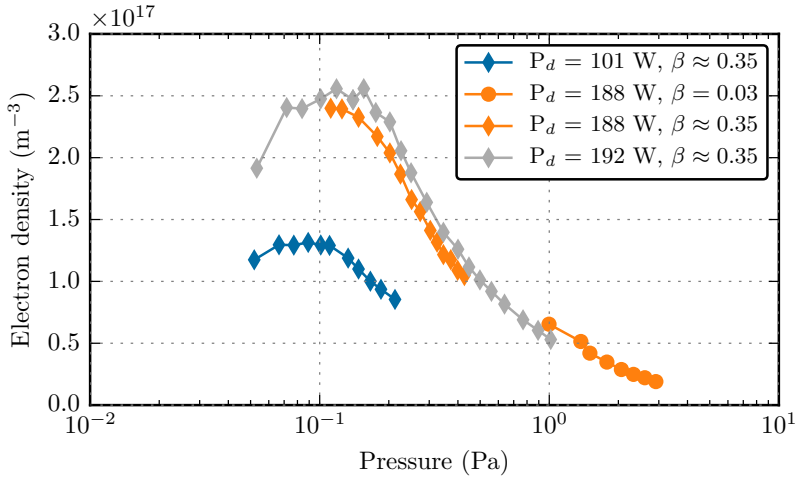

(a) Electron density versus pressure.

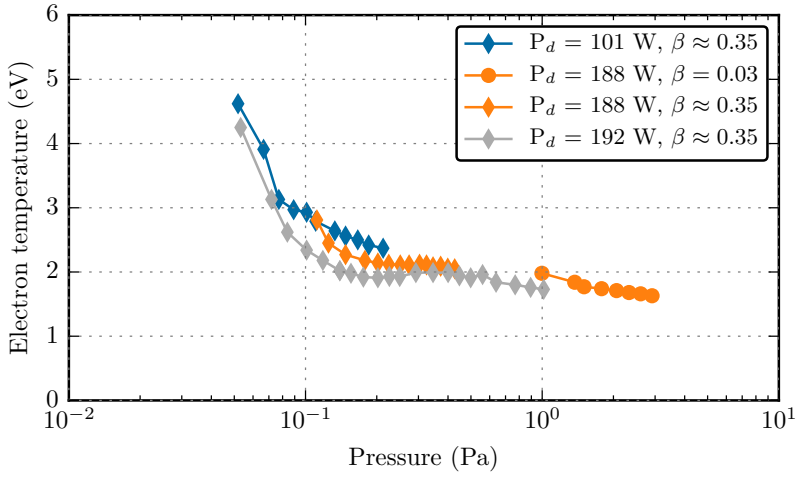

(b) Electron temperature versus pressure.

Figure 4.8: Electron density and temperature measured from EEDF integration by the VGPS system, at $x = 1.7\,\mathrm{cm}$, versus pressure in log scale. Different grids of transparency β are used above and below 1 Pa.

4.3.2 Varying discharge power

The evolution of T_e and n_e at constant pressure is shown Figure 4.9. Data on n_e was not corrected, and n_e increases linearly with discharge power, as shown Figure 4.9a. This increase is quasi proportional, as expected from the models (Figure 2.16) and validates the data corrections presented in the previous section.

The values of electron temperature T_e shown Figure 4.9b have been corrected manually to account for slight changes in pressure during the measurements. This is done by estimated the derivative of T_e with pressure at a given pressure from the slope of the curve Figure 4.8b, and using it in a first order limited development:

$$T_e(p) = Te(p') + \frac{\mathrm{d}Te}{\mathrm{d}p}(p') \ (p - p')$$

Once corrected, it can be seen that T_e is rather constant with discharge power P_d at all the pressures probed, as expected from the model (Figure 2.18). More comparisons with the model are presented Chapter 5.

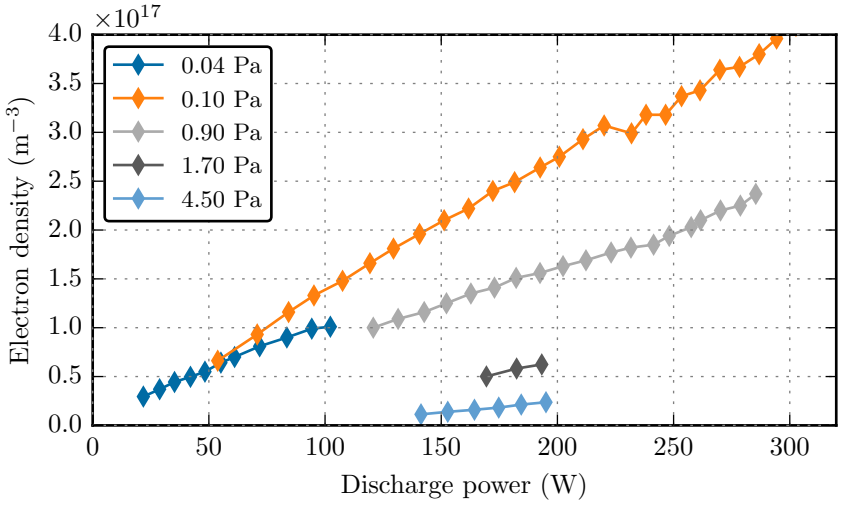

(a) Electron density versus discharge power.

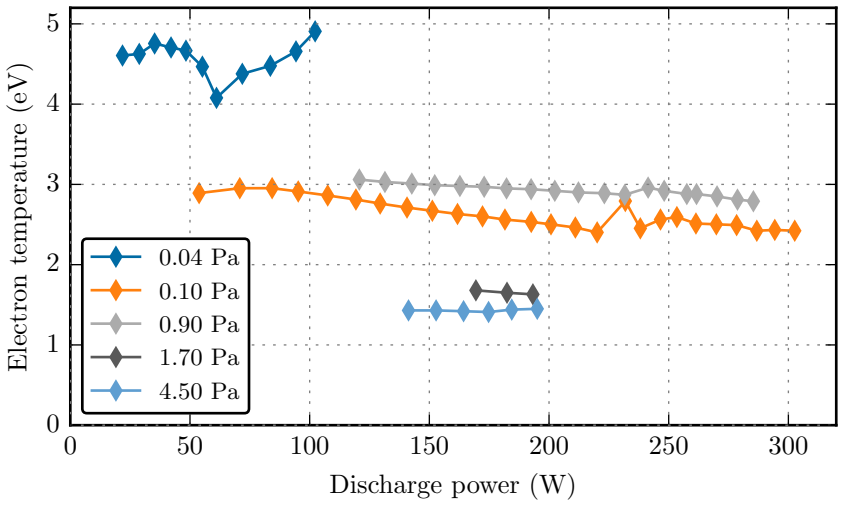

(b) Electron temperature versus discharge power.

Figure 4.9: Electron density and temperature versus discharge power. All data are taken at $x = 1.7\,\mathrm{cm}$, with a grid with $\beta \approx 0.35$.

4.3.3 Spatial distribution

The global model assumes an homogeneous bulk in the plasma. The limits of this assumption can be verified here. The current setup allows to easily measure n_e and T_e with a Langmuir probe within a 3 cm-long region along the x-axis, from nearly the plasma center to the vicinity of the exhaust grid. The axis were defined Figure 4.5b. Experiments with a new, longer probe were delayed due to the COVID-19 pandemic and will be featured in future works from Benjamin Esteves.

Figure 4.10a shows the electron density normalized to the value at $x = 5.5$ cm (close to the grids) at each pressure: the gradient is strong at high pressure, and n_e becomes quasi-constant at 0.05 Pa, although the spatial distribution is still not perfectly homogeneous. These data confirm strong gradients at high pressure, with electron density multiplied by 7 overs 3 cm towards the center at 4.5 Pa. This means that the plasma core gets progressively localized away from the probe as the pressure goes up. It explains that T_e does not reach a steady state with pressure at high pressure, and that n_e decreases faster than expected (see Chapter 5).

Figure 4.10b shows the evolution of T_e with distance, and the scenarios are different: at 0.8 Pa, the temperature profile is flat. Above this pressure, the temperature decreases towards the walls. But below this pressure, the electron temperature increases towards the grid ! This can be seen in Argon too, so it is not linked to negative ions. It can be seen as an experimental artefact, and it is related to the apparition of a population of cold electrons at low energy in the plasma bulk, that can be seen in the EEDF Figure 4.11. By superimposing theoretical maxwellian EEDF at the same temperature, one can see that the measured EEDF gets far from a Maxwellian when moving the probe closer to the center: the reason why these EEDF are far from Maxwellian in the bulk at very low pressure is not explained in this work.

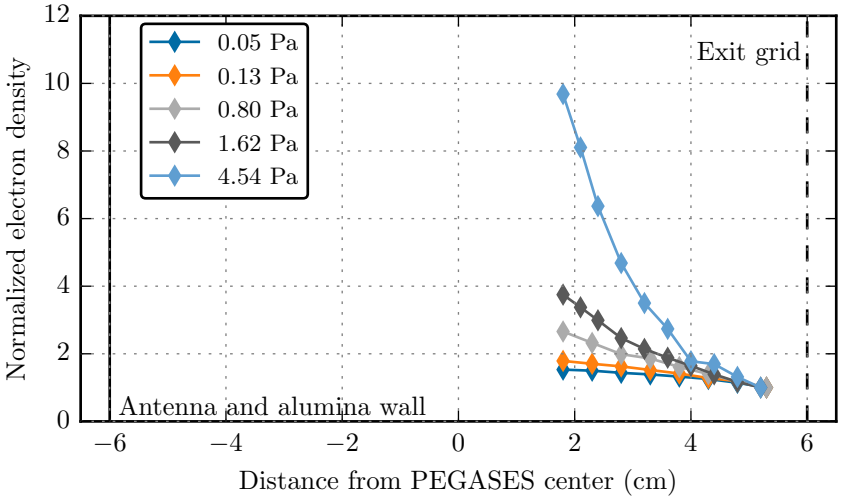

(a) Normalized electron density as a function of distance along the x-axis.

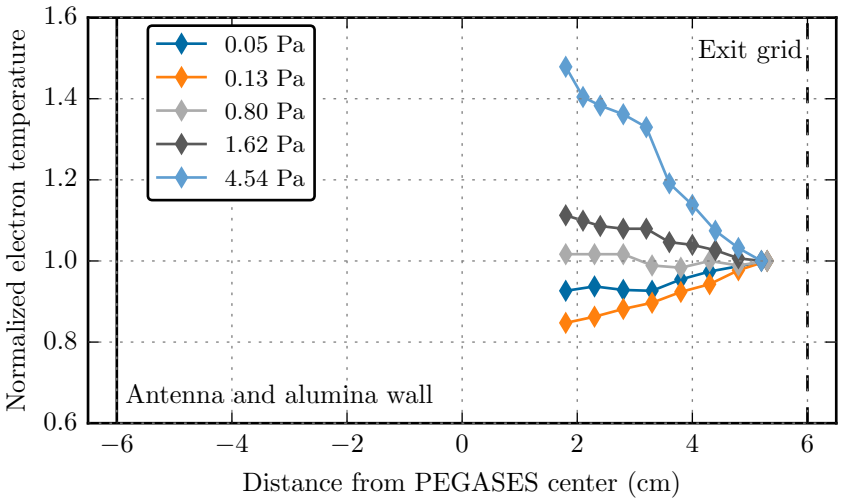

(b) Normalized electron temperature as a function of distance along the x-axis.

Figure 4.10: T_e and n_e for different plasma parameters as a function of distance along the x-axis in PEGASES, normalized to the value at $x = 5.5\,\mathrm{cm}$.

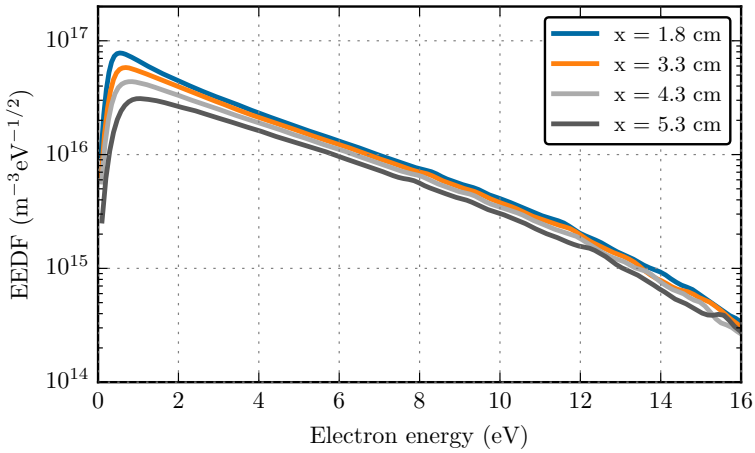

(a) EEDF obtained from the EEPF provided by VGPS.

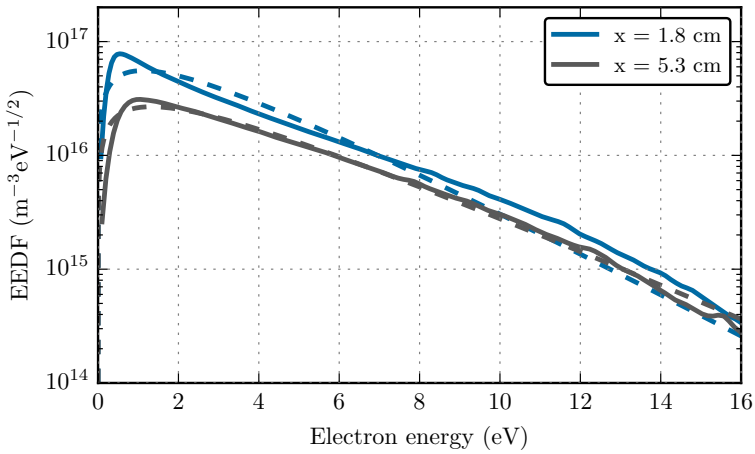

(b) Same curves, focusing on 1.8 cm and 5.3 cm, and adding dashed lines that are the Maxwellian EEDF at the same temperature.

Figure 4.11: EEDF measured with VGPS, at 0.13 Pa and 190 W (corresponding to the orange data on Figure 4.10) for different positions in the plasma, showing curves that are more Maxwellian near the grids than at the center.

4.3.4 Electronegativity

Bredin et al. [107] propose a deeper analysis to deduce the plasma electronegativity and the temperature of each species from the I-V curve, by fitting the simulated Langmuir curve Figure 4.1b to the real data. The fit function is $I(V) = I_e(V) + I_+(V) + I_-(V)$, its complete expression is found section 4.1.1. The parameters of the fit are:

- the positive ion density n_+;
- the electron density n_e;
- the electron temperature T_e;
- the negative ion temperature T_-;
- the positive ion temperature T_+.

The negative ion density is then calculated assuming plasma neutrality. The complete method from Bredin et al. [107] is not fully reproduced here, only the first fit on the I-V curve is done, not the second on the second derivative.

By fitting the I-V, one finds again n_e and T_e that were previously calculated by integration of the EEPF. It is worth comparing the outputs of both methods before going any further. Concerning electron densities, fitting the I-V curve leads to values in good agreement with the calculations using the EEDF done from the VGPS setup, but with a constant factor 2 lower, as shown Figure 4.12a. This factor 2 also appears in argon plasmas and is therefore not linked to the molecular or electronegative nature of the I_2 plasma. The values calculated with the EEDF are considered more reliable and are kept for comparisons with the model in Chapter 5. Concerning electron temperatures, the trend is the same but the values are lower, as shown Figure 4.12b. It will be shown in the next chapter that the values calculated with the EEDF are closer to the model predictions. Nonetheless, this agreement is considered good, and one can now look at the electronegativity values given by the fit.

Unfortunately, the available data are not sufficient to constrain the positive and negative ion temperatures. This is partly due to the fact that the function $I(V)$ is defined by pieces below and above the plasma potential V_p, and that very few data are available above the plasma potential. Indeed, this electron saturation region is the most likely to damage to probe, so the

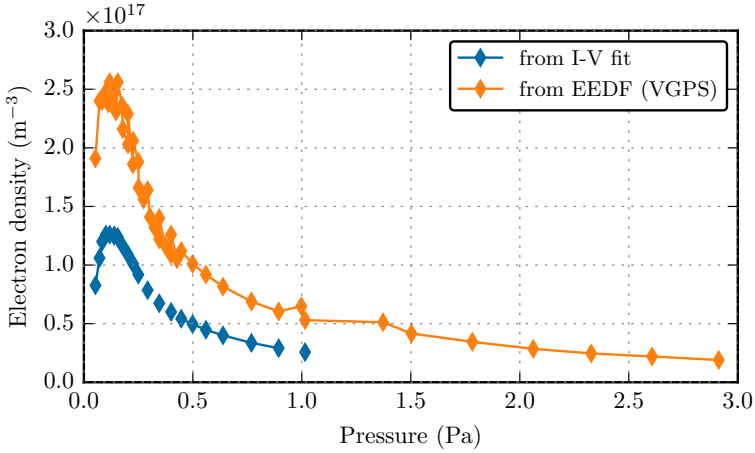

(a) Electron density at 190 W provided by VGPS based on the EEDF, or calculated via a fit of the I-V curve. Data at 188 W and 192 W from EEDF were adjusted to 190 W and concatenated, leading to some additional variation on the data. Both curves differ by a ratio of 2.

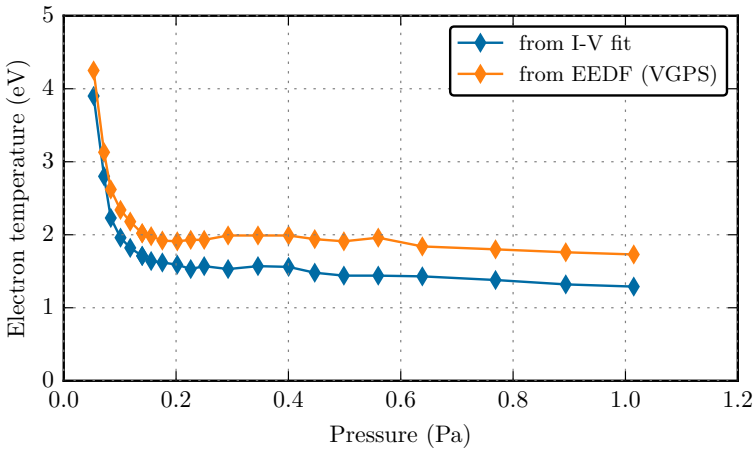

(b) T_e at 190 W provided by VGPS based on the EEDF, or calculated via a fit of the I-V curve. Between 0.2 Pa and 1 Pa, the difference is around 0.5 eV.

Figure 4.12: Outputs of the I-V fit compared to the EEDF method used by the VGPS data analysis tool.

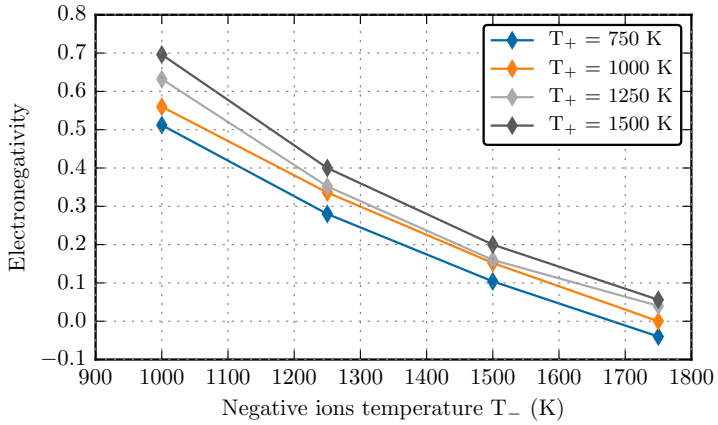

Figure 4.13: The calculated electronegativity at 0.14 Pa and 190 W depending on positive and negative ions temperature, for a certain fitting method and set of initial conditions.

VGPS system stops the measurements a few volts only after V_p is reached. To compensate, one can impose a positive and negative ion temperature in the fitting process. As no measurements of such temperatures are available, an estimate has to be provided. The other parameters of the fit are very sensitive to those temperatures: Figure 4.13 shows the value of electronegativity retrieved by the fit depending on the temperatures imposed for a specific data point, varying from −0.05 to 0.7! Additional complications appeared in the analysis process due to the bad fit at voltage under −10 V: the model for the effective probe radius that worked for Bredin et al. [107] and their probe with a diameter of 50 µm may not be adapted to the probe used here, of diameter 200 µm. Such problems, so as to the high variability of the fit parameters depending to the initial conditions, lead to date, in this work, to non reproducible results. Therefore, the findings are not reported here but most of the methods showed a negligible electronegativity at 190 W for the pressure tested (0.1 Pa to 1 Pa), validating the approximation of $\alpha = 0$ used to get T_e and n_e from the EEDF. At given ion temperatures, this fit can be further improved by adopting the solutions from Bredin et al. [107]: fitting the second derivative as well as the main curve, or using the so-called iterative method. But further improvements will necessitate an independent measurement of the ion temperatures.

4.4 Conclusions

It is shown in this chapter that the behavior of the electron density and temperature is qualitatively coherent with the model predictions and similar to what happens in an atomic xenon or argon plasma. n_e and T_e are retrieved by integrating the EEDF provided by the VGPS acquisition system from PlasmaSensors. At constant pressure, n_e is proportional to the discharge power P_d, and T_e is mostly constant with P_d. When varying pressure, T_e shows a sharp increase when moving towards very low pressure, and n_e presents a maximum around 0.1 Pa. A phenomenon of plasma localization is exhibited by measurements taken along the x-axis of the thruster next to the grid. It shows strong spatial gradients of n_e at high pressure, as the plasma gets localized away from the grids, enhancing a limit of the global model. A try is given at estimating the plasma electronegativity by fitting the I-V curve to a theoretical formula, a method inspired by Bredin et al. [107]: if this does not allow yet to retrieve the plasma electronegativity, it confirms within some margins the analysis done through integration of the EEDF measured with the Langmuir probe. Measuring the temperature of positive and negative ions would constrain the fit process and help retrieve the electronegativity. More precise comparisons between the global model and the experimental data from Chapter 3 and 4 are done Chapter 5.

Chapter 5

Comparison of model and experiments

Thanks to the work presented in the previous chapters, four optical diagnostics and one electrical diagnostic are available to measure absolute values of density and temperature of I, density of I_2 and density and temperature of the electrons in the plasma. In this chapter, we see how these measurements relate to each other and to the model predictions by showing successive comparisons of the results of the diagnostics with the related predictions of the global model. We discuss how the model captures the plasma dynamics observed in the experiments, and how these comparisons can constrain unknown parameters such as the I wall recombination rate. Some leads to explain the discrepancies are also explored, such as modifying the I_2 particle balance or electron power balance equation.

5.1 Methodology

To compare the model predictions and the experimental data, several parameters used in the code need to be computed. In particular, the gas temperature and the grid transparency are model inputs with a great influence on the results. This section also clarifies the notion of pressure used in this work, and the spatial localization of all measurements.

5.1.1 Adapting the gas temperature

The code uses the gas temperature as an input, and this temperature is kept constant. Iodine atoms and molecules are considered at the same temperature, so that the gas temperature is considered equal to $T_I = T_{\mathrm{I}_2} = T_g$. The value of gas temperature used in this chapter is based on the measurements of T_I done by laser spectroscopy, it is constant with discharge power and increasing with pressure. It is used as a code input, with an analytic formula to compute T_g from the mass flow rate of iodine.

The I atomic temperature was measured with laser absorption and presented Figure 3.24b in Chapter 3. It was found that the measured T_I is well fitted by a first order polynomial function of pressure, which was $T_{\mathrm{mes}}(\mathrm{K}) = 88\ p(\mathrm{Pa}) + 796$ (3.8). A similar relation can be found with mass flow rate, for the first set of grids:

$$T_I\ (\mathrm{K}) = 54\ Q(\mathrm{sccm}) + 790 \qquad \textit{first grid} \tag{5.1}$$

With the second grid of higher transparency, one needs ten times more mass flow rate to reach the same pressure. The temperature is adapted so that the same pressure, the same temperature:

$$T_I\ (\mathrm{K}) = 5.4\ Q(\mathrm{sccm}) + 790 \qquad \textit{second grid}$$

The temperature used in the code is shown Figure 5.1 together with all the related data. The data considered is the *measured* temperature along the line of sight, considered a good approximation of an average gas temperature. More information about the gas temperature is given section 3.4.4.

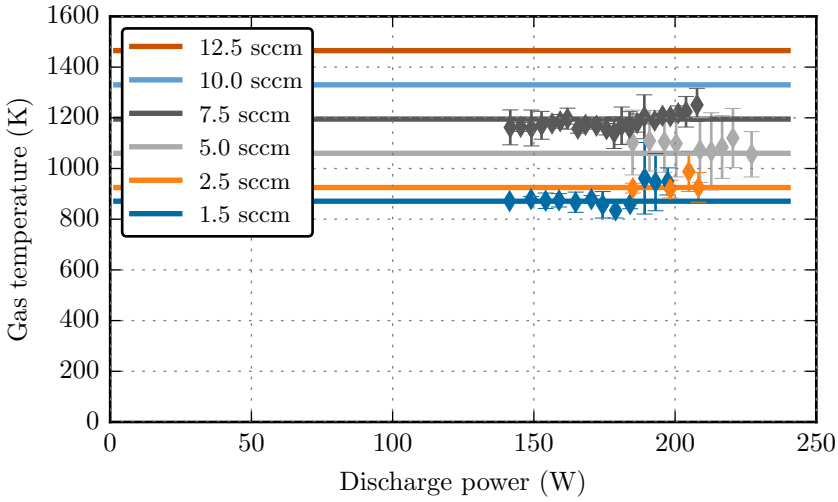

Figure 5.1: Measurements of I temperature by laser absorption (diamonds) with the first grid, reproduced from Figure 3.24a; and temperature used in the global model (solid lines), from equation (5.1). The errorbars are experimental errors, as detailed section 3.4.

5.1.2 Adapting the grid transparency

Motivation The model uses a mass flow rate as input, not a pressure. To estimate the exhaust rate out of the plasma chamber, knowing the grid transparency is crucial. A good estimate of the exhaust rate ensures that the pressure predicted by the model for a given iodine mass flow rate is coherent with the pressure measured during the experiments. It is shown that using the real grid transparency does not predict the good pressure. The discrepancy is too big to be linked to the densities or temperatures of the species, but originates from the model of the flow though the holes. In this work, the grid transparency is therefore used as an ad-hoc parameter that is adapted so that the pressure measured is close to the pressure predicted. The following paragraphs contain more explanations and an attempt to explain the discrepancies between the physical transparency and the ad-hoc parameters used, so that a realistic model could be developed in the future.

Geometrical transparency Two different grids were used during the experiments, shown Figure 5.2. Both grids placed on PEGASES are 12 cm wide and 8 cm high. Grid 1 is simply a full plate in which a 1 cm diameter hole is drilled, in the center. The *geometrical grid transparency* of grid 1 for neutrals and ions $\beta = \beta_i = \beta_0$ is therefore 0.8 %. Grid 2 is covered with around 4500 holes of 1 mm in diameter in the middle of which a 1 cm-diameter hole was later drilled. The *geometrical grid transparency* of grid 2 for neutrals and ions $\beta = \beta_i = \beta_0$ is therefore around 35 %.

Effective transparency without plasma The neutral flux model used in the plasma, presented section 2.3.4, assumes perfect holes with no grid thickness, and a perfect vacuum behind it. Both assumptions take the model quite off the reality. This leads to a bad estimate of the pressure for a given mass flow rate. This is corrected by using an effective grid transparency β_{eff}. It can be computed for a case without plasma using the fact that, at steady state:

$$Q_0 = \frac{1}{4}[\mathrm{I_2}] v_{th,\mathrm{I_2}} \beta_{\text{eff}} \mathcal{A}_{\text{grid}} \tag{5.2}$$

To find the effective grid transparency β_{eff}, one needs to know the mass flow rate, the I_2 density and the gas temperature. All these were measured with broadband absorption spectroscopy (as presented section 3.5), with grid 1. This leads to an *effective grid transparency without plasma* of grid 1 of 1.4 %, as shown Figure 5.3.

(a) Grid 1, used during the optical diagnostics. There is only one hole. The center hole is 1 cm in diameter.

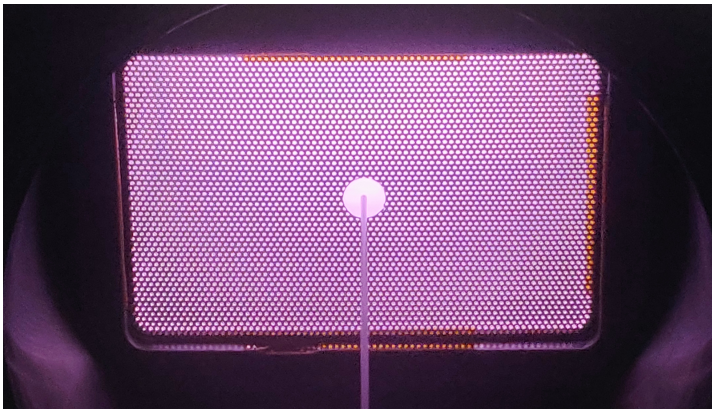

(b) Grid 2, used during the electrical diagnostics to reach a lower pressure for a given mass flow rate, picture taken while running Langmuir probe diagnostics in an argon plasma. The center hole is still 1 cm in diameter, surrounded by around 4500 holes of 1 mm in diameter.

Figure 5.2: Grids used during the experiments detailed in this work. The grids were insulated from the vacuum chamber and left at floating potential.

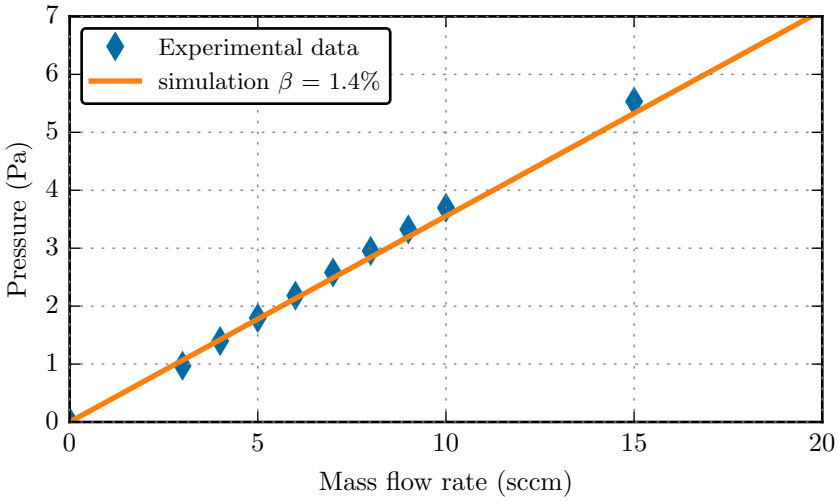

Figure 5.3: With an effective grid transparency of 1.4 %, a pure I_2 gas and no plasma, equation (5.2) predicts well the gas behavior. Reproduced from Figure 3.34.

Effective transparency with plasma This grid transparency does not predict well the behavior of the plasma when the plasma is turned on, as shown Figure 5.4 where the actual full global model is run: using the same grid transparency leads to underestimating the neutral fluxes out of the thruster, and therefore overestimating the pressure.

This discrepancy can be explained by the flux model. The random thermal flux used in the model for the neutrals uses the bulk temperature and density. If the gas is not homogeneous, a more accurate flux model Γ' should use the edge values of density and temperature. We define here the average values with a subscript 0, there are the ones used traditionally in the model. The subscript *grid* denotes values in the vicinity of the grid hole. If the plasma is supposed isobar, we have:

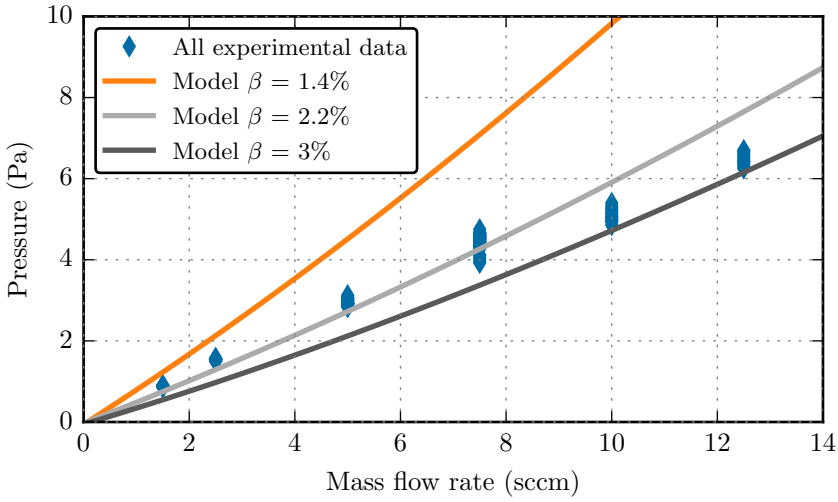

Figure 5.4: For the first grid, gas pressure in the plasma as a function of mass flow rate, for different grid transparencies, as predicted by the model and compared to the experimental data.

$$\begin{aligned}\Gamma' &= \frac{1}{4} n_{\text{grid}} v_{th,\text{grid}} \\ &= \frac{1}{4}\left(n_0 \frac{T_0}{T_{\text{grid}}}\right)\left(v_{th,0}\sqrt{\frac{T_{\text{grid}}}{T_0}}\right) \\ &= \Gamma_0 \sqrt{\frac{T_0}{T_{\text{grid}}}}\end{aligned}$$

This formula needs to be validated experimentally, by measuring T_{grid} that is not available in this work. In a case where the central temperature is higher than the gas temperature next to the grid hole, this leads to a flux higher than the one used in the model, hence a lower pressure. This is what is seen experimentally, in the discrepancy shown Figure 5.4.

For the first grid, an *effective grid transparency with plasma* of 2.2 % is used, an ad-hoc value found by trial and error. If the model presented

	Grid 1	Grid 2
Geometrical transparency	0.8%	around 35%
Effective transparency without plasma	1.4%	unknown
Effective transparency with plasma	2.2%	22%

Table 5.1: Summary of grid properties, as measured directly on the grid (geometrical) or estimated by trial and error for use in the simulations (effective).

above is good, this would correspond to a temperature in the vicinity of the grid 2.5 times lower than the average gas temperature in the plasma. Such a gap is plausible, as $T_g \approx 1000\,\mathrm{K}$, $T_{\mathrm{walls}} \approx 300\,\mathrm{K}$ and we can expect $T_g > T_{\mathrm{grid}} > T_{\mathrm{walls}}$, as the thermal conductivity of the grid with the outside is not as good as the walls, but still non zero. With the second grid, an *effective grid transparency with plasma* of 22 % is used, as shown Figure 5.5. A summary is given Table 5.1. It is considered that using the same effective transparency for each flow rate and power yields a good enough agreement, so that the effective transparency is not recalculated at each flow rate and power to ease the simulations. These ad-hoc modifications ensure that the pressures predicted by the model for a given mass flow rate are coherent with the experiments.

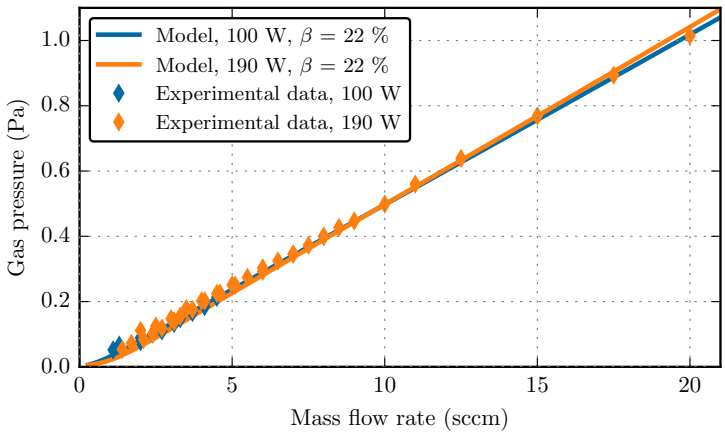

Figure 5.5: For the second grid, gas pressure in the plasma as a function of mass flow rate, for different grid transparencies, model and experimental.

5.1.3 What about the electron pressure?

What species contribute to the pressure measured during experiments? This is important to understand, to know whether the model curves shall be drawn using the total pressure as x-axis, or only the neutral partial pressure, also called gas pressure.

Nearly every publication of a plasma global model ([38, 77, 78] to only cite a few) use the neutral partial pressure as x-axis. The key question for this work is what pressure is actually measured by the capacitance manometer on PEGASES, as using the wrong pressure would make the comparisons less relevant. It should be noted first that this question is only important at very low pressure, as from 0.8 Pa of total pressure, the electrons are predicted to account for less than 10 % of the total pressure. This is shown Figure 5.6, where each species was described as an ideal gas. The ion pressure is always negligible. On this figure, the global model predictions are used. The global model is later shown to overestimate electron density by a factor of 3 on average, and the electron temperature by 40 %, so the electron partial pressure is overestimated on this plot by a factor 4 to 5 compared to the measurements.

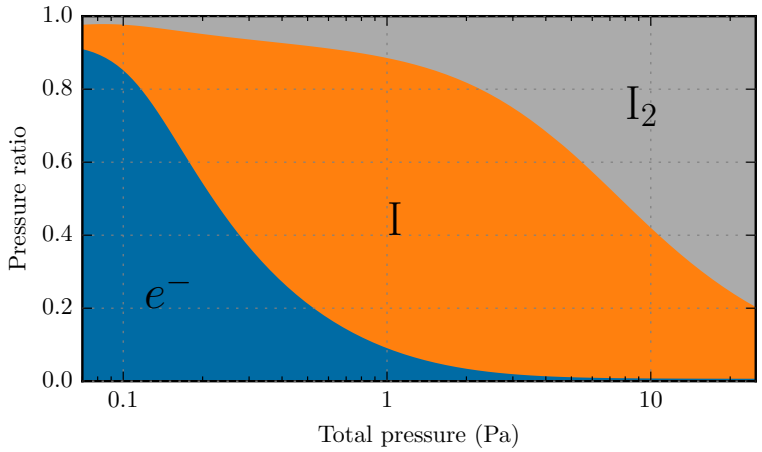

Figure 5.6: Contribution on total pressure of each species, as a function of the *total* plasma pressure, as predicted by the global model. The pressure on the x-axis accounts for the electron pressure.

According to the model, the total pressure should increase significantly when the discharge power is increased for a constant mass flow rate. During the experiments, it was shown that the dependency of the pressure with power was nearly negligible (Figure 5.5). This means that the measured pressure is independent from the electron partial pressure. Liard et al. [110] have studied similar effects with time, suggesting that the excess electron pressure modifies the effective pumping speed outwards of the reactor, keeping the overall pressure constant. To account for this phenomenon, as well as to better describe the plasmas studied here and to be coherent with the literature, the pressure used, unless mentioned otherwise, is the neutral partial pressure.

5.1.4 Where are the measurements done?

This paragraph and Figure 5.7 recall the origin of the experimental data used in this chapter. The global model predictions are the average data, direct outputs of the model, not modified to account for any 1D, 2D or 3D effects.

The Langmuir probe data are taken with the probe tip located at the coordinates $(x, y, z) = (1.7\,\text{cm}, 0, 0)$ in PEGASES. This is the center of the thruster on the vertical axis, and exactly between both windows on the y-axis, but not in the center on the x-axis: it is at 7.7 cm from the RF antenna side, and 4.3 cm of the exhaust grid. This is so because the first probe used was too short too reach the center of the ionization chamber, and measurements could not be repeated with a longer probe in time due to COVID-19 confinement rules.

The raw optical measurements are averaged along the y-axis - between the windows - and along the x-axis because of the two to nine passes that are done with the lamp or the laser at different x locations, as shown Figure 3.14 for the laser absorption setup, and Figure 3.31 for the broadband absorption setup. The experimental data used in this chapter are values at the center, computed with 1D models presented Chapter 3, assuming a cosine-distribution of I atoms, a quadratic distribution of I_2 molecules, and windows filled with a pure I_2 isobar gas.

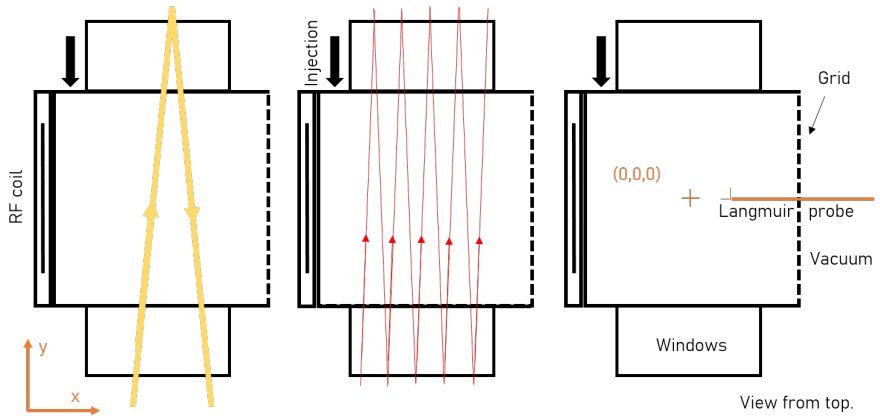

Figure 5.7: Measurement localization: absorption path for broadband (left) and IR laser absorption (center), and position of the Langmuir probe (right).

5.2 Neutral dynamics: I_2 dissociation

The data used to constrained neutral dynamics comes from the optical diagnostics detailed in Chapter 3. These diagnostics were operated at relatively high pressure, above 1 Pa. It was shown section 4.3.3 that n_e and T_e were greatly localized along the x-axis at these pressures. The optical diagnostics were done using several passes in the plasma at different locations on the x-axis, which has an averaging effect. *The following analysis assumes that the neutral populations are homogeneous along the x-axis within PEGASES.* Because the average values of the I_2 density are biased due to the large Brewster-angle windows fill with non-ionized gas, the experimental densities used for comparisons are the values at the center, computed Chapter 3.

5.2.1 I iodine atoms

The I density measured in the plasma is around 1.4 times lower than predicted by the global model, as shown Figure 5.8 as a function of pressure. The trend with pressure is also well predicted, but the discrepancy is higher than the errorbar of the I measurements. The errorbars plotted are the systematic error due to the uncertainty on the cross section used, $1050 \pm 250\,\mathrm{fm}^2$ [91]. There are the main contributor to the error in this measurement.

Figure 5.8 shows the trend with discharge power: it is also well respected, notwithstanding the discrepancy in absolute values. The I density is quasi-constant with power under 5 sccm, and a slight increase at 7.5 sccm can be seen in both the measurements and the simulations.

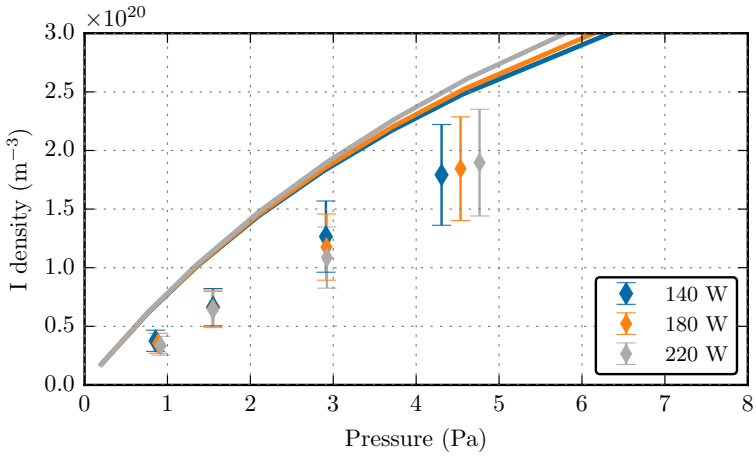

Figure 5.8: Measured I density at the center of the plasma, compared to the prediction of the global model, as a function of gas (neutral) pressure.

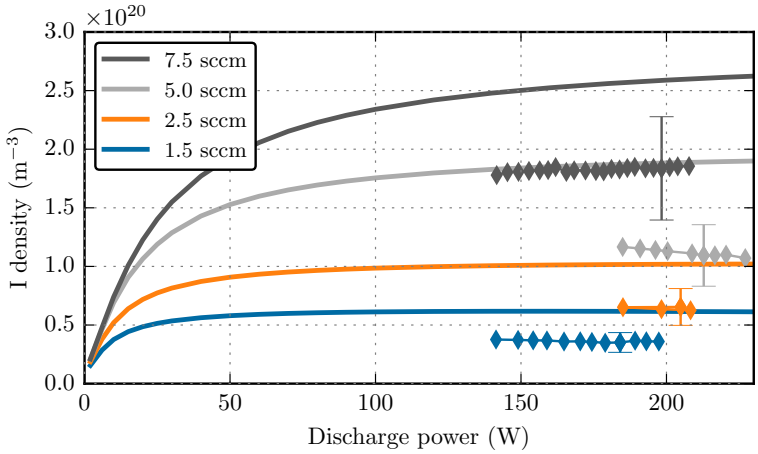

Figure 5.9: Measured I density at the center of the plasma, compared to the prediction of the global model, as a function of the discharge power, for four different mass flow rates.

5.2.2 I_2 iodine molecules

The model underestimates the central density of I_2, especially at low power, as shown Figure 5.10. It also predicts that I_2 density should increase with pressure, but the few experimental data points available show that the central density is rather constant with pressure at a constant discharge power.

At fixed mass flow rate and varying the discharge power, the trend is qualitatively well found as the I_2 density is predicted to decrease after 100 W of discharge power, as shown Figure 5.11. The dependency with discharge power is stronger than predicted.

The errorbars displayed are experimental errorbar linked to the measurement uncertainty only, and do not account for any additional uncertainty brought by the 1D model used to compute central density from the line-of-sight density of I_2.

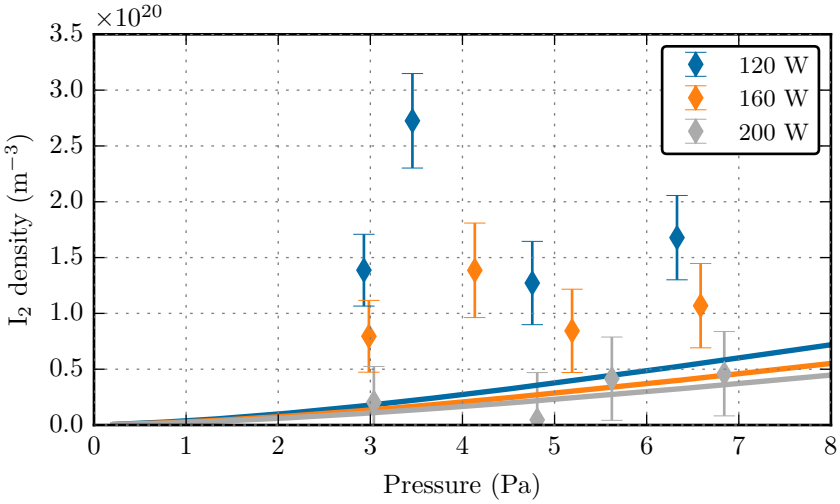

Figure 5.10: Measured I_2 density at the center of the plasma, compared to the prediction of the global model, as a function of gas (neutral) pressure.

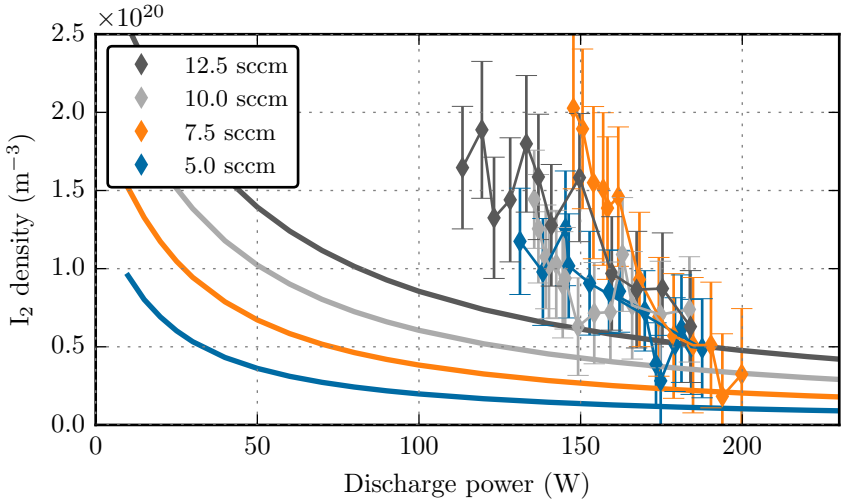

Figure 5.11: Measured I_2 density at the center of the plasma, compared to the prediction of the global model, as a function of the discharge power, for four different mass flow rates.

5.2.3 I_2 dissociation degree

Using the independent measurements of I and I_2, a dissociation degree, defined here as $[I]/([I]+[I_2])$ can be directly computed. Previous estimations of the dissociation degree (Figure 3.26) used the pressure measured by the capacitance manometer to infer information about the gas, the method presented here is not relying on pressure measurements.

Data about I and I_2 density are not available at the exact same power and pressure, so that a direct calculation of the dissociation degree is not possible. The following curves as plotted as such. Figure 5.12, for each discharge power plotted, [I] is fitted by a straight line from 0 Pa to 5 Pa: $[I] = a_I\ p + b_I$. $[I_2]$ is fitted by a straight line between 2.5 Pa to 7 Pa: $[I_2] = a_{I_2}\ p + b_{I_2}$. The dissociation degree for this power is then numerically calculated as $[I]/([I]+[I_2])$ using the analytical fits, and this is considered valid between 2 Pa to 5.5 Pa. Figure 5.13 follows the same logic.

On each curve, a single typical errorbar is presented, for readability. It does not correspond to a real data point. The errorbars of both measurements are independent and are added up, leading to a very large uncertainty. Most of this uncertainty is systematic, not random, and is due to the large uncertainty on the I cross section used in the laser absorption experiment.

As expected from the I and I_2 measurements, the dissociation degree is overestimated by the global model, shown Figure 5.12. The agreement is good at 200 W. Figure 5.13 highlights also that the evolution in $[I_2]$ with discharge power lead to relatively rapid changes of the dissociation degree, this dependency with power is stronger than predicted by the model. As the experimental data concerning I atoms were in rather good agreement with the model, the discrepancies between model and experiments for the dissociation degree are mostly due to the discrepancy in I_2 density.

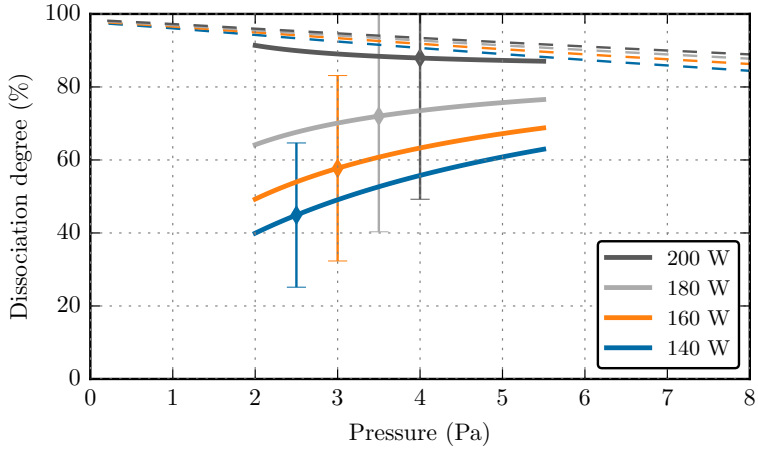

Figure 5.12: Dissociation degree ([I] / [I] + [I_2]) at the center of the plasma, estimated from measurements (full lines) compared to the prediction of the global model (dashed lines), as a function of gas (neutral) pressure.

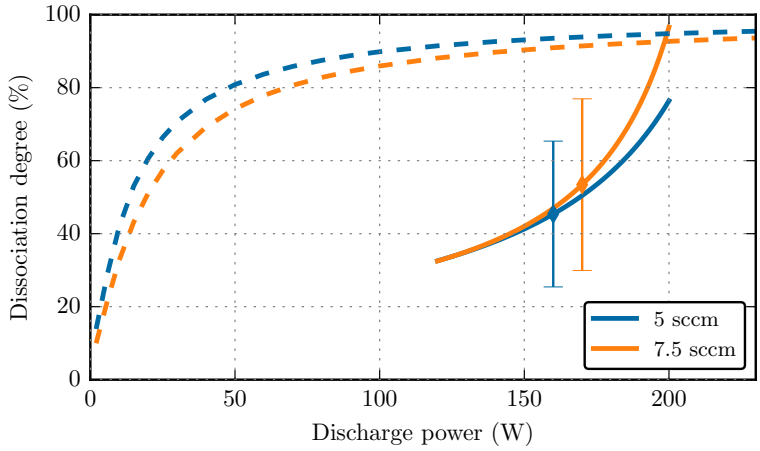

Figure 5.13: Dissociation degree ([I] / [I] + [I_2]) at the center of the plasma, etimated from measurements (full lines) compared to the prediction of the global model (dashed lines), as a function of the discharge power, for two different mass flow rates.

5.3 Plasma parameters: n_e and T_e

5.3.1 Electron density

The electron density is slightly overestimated by the global model, and the trends are well predicted. As a function of pressure, Figure 5.14 shows that the maximum measured density is around three times lower than the maximum electron density predicted. This maximum also appears at lower pressure. The electron density also decreases faster than expected at higher pressure, which is at least partially due to the plasma localization next to the antenna, away from the probe. A 1D model of electron distribution along the x-axis, from the antenna to the grid, would allow to take this localization into account and correct the model, or the experimental data.

About the variation with power, Figure 5.15 shows that the trends are well predicted, n_e is a linear function of the discharge power at all pressures probed.

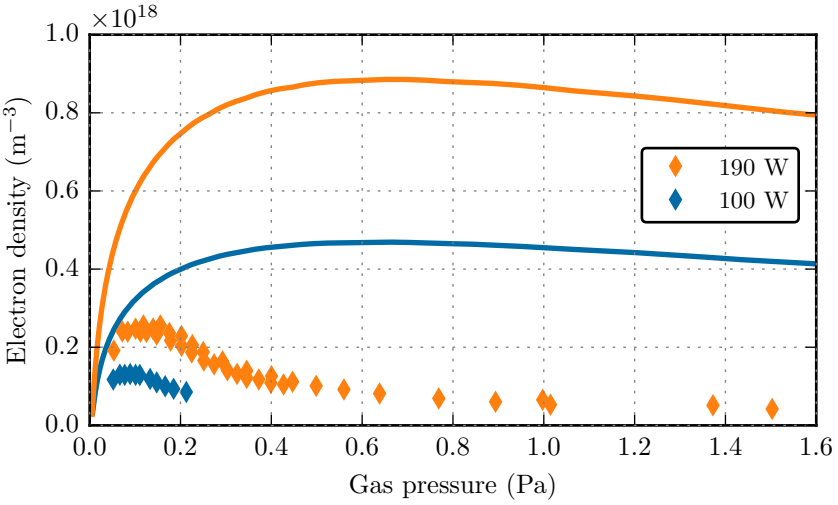

(a) n_e as a function of pressure, linear-scale, focusing on lower pressure data.

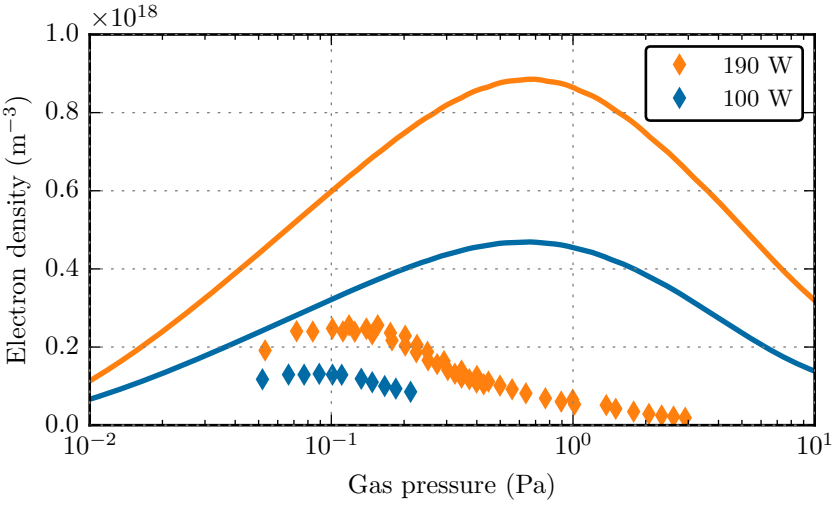

(b) n_e as a function of pressure, log-scale, full experimental dataset.

Figure 5.14: Electron density as a function of gas pressure, as predicted by the model and as measured. Two representations of the same data.

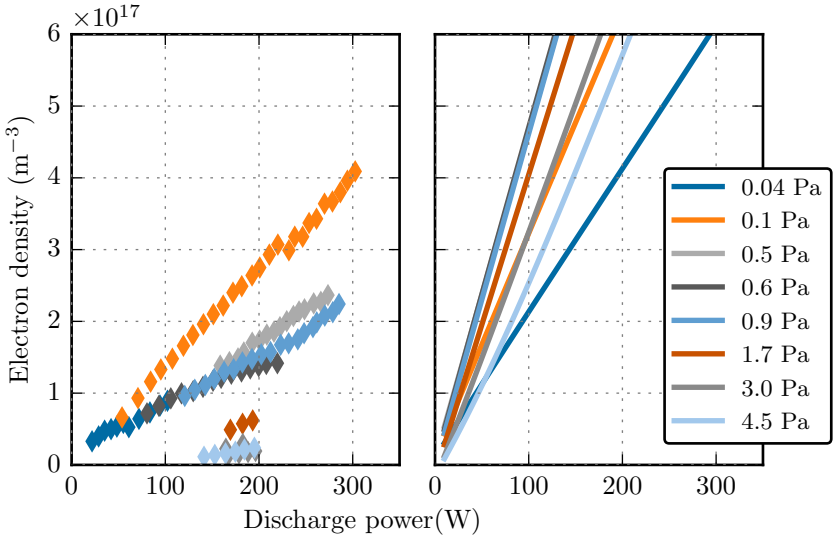

Figure 5.15: Electron density as a function of discharge power for a large set of gas pressure, measured (left) and predicted by the global model (right).

5.3.2 Electron temperature

The electron temperature is slightly overestimated a low pressure, under 1 Pa, as seen Figure 5.16. This is mostly due to a rate of temperature decrease that is underestimated in the model: T_e measured reached a constant value with pressure as soon as 0.3 Pa, where the model predicts this should happen only above 1 Pa. Figure 5.16b shows that, from 1 Pa, T_e that had reached a rather constant value decreases again, this is most probably due to the plasma localization away from the probe at high pressure.

The trends with discharge power are also well respected, as shown Figure 5.17. The electron temperature is constant at nearly all pressures, as expected.

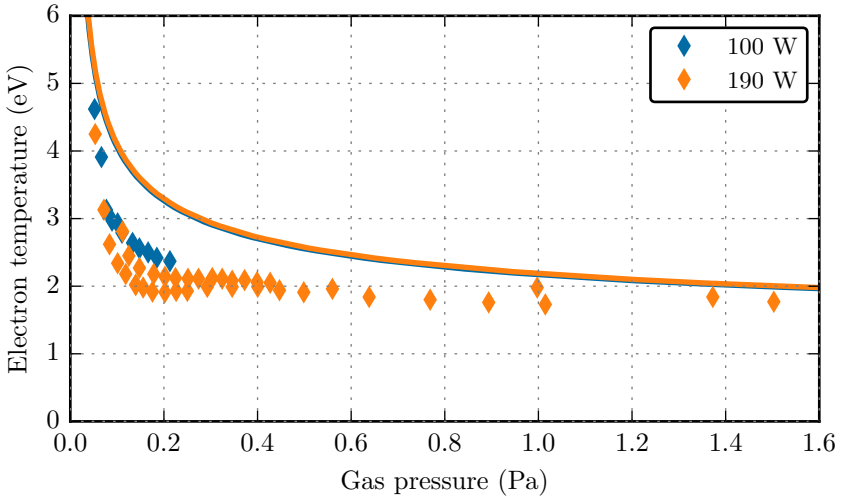

(a) T_e as a function of pressure, linear-scale, focusing on lower pressure data.

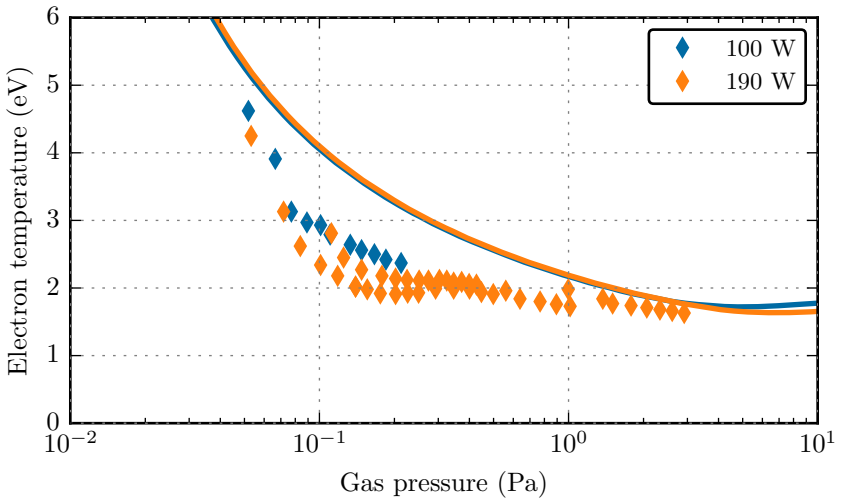

(b) T_e as a function of pressure, log-scale, full experimental dataset.

Figure 5.16: Electron temperature as a function of gas pressure, as predicted by the model and as measured. Two representations of the same data.

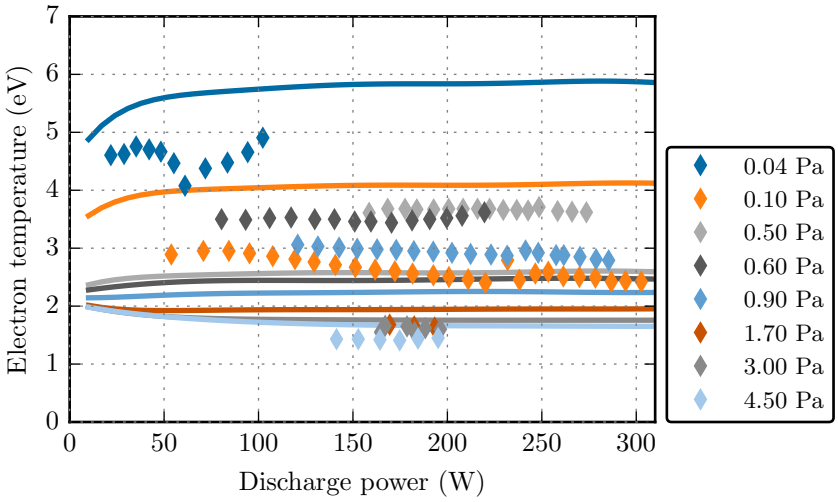

Figure 5.17: Electron temperature as a function of discharge power for a large set of gas pressure, measured and predicted by the global model.

The next three sections present leads to explain the discrepancies between the model predictions and the experimental data, by varying three major parameters. The underestimated I_2 density in the model can be corrected by increasing the wall recombination, or decreasing the dissociation rate. The overestimated electron density in the model can be corrected by increased the electron power losses. Can any of these changes explain a part or the totality of the discrepancies?

5.4 Estimation of the wall recombination

The dissociation degree measured is lower than the dissociation predicted: this can mean that either the sources of I_2 are underestimated, or the loss processes of I_2 are overerestimated. It was shown Figure 2.25a, reproduced below on Figure 5.18 that the wall recombination of I atoms is a major source of I_2 in the plasma, even bigger than I_2 injection through the pipes for the nominal cases studied, at 150 W and 10 sccm. The wall recombination rate of I being also very poorly known, one can try to increase the value of γ_{rec} in the model, from the value of 0.1 used until now. This is done in the present section. If this leads to a better agreement with the experimental data, a conclusion on the value of γ_{rec} could be drawn, even though the experiments were not designed for this.

5.4.1 I iodine atoms

Increasing γ_{rec} to 0.5 brings the model closer to the experiments in absolute values above a few Pa. The predictions below 1 Pa are not affected. But a greater γ_{rec} would mean that the I density is really non-linear with pressure, when the measurements show that [I] is rather linear with pressure on the four available data points, as shown Figure 5.19. A more systematic analysis while varying pressure will make the comparison of trends more relevant.

This problem - absolute values get better when increasing γ_{rec}, but not the trends - is seen with discharge power as well, Figure 5.20. The expected I density decreases when γ_{rec} increases, but then the I density should be increasing with power.

5.4.2 I_2 iodine molecules

Like for I atoms, increasing γ_{rec} to 0.5 brings the model closer to the experiments in absolute values above a few Pa, as shown Figure 5.21. But a greater γ_{rec} would mean that the I_2 density is really increasing with pressure, when the measurements show that [I] is rather constant with pressure on the four available data points at the pressures probed. A more systematic analysis while varying pressure will make the comparison of trends more relevant.

The effect on the trend with discharge power is really light, as the slope of the predicted density does not depend much on γ_{rec}, as shown Figure 5.22.

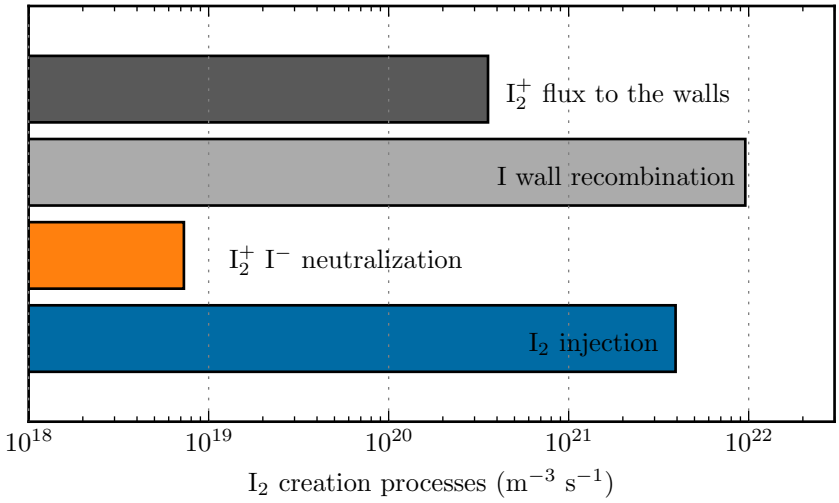

(a) I_2 gains

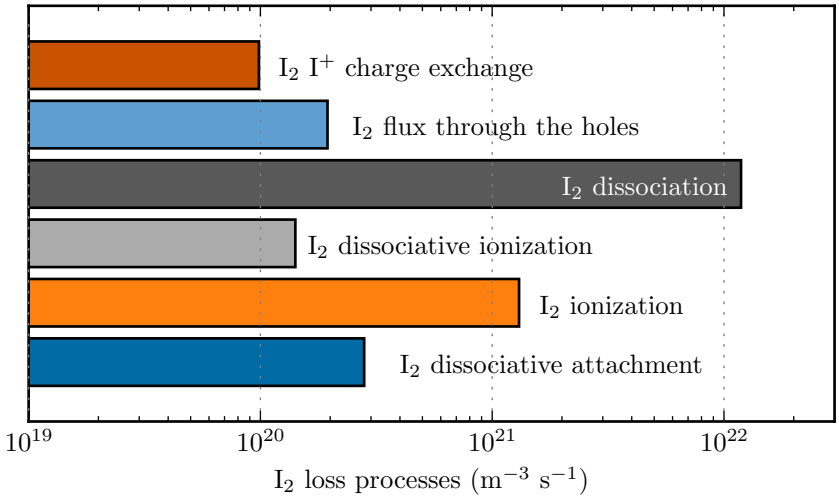

(b) I_2 losses

Figure 5.18: I_2 gain and loss mechanisms in an iodine plasma at $P_d = 150\,\mathrm{W}$ and $Q_0 = 10\,\mathrm{sccm}$, corresponding to $0.5\,\mathrm{Pa}$, reproduced from Figure 2.25a.

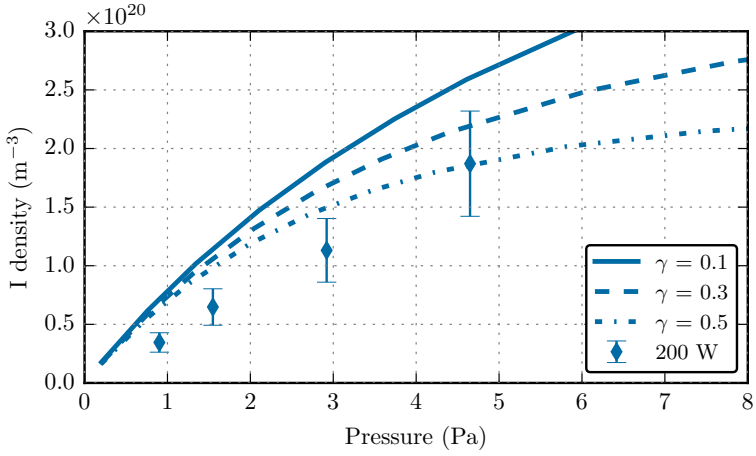

Figure 5.19: I density measured at 200 W and different pressures, and outputs of the global model for different values of γ_{rec}: 0.1 (solid lines), 0.3 (dashed lines) and 0.5 (mixed lines).

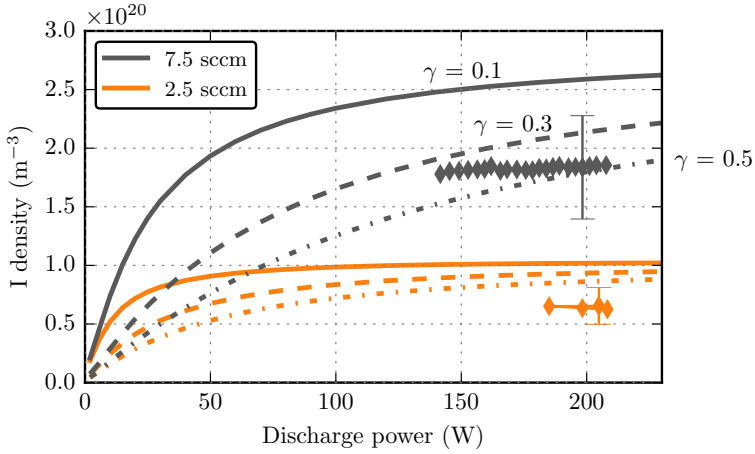

Figure 5.20: I density measured at 2.5 sccm and 7.5 sccm and different discharge power, and outputs of the global model for different values of γ_{rec}: 0.1 (solid lines), 0.3 (dashed lines) and 0.5 (mixed lines).

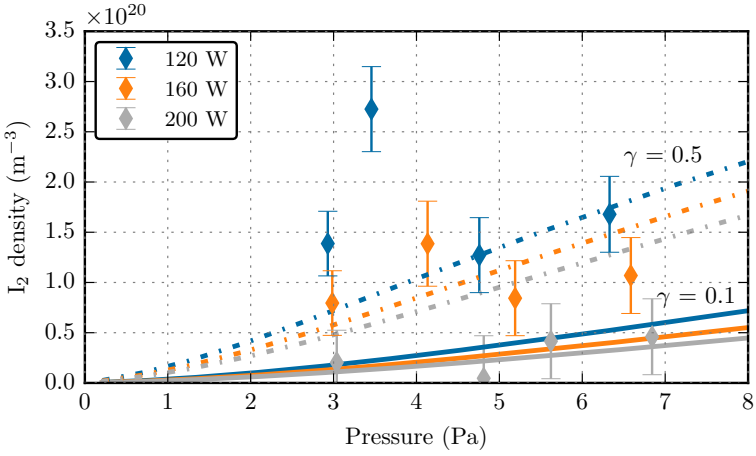

Figure 5.21: I_2 density measured at 120 W, 160 W and 200 W and different pressures, and outputs of the global model for different values of γ_{rec}: 0.1 (solid lines) and 0.5 (mixed lines).

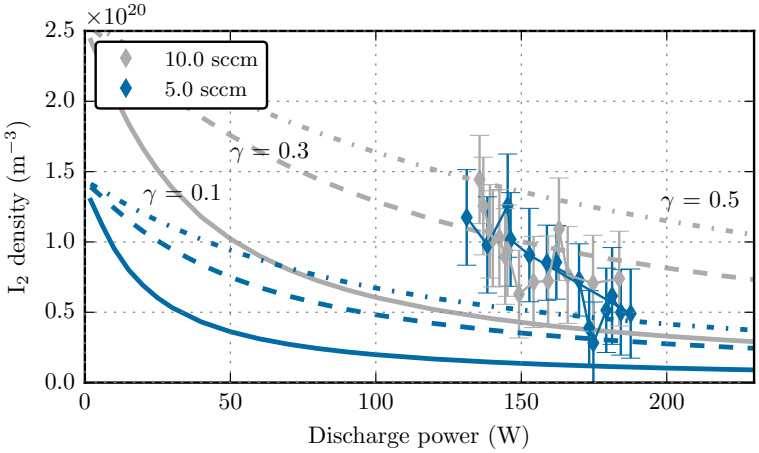

Figure 5.22: I_2 density measured at 5 sccm and 10 sccm and different discharge power, and outputs of the global model for different values of γ_{rec}: 0.1 (solid lines), 0.3 (dashed lines) and 0.5 (mixed lines).

5.4.3 I_2 dissociation degree

Joining the previous analyses allows to compare the evolution of the dissociation degree $[I]/([I] + [I_2])$, decreasing when γ_{rec} is increased. The absolute values are in better agreement but the trend in pressure still cannot explain the fact that the dissociation degree increases with pressure, Figure 5.23. The discrepancy in the dissociation degree comes mainly from discrepancy between the measurements and predictions of I_2 density, as shown in the previous paragraph.

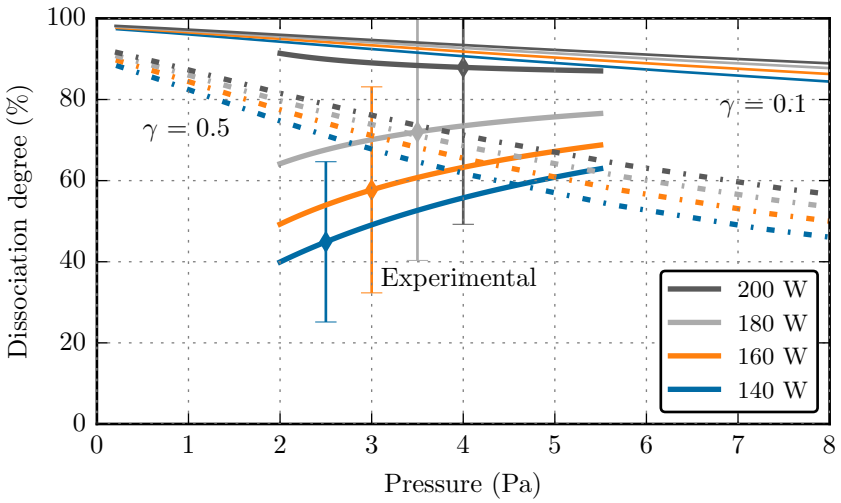

Figure 5.23: I_2 dissociation degree measured at 140 W, 160 W, 180 W and 200 W and different pressures, and outputs of the global model for different values of γ_{rec}: 0.1 (solid lines) and 0.5 (mixed lines).

The strong increase with pressure is also not better explained by a larger γ_{rec}, as shown Figure 5.24.

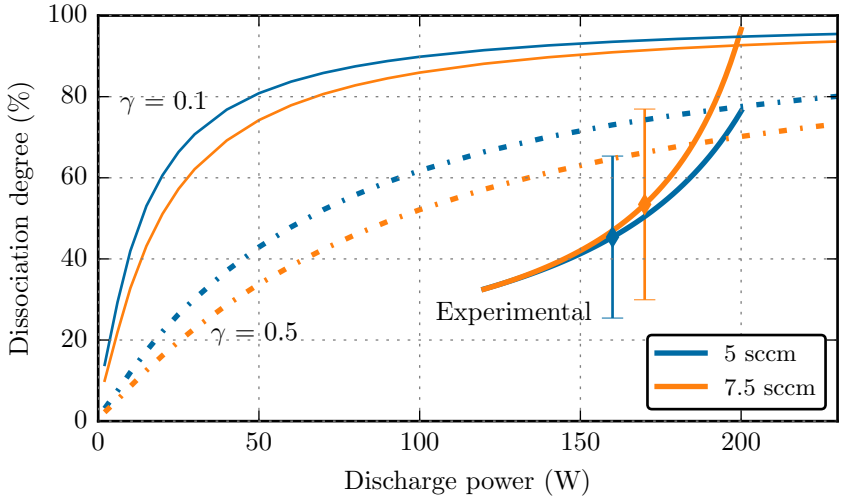

Figure 5.24: I_2 dissociation degree measured at 5 sccm and 7.5 sccm and different discharge power, and outputs of the global model for different values of γ_{rec}: 0.1 (solid lines) and 0.5 (mixed lines).

5.4.4 Electron density and temperature

As expected from the analysis section 2.9 and shown Figure 5.25, varying the wall recombination coefficient has no impact on n_e and T_e in the parameter space studied.

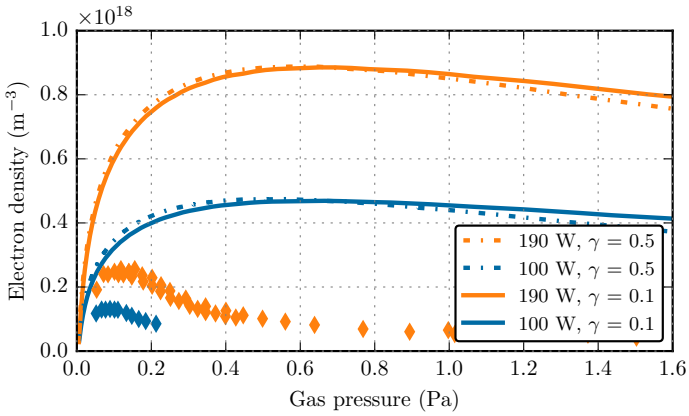

(a) Electron density

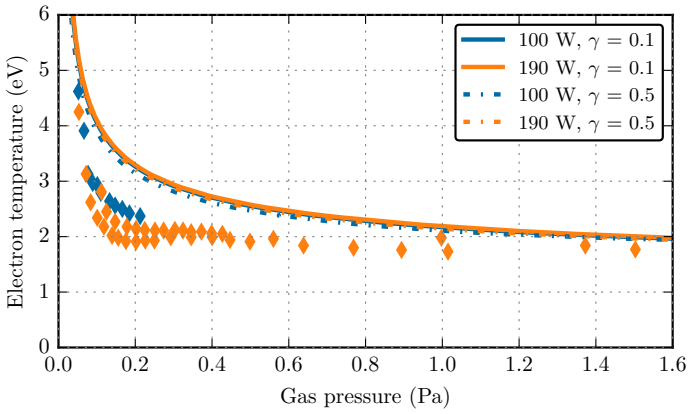

(b) Electron temperature

Figure 5.25: Electron density and temperature measured at 100 W and 190 W and different pressures, and outputs of the global model for different values of γ_{rec}: 0.1 (solid lines) and 0.5 (mixed lines).

5.4.5 Conclusion on $\gamma_{\mathbf{rec}}$

The fact that the global model overestimates the dissociation of I_2 molecules led to believe that increasing the wall recombination rate would improve the model predictions, to better fit the measurements, as wall recombination is the first source of I_2, from I atoms. In absolute values a value of $\gamma_{\mathrm{rec}} = 0.5$ would be optimal, but the trends observed are not coherent with such a value. Especially, the fact that the I density is nearly linear with pressure is better fitted by $\gamma_{\mathrm{rec}} = 0.1$ or lower.

With the present dataset, and given the uncertainty on the absolute values, the trends are estimated more reliable and it can be concluded that using $\gamma_{\mathrm{rec}} = 0.1$ leads to the best possible agreement of model and experimental data, all other things kept equal.

5.5 An overestimated dissociation rate?

The previous section studied the effect of varying the main source of I_2, the wall recombination of I atoms. This section studies the effect of varying the main loss process of I_2, the direct dissociation by electron impact. As shown Figure 5.18, more than 10 times more I_2 molecules are lost by direct dissociation than by any other processes. If lowering the dissociation rate yields a better agreement to the experimental data, this would motivate to do more calculation on the theoretical cross-sections. To explore the influence of this parameter, the present section compares the reference simulation with another simulation where the I_2 dissociation cross-sections, and therefore the dissociation rate, were divided by 10. The effects of this modification are similar, and slightly better, to what happens when γ_{rec} was multiplied by 5 to $\gamma_{\text{rec}} = 0.5$: the absolute values are closer to the models, even at low pressure. The trends are modified so that [I] is not predicted constant with pressure, but the new predictions are still rather consistent with the experimental data.

5.5.1 I iodine atoms

Dividing the dissociation rate K_{diss} by 10 brings the model closer to the experimental data in absolute values (Figure 5.26) but also changes the trend with discharge power (Figure 5.27). The agreement in trend is less good but still acceptable given the experimental uncertainty.

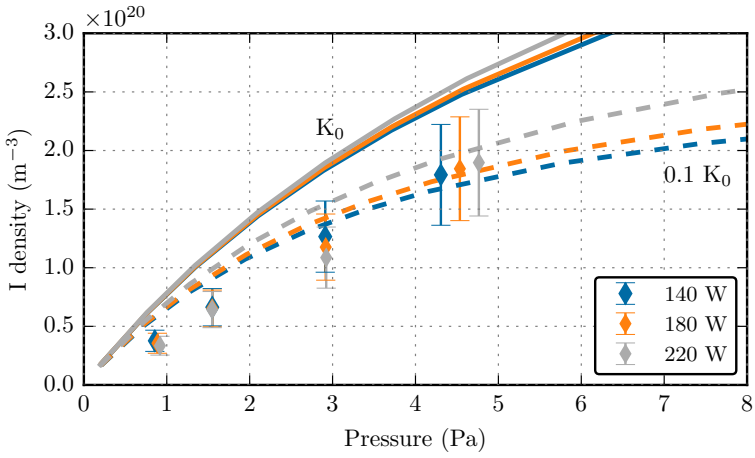

Figure 5.26: I density measured at 140 W, 180 W and 220 W and different pressures, and outputs of the global model for different values of K_{diss}, nominal (solid lines) or multiplied by 0.1 (dashed lines).

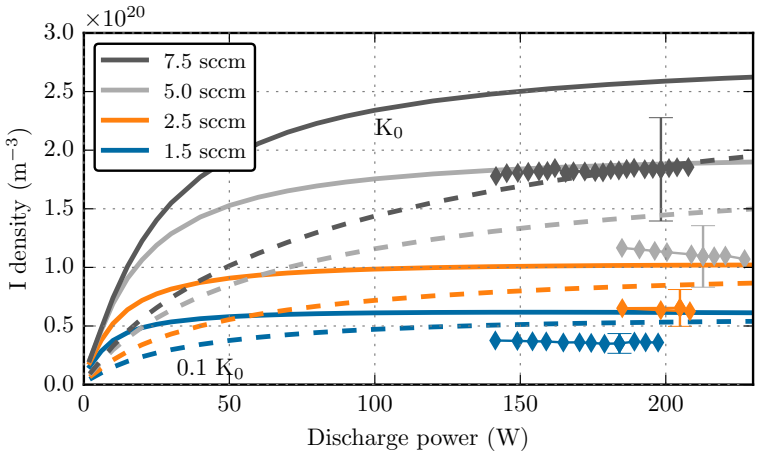

Figure 5.27: I density measured at 1.5 sccm, 2.5 sccm, 5 sccm and 7.5 sccm and different discharge power, and outputs of the global model for different values of K_{diss}, nominal (solid lines) or multiplied by 0.1 (dashed lines).

5.5.2 I_2 iodine molecules

Dividing K_{diss} by 10 has nearly the same positive impact on $[I_2]$ than multiplying γ_{rec} by 5, as shown Figure 5.28 and Figure 5.29. If the absolute values are better, the predicted trends are getting further away from the measured trends, as decreasing K_{diss} increases the dependency with pressure.

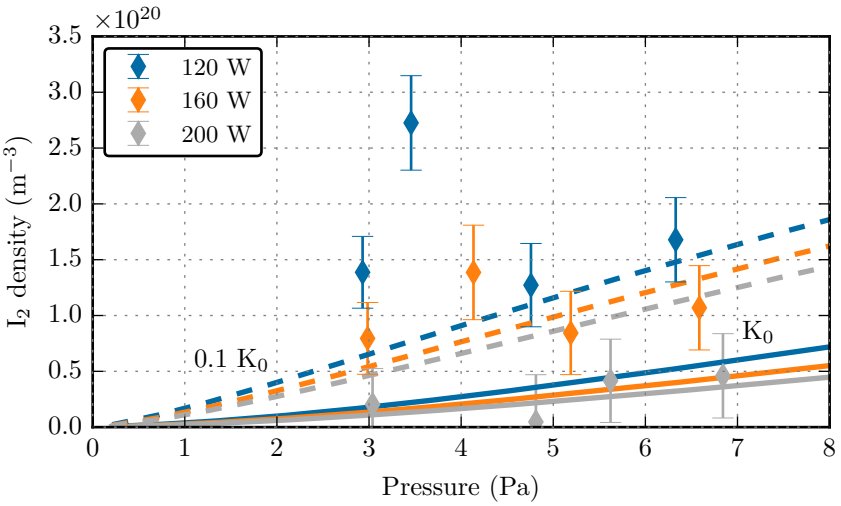

Figure 5.28: I_2 density measured at 120 W, 160 W and 200 W and different pressures, and outputs of the global model for different values of K_{diss}, nominal (solid lines) or multiplied by 0.1 (dashed lines).

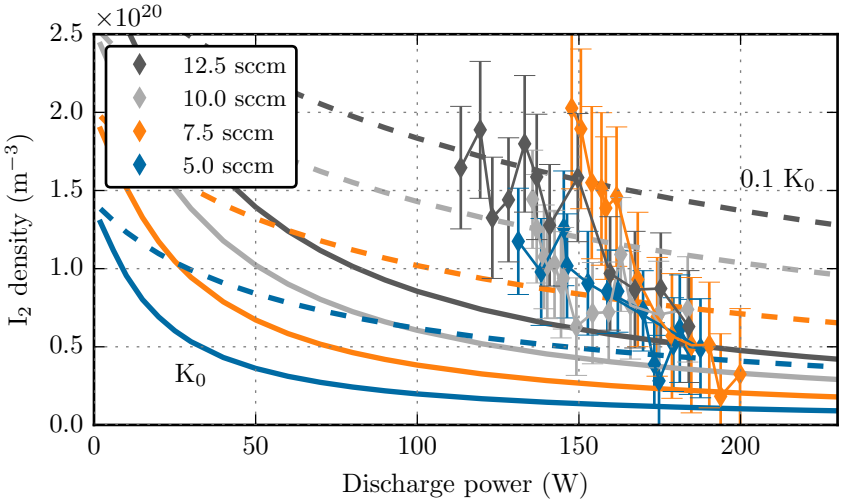

Figure 5.29: I_2 density measured at 5 sccm and 10 sccm and different discharge power, and outputs of the global model for different values of K_{diss}, nominal (solid lines) or multiplied by 0.1 (dashed lines).

5.5.3 I_2 dissociation degree

As expected from the I and I_2 predictions, decreasing the dissociation rate brings the absolute values of dissociation degree closer to the predictions, without explaining the observed trends, as shown Figure 5.30. This is similar to what happens when γ_{rec} in increased from 0.1 to 0.5.

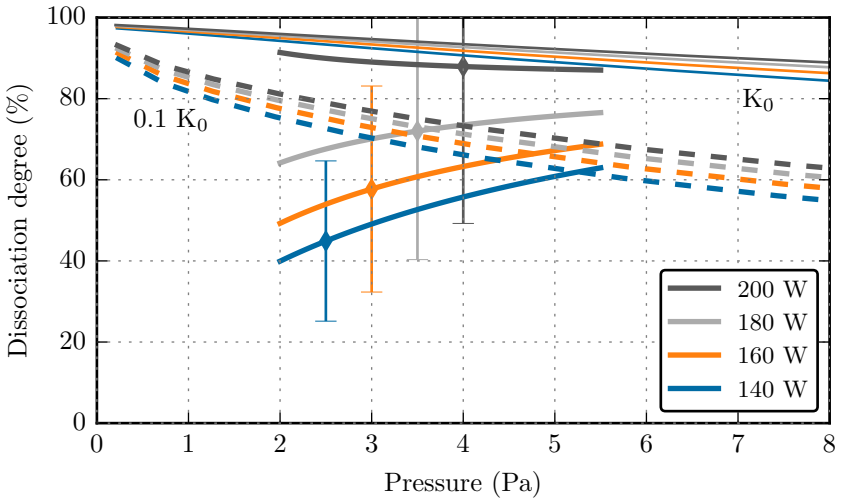

Figure 5.30: I_2 dissociation degree measured at 140 W, 160 W, 180 W and 200 W and different pressures, and outputs of the global model for different values of K_{diss}, nominal (solid lines) or multiplied by 0.1 (dashed lines).

5.5.4 Electron density and temperature

Reducing the dissociation degree slightly increases the expected electron density, taking it further away from the experimental data, as shown Figure 5.31. Dividing the dissociation rate by 10 has virtually no impact on the electron temperature.

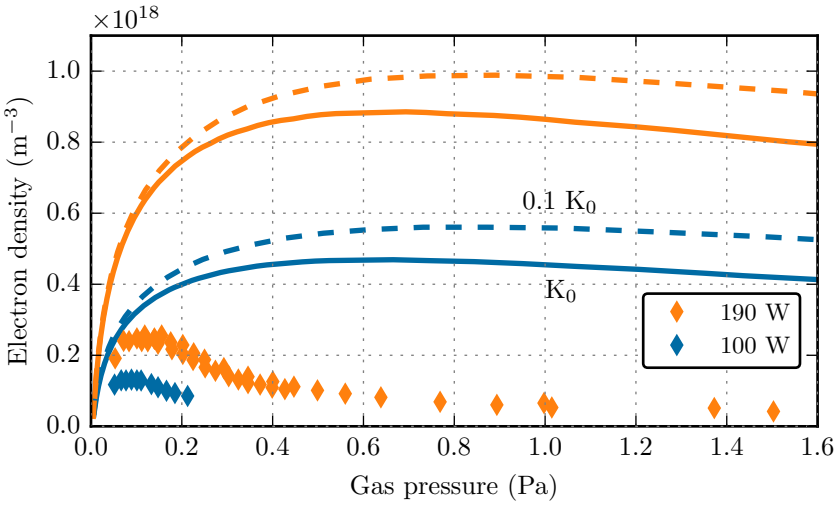

Figure 5.31: Electron density measured at 100 W and 190 W and different pressures, and outputs of the global model for different values of K_{diss}, nominal (solid lines) or multiplied by 0.1 (dashed lines).

5.5.5 Conclusion on the dissociation rate

To better fit the experimental data, decreasing K_{diss} is relatively equivalent to increasing γ_{rec}, but with a slightly better agreement on the neutrals and slightly worse agreement on the electron density. Again, the trends are considered more reliable here, so that it can be concluded that the dissociation rate used in this work is not widely overestimated.

5.6 Underestimated power losses?

The electron density is overestimated in the model compared to what is actually measured. A good way to reduce the predicted density is to increase the power losses. This can be done by adding loss processes, or by increasing the effects of existing loss processes. If the modified process does not appear in any particle balance equation, this is equivalent: it leads to an effective increase of P_{loss}.

To modify P_{loss}, we choose here to modify the main contributor to the power losses. Figure 2.31 shows that the main power loss process for the electrons is the excitation of I atoms. The corresponding term in the power balance equation is $P_{\text{loss, exc}} = \varepsilon_{\text{exc}} n_e [\text{I}] K_{\text{exc}} \mathcal{V}$ (presented section 2.5). It can be increased by changing the excitation threshold energy ε_{exc} or the excitation rate K_{exc}. Increasing the excitation rate or energy of I does not affect the particle balance equations, but changes the power balance. This is shown to bring the model predictions of n_e much closer to measurements and, interestingly, also acts favorably on the other predictions.

Increasing the electron power losses yields to better agreement with the experimental data: this should motivate to either recalculate the excitation cross-sections and energies used in the model, or find new power loss channels that are neglected for now, such as the molecular excitation of I_2, whether vibrational, rotational or electronic, that is neglected in this work.

5.6.1 I iodine atoms

While the creation process or losses of I are unchanged, increasing power losses by increasing $P_{\text{loss, exc}}$ yields the same effect than changing γ_{rec} or K_{diss}: a better agreement in absolute values, not in trends with pressure (Figure 5.32) or discharge power.

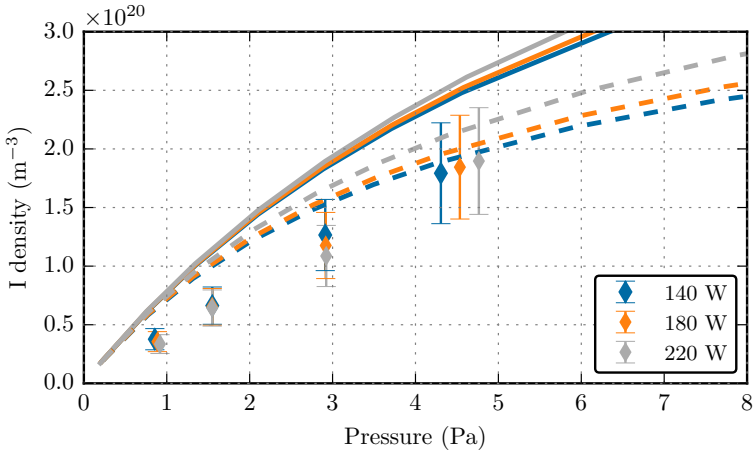

Figure 5.32: I density measured at 140 W, 180 W and 220 W and different pressures, and outputs of the global model for different values of $P_{\text{loss, exc}}$, nominal (solid lines) or multiplied by 5 (dashed lines).

5.6.2 I_2 iodine molecules

Multiplying $P_{\text{loss, exc}}$ by 5 has nearly the same impact on $[I_2]$ than multiplying γ_{rec} by 5, as shown Figure 5.33. Nonetheless, the trends are still rather coherent with the experimental data using this modified rate.

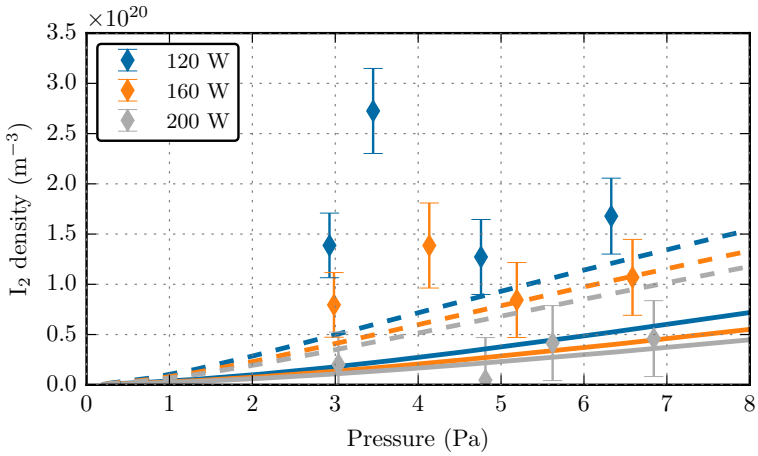

Figure 5.33: I_2 density measured at 120 W, 160 W and 200 W and different pressures, and outputs of the global model for different values of $P_{\text{loss, exc}}$, nominal (solid lines) or multiplied by 5 (dashed lines).

5.6.3 I_2 dissociation degree

As expected from the I and I_2 predictions, increasing the I excitation power losses bring the absolute values of dissociation degree closer to the predictions, without explaining the observed trends, as shown Figure 5.30.

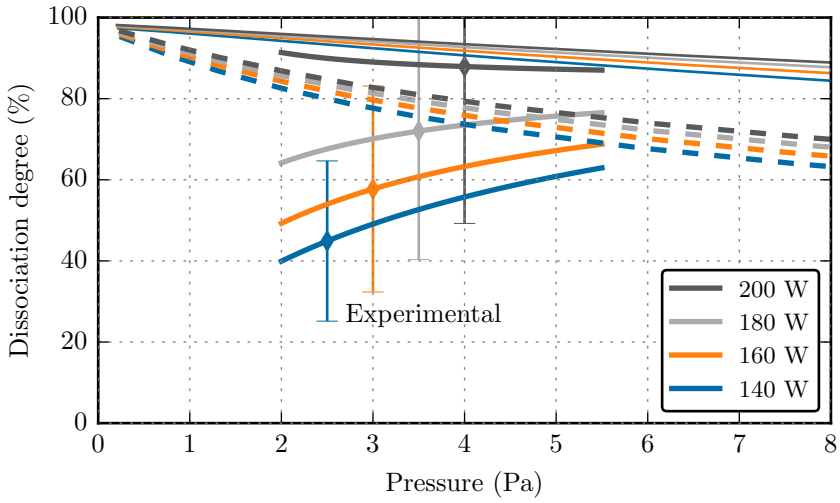

Figure 5.34: I_2 dissociation degree measured at 140 W, 160 W, 180 W and 200 W and different pressures, and outputs of the global model for different values of $P_{\text{loss, exc}}$, nominal (solid lines) or multiplied by 5 (dashed lines).

5.6.4 Electron density and temperature

As multiplying $P_{\text{loss, exc}}$ only impacts the power balance equation, its main effect is on the electron density n_e. It decreases the simulations so that the discrepancy with the experimental data in only a factor 2 on the maximum. The location of the maximum, around 0.1 Pa, is also well predicted, as shown Figure 5.35. Multiplying $P_{\text{loss, exc}}$ by 5 has virtually no import on the electron temperature.

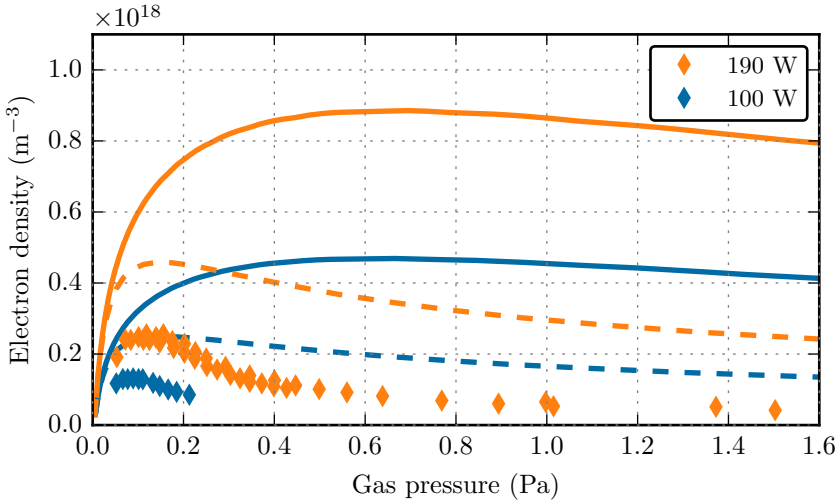

Figure 5.35: Electron density measured at 100 W and 190 W and different pressures, and outputs of the global model for different values of $P_{\text{loss, exc}}$, nominal (solid lines) or multiplied by 5 (dashed lines).

5.6.5 Conclusion on the power losses

The excess of electrons predicted by the model compared to actual measurements can be partly explained by underestimated power loss processes. It is shown that increasing the power losses, as shown here through $P_{\text{loss, exc}}$, can also explain the discrepancies in I and I_2 density. Underestimated power losses are therefore the best lead studied here to explain the discrepancies between the model and the experiments.

5.7 Conclusions

The pumping model used in the model is not valid for the comparison, resulting in a large underestimation of the neutral flux through the grids. To ensure that the pressure predicted by the model for a given mass flow rate is coherent with the experimental data, an empirical model of grid transparency is presented, to justify the use of ad-hoc values. While the data treatment can be further improved by 1D models of the iodine plasma in the thruster, the comparisons between the global model and the experiments reveal an overall good agreement in trends and values, especially for n_e and T_e. It is shown that the model predicts well most of the trends, except the evolution of central I_2 density with pressure. The agreement in absolute values is also quite good, but the model overestimates the dissociation of I_2 in I atoms, and the electron density. The discrepancies range between 30 % (for I atoms), a factor of 3 (for the electron density), and an order of magnitude for I_2 densities at the center. To improve the predictions, it is possible to modify the I_2 particle balance coefficients: increasing γ_{rec} or decreasing the I_2 dissociation rate does improve the agreement of I and I_2 densities in absolute values the same way, but the trends are better explained by a γ_{rec} factor around 0.1. It is also possible to modify the electron power balance: increasing the power losses reduces the predicted electron density, giving a relatively good agreement with the experimental data of electron parameters, and this also reduces the I_2 dissociation, improving the model predictions for the neutrals.

To try and correct the model, efforts should therefore be focused on improving the power loss model, which is the main parameter that can improve the model predictions for both the neutrals and the electrons. As an example, power losses due to the molecular nature of I_2 are assumed throughout this work to be very low, and could have been underestimated.

Conclusions and perspectives

After introducing space propulsion and electric propulsion, the first chapter of this work presented how the present work finds its rationale in the NewSpace dynamics of the late 2010s and early 2020s, where new actors in the propulsion sector serve new clients envisioning large satellite constellations. In particular, the quest for less expensive propellants is at the core of a new interest in iodine, but the underlying complex theory of iodine plasmas is lacking behind empirical observations of the good performances of iodine in laboratory thrusters. Iodine plasmas can participate in a wider and better use of propulsion in space, provided that they are well understood and dispose of reliable diagnostics. The second section presented the experimental room. It particularly presented a vacuum setup dedicated to iodine and how it was modified to be able to cope with several successive measurement campaigns. From a practical point of view, using iodine in an experimental setup for nearly two years shows that an industrial generalization of this propellant for the electric propulsion industry is not a utopia, providing the setups and processes are correctly adapted.

The second chapter and the first appendix present a global model of an iodine inductively coupled plasma, whose code is fully rewritten to ease parametric studies and uncertainty quantification, and enable fast chemistry modifications. Motivated by measurements of high values of electronegativity in some iodine plasmas by Grondein [46], several electronegative features are incorporated and are shown to affect the results mainly above a few Pa, where the electronegativity is calculated to be between 1 and 10. The plasma behaves quite differently at very low pressures and at pressures higher than a few Pa. A method is presented to calculate errorbars for all outputs of the

model, based on estimations of the uncertainty of the model inputs such as the wall recombination rate of I atoms, or the reaction rate of each reaction. Preliminary errorbars are presented, as a first step towards a more systematic uncertainty quantification approach in global models, to evaluate our confidence in the model and to guide further efforts to improve the reaction set. The dominant processes for creation and loss of each species are exhibited, as well as the main processes of power losses, to pave the way for reduced reaction sets for use in more complex codes such as the PIC code developed by Lucken [56]. Four parameters used as model inputs are specifically studied: the grid transparency β_0, the wall recombination rate of I atoms γ_{rec}, the gas temperature T_g, and the shape of the electron energy distribution function. It is shown that β_0 and γ_{rec} does not affect n_e or T_e, that γ_{rec} has a strong effect on the dissociation degree mainly at high pressure, that increasing the gas temperature increases pressure but decreases neutral densities, and that the model is rather independent from the distribution used (Maxwellian or Druyvesteyn), except for T_e that changes to adapt the rates and maintain the plasma balance. The rewritten code of the global model accelerates parametric analysis to isolate and understand the impact of every parameter of the model, and enables some uncertainty quantification. These studies led to new understandings of, on one hand, how hypotheses in the model could affect the predictions and, on the other hand, what design drivers are available for real propulsion systems. Such a work should also motivate the community to better track uncertainties in the models so that no code is run without errorbars, to work towards making their code available online, to open-source them, and to embrace a more collaborative approach for their developments. Future works in modeling of iodine plasmas shall also focus on 1D and 2D models, to go beyond the volume averages of global models.

The third and fourth chapters of this work focus on diagnostics developed to characterize the iodine plasmas. Four different optical diagnostics using spectroscopy to gather information about the density and temperature of the neutral species I and I_2 are presented. The diagnostics are demonstrated in the case of a relatively high-pressure plasma, between 0.9 Pa and 4.5 Pa, in the ionization chamber of the PEGASES thruster, without magnetic barrier nor acceleration stage. Emission spectroscopy is first implemented by collecting the light emitted by the iodine plasma with a spectrometer. Identification of the molecular and atomic emission bands and lines leads to qualitative information about the prominence of species in different setups and at different operating conditions. It also helps identifying strong lines and bands that can be probed by laser or broadband absorption. Infra-red laser absorp-

tion is performed using a Titanium-Sapphire laser on two of the strongest lines of the I atom, at $10\,969\,\mathrm{cm}^{-1}$ and $11\,036\,\mathrm{cm}^{-1}$ (911 nm and 906 nm). It exhibits rich hyperfine structures that are explored and characterized with Doppler-free spectroscopy. A saturation analysis is also performed to fully characterize the transition. This experiment leads to the temperature of atomic iodine with a very large signal-to-noise ratio. A very weak dipolar magnetic and electric quadrupolar transition at $7603\,\mathrm{cm}^{-1}$ (1.315 µm), within the fine structure of the fundamental state of the I atom, was probed by laser absorption. Absorption data successfully leads to the line-of-sight integrated temperature and density of the I atoms within the ion source. A measurement campaign is presented using broad-band absorption spectroscopy on I_2 molecules. An absorption continuum of the I_2 molecule allows to effectively retrieve the I_2 density from absorption between 480 nm and 500 nm. I temperature, I density and I_2 density from these experiments are values integrated along the laser or lamp line-of-sight: 1D models are proposed to estimate the repartition within PEGASES, and to get an estimate of the dissociation degree of I_2 in the plasma. Using a Langmuir probe, n_e and T_e are then retrieved by integrating the EEDF provided by the VGPS acquisition system from PlasmaSensors. At constant pressure, n_e is proportional to the discharge power P_d, and T_e is mostly constant with P_d. When varying pressure, T_e shows a sharp increase when moving towards very low pressure, and n_e presents a maximum around 0.1 Pa. A phenomenon of plasma localization is exhibited by measurements taken along the x-axis of the thruster next to the grid. It shows strong spatial gradients of n_e at high pressure, as the plasma gets localized away from the grids, enhancing a limit of the global model. A try is given to estimate the plasma electronegativity by fitting the I-V curve to a theoretical formula, a method inspired by Bredin et al. [107]: if this does not allow yet to retrieve the plasma electronegativity, it confirms within some margins the analysis done through integration of the EEDF measured with the Langmuir probe. Laser Induced Fluorescence and photodetachment experiments are logical next steps of using spectroscopy to characterize the plasma, this time for charged species I^+ and I^-. Other future measurements need to include optical accesses more resistant to iodine to reduce dead volumes, radial measurements, localized measurements (for example with Laser-Induced Fluorescence), measurements at lower pressure (for example with Cavity Ring-Down spectroscopy to increase the signal-to-noise ratio), measurements of the temperatures of positive and negative ions to enable the retrieval of the plasma electronegativity from the Langmuir probe data and more precise 1D or 2D models of neutral distribution.

The comparisons of these data to the model, done in the fifth chapter, lead to precautions conclusions about iodine plasmas for use as propellant for electric propulsion. The pumping model used in the model is not valid for the comparison, resulting in a large underestimation of the neutral flux through the grids. To ensure that the pressure predicted by the model for a given mass flow rate is coherent with the experimental data, an empirical model of grid transparency is presented, to justify the use of ad-hoc values. While the data treatment can be further improved by 1D models of the iodine plasma in the thruster, the comparisons between the global model and the experiments reveal an overall good agreement in trends and values, especially for n_e and T_e. It is shown that the model predicts well most of the trends, except the evolution of central I_2 density with pressure. The agreement in absolute values is also quite good, but the model overestimates dissociation of I_2 in I atoms, and the electron density. The discrepancies range between 30 % (for I atoms), a factor of 3 (for the electron density), and an order of magnitude for I_2 densities at the center. To improve the predictions, it is possible to modify to I_2 particle balance coefficients: increasing γ_{rec} or decreasing the I_2 dissociation rate does improve the agreement of I and I_2 densities in absolute values the same way, but the trends are better explained by a γ_{rec} factor around 0.1. It is also possible to modify the electron power balance: increasing the power losses reduces the predicted electron density, giving a relatively good agreement with the experimental data of electron parameters, and this also reduces the I_2 dissociation, improving the model predictions for the neutrals. To try and correct the model, efforts should therefore be focused on improving the power loss model, which is the main parameter that can improve the model predictions for both the neutrals and the electrons. As an example, power losses due to the molecular nature of I_2 are assumed throughout this work to be very low, and could have be underestimated.

Appendix A

Insights on LPP0D

The global model presented chapter 2 is written in different files, to ease reutilization, parametric analyses, shared work with multiple developers, etc. The code is written in python. It is named LPP0D, for Laboratoire de Physique des Plasmas Zero Dimension. By the time this thesis is written, it is hosted on a private git server at LPP but shall be opened in the future, under an open-source license. The principal design drivers were:

- The code shall work with different gases;
- The user shall be able to run a parametric analysis without changing the equations;
- The user shall be able to easily add or remove a chemical reaction.

The code architecture is shown Figure A.1. The main principles are recalled here. The user interface is an *init.txt* text file, in which the user specifies: the gas used (for example: I_2), the species considered (for example: I_2, I, I^+, ${I_2}^+$, I^-, electrons), the reactions considered in gas phase or at the walls (see Table 2.1), the gas being injection in the thruster, the thruster geometry, the grid transparency, and several parameters such as the input mass flow rate, the wall temperature, or the coil frequency.

This *init.txt* file is read by two different python functions:

- *generate_objects* generates three python objects: *chem*, *thruster*, and *params*. The *chem* object is an instantiation of the *Chemistry* class and its attributes are related to the gas, such as a dictionary containing all the reactions, themselves described with their reactants, products, and rates. The *thruster* object contains all parameters related to the thruster, and many functions to calculate all the volumes and areas that appear in the equation set. The *params* object is a instantiation of the *Parameters* class and contains all the remaining parameters.

- *generate_diff* generates the differential system corresponding to the seven equations described in section 2.5. It does it by following the exact logic that was described sections 2.3 and 2.4, with for example to nested loops looping within the species and the equations defined in the *init.txt* file. Fluxes are also calculated so that the wall interactions are included. Many parameters of the equations are attributes of the *chem*, *thruster*, and *params* objects. For example, the thruster volume is written as *thruster.volume()* in the equation set.

A function *solve* solves the differential system and outputs the temperatures and densities of each species listed in the *init.txt* file.

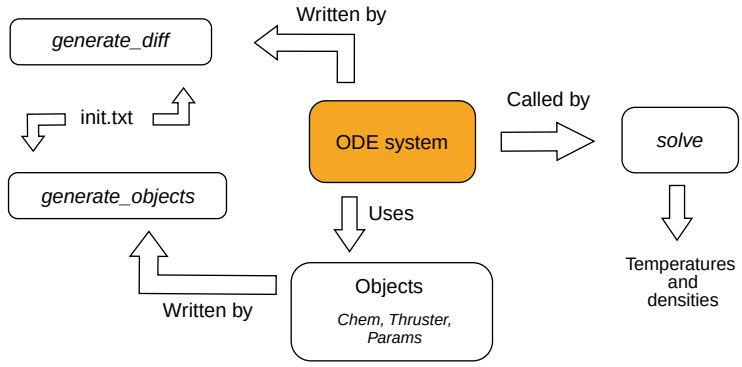

Figure A.1: Graphical representation of the code architecture.

The code fulfills the primary objectives: to change gas, the user only needs to change the *init.txt* file and add an excel or csv file for the reaction rates in the working directory. It was successfully tested on iodine, xenon and krypton. To run a parametric analysis, the corresponding objects can be modified in the analysis jupyter notebook, without changing any of the back-end code. A reaction is removed by only commenting the corresponding line in the *init.txt* file and regenerating the ODE system.

More codes related to the global model were developed during the thesis but not presented here. For the uncertainty quantification, a bash interface was developed so that the code can run on the lab clusters, running on slurm. The modularity of the code helps other projects of the team. For example, the *chemistry parser* building an ODE system from a text file containing a list of species and equations is reused in the frame of a collisional-radiative model for xenon [68].

Appendix B

Measuring the discharge power

A plasma discharge is characterized by its *discharge power* P_d, this is not equal to the RF power coming out from the generator. Godyak et al. [63] mention "poorly defined discharge conditions" as a typical experimental flaw. This appendix explains how the discharge power is measured in this thesis, to mitigate such a problem. The discharge power is the power actually dissipated in the plasma, and is lower than the RF power reaching PEGASES due to several loss phenomena in the matching circuit and the coil. This coil power does not reach the discharge and is noted P_c. The RF power is itself equal to the RF forward power sent by the RF generator minus any power reflected due to impedance mismatches.

$$P_d = P_{RF} - P_{\mathrm{c}} = P_{\mathrm{forward}} - P_{\mathrm{reflected}} - P_{\mathrm{c}}$$

A formal power transfer efficiency η_{PTE} can also be defined:

$$\eta_{\mathrm{PTE}} = \frac{P_d}{P_{RF}} = 1 - \frac{P_c}{P_{RF}}$$

Godyak et al. [111] give a recognized method to calculate the discharge power from the RF power in an ICP discharge, by measuring the current flowing in the antenna with and without plasmas. The matching circuit loss is a function of the coil current I_c. When the plasma is off - hence for a zero mass flow rate - and $I = I_c$:

$$P_d(I_c) = 0 = P_{RF} - P_c(I_c)$$

Measuring both RF power and coil current in PEGASES running without any gas injection gives a complete characterization of the circuit losses $P_c(I_c)$. In this work, the real plasma power P_d is calculated by measuring the coil current I_c with a PEARSON current probe during plasma operation and substracting $P_c(I_c)$ from the RF power indicated by the RF generator. Figure B.1 shows on the y-axis the RF power from the generator (any reflected power has been substracted) and on the x-axis the corresponding current measured in the coil with a Pearson current monitor while maintaining a zero mass flow rate. The current shown in this entire paragraph is the peak-to-peak value of the sinusoidal RF current. To get the effective current, one should use $I_c = 2\sqrt{2}I_{\text{eff}}$.

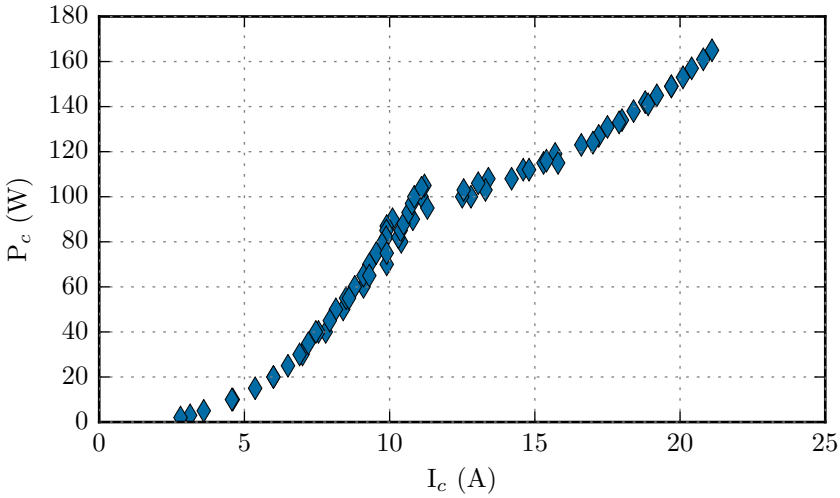

Figure B.1: Measured coil current amplitude (on the x-axis) as a function of the RF power read on the RF generator (y-axis) without plasma. Plotted like this, the distance under the curve is the power dissipated by the coil and matchbox for a given current.

The first remarkable phenomenon is the strong break in the power slope, and the second less remarkable phenomena is the presence of an hysteresis

near this breaking point. This is a characteristic of the ferrite material in which the antenna is placed. Every further experiments in this work show that during plasma operation, the peak-to-peak current never reaches more that 10 A. Therefore, an analytical formula of $P_c(I_c)$ is found by fitting the first part of the curve by a power law, neglecting hysteresis. Such a fit is shown Figure B.2 alongside the previous model from Bredin [54] which considered that $P_c = R_0 I_{\text{eff}}^2 = (R_0/8) I_c^2$. Once again, I_c is the peak-to-peak current.

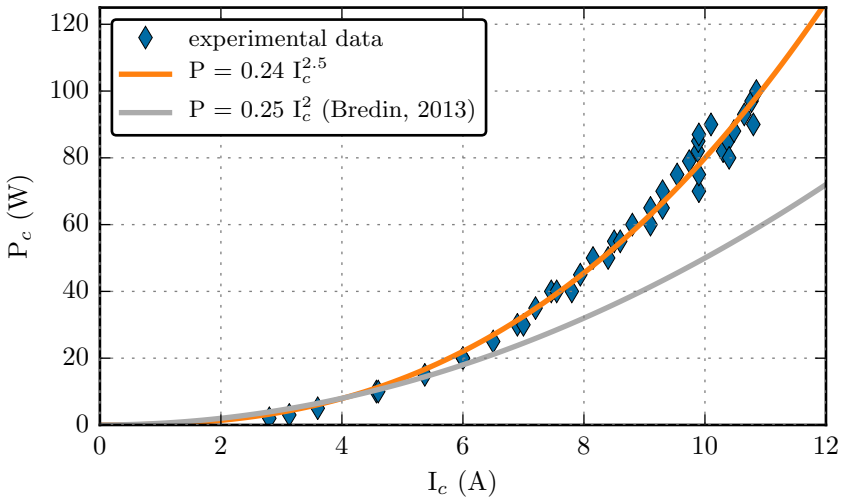

Figure B.2: Coil current amplitude (on the x-axis) as a function of the RF power (y-axis) without plasma, fitted with a power law (orange curve). The model from Bredin [54] is equivalent to having a matchbox resistance of 4 Ω.

The power lost in the matchbox and the antenna is then

$$P_c = 0.24\ I_c^{2.5} = 3.2\ I_{\text{c,eff}}^{2.5}$$

Following the notation from Godyak et al. [111] that calls resistance any prefactor in the power law here, it can be said that the matchbox and the antenna have a joined resistance of $R_c = 3.2\,\Omega$, in a convention where $P_c = R_c\ I_{\text{c,eff}}^{2.5}$. Previous work on PEGASES by Bredin [54] used a resistance of 4 Ω in a model where $P_c = R_c\ I_{\text{c,eff}}^2$. Both laws are close at current amplitudes

under 6 A but diverge at greater currents that do appear in the experiments. The power transfer efficiency in this work is then to be significantly lower for some data points. The current work shows that P_c follows a power law in $I_c^{2.5}$. Such a power law with an index greater than 2 is characteristic of an inductive behavior, and Godyak et al. [111] had stated a factor 2.1 in their setup. Through the present work, the discharge power is then linked to the RF power and the coil current by

$$P_d = P_{RF} - 0.24\ I_c^{2.5}$$

This corresponds to a power transfer efficiency depending on coil current amplitude and RF or discharge power:

$$\eta_{\text{PTE}} = 1 - \frac{0.24\ I_c^{2.5}}{P_{RF}} = \frac{P_d}{P_d + 0.24\ I_c^{2.5}}$$

As an example, the power transfer efficiency is measured in the plasma while varying pressure during a Langmuir probe measurement, for two fixed discharge power. The results are shown Figure B.3, the power transfer efficiency is between 85 % and 93 %, is higher at 192 W that at 101 W, and presents a maximum for a certain pressure. The pressure corresponding to the maximum is higher for the highest power.

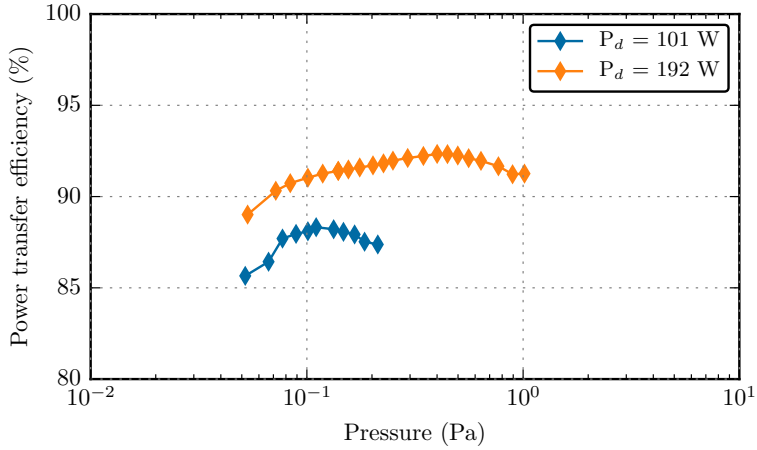

Figure B.3: Power transfer efficiency of the ion source used with I_2, as a function of pressure, for two fixed discharge powers.

Appendix C

Extrapolating cross-sections

C.1 Context and motivation

To get the value of the reaction rate at electron energies above several eV, one needs values of the cross-sections at higher energies, up to several hundreds of eV to integrate over the EEDF. The extrapolations used are explained and illustrated here. Not extrapolating cross-sections is equivalent to extrapolating by 0 and can lead to underestimations of the reaction rate. Under 5 eV, it matters only (but not much) for I_2 dissociation and I_2 elastic collisions.

C.2 I excitation

Figure C.1a shows the available cross-sections for excitation of the I atom from Hamilton [33] (available up to 54.3 eV) and three possible extrapolations at high energy. The extrapolation used in this work is done with a law proportional to $\ln(T_e)/T_e$ [69]. The resulting rates for each possible extrapolation are shown Figure C.1b: the choice of extrapolation does affect the rate only after 20 eV.

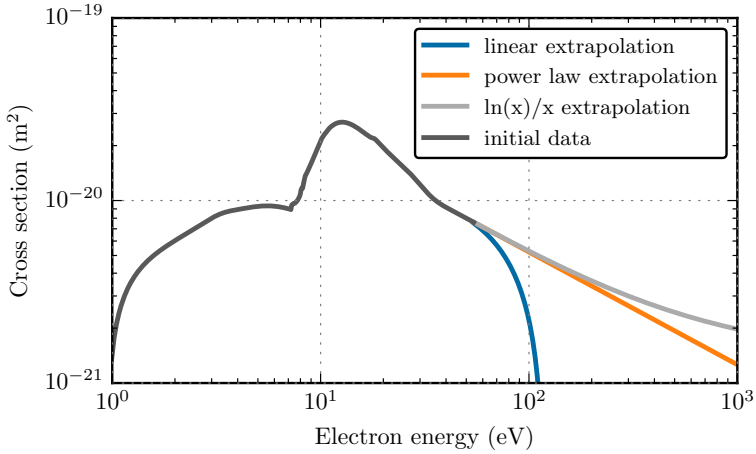

(a) I excitation cross-sections and possible extrapolations.

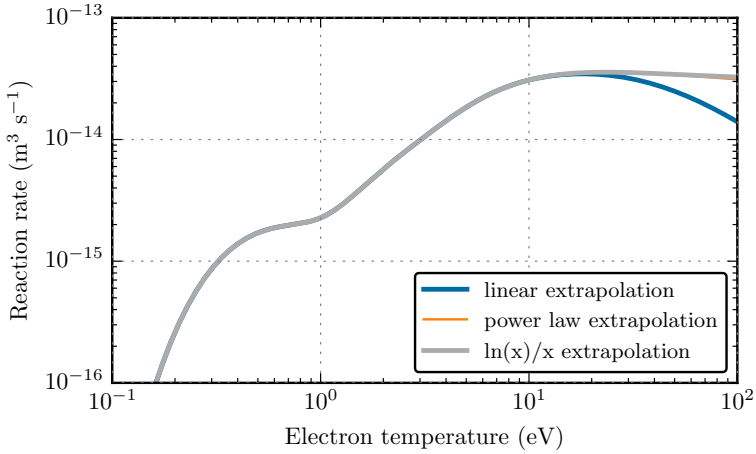

(b) I excitation reaction rate based on integration of the extrapolated cross-section over a Maxwellian EEDF.

Figure C.1: Extrapolation for excitation of I.

C.3 I elastic collisions

Figure C.2a shows the available cross-sections for elastic collisions of electrons with I atoms from Hamilton [33] (available up to 50 eV) and three possible extrapolations at high energy, as well as the one used at low energy. The extrapolation used in this work is done with a law proportional to $1/T_e$ [69]. The resulting rates for each possible extrapolation are shown Figure C.2b: the choice of extrapolation does affect the rate only after 30 eV.

C.4 I_2 elastic collisions

Figure C.3a shows the available cross-sections for elastic collisions of electrons with a I_2 molecule from Hamilton [33] (available up to 9.97 eV) and three possible extrapolations at high energy, as well as the one used at low energy. The extrapolation used in this work is done with a law proportional to $1/T_e$ [69]. The resulting rates for each possible extrapolation are shown Figure C.3b: the choice of extrapolation does affect the rate after 5 eV.

C.5 I_2 dissociation

Figure C.4a shows the available cross-sections for dissociation by electron impact of the I_2 molecule from Hamilton [33] (available up to 9.99 eV) and three possible extrapolations at high energy, as well as the one used at low energy. The extrapolation used in this work is done with a law proportional to $\ln(T_e)/T_e$ [69]. The resulting rates for each possible extrapolation are shown Figure C.4b: the choice of extrapolation does affect the rate after 4 eV.

C.6 I_2^+ dissociation

Figure C.5a shows the available cross-sections for dissociation by electron impact of the I_2^+ molecule from Hamilton [33] (available up to 100 eV) and three possible extrapolations at high energy, as well as the one used at low energy. The extrapolation used in this work is done with a law proportional to $\ln(T_e)/T_e$ [69]. The resulting rates for each possible extrapolation are shown Figure C.5b: the choice of extrapolation does only affect the rate after 30 eV.

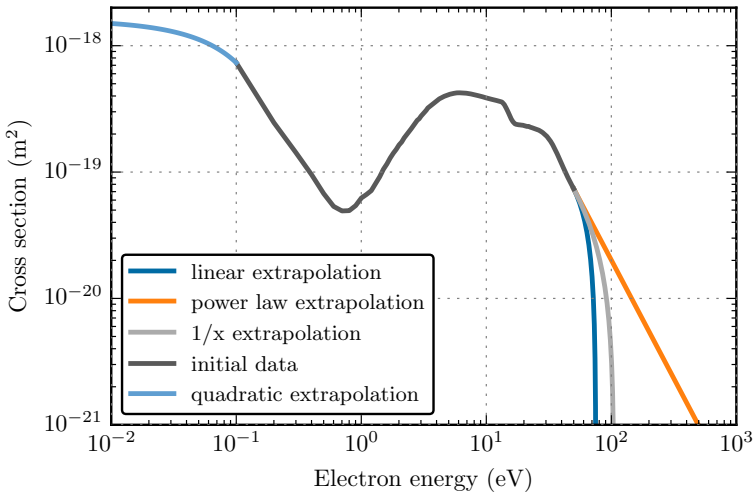

(a) I elastic cross-sections and possible extrapolations.

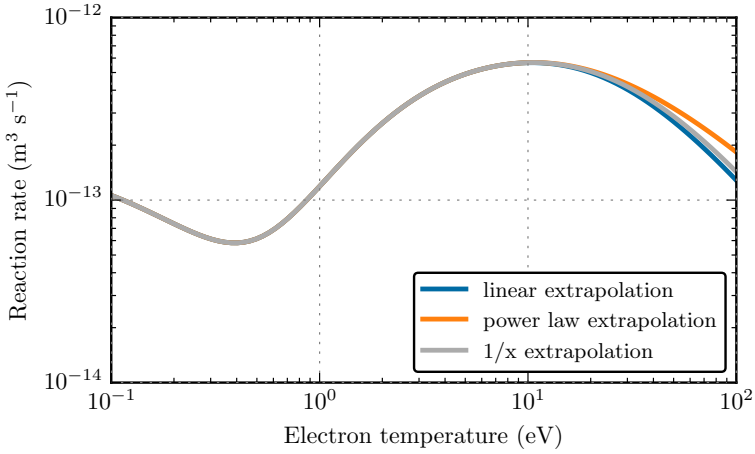

(b) I elastic collision reaction rate based on integration of the extrapolated cross-section over a Maxwellian EEDF.

Figure C.2: Extrapolation for elastic collisions on I.

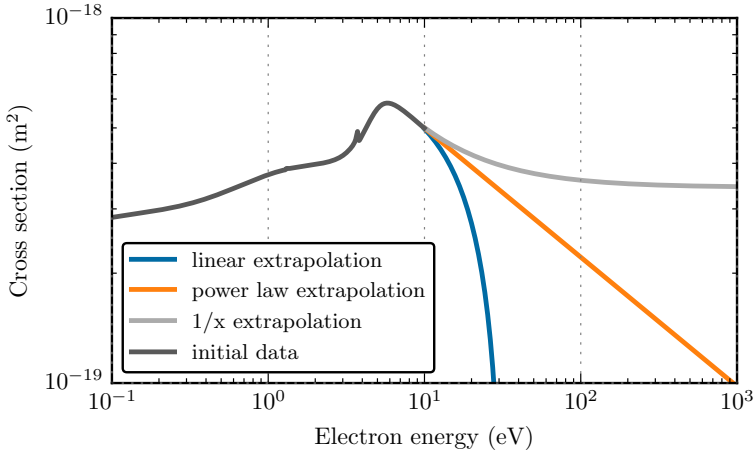

(a) I_2 elastic cross-sections and possible extrapolations.

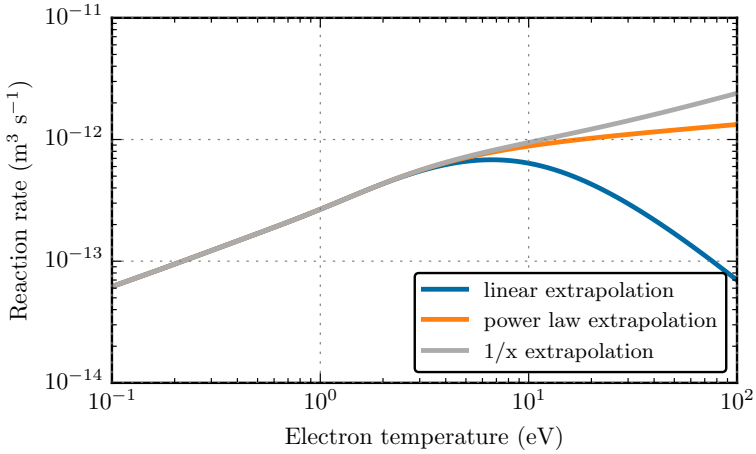

(b) I_2 elastic collision reaction rate based on integration of the extrapolated cross-section over a Maxwellian EEDF.

Figure C.3: Extrapolation for elastic collisions on I_2.

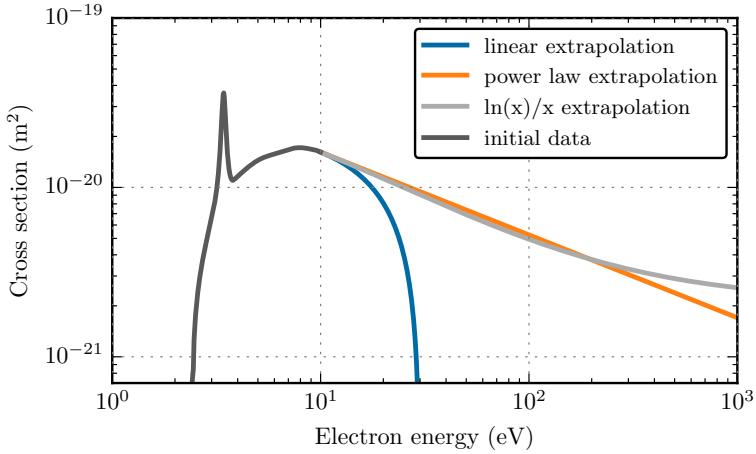

(a) I_2 dissociation cross-sections and possible extrapolations.

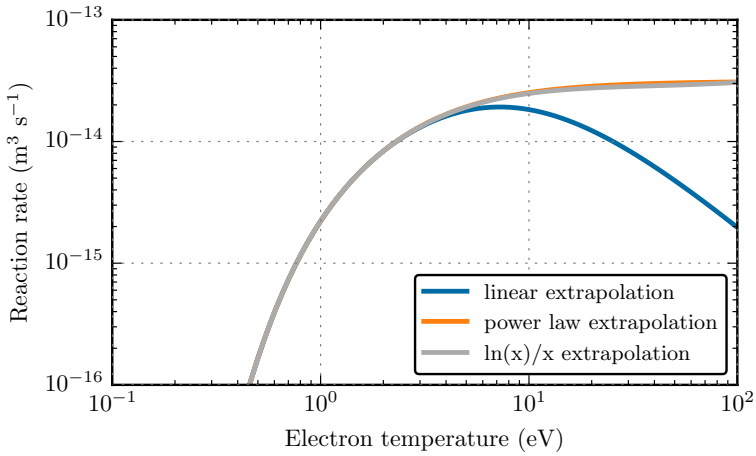

(b) I_2 dissociation reaction rate based on integration of the extrapolated cross-section over a Maxwellian EEDF.

Figure C.4: Extrapolation for I_2 dissociation.

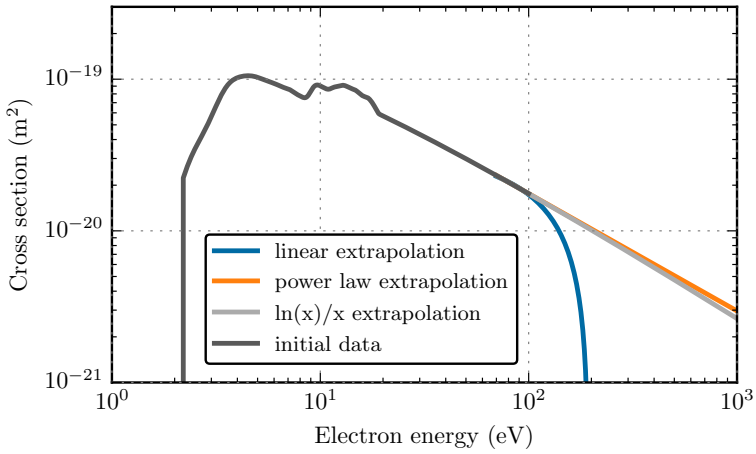

(a) I_2^+ dissociation cross-sections and possible extrapolations.

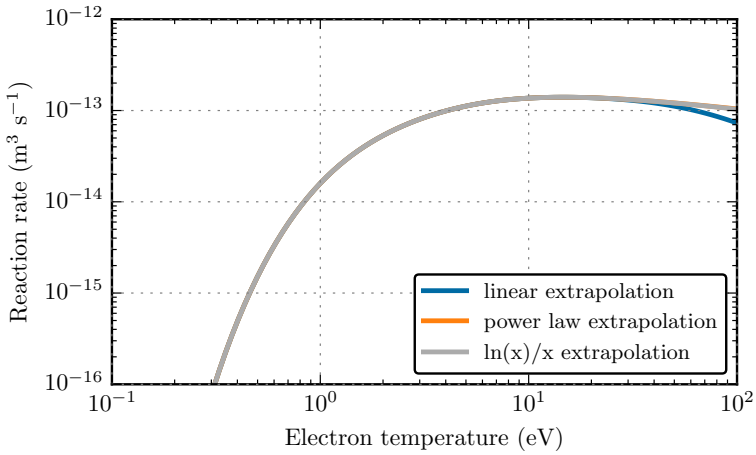

(b) I_2^+ dissociation reaction rate based on integration of the extrapolated cross-section over a Maxwellian EEDF.

Figure C.5: Extrapolation for the I_2^+ dissociation.

Appendix D

Matchboxes

The purpose of this appendix is to provide an analysis of the matchbox mounted on PEGASES during the thesis - whose equivalent circuit is shown Figure D.12 - and some guidance to understanding it, or for redesigning it. The reasoning is largely based on the explanations by Bowick [112] that treats mostly resistive loads, and adapted using work by Lieberman and Lichtenberg [36] and some hints of the actual design of the PEGASES matchbox found in the thesis of Leray [52] and Popelier [53].

D.1 Basics of RF circuits

D.1.1 Components

An electric component is described by its complex impedance $Z = R + jX$. $R = \mathrm{Re}(Z)$ is called the resistance, and $X = \mathrm{Im}(Z)$ is called the reactance. An ideal resistor has a real impedance $Z = R$. An ideal inductor has an imaginary impedance that is a function of the angular frequency of the current going through it: $Z_L = X_L = jL\omega$, and L is called the inductance. An ideal capacitor also has an imaginary impedance depending on the angular frequency of the current going through it: $Z_C = X_C = 1/jC\omega = -j/C\omega$, and C is called the capacitance. This implies, when dealing with a purely reactive (i.e. imaginary) impedance, that $X > 0$ for inductors and $X < 0$ for capacitors.

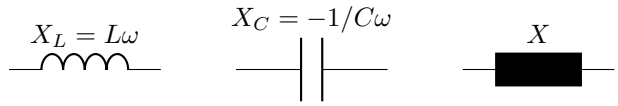

Figure D.1: Left: an inductor. Center: a capacitor. Right: a generic reactance, representing an inductor if $X > 0$ or a capacitor if $X < 0$.

D.1.2 The need for impedance matching

On simple DC circuits like the one shown on Figure D.2, considering that the load L has a load resistance R_L and that the source S has a source resistance R_S, we write V_L the voltage across the load, so that the classical voltage-divider phenomenon is:

$$V_L = \frac{R_L}{R_S + R_L} V_S$$

The corresponding power reaching the load P_L is then:

$$P_L = \frac{V_L^2}{R_L} = \frac{R_L}{(R_S + R_L)^2} V_S^2 = \eta \frac{V_S^2}{R_S}$$

With

$$\eta = \frac{R_L/R_S}{(1 + R_L/R_S)^2}$$

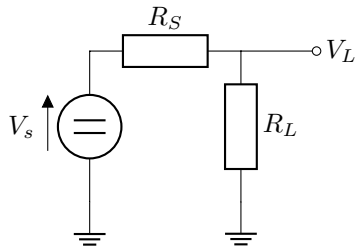

Figure D.2: A simple DC circuit illustrating the voltage divider effect, with a DC voltage source on the left with its equivalent resistance R_S, and a purely resistive load R_L.

The load power P_L is then always inferior to the source power, the Maximum Power Transfer Theorem stats that it is maximum when $R_L = R_S$, as shown Figure D.3. The same logic applies in an AC circuit where load and sources show a reactance in addition to their resistance, like in Figure D.4. In such a case, the maximum power transfer occurs when the load impedance Z_L is equal to the complex conjugate of the source impedance $Z_L = R_{\text{load}} + jX_{\text{load}} = R_S - jX_S = Z_S^*$.

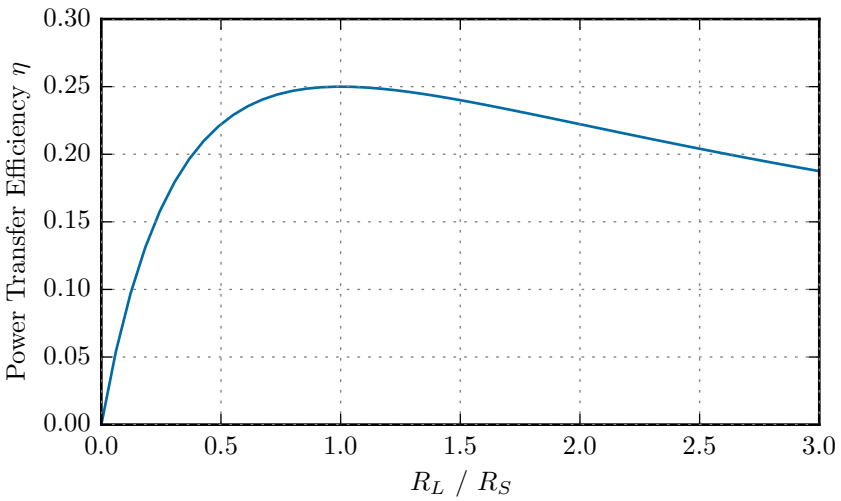

Figure D.3: Power transfer efficiency as a function of the ratio R_L/R_S.

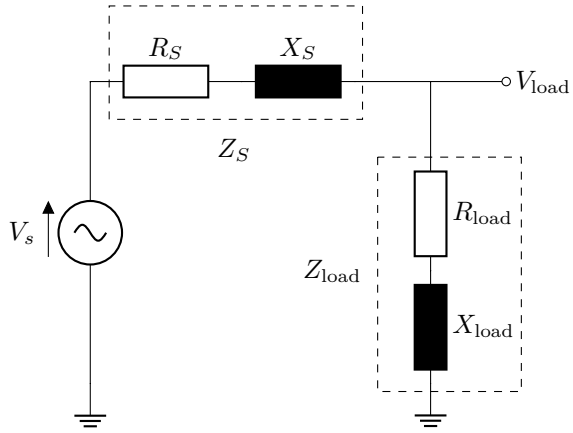

Figure D.4: A simple RF circuit illustrating the voltage divider effect.

The impedance of the entire system (matchbox, antenna, plasma) is different whether the plasma is ON or OFF, it changes depending on the plasma parameters, and it is anyway different from the source impedance: there is a need for an impedance matching circuit, or matchbox, to transform the load impedance into an impedance as close as possible to the complex conjugate of the source impedance so as to maximize the power transfer from the generator to the plasma.

D.1.3 Impedance matching

In this section, we consider the situation presented by Lieberman and Lichtenberg [36] p. 469 and we use the intuitive method from Bowick [112] to design the corresponding matchbox. The situation is reproduced Figure D.5: an ICP plasma and its coil, of equivalent resistance $R_{\text{load}} = 12.3\,\Omega$ and reactance $X_{\text{load}} = 190\,\Omega$. This reactance is positive, meaning that it corresponds to an inductive component. For a plasma frequency of $f = 13.56\,\text{MHz}$, it is equivalent to an inductor of inductance $L_{\text{load}} = X_{\text{load}}/\omega = X_{\text{load}}/2\pi f = 2.23\,\mu\text{H}$. The RF generator has an apparent resistance of $50\,\Omega$ and no reactance.

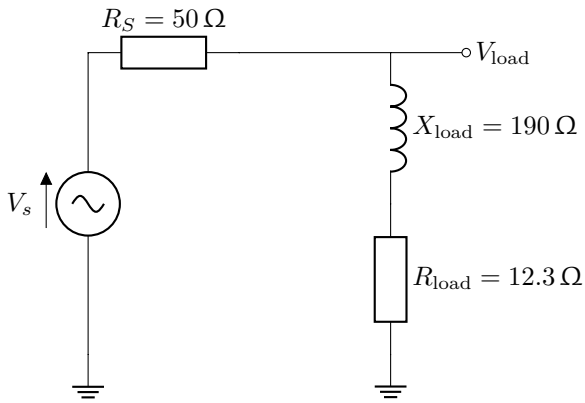

Figure D.5: Equivalent circuit of a RF generator plugged to a coil and generating an ICP plasma. A matching circuit, or matchbox, is needed to optimize power transfer.

A solution for the matching stage is proposed by Lieberman and Lichtenberg [36], as well as a mathematical method to derive the value of the capacitors. Let's use the more intuitive method by Bowick [112].

Step 1: transform into a pure resistive load

The first step is to transform the circuit into a new one with a pure resistive load, where the matching is easier to design. This is done by adding a series reactance to absorb the load reactance. As the impedance of components connected in series is the sum of the impedance, the absorbing reactance must be opposite to the load reactance. The load reactance $X_{\text{load}} = \omega L_{\text{load}}$ being positive, the absorbing reactance X_{abs} is negative and therefore corresponds to a capacitor, but let's keep the generic reactance for now.

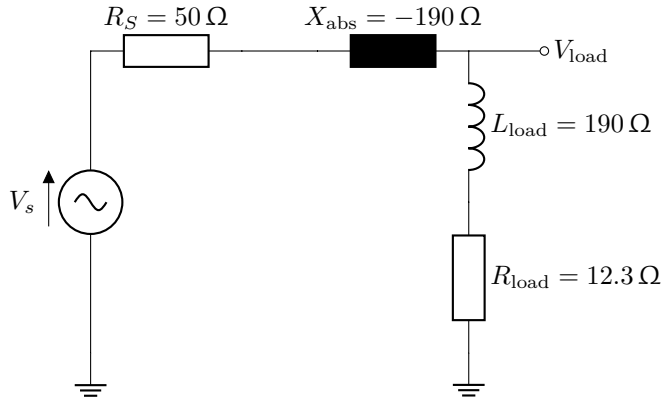

Figure D.6: Equivalent circuit after adding one capacitor.

Step 2: match the pure resistive load

Now, at the given frequency, the impedance seen from the source is a pure resistance of $12.3\,\Omega$. Let's use the method from Bowick [112] to match this load with a L-network, with the series matching element on the load side, as the series matching element should be placed on the side of lowest resistance. We choose to place the negative impedance component in the shunt leg, for a reason that will appear obvious shortly after. We aim at:

$$Q_S = Q_{\text{load}} = \sqrt{\frac{R_S}{R_{\text{load}}} - 1} = 1.75$$

And given the placement of the series reactance next to the load, we have the respective Q factor of each branch:

$$Q_{\text{series}} = \frac{X_{\text{series}}}{R_{\text{load}}}$$
$$Q_{\text{shunt}} = -\frac{R_S}{X_{\text{shunt}}}$$

Solving this system we find $X_{\text{series}} = 21.5\,\Omega$ and $X_{\text{shunt}} = -28.6\,\Omega$. Keeping the generic reactances for now, this is the resulting circuit:

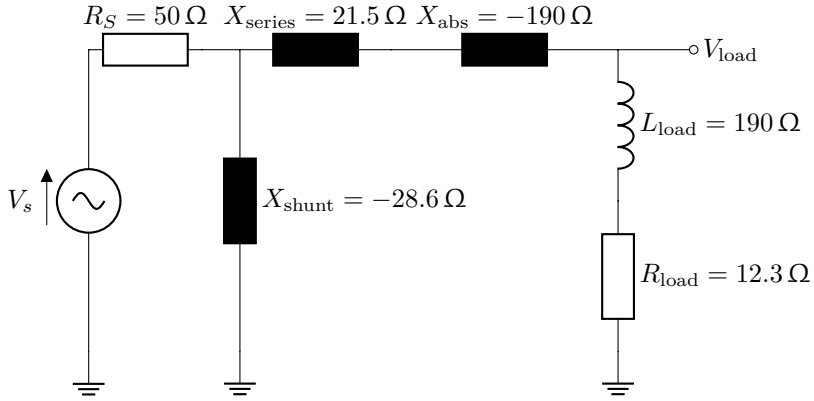

Figure D.7: A L-network is added to the circuit so that the impedances are now matched. The black boxes indicated generic reactances.

The absorption and series reactance, in parallel, can now be joined in a single component of reactance $-168.5\,\Omega$. We can see that although a typical L-network features one inductor and one capacitor, the very high inductance of the load leads to a L-network with two negative reactances, hence two capacitors. Calculating the values of the capacitors for a frequency of 13.56 MHz, we have the final matched circuit shown Figure D.8.

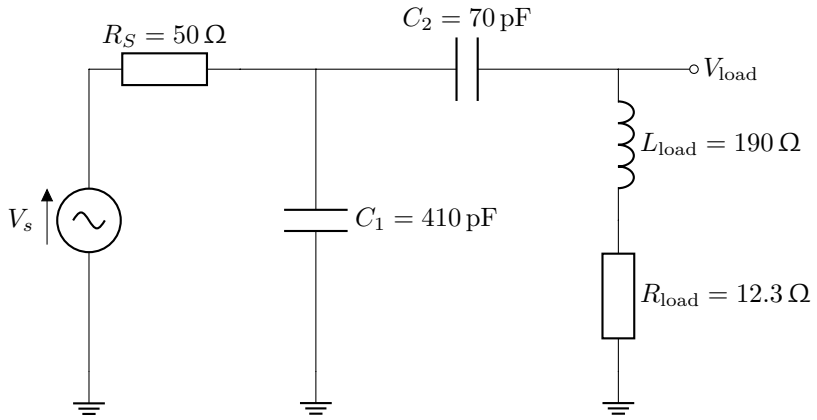

Figure D.8: Final design of the matchbox. The results are the same than the one obtained in an analytical way in the example from Lieberman and Lichtenberg [36], p469.

D.2 The PEGASES matchbox

Designing a real matchbox for PEGASES would follow the same rules, changing the components value to account to the frequency of 4 MHz. However, Leray [52] states that having the antenna connected to the ground on one side, and to the RF power on the other side creates a damaging asymmetry: most of the capacitive power deposition appears nears one end of the antenna, inducing large potential fluctuations in the plasma. The second capacitor is then moved after the load to mitigate this issue without changing the matching, giving the system in Figure D.9.

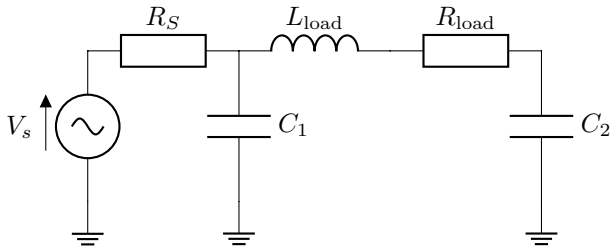

Figure D.9: Transforming the L-network into a more symmetrical matching circuit.

Such a circuit is completely equivalent to the "push-pull" version shown Figure D.10, where we can interpret the new symmetry as a *virtual ground* in the middle of the antenna.

This is not how the matchbox is designed for PEGASES. According to Popelier [53], there is an interest in raising the current and lowering the voltage in the antenna, so a transformer is added in the matchbox. As a transformer also acts as an impedance-modifier, a circuit such as the one Figure D.10 is used to match the impedance between the secondary coil of the transformer and the antenna. Another matching capacitor is added parallel to the transformer to match the primary coil of the transformer to the RF generator. The matching circuit is now shown Figure D.11.

One should note that if the general principles still follow, all values of components are changing at each of the steps presented here. Several more

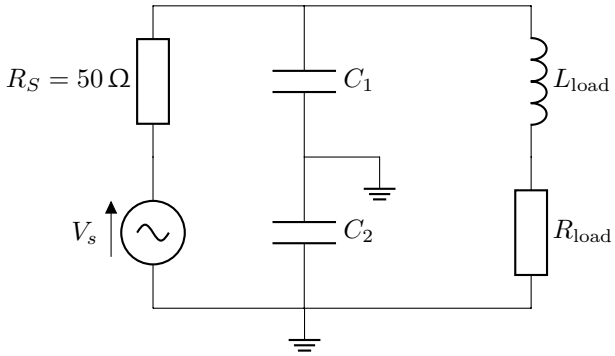

Figure D.10: This circuit is completely equivalent to the one shown Figure D.10, enhancing the symmetrical aspect of the matching circuit.

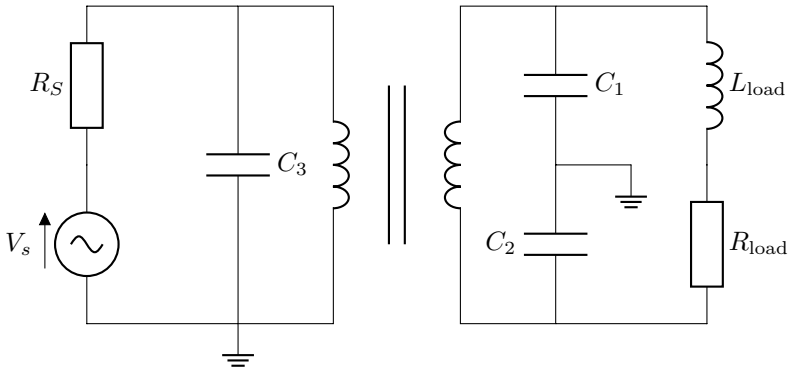

Figure D.11: There are now three layers of matching circuits: the capacitance C_3, the transformer (whose primary purpose is to raise the current) and the L-network described before.

changes will lead to the final design: C_1 and C_2 are made variable capacitors to adjust for plasma impedance changes, two more identical capacitors are added in parallel to C_1 and C_2 so as the variable capacitors can be smaller. C_1 and C_2 are made dependent, so that they have the same value and are changed using the same control. C_3 is made variable too.

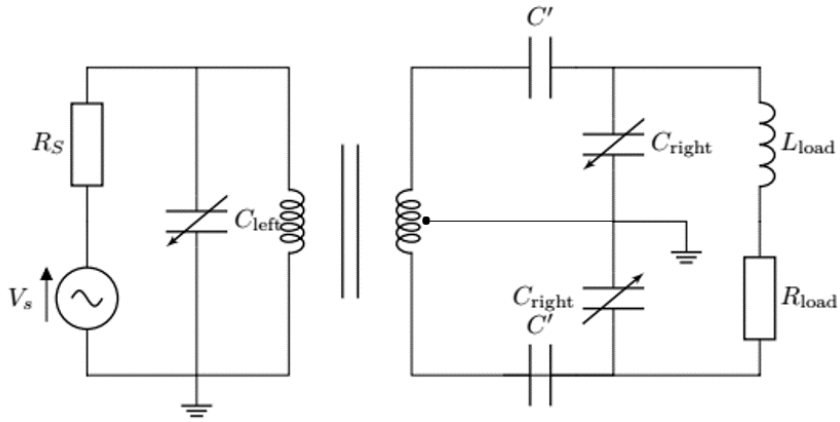

Figure D.12: Final design of the PEGASES matchbox.

The final Figure D.12 is the actual design of the matchbox mounted on PEGASES during my thesis. The component values are not known and the matching in never perfect, for any gas. The purpose of this entire appendix is to expose my understanding of the matchbox and some leads to improve it.

Bibliography

[1] K. E. Tsiolkovsky; "Investigation of Universal Space by Means of Reactive Devices"; (1903). Cited page 6

[2] E. Kyle; "Ariane 5 Data Sheet"; (2020). http://www.spacelaunchreport.com/ariane5.html. Cited page 9

[3] D. Krejci, A. Reissner, B. Seifert, D. Jelem, T. Hörbe, F. Plesescu, P. Friedhoff and S. Lai; "Demonstration of the IFM Nano FEEP Thruster in Low Earth Orbit"; in "4S Symposium", (p. 13) (2018). Cited page 9

[4] D. M. Goebel and I. Katz; *Fundamentals of Electric Propulsion: Ion and Hall Thrusters*; volume 1 (John Wiley & Sons, 2008); ISBN:978-0-470-43626-4. Cited pages 9, 12, and 56

[5] S. Mazouffre; "Electric Propulsion for Satellites and Spacecraft: Established Technologies and Novel Approaches"; Plasma Sources Science and Technology **25**(3), p. 033002 (2016). Cited page 10

[6] E. Y. Choueiri; "A Critical History of Electric Propulsion: The First 50 Years (1906-1956)"; Journal of Propulsion and Power **20**(2), pp. 193–203 (2004). Cited pages 11, 12, and 22

[7] H. Oberth; *Wege Zur Raumschiffahrt* (Druck und Verlag von R. Oldenbourg, Munich and Berlin, 1929). Cited page 11

[8] E. Stuhlinger; *Ion Propulsion for Space Flight* (McGraw-Hill, New York, 1964). Cited page 12

[9] S. A. Feuerborn, J. Perkins and D. A. Neary; "Finding a Way: Boeing's All Electric Propulsion Satellite"; in "49th

AIAA/ASME/SAE/ASEE Joint Propulsion Conference", (American Institute of Aeronautics and Astronautics, San Jose, CA, 2013). http://arc.aiaa.org/doi/10.2514/6.2013-4126. Cited page 12

[10] J. R. Wertz and W. J. Larson (editors); *Space Mission Analysis and Design*; Space Technology Library; 3rd ed edition (Microcosm ; Kluwer, El Segundo, Calif. : Dordrecht ; Boston, 1999); ISBN:978-0-7923-5901-2. Cited page 13

[11] J. Jackson, J. Cassady, M. Allen, R. Myers, T. Tofil, D. Herman and E. Pencil; "Development Of High Power Hall Thruster Systems To Enable The NASA Exploration Vision"; in "Space Propulsion", (p. 12) (Barcelo Renacimiento Hotel, Seville, Spain, 2018). https://ntrs.nasa.gov/archive/nasa/casi.ntrs.nasa.gov/20180003521.pdf. Cited page 14

[12] A. Vance; *Elon Musk: Tesla, SpaceX, and the Quest for a Fantastic Future* (Eyrolles, 2017); ISBN:978-2-212-42483-6. Cited page 15

[13] R. Zubrin; *The Case for Space* (Prometheus, 2019); ISBN:978-1-63388-534-9. Cited page 15

[14] E. Kisliuk; "Commercial Orbital Transportation Services (COTS)"; (2015). http://www.nasa.gov/commercial-orbital-transportation-services-cots. Cited page 16

[15] H. Heidt, J. Puig-Suari, A. Moore, S. Nakasuka and R. Twiggs; "CubeSat: A New Generation of Picosatellite for Education and Industry Low-Cost Space Experimentation"; in "14TH Annual/USU Conference on Small Satellites", (p. 19) (2000). https://digitalcommons.usu.edu/smallsat/2000/All2000/32/. Cited page 17

[16] S. Yacoubi; *The Impact of NewSpace and the Diversification of the Space Industry on Business Models*; Master's thesis; École polytechnique - HEC Paris (2019). Cited page 18

[17] H. Curtis; "CubeSat Thrusters: An Overview of in-Space Propulsion Products for Small Satellites"; (2019). https://blog.satsearch.co/. Cited page 19

[18] J. W. Dankanich, M. Selby, K. A. Polzin, H. Kamhawi, T. Hickman and L. Byrne; "The Iodine Satellite (iSat) Project Development towards Critical Design Review (CDR)"; in "52nd AIAA/ASME/SAE/ASEE Joint Propulsion Conference", (2016). https://doi.org/10.2514/6.2016-4540. Cited page 20

[19] L. R. Shepherd and A. Cleaver; "The Atomic Rocket - 4"; Journal of the British Interplanetary Society **8**, pp. 59–70 (1949). Cited page 22

[20] E. Stuhlinger; "Possibilities of Electrical Space Ship Propulsion"; in "5th International Astronautical Congress", (pp. 100–119) (1954). Cited page 22

[21] G. Brewer; *Ion Propulsion: Technology and Applications* (1970). Cited page 22

[22] E. B. Saloman; "Energy Levels and Observed Spectral Lines of Xenon, Xe I through Xe LIV"; Journal of Physical and Chemical Reference Data **33**(3), pp. 765–921 (2004). Cited pages 23 and 26

[23] A. Kramida, Yu. Ralchenko, J. Reader and NIST ASD Team; "NIST Atomic Spectra Database (Ver. 5.7.1)"; National Institute of Standards and Technology, Gaithersburg, MD. (2018). https://physics.nist.gov/asd. Cited pages 23, 49, 119, 123, 124, and 176

[24] J. E. Bailey; *Ullmann's encyclopedia of industrial chemistry fully networkable database* (Wiley-VCH, 2001). Cited page 23

[25] P. Dietz, W. Gärtner, Q. Koch, P. E. Köhler, Y. Teng, P. R. Schreiner, K. Holste and P. J. Klar; "Molecular Propellants for Ion Thrusters"; Plasma Sources Science and Technology **28**(8), p. 084001 (2019). Cited page 23

[26] Guyton-Morveau, Monge, Berthollet, Seguin, Vauquelin, Adet, Hassenfratz, C. Prieur, Chaptal, Parmentier, Deyeux, Bouillon-Lagrange, Collet-Descotils, A. Laugier, Gay-Lussac and Thenard; *Annales de Chimie, ou Recueil de Mémoires concernant la Chimie et les Arts qui en dépendent, et spécialement la Pharmacie.*; volume 88 (1813). https://books.google.fr/books?id=YGwri-w7sMAC. Cited page 24

[27] G. P. Baxter, C. H. Hickey and W. C. Holmes; "The Vapor Pressure of Iodine"; Journal of the American Chemical Society **29**(2), pp. 127–136 (1907). Cited pages 24 and 25

[28] D. R. Stull; "Vapor Pressure of Pure Substances. Organic and Inorganic Compounds"; Industrial & Engineering Chemistry **39**(4), pp. 517–540 (1947). Cited pages 24 and 25

[29] A. Kono and S. Hattori; "Radiative-Lifetime Measurements for I i and I Ii"; Journal of the Optical Society of America **69**(2), p. 253 (1979). Cited pages 24 and 25

[30] T. E. Steinberger and E. E. Scime; "Laser-Induced Fluorescence of Singly Ionized Iodine"; Journal of Propulsion and Power **34**(5), pp. 1235–1239 (2018). Cited pages 25, 117, and 176

[31] INRS; "Fiche Toxicologique N°207"; (2006). http://www.inrs.fr/publications/bdd/fichetox/fiche.html?refINRS=FICHETOX_207. Cited page 25

[32] J. E. Hansen and W. Persson; "Revised Analysis of Singly Ionized Xenon, Xe II"; Physica Scripta **36**(4), pp. 602–643 (1987). Cited page 26

[33] J. R. Hamilton; "Iodine: I2 Molecule and I Atom"; *Technical report*; Quantemol (2015). Cited pages 26, 47, 49, 52, 257, and 259

[34] L. Minnhagen; "The Energy Levels of Neutral Atomic Iodine."; Arkiv Fysik **21** (1962). Cited pages 26, 49, 52, 124, and 176

[35] W. C. Martin and C. H. Corliss; "The Spectrum of Singly Ionized Atomic Iodine (I Ii)"; Journal of Research of the National Bureau of Standards Section A: Physics and Chemistry **64A**(6), p. 443 (1960). Cited pages 26, 120, and 176

[36] M. A. Lieberman and A. J. Lichtenberg; *Principles of Plasma Discharges and Materials Processing*; 2nd ed edition (Wiley-Interscience, Hoboken, N.J, 2005); ISBN:978-0-471-72001-0. Cited pages 26, 27, 45, 59, 67, 71, 265, 269, and 272

[37] E. G. Thorsteinsson and J. T. Gudmundsson; "A Global (Volume Averaged) Model of a Chlorine Discharge"; Plasma Sources Science and Technology **19**(1), p. 015001 (2010). Cited pages 27, 61, 62, 64, 65, 68, 69, and 70

[38] P. Chabert, J. Arancibia Monreal, J. Bredin, L. Popelier and A. Aanesland; "Global Model of a Gridded-Ion Thruster Powered by a Radiofrequency Inductive Coil"; Physics of Plasmas **19**(7), p. 073512 (2012). Cited pages 27, 43, 67, 68, 149, and 211

[39] J. Szabo, M. Robin, S. Paintal, B. Pote, V. Hruby and C. Freeman; "Iodine Plasma Propulsion Test Results at 1 to 10 kW"; IEEE Transactions on Plasma Science **43**(1), pp. 141–148 (2015). Cited pages 27 and 29

[40] K. A. Polzin; "Iodine Satellite Propellant Feed Clog-Clearing Demonstration Testing"; NASA NTRS (NASA/TM—2018–220128), p. 28 (2018). Cited pages 27 and 37

[41] K. Holste, W. Gärtner, D. Zschätzsch, S. Scharmann, P. Köhler, P. Dietz and P. J. Klar; "Performance of an Iodine-Fueled Radio-Frequency Ion-Thruster"; The European Physical Journal D **72**(1) (2018). Cited pages 27, 28, and 29

[42] P. Grondein, T. Lafleur, P. Chabert and A. Aanesland; "Global Model of an Iodine Gridded Plasma Thruster"; Physics of Plasmas **23**(3), p. 033514 (2016). Cited pages 27, 43, 46, 47, 53, 60, 62, 63, 64, 65, 67, and 97

[43] K. Katsonis and C. Berenguer; "A Detailed Global Model of Iodine Plasma for Optimization and Diagnostics of Electric Thrusters"; Imperial Journal of Interdisciplinary Research (IJIR) **2**(12), p. 10 (2016). Not cited

[44] J. Martinez-Martinez, D. Rafalskyi and A. Aanesland; "Development and Testing of the NPT30-I2 Iodine Ion Thruster"; in "36th International Electric Propulsion Conference", (University of Vienna, Vienna, Austria, 2019). http://electricrocket.org/2019/811.pdf. Cited page 30

[45] M. Manente, F. Trezzolani, R. Mantellato, D. Scalzi, A. Schiavon, L. Cappellini, N. Bellomo, A. Gloder, E. Toson, M. Minute, D. Vallisari, M. Magarotto and D. Pavarin; "REGULUS: Know-How Acquired on Iodine Propellant"; in "36th International Electric Propulsion Conference", (University of Vienna, Vienna, Austria, 2019). Cited pages 27 and 30

[46] P. Grondein; *Investigation de l'iode Comme Propergol Pour La Propulsion Ionique à Grilles*; Ph.D. thesis; Université Pierre et Marie Curie (2017). https://tel.archives-ouvertes.fr/tel-01478401/. Cited pages 27, 28, 31, 36, 60, 113, 116, 119, and 245

[47] J. Szabo; "Performance Evaluation of an Iodine Vapor Hall Thruster"; in "47th AIAA/ASME/SAE/ASEE Joint Propulsion Conference & Exhibit", (2011). https://doi.org/10.2514/1.B34291. Cited page 29

[48] P. Chabert; "Propulseur à Plasma Électronégatif"; (2007). https://bases-brevets.inpi.fr/fr/document/FR2894301.html. Cited page 30

[49] P. Chabert, A. Aanesland, A. Meige and G. Leray; "Propulseur à Plasma Électronégative à Injection Optimisée."; (2010). https://bases-brevets.inpi.fr/fr/document/FR2939173.html. Cited page 30

[50] A. Aanesland, P. Chabert, M. Irzyk and S. Mazouffre; "Procédé et Dispositif Pour La Formation d'un Faisceau Plasma"; (2012). https://bases-brevets.inpi.fr/fr/document/FR2965697.html. Cited page 30

[51] D. Rafalskyi and A. Aanesland; "Dispositif de Formation d'un Faisceau Quasi-Neutre de Particules de Charges Opposées."; (2015). https://bases-brevets.inpi.fr/fr/document/FR3020235.html. Cited page 30

[52] G. Leray; *PEGASES: Plasma Propulsion with Electronegative Gases*; Ph.D. thesis; École polytechnique (2009). https://pastel.archives-ouvertes.fr/pastel-00005935/. Cited pages 31, 265, and 273

[53] L. Popelier; *Développement du propulseur PEGASES: source inductive à haute performance et accélération successive de faisceaux d'ions positifs et d'ions négatifs.*; Ph.D. thesis; École polytechnique (2012). https://tel.archives-ouvertes.fr/tel-00793098v1. Cited pages 31, 116, 265, and 273

[54] J. Bredin; *Développement de diagnostics électrostatiques pour le filtrage magnétique et la formation du plasma ion-ion dans le propulseur PEGASES*; Ph.D. thesis; École polytechnique (2013). https://tel.archives-ouvertes.fr/pastel-00993207. Cited pages 31, 60, 116, 189, and 255

[55] D. Renaud; *Caractérisation du propulseur PEGASES : diagnostics du filtre magnétique et du faisceau; optimisation de la*

géométrie.; Ph.D. thesis; Université d'Orléans (2016). https://tel.archives-ouvertes.fr/tel-01412571. Cited page 31

[56] R. Lucken; *Theory and Simulation of Low-Pressure Plasma Transport Phenomena, Application to the PEGASES Thruster*; Ph.D. thesis; Université Paris Saclay (2019). https://tel.archives-ouvertes.fr/tel-02435208. Cited pages 31, 43, 46, 47, 52, 57, 68, 113, and 246

[57] A. Aanesland, G. Leray and P. Chabert; "Pegases: Plasma Propulsion with Electronegative Gases"; in "44th AIAA/ASME/SAE/ASEE Joint Propulsion Conference & Exhibit", (American Institute of Aeronautics and Astronautics, Hartford, CT, 2008); ISBN:978-1-60086-992-1. Cited page 31

[58] T. Lafleur, D. Rafalskyi and A. Aanesland; "Alternate Extraction and Acceleration of Positive and Negative Ions from a Gridded Plasma Source"; Plasma Sources Science and Technology **24**(1), p. 015005 (2014). Cited pages 31 and 32

[59] T. Lafleur, D. Rafalskyi, P. Chabert and A. Aanesland; "Proof-of-Concept Demonstration of the PEGASES Plasma Thruster"; in "Joint Conference of 30th International Symposium on Space Technology and Science, 34th International Electric Propulsion Conference and 6th Nano-Satellite Symposium", (Hyogo-Kobe, Japan, 2015). Cited page 31

[60] D. Rafalskyi, L. Popelier and A. Aanesland; "Experimental Validation of the Dual Positive and Negative Ion Beam Acceleration in the Plasma Propulsion with Electronegative Gases Thruster"; Journal of Applied Physics **115**(5), p. 053301 (2014). Cited pages 31 and 180

[61] D. Rafalskyi and A. Aanesland; "Coincident Ion Acceleration and Electron Extraction for Space Propulsion Using the Self-Bias Formed on a Set of RF Biased Grids Bounding a Plasma Source"; Journal of Physics D: Applied Physics **47**(49), p. 495203 (2014). Cited page 31

[62] D. Rafalskyi and A. Aanesland; "Plasma Acceleration Using a Radio Frequency Self-Bias Effect"; Physics of Plasmas **22**(6), p. 063502 (2015). Cited page 31

[63] V. A. Godyak, R. B. Piejak and B. M. Alexandrovich; "Electron Energy Distribution Function Measurements and Plasma Parameters

in Inductively Coupled Argon Plasma"; Plasma Sources Science and Technology **11**(4), pp. 525–543 (2002). Cited pages 35 and 253

[64] P. Chabert and N. Braithwaite; *Physics of Radio-Frequency Plasmas* (Cambridge University Press, 2011); ISBN:978-1-139-49468-7. Cited pages 43, 45, 59, 60, 64, 67, 68, 69, 71, 180, and 183

[65] J. Hamilton; "Consultancy Project for LPP"; *Technical report*; Quantemol (2017). Cited pages 47, 49, and 52

[66] C. Greaves; "Ion-Ion Recombination in Iodine Afterglows"; Journal of Electronics and Control **17**(2), pp. 171–180 (1964). Cited pages 47 and 53

[67] T. H. Y. Yeung; "Recombination Coefficients for Positive and Negative Ions"; Proceedings of the Physical Society **71**(3), pp. 341–346 (1958). Cited pages 47 and 53

[68] T. Ben Slimane; *A Xenon Collisional Radiative Model for Electric Propulsion Application*; Master's thesis; École polytechnique (2020). Cited pages 49 and 251

[69] G. Tallents; *An Introduction to the Atomic and Radiation Physics of Plasmas.* (Cambridge University Press, 2018); ISBN:978-1-108-32173-0. Cited pages 49, 257, and 259

[70] E. Luc-Koenig, C. Morillon and J. Verges; "Etude Expérimentale et Théorique de l'Iode Atomique. Observation Du Spectre d'Arc Infrarouge, Classification et Structure Hyperfine"; Physica Scripta **12**(4), p. 199 (1975). Cited pages 49, 52, 119, 120, 123, and 138

[71] R. J. Peláez, C. Blondel, C. Delsart and C. Drag; "Pulsed Photodetachment Microscopy and the Electron Affinity of Iodine"; Journal of Physics B: Atomic, Molecular and Optical Physics **42**(12), p. 125001 (2009). Cited pages 49, 52, 157, and 176

[72] L. Mathieson and A. L. G. Rees; "Electronic States and Potential Energy Diagram of the Iodine Molecule"; The Journal of Chemical Physics **25**(4), pp. 753–761 (1956). Cited pages 52 and 158

[73] P. J. Chantry; "A Simple Formula for Diffusion Calculations Involving Wall Reflection and Low Density"; Journal of Applied Physics **62**(4), pp. 1141–1148 (1987). Cited page 57

[74] D. Bohm; *The Characteristics of Electrical Discharges in Magnetic Fields* (R.K Wakerling, A. Guthrie, Mcgraw-hill Book Company, Inc, 1949). Cited page 60

[75] N. S. J. Braithwaite and J. E. Allen; "Boundaries and Probes in Electronegative Plasmas"; Journal of Physics D: Applied Physics **21**(12), pp. 1733–1737 (1988). Cited page 61

[76] P. Chabert; "An Expression for the Hl Factor in Low-Pressure Electronegative Plasma Discharges"; Plasma Sources Science and Technology **25**(2), p. 025010 (2016). Cited pages 61, 62, 63, 65, 181, 184, and 185

[77] S. Kim, M. A. Lieberman, A. J. Lichtenberg and J. T. Gudmundsson; "Improved Volume-Averaged Model for Steady and Pulsed-Power Electronegative Discharges"; Journal of Vacuum Science & Technology A: Vacuum, Surfaces, and Films **24**(6), pp. 2025–2040 (2006). Cited pages 61, 69, and 211

[78] J. T. Gudmundsson; "On the Effect of the Electron Energy Distribution on the Plasma Parameters of an Argon Discharge: A Global (Volume-Averaged) Model Study"; Plasma Sources Science and Technology **10**(1), p. 76 (2001). Cited pages 63, 104, 105, 109, and 211

[79] C. Lee and M. A. Lieberman; "Global Model of Ar, O2 , Cl2, and Ar/O2 High-density Plasma Discharges"; Journal of Vacuum Science & Technology A: Vacuum, Surfaces, and Films **13**(2), pp. 368–380 (1995). Cited page 67

[80] S. Ashida and M. A. Lieberman; "Spatially Averaged (Global) Model of Time Modulated High Density Chlorine Plasmas"; Japanese Journal of Applied Physics **36**(Part 1, No. 2), pp. 854–861 (1997). Cited page 67

[81] E. Despiau-Pujo and P. Chabert; "Global Model of Instabilities in Low-Pressure Inductive Chlorine Discharges"; Plasma Sources Science and Technology **18**(4), p. 045028 (2009). Cited page 68

[82] F. Marmuse, R. Lucken, O. L. Maitre, P. Congedo and A. Bourdon; "Opening Chemical Reaction Paths in a Plasma Global Model: An Uncertainty Quantification Approach"; in "UQOP : Uncertainty Quantification and OPtimization", (p. 2) (Paris, France, 2019). https://hal.archives-ouvertes.fr/hal-02342241/. Cited page 85

[83] M. J. Druyvesteyn and F. M. Penning; "The Mechanism of Electrical Discharges in Gases of Low Pressure"; Reviews of Modern Physics **12**(2), pp. 87–174 (1940). Cited page 104

[84] U. Fantz; "Basics of Plasma Spectroscopy"; Plasma Sources Science and Technology **15**(4), pp. S137–S147 (2006). Cited page 116

[85] J. P. Booth, O. Guaitella, A. Chatterjee, C. Drag, V. Guerra, D. Lopaev, S. Zyryanov, T. Rakhimova, D. Voloshin and Y. Mankelevich; "Oxygen (^{3} P) Atom Recombination on a Pyrex Surface in an O $_2$ Plasma"; Plasma Sources Science and Technology **28**(5), p. 055005 (2019). Cited page 116

[86] D. Marinov, M. Foucher, E. Campbell, M. Brouard, P. Chabert and J.-P. Booth; "High Sensitivity Ultra-Broad-Band Absorption Spectroscopy of Inductively Coupled Chlorine Plasma"; Plasma Sources Science and Technology **25**(3), p. 035019 (2016). Cited pages 117, 157, 160, and 176

[87] J. Tiee, M. Ferris, G. Loge and F. Wampler; "Two-Photon Laser-Induced Fluorescence Studies of HS Radicals, DS Radicals, and I Atoms."; Chemical Physics Letters **96**(4), pp. 422–425 (1983). Cited page 117

[88] P. Brewer, P. Das, G. S. Ondrey and R. Bersohn; "Measurement of the Relative Populations of I (2P0 1/2) and I (2P0 3/2) by Laser Induced Vacuum Ultraviolet Fluorescence"; The Journal of Chemical Physics **79**(2), pp. 720–723 (1983). Cited page 117

[89] V. S. Letokhov; "Saturation Spectroscopy"; in "High-Resolution Laser Spectroscopy", , edited by K. Shimoda; Topics in Applied Physics; (p. 77) (Springer Berlin Heidelberg, 1976); ISBN:978-3-540-07719-0. Cited page 127

[90] C. Delsart; *Lasers et optique non linéaire: cours, exercices et problèmes corrigés : niveau M1-M2* (Ellipses, Paris, 2008); ISBN:978-2-7298-3856-0. Cited page 130

[91] T.-K. Ha, Y. He, J. Pochert, M. Quack, R. Ranz, G. Seyfang and I. Thanopoulos; "Absolute Integrated Band Strength and Magnetic Dipole Transition Moments in the 2P3/2 → P1/2

Fine Structure (with Hyperfine Structure) Transition of the Iodine Atom: Experiment and Theory"; Berichte der Bunsengesellschaft für physikalische Chemie **99**(3), pp. 384–392 (1995). Cited pages 134, 135, 138, 143, 148, 149, and 214

[92] Y. He, M. Quack, R. Ranz and G. Seyfang; "Diode Laser Detection of Iodine Atom Hyperfine Transitions during and after Infrared Multiphoton Excitation and Dissociation of CFJ with Short Pulse CO2 Lasers"; Chemical Physics Letters **215**(1), p. 9 (1993). Cited pages 134, 135, 148, and 149

[93] H.-J. Kunze; *Introduction to Plasma Spectroscopy*; number 56 in Springer Series in Atomic, Optical, and Plasma Physics (Springer, Heidelberg, 2009); ISBN:978-3-642-02232-6. Cited pages 143 and 145

[94] H. Griem, R; *Principles of Plasma Spectroscopy* (Cambridge University Press, 1997); ISBN:978-0-521-61941-7. Cited page 145

[95] P. N. Barnes and M. J. Kushner; "Ion-Ion Neutralization of Iodine in Radio-Frequency Inductive Discharges of Xe and I2 Mixtures"; Journal of Applied Physics **82**(5), pp. 2150–2155 (1997). Cited page 157

[96] J. Burkholder, S. Sander, J. Abbatt, J. Barker, R. Huie, C. Kolb, M. Kurylo, V. Orkin, D. Wilmouth and P. Wine; "Chemical Kinetics and Photochemical Data for Use in Atmospheric Studies, Evaluation No. 18"; *JPL Publication 15-10*; Jet Propulsion Laboratory; Pasadena (2015). `http://jpldataeval.jpl.nasa.gov/`. Cited pages 158 and 159

[97] A. Saiz-Lopez, R. W. Saunders, D. M. Joseph, S. H. Ashworth and J. M. C. Plane; "Absolute Absorption Cross-Section and Photolysis Rate of I2"; Atmos. Chem. Phys. (p. 8) (2004). Cited pages 158, 159, 160, 161, and 164

[98] J. Tellinghuisen; "Resolution of the Visible-Infrared Absorption Spectrum of I2 into Three Contributing Transitions"; The Journal of Chemical Physics **58**(7), p. 2821 (1973). Cited page 158

[99] P. Spietz, J. G. Martin and J. P. Burrows; "Effects of Column Density on I2 Spectroscopy and a Determination of I2 Absorption Cross Section at 500 Nm"; Atmos. Chem. Phys. (p. 15) (2006). Cited pages 158, 161, and 169

[100] W. Hargus, J. Lubkeman, K. Remy and A. Gonzales; "Investigation of Singly Ionized Iodine Spectroscopy in Support of Electrostatic Propulsion Diagnostics Development"; in "48th AIAA/ASME/SAE/ASEE Joint Propulsion Conference & Exhibit", (American Institute of Aeronautics and Astronautics, Atlanta, Georgia, 2012). http://arc.aiaa.org/doi/abs/10.2514/6.2012-4316. Cited page 175

[101] K.-S. Chung; "Mach Probes"; Plasma Sources Science and Technology **21**(6), p. 063001 (2012). Cited page 180

[102] D. Rafalskyi, T. Lafleur and A. Aanesland; "Electron Density Measurements in Highly Electronegative Plasmas"; Plasma Sources Science and Technology **25**(4), p. 047001 (2016). Cited page 180

[103] G. Curley; *The Dynamics of the Charged Particles in a Dual Frequency Capacitively Coupled Dielectric Etch Reactor.*; Ph.D. thesis; École polytechnique (2008). https://pastel.archives-ouvertes.fr/tel-00416652. Cited page 180

[104] V. A. Godyak and V. I. Demidov; "Probe Measurements of Electron-Energy Distributions in Plasmas: What Can We Measure and How Can We Achieve Reliable Results?"; Journal of Physics D: Applied Physics **44**(23), p. 233001 (2011). Cited pages 180 and 190

[105] F. F. Chen; "Lecture Notes on Langmuir Probe Diagnostics"; (2003). http://www.ee.ucla.edu/~ffchen/Publs/Chen210R.pdf. Cited page 180

[106] V. Désangles; *Forçage à Grande Échelle d'une Colonne de Plasma Faiblement Magnétisée : Influence d'une Cathode Émissive de Grande Taille*; Ph.D. thesis; Université de Lyon (2018). https://tel.archives-ouvertes.fr/tel-02087300/. Cited page 180

[107] J. Bredin, P. Chabert and A. Aanesland; "Langmuir Probe Analysis in Electronegative Plasmas"; Physics of Plasmas **21**(12), p. 123502 (2014). Cited pages 180, 181, 184, 186, 199, 201, 202, and 247

[108] H. Amemiya; "Probe Diagnostics in Negative Ion Containing Plasma"; Journal of the Physical Society of Japan **57**(3), pp. 887–902 (1988). Cited page 180

[109] V. A. Godyak and B. M. Alexandrovich; "Comparative Analyses of Plasma Probe Diagnostics Techniques"; Journal of Applied Physics **118**(23), p. 233302 (2015). Cited page 189

[110] L. Liard, A. Aanesland and P. Chabert; "Dynamics of Neutral Gas Depletion Investigated by Time- and Space-Resolved Measurements of Xenon Atom Ground State Density"; Journal of Physics D: Applied Physics **45**(23), p. 235201 (2012). Cited page 212

[111] V. A. Godyak, R. B. Piejak and B. M. Alexandrovich; "Experimental Setup and Electrical Characteristics of an Inductively Coupled Plasma"; Journal of Applied Physics **85**(2), pp. 703–712 (1999). Cited pages 253, 255, and 256

[112] C. Bowick; *RF Circuit Design* (Newnes, 2007); ISBN:978-0-08-055342-9. Cited pages 265, 269, and 270

Florian Marmuse **9 juillet 2020**

Plasmas d'iode: études expérimentales et numériques Application à la propulsion électrique

Résumé : L'iode est un carburant alternatif pour la propulsion électrique des satellites, avec des performances comparables à celles du xénon. En 2020, de tels systèmes de propulsion à l'iode sont déjà sur le marché. Ces bonnes performances sont liées à la très basse énergie de dissociation de I_2, produisant un plasma similaire à un plasma de xénon. À quel point peut-on négliger la nature moléculaire et électronégative des plasmas d'iode ? Un modèle global de plasma d'iode est amélioré et recodé en python, permettant des analyses paramétriques rapides, la quantification des incertitudes, et intégrant des effets électronégatifs. Des outils et procédures sont mis en place pour la pérennité des installations durant les expériences à l'iode. Quatre diagnostics optiques sont développés et installés sur la chambre d'ionisation du propulseur PÉGASES. Ils mènent, pour la première fois, à la température de I, ainsi qu'à la densité de I et I_2: spectroscopie d'émission, spectroscopie d'absorption laser et absorption saturée à $10\,969\,\mathrm{cm}^{-1}$ et $11\,036\,\mathrm{cm}^{-1}$, absorption laser à $7603\,\mathrm{cm}^{-1}$, et absorption large-bande de 480 nm à 500 nm. Confronter ces données et celles issues d'une sonde de Langmuir au modèle global montre que le modèle surestime la dissociation de I_2 et la densité électronique. Ces écarts peuvent être partiellement expliqués par des pertes de puissance sous-estimées dans le plasma, possiblement liées à sa nature moléculaire et électronégative. Ce travail donne des pistes pour de nouvelles études théoriques et de nouveaux diagnostics sur les plasmas d'iode. Il propose un modèle mis à jour et un panel de nouveaux diagnostics, utiles pour le développement de nouveaux systèmes de propulsion à l'iode.

Mots clés : Iode, propulsion, carburant, laser, modèle global, diagnostics.

Iodine plasmas: experimental and numerical studies Application to electric propulsion

Abstract: Iodine is an alternative propellant for the electric propulsion of satellites, offering performances comparable to xenon. As of 2020, propulsion systems running on iodine are already on the market. These good performances are linked to the very low dissociation energy of I_2, leading to a plasma similar to an atomic xenon plasma. To which extent can the molecular and electronegative nature of iodine plasmas be neglected? An existing global model for I_2 plasmas is further developed and fully recoded in python, to enable fast parametric studies, uncertainty quantification, and integrate electronegative effects. Tools and processes are developed to ensure the safety of operators and experimental setups during iodine experiments. Four optical diagnostics are developed and installed on the ionization chamber of the PEGASES thruster. They lead for the first time to the density and temperature of I, and the density of I_2: emission spectroscopy, laser absorption coupled to Doppler-free saturated absorption spectroscopy at $10\,969\,\mathrm{cm}^{-1}$ and $11\,036\,\mathrm{cm}^{-1}$, laser absorption spectroscopy at $7603\,\mathrm{cm}^{-1}$, and broadband absorption spectroscopy from 480 nm to 500 nm. Langmuir probe measurements yield the electron density and temperature. Confronting this data to the model shows that the model overestimates the molecular dissociation and the electron density. These discrepancies can be partly explained by underestimated power losses phenomena in the plasma, possibly linked to its molecular and electronegative nature. This work gives leads for future theoretical work and diagnostics on I_2 plasmas. It proposes an updated model and a set of new diagnostics for use to further develop iodine-based propulsion systems.

Keywords : Iodine, propulsion, propellant, laser, global model, diagnostics.